Quantum Transport in Indium Antimonide Nanowires

—

Investigating building blocks for Majorana devices

Quantum Transport in Indium Antimonide Nanowires
—
Investigating building blocks for Majorana devices

Proefschrift

ter verkrijging van de graad van doctor
aan de Technische Universiteit Delft,
op gezag van de Rector Magnificus Prof. ir. K.C.A.M Luyben,
voorzitter van het College voor Promoties,
in het openbaar te verdedigen op maandag 6 oktober 2014 om 12:30 uur

door

Ilse VAN WEPEREN

Natuurkundig ingenieur
geboren te Drachten.

Dit proefschrift is goedgekeurd door de promotoren:
Prof. dr. ir. L.P. Kouwenhoven
Prof. dr. E.P.A.M. Bakkers

Samenstelling van de promotiecommissie:

Rector Magnificus	Voorzitter
Prof. dr. ir. L.P. Kouwenhoven	Technische Universiteit Delft, promotor
Prof. dr. E.P.A.M. Bakkers	Technische Universiteit Delft, promotor
Dr. M.T. Wimmer	Technische Universiteit Delft
Prof. dr. T. Schäpers	Forschungszentrum Jülich
Prof. dr. ir. W. G. van der Wiel	Universiteit Twente
Prof. dr. J. Nygård	Niels Bohr Institute Kopenhagen
Prof. dr. Ya. M. Blanter	Technische Universiteit Delft
Prof. dr. ir. L.M.K. Vandersypen	Technische Universiteit Delft, reservelid

ISBN: 978-90-8593-195-9

Casimir PhD Series, Delft-Leiden 2014-22

Cover design: Avalon Designs || avalondesigns.nl
Printed by: Proefschriftmaken.nl || Uitgeverij BOXPress

Summary

Recently ideas to engineer Majorana fermions in the solid state have been developed. These Majoranas, quasiparticles that are their own antiparticle, have received much attention, as they are expected to fulfill non-Abelian exchange statistics and could potentially function as fault-tolerant quantum bits. This thesis focuses on a Majorana host system consisting of a semiconductor nanowire with a strong spin-orbit interaction contacted by a superconductor placed in a magnetic field. The properties of the semiconductor nanowire relevant to the stability and controllability of Majorana devices, namely its spin-orbit strength and its disorder, are studied experimentally for the case of indium antimonide (InSb) nanowires. The synthesis and electrical properties of small networks of nanowires, needed to probe the exchange statistics of Majoranas, are also investigated. Besides a study of their potential for Majorana devices, these experiments also explore the mesoscopic physics in InSb nanowires.

First the quantization of conductance at non-zero magnetic field is studied. Such conductance quantization, which has not been observed before in self-assembled nanowires, indicates ballistic transport and therefore a low degree of disorder. The conductance plateaus are studied as a function of source-drain bias and magnetic field, thereby enabling the extraction of the Landé g factor and the subband spacing. Next, it is shown that nanowires can cross and merge during growth, thereby forming nanocrosses. These nanocrosses, a proof of concept for the synthesis of nanowire networks, can be single-crystalline. Electrical characterization shows that the properties of these nanocross devices are similar to those of single nanowire devices, indicating a high transparency of the nanowire-nanowire interface. Furthermore, the spin-orbit interaction strength in dual-gated devices is extracted from weak anti-localization. In order to extract spin-orbit strength the effect of confinement on dephasing in presence of a magnetic field and on spin relaxation has to be determined. This has so far not been done for self-assembled nanowires. Combining measurements and numerical simulations of these confinement effects a Rashba spin-orbit strength of 0.5 – 1 eVÅ is obtained, corresponding to a spin-orbit energy of 0.25 – 1 meV. Weak anti-localization is also studied as a function of temperature, angle of the magnetic field with respect to the nanowire and asymmetry of the applied gate voltages. Lastly, disorder is studied by extraction of low-temperature field-effect mobility. Adsorption of molecules onto the nanowire surface and the substrate is shown to strongly affect conductance. Reproducibly a mobility of approximately 25,000

cm^2/Vs, on par with the highest reported field-effect mobilities in self-assembled nanowires, is obtained.

Based on the results on spin-orbit strength and mobility a topological gap, the figure of merit of the stability and controllability of Majoranas, of several hundreds of millikelvin to approximately two Kelvin is estimated. Although this estimate does not contain all parameters that characterize Majorana devices, it is promising for InSb-nanowire-based Majorana devices.

Spin-orbit interaction and one-dimensional ballistic transport are thought to lead also to a quasi-helical state, in which spin and momentum are strongly correlated. Although detection of a helical signature in measurements of quantized conductance likely requires less disorder than is currently present in InSb nanowires, a more indirect signature can possibly be obtained.

Samenvatting

Recentelijk zijn ideen ontwikkeld om Majorana fermionen te creëren in vaste stof. Deze Majoranas, quasi-deeltjes die hun eigen antideeltje zijn, staan in de belangstelling omdat ze worden verwacht niet-Abelse statistiek te vertonen onder verwisseling van deeltjes. Ook kunnen ze mogelijk fungeren als fouttolerante kwantum bits. Dit proefschrift beschouwt een systeem dat Majoranas kan herbergen bestaande uit een halfgeleider nanodraad met sterke spin-baanwisselwerking in contact met een supergeleider geplaatst in een magneetveld. De eigenschappen van de halfgeleider nanodraad relevant voor Majorana *devices*, namelijk de sterkte van de spin-baanwisselwerking en de mate van wanorde, worden experimenteel onderzocht voor het geval van indium antimoon (InSb) nanodraden. De synthese en elektrische eigenschappen van kleine netwerken van nanodraden, nodig voor het meten van van de niet-Abelse statistiek van Majoranas, worden ook onderzocht. Behalve een onderzoek naar hun geschiktheid voor Majorana *devices* verkennen deze experimenten ook de mesoscopische fysica in InSb nanodraden.

Ten eerste is de kwantisatie van geleiding bij eindig magneetveld bestudeerd. Zulke kwantisatie van geleiding, nog niet eerder waargenomen in zelf-opgebouwde (*self-assembled*) nanodraden, wijst op ballistisch transport en daarmee een laag niveau van wanorde. De geleidingsplateaus worden bestudeerd als functie van het voltage dat is aangelegd over de nanodraad en de magneetveldsterkte, waaruit de Landé g factor en het energieverschil tussen de eerste en tweede subband worden bepaald. Vervolgens wordt aangetoond dat nanodraden kunnen kruizen en versmelten tijdens hun groei, resulterend in nanokruizen. Deze nanokruizen, die het concept nanodraadnetwerken aantonen, kunnen monokristallijn zijn. Elektrische karakterisatie toont aan dat de eigenschappen van nanokruis *devices* vergelijkbaar zijn met die van enkele nanodraad *devices*. Dit wijst op een hoge mate van transparantie van het nanodraad-nanodraad grensvlak. Vervolgens is de sterkte van de spin-baanwisselwerking verkregen uit metingen van zwakke anti-lokalisatie. Om dit te doen moet het effect van opsluiting op zowel het verlies van fase-informatie van elektronen in een magneetveld als op de relaxatie van de spin worden bepaald. Tot nu toe is dit voor zelf-opgebouwde nanodraden nog niet gedaan. Door transportmetingen en simulaties van de effecten van zulke opsluiting te combineren is een Rashba spin-baanwisselwerkingssterkte $\alpha \sim 0.5 - 1$ eVÅ verkregen, hetgeen overeen komt met een spin-baanwisselwerkingsenergie van 0.25 – 1 meV. Ook is zwakke anti-lokalisatie onderzocht als functie van de temperatuur, de hoek van het magneetveld ten opzichte van de nanodraad en de mate van asymmetrie van de *gate* voltages. Als laatste is de mate van wanorde bestudeerd door de bepaling van lage-temperatuur veldeffectmobiliteit. De adsorptie van moleculen op het oppervlakte van de nanodraad en op het substraat blijkt de geleiding sterk te beïnvloeden. Herhaaldelijk is een mobiliteit van rond de 25,000 cm^2/Vs, vergelijkbaar met de hoogste gerapporteerde veldeffectmobiliteiten in zelf-opgebouwde nanodraden, verkregen.

Gebaseerd op de resultaten op het gebied van spin-baanwisselwerking en mobiliteit kan de topologische kloof (*topological gap*), het prestatiegetal van de stabiliteit en controlleerbaarheid van Majorana fermionen, woren bepaald. Deze topologische kloof bedraagt enkele honderden milliKelvin tot bij benadering twee Kelvin. Hoewel deze schatting niet alle parameters bevat die Majorana *devices* karakteriseren, is deze topologische kloof veelbelovend voor Majorana *devices* gebaseerd op InSb nanodraden.

De combinatie van spin-baanwisselwerking en eendimensionaal ballistisch transport creëert naar verwachting ook een quasi-helische toestand waarin spinrichting en impuls een sterke correlatie hebben. Hoewel de detectie van een helische toestand door middel van metingen van gekwantiseerde geleiding waarschijnlijk een lagere mate van wanorde vereist dan nu aanwezig is, kan mogelijkerwijs wel een meer indirecte aanwijzing voor de aanwezigheid van zo'n helische toestand worden verkregen.

Contents

CHAPTER 1

INTRODUCTION

1.1 Quantum computing

The microscopic world, governed by the laws of quantum mechanics, seems at first too strange to comprehend, let alone to control and to put to use. Still, this is exactly what building a quantum computer entails: using the bizarre concepts of the quantum world, such as superposition states — a particle can be in two states at the same time — or quantum measurement — the state of a particle is altered by its detection — and turning these seemingly impractical properties into technology. In fact, these quantum properties give a quantum computer its advantages with respect to its classical counterpart. Quantum algorithms, procedures that make use of the quantum mechanical properties of the computer, are predicted to solve certain problems, such as factoring large numbers or searching unstructured databases, faster than classical algorithms [1]. Therefore some problems that are intractable on a classical computer can be solved on a quantum computer. Quantum computers are expected to outperform classical computers for instance in the field of data decryption [2]. They are also expected to allow simulations of quantum systems [2], for which classical computers are not well-equipped. Simulations of quantum systems are very valuable as they allow us to better understand the interactions between elements, and would for instance be key to the development of new medicine and new materials. Related quantum technologies are expected to allow exchange of information using quantum states, which facilitates safe data transfer, and to allow more accurate definitions of our standard of measurements [2]. More applications of quantum technologies will likely be developed in the future. Governed by these prospects, research on the building blocks of a possible quantum computer — its hardware — is ongoing in numerous systems.

1.2 Quantum bits

As in classical hardware, the elemental unit of computation in a quantum computer is a two-level system. Unlike a classical bit, which can be only 1 or 0, in a quantum bit (qubit) superposition states, such as $\frac{1}{\sqrt{2}}(0+1)$ are possible [1]. Such states will have to be initialized, read out and manipulated to be able to function as information carriers [3]. The manipulation of a quantum bit — for instance changing its state from 0 to 1 — is done, similarly to classical computation, by creating a suitable interaction between the two-level system and control technology. For instance, applying a light pulse or a voltage pulse can result in the desired operation.

In this respect the superposition state is what makes a qubit potentially powerful, but also makes its operation challenging [2]: not only can there be a 'classical' error in which a bit unintentionally changes its value — a bit flip —, the coherence of the superposition state can also be lost. In the superposition state $\frac{1}{\sqrt{2}}(0+1)$ above, a change of phase of the 1 state by π will result in $\frac{1}{\sqrt{2}}(0-1)$, a state different from its initial state, and therefore constitutes a loss of information. Such loss of coherence will limit the time during which the qubit can be used in computation. As the loss of coherence results from interactions of the qubit with its environment, this creates the problematic situation that interactions with the outside world are essential to qubit operation, but at the same time lead to loss of the qubit state.

Remedies for the loss of coherence of these fragile qubits are being developed, such as dynamical decoupling techniques [4] to preserve coherence and quantum error correction schemes [5], in which redundancy is used to correct qubits that have undergone an unwanted alteration. An alternative approach is also pursued, in which one searches for more robust hardware: fault-tolerant quantum bits that are not hindered by their environment, while still being able to control the quantum state. This is where topological qubits are envisioned to play a role.

1.3 Topological quantum bits: non-Abelian anyons

The field of topology studies the properties of space that are preserved under continuous deformation [6]. Such continuous deformations can be stretching or bending a geometry, but not tearing it or gluing segments together. In other words, topology is about properties that are robust to local perturbations, which is what is needed to make fault-tolerant quantum bits.

Where in nature can one find such a topological system? It has been shown that non-Abelian states of matter posses these topological properties [7]. In order to understand what makes a non-Abelian state different from an ordinary (Abelian) state, we consider the effects of interchanging particles (see also Figure 1.1), i.e. quantum exchange statistics [8]. In three dimensions, exchanging the position of two particles with the initial state Ψ can only result in either the same final state Ψ or in the state $-\Psi$. In this second case an overall phase of π has been obtained by exchange[1]. The particles are said to be bosons and fermions respectively.

---

[1] Note that the phase described here is different from that of the superposition state in Section 1.2. In the previous section the phase, φ, concerns only the component 1 in the state $0+e^{i\varphi}1$. Here it is a prefactor of the full quantum state $e^{i\varphi}\Psi$.

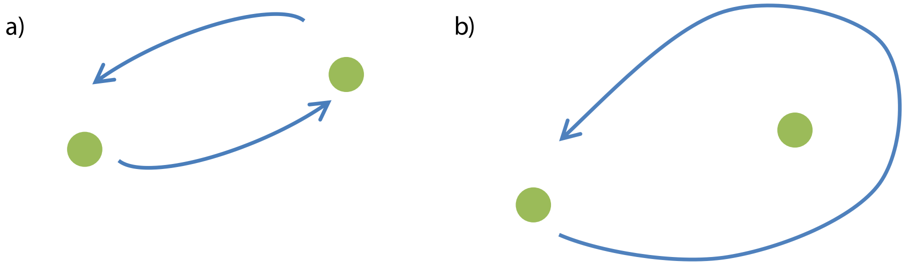

Figure 1.1: Exchange of particles. **a)** A swap, or exchange, of two particles. **b)** A double swap equals moving the one particle around the other one in a full loop.

In two dimensions particle exchange can have more striking effects. An intuitive explanation [9] of the difference between particle exchange in two and three dimensions relies on two succesive exchanges, which equals a full circulation of one particle around another one (see Figure 1.1b). In three dimensions such a loop can be continuously deformed into the identity operation by pulling the loop to a side, so that it does not encircle the particle any more. Since a double exchange equals identity, a single exchange can only yield a phase of 0 or π. However, by restricting the loop to two dimensions a continuous deformation to a trivial loop cannot be made, and therefore the circulation cannot be reduced to the identity operation. A single exchange can lead to a(ny) phase different from 0 or π. Particles with this exchange statistics are anyons. Furthermore, under certain conditions exchange of particles can lead to a final state that is a unitary transformation of the initial state, with as a final state a different ground state of the system [8]. In other words, the effect of exchanging — also known as braiding — is to perform an operation on the particles. In this case the particle is called a non-Abelian anyon. It is non-Abelian because the state after several exchanges of the particles depends on the order in which exchanges have been performed. This can be understood by considering that the braiding operation can be represented by a unitary matrix. Repeated exchange is represented by a multiplication of matrices. Matrix multiplication is in general non-commutative (non-Abelian): the result depends on the order in which these operations are performed.

The non-Abelian state combines properties that make it very suitable for computing: its topological properties make it insensitive to local disturbances, while its exchange statistics allows one to manipulate the quantum state, thereby performing the desired operations [10].

Several systems have been proposed to host non-Abelian anyons [8], but so far there is no experimental proof of the existence of such particles. One of the systems in which non-Abelian anyons may appear is that of a topological superconductor. In this system the non-Abelian anyons take the form of Majorana fermions.

1.4 Solid state Majorana fermions

Majorana fermions arise as real solutions of the Dirac equations [11]. They are therefore their own anti-particle: $\Psi^\dagger = \Psi$. They are sought after in elementary particle physics [12], but have also been shown theoretically to arise in certain carefully engineered condensed matter systems [13],[14]. Several properties of the Majorana states in condensed matter systems are listed here [15] to give an idea how they can function as qubits.

- A conventional fermion can be written as the sum of two Majorana fermions

  $$f = \frac{\gamma_1 + i\gamma_2}{2} \tag{1.1}$$

  using a fermion annihilation (creation) operator f ($f^\dagger$) and Majorana fermion operator γ. The inverse relation is given by

  $$\gamma_1 = f + f^\dagger \tag{1.2}$$

  and

  $$\gamma_2 = i(f - f^\dagger) \tag{1.3}$$

  showing that Majorana fermions are indeed their own anti-particle: $\gamma^\dagger = \gamma$. Although all fermions can be written as a sum of two Majorana fermions, this description is only a meaningful statement when the Majorana fermions are spatially separated so they can be addressed individually.

- Using the fermionic anti-communication relation it is shown that

  $$\{\gamma_i, \gamma_j\} = 2\delta_{ij} \tag{1.4}$$

  which results in $\gamma_i^\dagger \gamma_i = \gamma_i^2 = 1$. One therefore cannot speak about the occupancy of a Majorana mode in the same way as the occupation of for instance a fermionic state.

  Instead a series of Majorana fermions can be described by its fermionic number state $|n_1, n_2, ...n_N\rangle$ with $n_i = f_i^\dagger f_i$. Without interaction between these Majorana fermions their energy will be zero (see Section 2.1 and Section 2.2), independent of the corresponding fermionic states being occupied or not, thereby forming a degenerate ground state. The sum of the fermionic occupation $\sum_{i=1}^{N} n_i$ being even or odd defines the parity of the state.

- Topological qubits can be defined using four Majorana fermions (two fermions). The two-level system is given by two fermionic states of the same parity, meaning that qubit states 0 and 1 are either given by fermion number states $\{|00\rangle, |11\rangle\}$ (even parity) or by $\{|01\rangle, |10\rangle\}$ (odd parity).

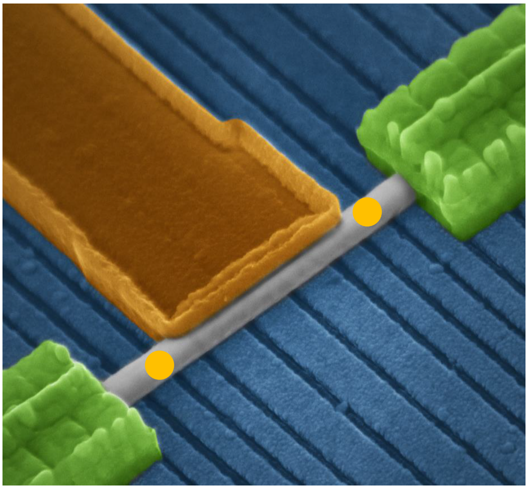

Figure 1.2: Coloured scanning electron microscope image of an actual hybrid semiconductor-superconductor device. The InSb nanowire is depicted in grey, the superconductor metal (NbTiN) in gold, gates underneath the device are blue. The green (non-superconducting metal) contacts to the nanowire are used to detect Majorana fermions as reported in [17]. The expected positions of the pair of Majorana fermions are depicted by the orange dots.

> It can be shown [15],[16] that repeated braiding in such a system with four Majorana fermions brings the system from one ground state to another (e.g. from $|00\rangle$ to $|11\rangle$). Furthermore, the outcome of a series of braiding operations depends on the order in which they are performed, i.e. Majorana fermions satisfy non-Abelian exchange statistics.
>
> In a qubit context braiding corresponds to a single-qubit rotation over an angle $\frac{\pi}{2}$ around the x, y or z axis of the Bloch sphere (an explanation of the Bloch sphere is found in [1]). The rotation axis depends on which two out of the four Majorana fermions are exchanged.

The above list of properties gives two reasons to create Majorana fermions in the solid state: first, they may allow detection of a non-Abelian state of matter, and second, they may allow fault-tolerant quantum computation. Although the topologically protected braiding operations do not constitute a full set of operations needed to perform quantum algorithms, they can be complemented by operations that are not topologically protected [7].

Theoretical explorations have identified several solid state systems that could host Majorana fermions [14], [12]. This thesis focuses on one such system, a semiconductor nanowire in contact with a superconductor [18],[19] shown in Figure 1.2.

1.5 Majorana fermions in nanowire-based devices: material requirements

The first sections of the theory chapter of this thesis, Section 2.1 and Section 2.2, describe how in such a hybrid semiconductor-superconductor system Majorana fermions arise. This description allows us to define in Section 2.2.1 in a qualitative way the requirements that a nanowire device has to fulfill to create Majorana fermions. These requirements are summarized here as they are the motivation for the research in the experimental chapters of this thesis.

1. Superconductivity is induced in the nanowire.
2. The semiconductor nanowire has a large spin-orbit interaction and a large Landé g factor.
3. There is little disorder in the nanowire. The nanowire has a high mobility or shows ballistic transport signatures.
4. Small networks of nanowires can be formed.

The last item is not a requirement for creation of Majorana, but rather a requirement for braiding. The research described in this thesis focuses on the 2^{nd}, 3^{rd} and 4^{th} requirement. Induced superconductivity, although central to Majorana fermion physics, is not considered.

1.6 Aim and contents of this thesis

This thesis describes a number of experiments in which the properties of the semiconductor relevant to Majoranas, namely the spin-orbit interaction strength, the degree of disorder and the ability to create nanowire networks, are investigated. While these material requirements for Majorana devices unify the research described in this thesis, the mesoscopic physics encountered in InSb nanowires is interesting in its own right. Moreover, InSb nanowires may also be suitable for purposes other than the study of Majorana fermions. The experimental chapters are therefore not limited to findings relevant to Majorana research, but rather focus on the physics observed in these nanostructures.

The remainder of this thesis is structured as follows.

- In Chapter 2 the theory necessary to understand the material requirements listed in the previous section as well as the experiments in Chapters 4 – 7 is described. Section 2.1 and Section 2.2 describe the emergence of Majorana fermions in a hybrid semiconductor-superconductor system. Section 2.3 describes the theory of quantized conductance with and without spin-orbit interaction, applicable in part to Chapter 4. Section 2.4 and Section 2.5 describe theory on (Rashba) spin-orbit interaction and quantum interference relevant to Chapter 6.

- Chapter 3 explains the experimental and numerical methods used to study InSb nanowires.
- Chapter 4 describes the observation of quantized conductance, indicating quantum ballistic transport, in an InSb nanowire.
- Chapter 5 describes the formation and electronic properties of InSb nanocrosses. This is a first step towards small networks of nanowires.
- Chapter 6 describes the extraction of spin-orbit interaction strength from measurements of magnetoconductance in InSb nanowire devices.
- Chapter 7 returns to the topic of disorder in nanowires by describing measurements of field-effect mobility in InSb nanowires.
- Chapter 8 summarizes the experimental findings, discusses the resulting topological gap, gives ideas for further study and identifies alternatives to n-type InSb-nanowire based Majorana devices. The last topic of this chapter assesses the feasibility of detection through measurements of quantized conductance of the quasi-helical state that arises in a one-dimensional system with strong spin-orbit interaction.

CHAPTER 2

THEORY

This chapter starts in Section 2.1 with a description of a toy model known as the Kitaev chain [20] that shows that Majorana fermions appear in a spinless p-wave superconductor. It is shown in Section 2.2 that such a spinless p-wave superconductor can also be created in a hybrid semiconductor-superconductor device [18],[19], that can therefore also host Majoranas. Section 2.1 and Section 2.2 are mostly based on [15], that provides a good introduction to Majorana fermion physics. Subsequently material requirement for creation of Majoranas in such hybrid devices are identified in Section 2.2.1.

Section 2.3 describes the quantization of conductance in a one-dimensional system, observed in Chapter 4. The conductance of the quasi-helical state that arises when a magnetic field and spin-orbit interaction are introduced is also outlined. Rashba spin-orbit interaction and the resulting spin precession and spin relaxation are discussed in Section 2.4. Weak-field magnetoconductance measurements in a diffusive sample, presented in Chapter 6, allow extraction of Rashba spin-orbit interaction strength. Section 2.5 presents the underlying theory of quantum diffusive transport.

2.1 The Kitaev chain

Consider a Hamiltonian that describes a tight-binding chain with p-wave superconducting pairing,

$$H_{\text{chain}} = -\mu \sum_{i=1}^{N} n_i - \sum_{i=1}^{N-1} \left(t c_i^\dagger c_{i+1} + \Delta c_i c_{i+1} + h.c. \right), \tag{2.1}$$

in which μ denotes the electrochemical potential, Δ the superconducting gap and t the hopping amplitude between sites. $h.c.$ denotes hermitian conjugate. Δ and t are the same for all sites, and the superconducting phase is zero, giving $\Delta = |\Delta|$. Electron creation (annihilation) on site i is described by $c_i^\dagger$ (c_i). The number operator is defined as $n_i = c_i^\dagger c_i$. Note that Equation (2.1) does not contain spin indices: it is an

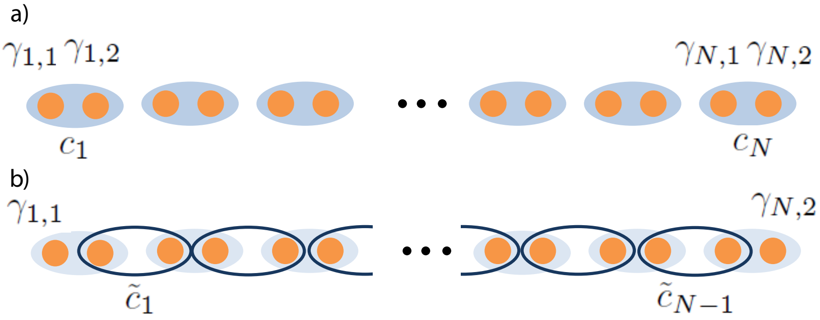

Figure 2.1: A tight-binding chain with p-wave pairing. **a)** Each fermion, denoted by its annihilation operator, c_i, can be represented as two Majorana fermions, $\gamma_{i,1}$ and $\gamma_{i,2}$. **b)** Under certain conditions (see text) the chain can be described by a coupling of Majoranas of neighbouring fermions, creating new fermions, denoted by $\tilde{c}_i$. Note that a non-local fermion is formed by coupling the two Majoranas at the ends of the chain, $\gamma_{1,1}$ and $\gamma_{N,2}$.

equation for a single spin, and therefore for an effectively spinless system. Also note that the superconducting pairing is of p-type: pairing occurs between electrons with the same (suppressed) spin on adjacent sites. The chain is shown in Figure 2.1.

Majorana operators, obtained by writing the fermion operators as composed of a real and an imaginary part, are defined as

$$c_i = \frac{1}{2}(\gamma_{i,1} + i\gamma_{i,2}) \tag{2.2}$$

and

$$c_i^\dagger = \frac{1}{2}(\gamma_{i,1} - i\gamma_{i,2}). \tag{2.3}$$

Now consider the situation $\mu = 0$, $t = \Delta$. Inserting Equation (2.2) and Equation (2.3) into Equation (2.1) results in

$$H_{\text{chain}} = -it \sum_{i=1}^{N-1} \gamma_{i,2}\gamma_{i+1,1}. \tag{2.4}$$

This corresponds to a pairwise coupling of Majoranas of neighbouring fermions that can be described in terms of fermion operators

$$\tilde{c}_i = \frac{\gamma_{i+1,1} + i\gamma_{i,2}}{2}. \tag{2.5}$$

The Hamiltonian can be expressed in terms of these new fermions,

$$H_{\text{chain}} = 2t \sum_{i=1}^{N-1} \tilde{c}_i^\dagger \tilde{c}_i, \tag{2.6}$$

showing that these states have an energy $2t$. This situation is shown schematically in Figure 2.1b.

Importantly, the Majorana operators on the edge of the wire, $\gamma_{N,2}$ and $\gamma_{1,1}$, are absent from Equation (2.4). Similar to the Majorana pairs of Equation (2.5) these can be expressed as a fermionic state,

$$\tilde{c}_M = \frac{1}{2}(\gamma_{N,2} + i\gamma_{1,1}). \tag{2.7}$$

Equation (2.7) is however not a normal fermionic state, but rather a non-local one. Moreover, as $\tilde{c}_M$ is absent from Equation (2.4) it is a state at zero energy. The state can be either filled with a fermion (corresponding to $\tilde{n}_M = \tilde{c}_M^\dagger \tilde{c}_M = 1$), or be empty ($\tilde{n}_M = \tilde{c}_M^\dagger \tilde{c}_M = 0$), but it will have the same (zero) energy, meaning that it is a twofold degenerate state. It can be shown [20] that the presence of such Majorana end states is not restricted to $\mu = 0,\ t = \Delta$. They occur if the chemical potential lies within the gap, $|\mu| < 2t$, although in the general case they are not localized at a single site, but decay exponentially away from the edges.

Anticipating a description of a system based on a one dimensional nanowire, the Hamiltonian describing the continuum version of Equation (2.1) is introduced. It is given by

$$H_{1D}^{pw} = \int dx \left[\Psi^\dagger(x) \left(\frac{\hbar^2 k_x^2}{2m^*} - \mu \right) \Psi(x) + \Psi(x) |\Delta| \hbar k_x \Psi(x) + h.c. \right] \tag{2.8}$$

with real-space creation (annihilation) operator, $\Psi^\dagger(x)$ ($\Psi(x)$), momentum, $\hbar k_x$, and effective mass, m^*.

2.2 Majorana fermions in hybrid semiconductor-superconductor devices

We now seemingly change topic and consider a one-dimensional nanowire with Rashba spin-orbit interaction (SOI) in the presence of a magnetic field, B. The nanowire is contacted by a superconductor, giving a proximity pairing potential Δ. The nanowire axis is along $\hat{x}$, giving momentum, $\hbar k_x$. Rashba SOI (see Section 2.4), assuming electric field $\vec{E} = E\hat{z}$, is described by $-\alpha_R k_x \sigma_y \hat{y}$. B is oriented along $\hat{z}$, perpendicular to the SOI field, giving rise to a Zeeman field, $g\mu_B B$, with g factor, g, and the Bohr magneton, μ_B. This geometry is shown schematically in Figure 2.2. The Hamiltonian describing this system is

$$H = \sum_{\sigma=\uparrow,\downarrow} \int dx \left[\Psi_\sigma^\dagger(x) \left(\frac{\hbar^2 k_x^2}{2m^*} - \mu - \alpha_R k_x \sigma_y + \frac{g\mu_B B \sigma_z}{2} \right) \Psi_\sigma(x) + \Psi_\downarrow(x) \Delta \Psi_\uparrow(x) + h.c. \right] \tag{2.9}$$

A justification of the form of the superconducting pairing term is given in [14].

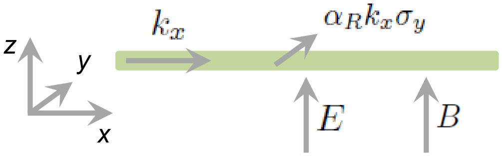

Figure 2.2: Orientation of the nanowire and the directions of relevant fields. The nanowire axis is placed along $\hat{x}$, with spin-orbit interaction, $\alpha_R k_x \sigma_y$, in the $\hat{y}$ direction due to an electric field, $E\hat{z}$. Magnetic field, B, points along $\hat{z}$.

To understand the physics resulting from these components we first consider the single subband spectrum without superconductivity and magnetic field, $\Delta = B = 0$ in Figure 2.3a. The SOI lifts the spin degeneracy, shifting the momentum of the two spin states, ← and →, by $\pm k_{so} = \pm \frac{m\alpha_R}{\hbar^2}$. The corresponding spin-orbit energy scale is $E(k_{so}) = E_{SO} = \frac{m\alpha^2}{2\hbar^2}$.

Application of a magnetic field creates an anti-crossing at $k_x = 0$ of size $g\mu_B B$ (Figure 2.3b). The energy of the upper (lower) subband, $E_\pm$, is given by

$$E_\pm = \frac{\hbar^2 k_x^2}{2m^*} \pm \sqrt{\left(\frac{g\mu_B B}{2}\right)^2 + (\alpha_R k_x)^2}\,. \tag{2.10}$$

Momentum and spin are correlated. For instance, in the lower subband spin is oriented ↓ at $k_x = 0$ as a result of the Zeeman field, but → (←) at large negative (positive) k_x due to the SOI. When the electrochemical potential is placed within the Zeeman gap (see Figure 2.3b) only states at large positive and negative k_x contribute to transport. At weak B these states with opposite direction of propagation will have nearly opposite spins, thereby resembling a helical state [18].

This peculiar band structure allows effective p-wave pairing in the presence of an s-wave superconductor. To understand this we consider the situation $\alpha_R k_{so} \approx E_{SO} \ll g\mu_B B$ in which the bands are nearly spin-polarized and well-separated, so that at low electrochemical potential the upper subband can be neglected (Figure 2.3c). We focus on the lower subband, described by operator Ψ_-

$$\Psi_- = \frac{1}{\sqrt{1+\gamma^2}}\left(\Psi_\downarrow + i\gamma\Psi_\uparrow\right) \tag{2.11}$$

with $\gamma = \frac{\alpha_R k_x}{g\mu_B B} \ll 1$. We turn on $\Delta \ll g\mu_B B$. The pairing term $\Psi_\downarrow(x)\Delta\Psi_\uparrow(x)$ in Equation (2.9) can be expressed in terms of Ψ_- using Equation (2.11), yielding an expression for the lower subband

$$H_{\text{eff}} \sim \int dx \left[\Psi_-^\dagger(x)\left(\frac{\hbar^2 k_x^2}{2m^*} - \mu_{\text{eff}}\right)\Psi_-(x) + i\Delta_{\text{eff}}\Psi_-(x)\hbar k_x \Psi_-(x) + h.c.\right], \tag{2.12}$$

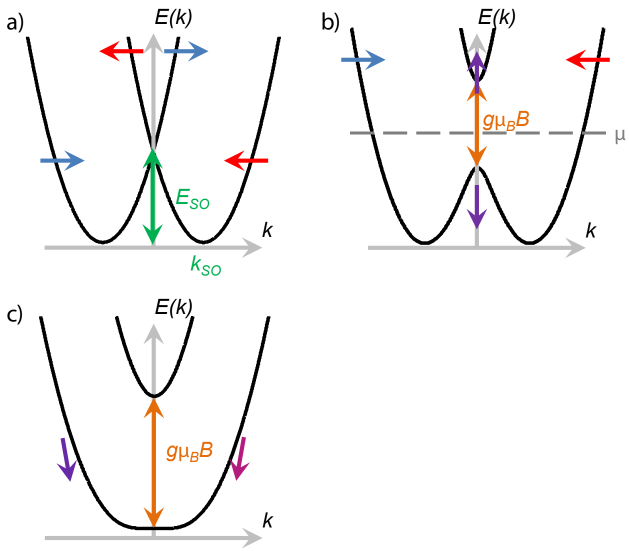

Figure 2.3: Nanowire energy spectrum in the presence of Rashba SOI and magnetic field, B. **a)** The Rashba SOI leads to a spin splitting in the absence of B. The spin of each subband is indicated, as well as the spin-orbit wave vector, k_{so}, and the spin-orbit energy, E_{SO}. **b)** A magnetic field perpendicular to the spin-orbit field leads to an avoided crossing at $k = 0$ with size $g\mu_B B$. μ denotes the electrochemical potential. Here $E_{SO} \approx g\mu_B B$. **c)** At $g\mu_B B \gg E_{SO}$ subbands are nearly spin-polarized, but maintain a small misalignment in spin due to SOI.

with effective p-wave pairing amplitude, $\Delta_{\text{eff}} \sim \frac{\alpha_R \Delta}{g\mu_B B}$, and with effective potential, $\mu_{\text{eff}} = \mu + \frac{g\mu_B B}{2}$ [21]. Equation (2.12) describes spinless p-wave pairing, as can be verified by comparison to Equation (2.8). As Majorana fermions appear in spinless p-wave superconductors (see Section 2.1) the hybrid semiconductor-superconductor system too can host Majorana fermions.

The energy spectrum of the proximitized spin-orbit nanowire (Figure 2.4a) contains two energy gaps, one at $k = 0$, denoted by E_0, and one at $k \approx 2k_{SO}$, denoted by E_1. E_0 is given by [18]

$$E_0 = |g\mu_B B - \sqrt{\Delta^2 + \mu^2}|. \tag{2.13}$$

Increasing B from zero, the gap at $k = 0$ will therefore close (shown in Figure 2.4b) when

$$g\mu_B B = \sqrt{\Delta^2 + \mu^2} \tag{2.14}$$

and re-open when B is increased further. We distinguish between the parity dominated regime that occurs before the gap closes, $g\mu_B B < \sqrt{\Delta^2 + \mu^2}$, and the Zeeman

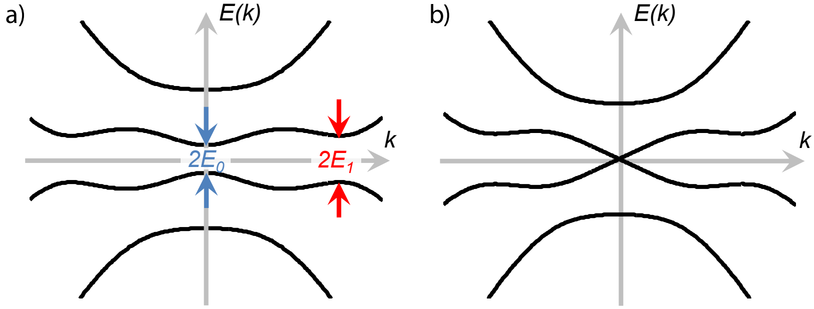

Figure 2.4: Electron-hole symmetric spectra of the hybrid semiconductor-semiconductor system. The spectra are obtained by the introduction of Nambu spinors to derive a matrix representation of Equation (2.9) [15]. **a)** The spectrum contains a gap at $k = 0$, which can be closed and opened by controlling the electrochemical potential and the magnetic field. A second gap is created at larger k. **b)** Under certain conditions (see main text) the gap at $k = 0$ closes, giving rise to Majoranas at $E = 0$. Note that these spectra describe an infinite, homogeneous system.

dominated regime after re-opening of the gap, $g\mu_B B > \sqrt{\Delta^2+\mu^2}$. As shown above, Majoranas appear when $\Delta \ll g\mu_B B$, $\mu = 0$, corresponding to the Zeeman dominated regime. A more involved derivation [18],[19] shows that Majoranas appear not only when this condition is fulfilled, but always when $g\mu_B B \geq \sqrt{\Delta^2+\mu^2}$. The device is in a topological state, with Majorana fermions situated at the end of the region where nanowire and superconductor overlap.

The gap at larger k, E_1, equals $|\Delta|$ when $g\mu_B B \ll E_{SO}$, while when $g\mu_B B \gg E_{SO}$ it is reduced to $E_1 = 2\,\Delta\sqrt{\frac{E_{SO}}{g\mu_B B}}$ [22]. The smaller of the two gaps in the topological state defines the effective (topological) gap, $E_{tg} = \min(E_0, E_1)$. Note that this expression does not include disorder.

The above theory can be extended to multi-subband systems [23], provided the number of channels is odd and the wire width does not exceed the superconducting coherence length [14].

2.2.1 Experimental requirements

The description of the conditions under which Majoranas appear also shows how to control them, namely with the magnetic field and with the electrochemical potential. The electrochemical potential can be changed locally with gates, placed for instance underneath the nanowire as shown in Figure 2.5a, making gates a powerful tool to position Majoranas and to controllably move them[1].

Requirements for creation of Majorana fermions in hybrid semiconductor-superconductor devices following from Section 2.2 are defined are follows.

---

[1] Besides gate-controlled schemes, also flux-controlled schemes for manipulation of Majoranas have been devised [24].

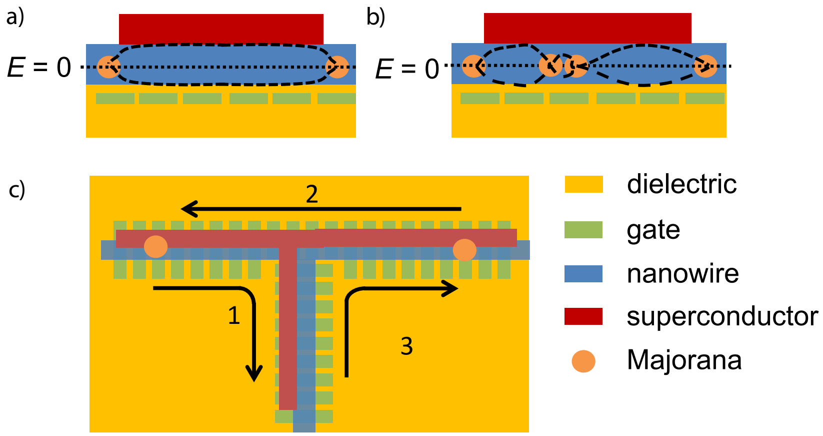

Figure 2.5: Schematics of nanowire-based devices to create and braid Majorana fermions. A legend is shown in the bottom right of the figure. **a)** A nanowire is deposited onto gates and (partially) covered with a superconductor. The gates tune the electrochemical potential in such a way that in the presence of a magnetic field Majoranas arise at the ends of the nanowire. The energy spectrum in the nanowire is gapped (indicated with dashed lines). **b)** Disorder leads to variations in the electrochemical potential, which may lead to an unintentional closing of the gap (indicated with dashed lines). At these points additional unwanted Majoranas arise. **c)** The exchange of Majoranas can take place in a T-shaped junction of two nanowires. One Majorana is (1) stored in the vertical part of the T, while (2) the other Majorana is moved across. Then (3) the first Majorana is moved to the right. This effectively exchanges the Majoranas.

1. The ability to **induce superconductivity in a nanowire**. Moreover, induced superconductivity has to be maintained in a magnetic field, favoring superconductors with a large critical field.

2. A semiconductor material with **strong spin-orbit interaction** to create the spin misalignment needed to create the effective p-wave pairing of Equation (2.12). Furthermore, a strong spin-orbit interaction creates a larger E_1 at large B and makes the system less vulnerable to disorder [25].

3. A semiconductor material with a **large g-factor**, so that the magnetic field required to create the Zeeman field of Equation (2.14) is relatively small. This allows one to maintain the induced superconductivity in the presence of a magnetic field.

4. **Low disorder** in the nanowire, as disorder leads to fluctuations in the electrochemical potential that may result in closing of the topological gap and therefore the creation of unwanted pairs of Majorana fermions as shown in Figure 2.5b. This calls for materials with a large mean free path, experimentally verified by measurements of **high mobility** or **ballistic transport**.

5. In order to probe the non-Abelian exchange statistics discussed in Section 1.3, nanowire junctions have to be created, forming a two-dimensional **network of nanowires** on which braiding operations can be performed. The exchange operations on such a nanowire junction (shown schematically in Figure 2.5c) are equivalent to exchange on a two-dimensional plane [21].

Sau *et al.* [26] study the topological gap as a function of the above parameters and find that, assuming a good superconductor-nanowire interface, obtaining as large as possible spin-orbit energy and a high mobility are most important.

2.3 Quantized conductance in quantum point contacts

Ballistic transport in one dimension results in conductance quantization. Hence such quantization can occur in clean semiconductor nanowires. SOI in combination with a magnetic field alters the quantization as will be explained in Section 2.3.1.

We consider transport through a one-dimensional channel of size L connected to reservoirs [27]. Confinement leads to quantized states normal to the wire axis. As before the propagation direction is taken along $\hat{x}$. The wave function can then be written as

$$\psi_n(k_x)(x,y,z) = \chi_n(y,z)\frac{1}{\sqrt{L}}e^{ik_x x}. \tag{2.15}$$

We furthermore assume a parabolic energy dispersion along the wire, giving a spectrum

$$E_n(k_x) = E_n + \frac{\hbar^2 k_x^2}{2m^*}, \tag{2.16}$$

with E_n the energy of the n^{th} subband.

The current contribution of states within the interval dk_x, $dI(k_x)$, is then expressed as

$$dI(k_x) = e\sum_{n,s}\frac{dk_x}{2\pi}v_x f(k_x) \tag{2.17}$$

where now a summation over all modes, n, and over the z-component of spin, $s = \frac{\pm\hbar}{2}$, is made. v_x denotes velocity. The Fermi-Dirac distribution function, $f(k_x)$, is given by

$$f(k_x) = f\left(E(k_x)-\mu\right) = \frac{1}{1+e^{\frac{E(k_x)-\mu}{k_B T}}}. \tag{2.18}$$

Using $dE = \hbar v_x dk_x$ the current contribution of Equation (2.17) can be expressed as

$$dI(E) = \frac{e}{h}\sum_{n,s} f(E)dE. \tag{2.19}$$

Note that the density of states, proportional to $\frac{dk_x}{dE}$, and velocity, cancel each other, thereby leading to a current contribution that only depends on the Fermi-Dirac distribution function.

Current is calculated by integrating over energy, with reservoirs at electrochemical potentials μ_L and μ_R respectively, giving

$$I = \frac{e}{h}\sum_{n,s}\int dE\left(f_L(E) - f_R(E)\right) = \frac{e^2}{h}\sum_{n,s} f_L(E_n)V \tag{2.20}$$

using $f_L(E) - f_R(E) = \frac{\partial f_L(E)}{\partial \mu_L}\left(\mu_L - \mu_R\right) = -\frac{\partial f_L(E)}{\partial E}eV$, valid when $\mu_L - \mu_R = eV$ is small, with voltage difference, V. Conductance $G = \frac{I}{V}$ is therefore quantized

$$G = \frac{e^2}{h}\sum_{n,s} f_L(E_n). \tag{2.21}$$

When $\mu > E_n$ $f_L(E_n) = 1$ and each spin-degenerate channel contributes $g_Q = \frac{2e^2}{h}$ to the conductance, while otherwise $f_L(E_n) = 0$. This leads to a stepwise increase in conductance with electrochemical potential shown in Figure 2.6a. Although this derivation assumes a one-dimensional channel, it was found that the above description also applies to a short constriction connected to wide reservoirs [28], [29].

2.3.1 Conductance of the quasi-helical state

The energy spectrum of Equation (2.10), that describes a one-dimensional system in the presence of spin-orbit interaction and a magnetic field can contain local extrema at energy E_i (see Figure 2.3b). The conductance can in this case be obtained [30] by examining the separate contributions of parts of the spectrum between local extrema and applying the approximation of small bias given below Equation (2.20). This yields

$$G = \frac{e^2}{h}\sum_{n,s}\sum_{i}\beta_i^{(n,s)} f_L(E_i^{(n,s)}) \tag{2.22}$$

in which β_i is +1 (-1) when E_i is a local minimum (maximum). Conductance at a given electrochemical potential can thus be found by counting the number of local extrema in the spectrum.

Application of Equation (2.22) in the absence of SOI and magnetic field yields conductance steps of $\frac{2e^2}{h}$ (spectrum and resulting conductance are shown in Figure 2.6a). Introducting SOI does not alter the conductance. If a magnetic field applied perpendicular to the spin-orbit field is added a Zeeman gap opens. With increasing μ the conductance now first increases to $\frac{2e^2}{h}$ when the electrochemical potential reaches the bottom of the first subband, but reduces again to $\frac{e^2}{h}$ when the local maximum at $k = 0$ is passed (Figure 2.6b). Increasing μ above the Zeeman gap brings the conductance back to $\frac{2e^2}{h}$. The Zeeman gap thus results in a region of reduced conductance.

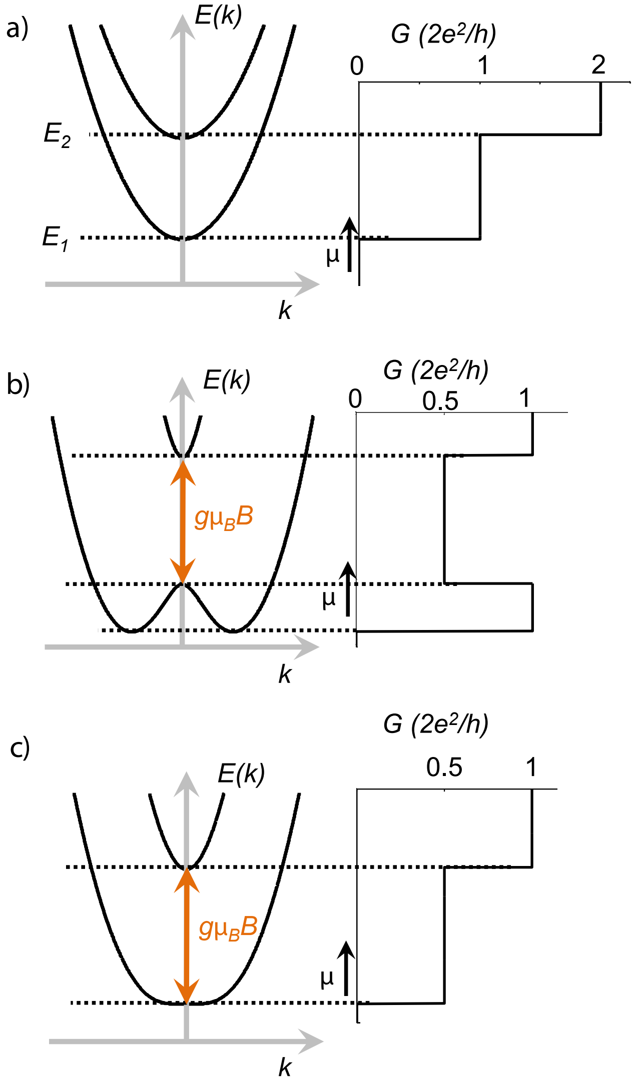

Figure 2.6: Energy spectra, $E(k)$, and conductance as a function of electrochemical potential, $G(\mu)$, in a (quasi-)one-dimensional channel with spin-orbit interaction, characterized by E_{SO} (see Section 2.2), and magnetic field, with associated eneryg scale $g\mu_B B$, the Zeeman energy. **a)** $E_{SO} = g\mu_B B = 0$. **b)** $g\mu_B B \approx E_{SO}$. A magnetic field oriented perpendicular to the spin-orbit field opens a Zeeman gap at $k = 0$. The lower subband is W-shaped with two local minima and a local maximum at $k = 0$. This leads to a reduction of conductance from $\frac{2e^2}{h}$ to $\frac{e^2}{h}$ when μ is placed within the Zeeman gap. This panel shows only the spectrum near the bottom of the first subband and the corresponding conductance region. **c)** At large magnetic field, $g\mu_B B \gg E_{SO}$, the conductance increases in steps of $\frac{e^2}{h}$.

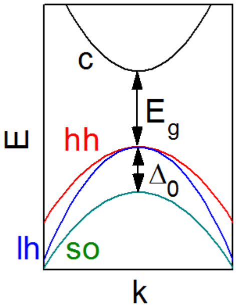

Figure 2.7: Band structure parameters obtained within the Kane model. c denotes the conduction band, hh the heavy hole band, lh the light hole band and so the spin split-off band. Bandgap E_g and spin-orbit splitting Δ_0 are indicated.

A further increase of the magnetic field yields the spin-split spectrum shown in Figure 2.6c. The conductance increases in steps of $\frac{e^2}{h}$ with no signature of SOI in $G(\mu)$.

The quasi-helical state is best observed when the energy interval with $G = \frac{2e^2}{h}$, corresponding to μ between the minima and local maximum of the lowest subband in Figure 2.6b, is similar in size to the energy range with $G = \frac{e^2}{h}$. Referring to Figure 2.3b this occurs when $E_{SO} \approx g\mu_B B$. Note however that when E_{SO} is small the $\frac{2e^2}{h}$ plateau at the bottom of the first subband may be obscured by the finite slope between zero conductance and the first conductance plateau. If this occurs a $G(\mu)$ similar to Figure 2.6c will be obtained.

2.4 Rashba spin-orbit interaction

Spin-orbit interaction (SOI) emerges in an approximation from the Dirac equation as [31]

$$H_{SO} = -\frac{\hbar^2}{4m_0^2c^2}\vec{\sigma}\cdot\vec{p}\times\nabla V_0 \tag{2.23}$$

with the free electron mass, m_0, the velocity of light, c, the Pauli matrices $\vec{\sigma} = (\sigma_x, \sigma_y, \sigma_z)$, momentum, $\vec{p}$, and the Coulomb potential of the atomic core, V_0. Heavy elements that have larger Coulomb potentials in their atomic cores will therefore have a larger SOI.

In a semiconductor crystal SOI affects the bandstructure [31],[27]. The band structure near band extrema, such as the minimum of the conduction band or maximum of the valence band, can be described by the k·p method. The (extended) Kane model considers several bands close to the bandgap. Band edge parameters are defined, such as the coupling between valence and conduction band states,

$$P_0 = \frac{\hbar}{m_0}\langle S|p_x|X\rangle, \tag{2.24}$$

with $|S\rangle$ the lowest conduction band state and $|X\rangle$ one of the highest valence band state, and the spin-orbit splitting Δ_0,

$$\Delta_0 = -\frac{3i\hbar}{4m_0^2c^2}\langle X|[(\nabla V)\times\vec{p}]_y|Z\rangle, \tag{2.25}$$

that arises between the valence band states due to spin-orbit interaction (see Figure 2.7). $|Z\rangle$ is another one of the highest valence band states. Heavier elements will have a larger Δ_0. SOI also affects the effective mass of the electrons and leads to g-factors different from $g = 2$, the g-factor of a free electron in vacuum [27].

Additional effects arise when the spatial inversion symmetry in the crystal is broken, for instance due to a non-centrosymmetrical lattice or due to external fields. The first type of inversion asymmetry, occuring for instance in wurtzite and zinc-blende crystals, is called bulk inversion asymmetry, the second structural inversion asymmetry. Bulk inversion asymmetry, also referred to as Dresselhaus SOI, is described by [32]

$$H_D = \gamma_D\left[\sigma_x k_x(k_y^2 - k_z^2) + \sigma_y k_y(k_z^2 - k_x^2) + \sigma_z k_z(k_x^2 - k_y^2)\right] \tag{2.26}$$

with γ_D the Dresselhaus spin-orbit coefficient. Equation (2.26), including the expression for γ_D in terms of band edge parameters, can be derived from the extended Kane model [33]. The Dresselhaus interaction is absent for transport along certain crystallographic directions, such as $\vec{k}$ along [111] [31], the growth axis of the InSb nanowires used in this thesis (see Section 3.1). We therefore focus on structural inversion asymmetry, also referred to as Rashba SOI.

Rashba SOI described by [31]

$$H_R = e\alpha_0\vec{\sigma}\cdot\vec{k}\times\vec{E}, \tag{2.27}$$

with α_0 (Å^2) a material-specific prefactor and $\vec{E} = \nabla V$ the electric field. Assuming $\vec{E} = E\hat{z}$ and $\vec{k} = (k_x, k_y, 0)$, which describes a quantum well with electric field perpendicular to the plane of motion, Equation (2.27) can be expressed as

$$H_R^{2D} = \alpha_R\left(\sigma_x k_y - \sigma_y k_x\right) \tag{2.28}$$

with Rashba SOI strength $\alpha_R \approx e\alpha_0\langle E_V(z)\rangle$, in which $\langle E_V(z)\rangle$ is the average electric field in the valence band over the conduction band wave function.

A more detailed expression for α_R [33], obtained from the extended Kane model, consists of an external field contribution, $\langle\alpha_0\rangle$, and an interface contribution, $\langle\alpha_{\text{int}}\rangle$,

$$\alpha_R = \langle\alpha_0\rangle + \langle\alpha_{\text{int}}\rangle. \tag{2.29}$$

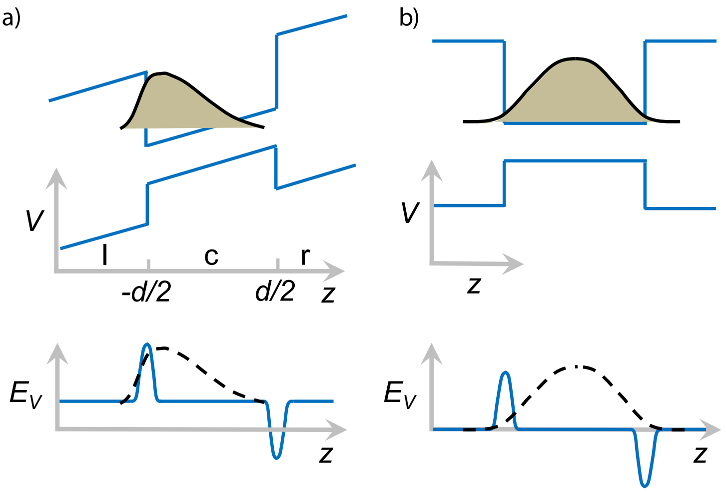

Figure 2.8: Electrostatic potential, electric field and wave function in a quantum well with and without structural inversion asymmetry. **a)** Top: an external voltage applied across the quantum well leads to a tilted potential (blue lines) and skewed wave function distribution (black and grey). The potential well has width d and runs from $-\frac{d}{2}$ to $\frac{d}{2}$. l denotes the left barrier, c the quantum well and r the right barrier. Bottom: the resulting electric field in the valence band, $E_V(z)$ (blue curve), averaged over the wave function (dashed lines) gives a non-zero α_R. **b)** Top: in the absence of an external voltage the wave function distribution is symmetric with respect to the center of the quantum well. Bottom: $\langle\alpha_0\rangle = 0$ due to the absence of V_{ext}. The interface contributions cancel each other ($\langle\alpha_{\text{int}}\rangle = 0$), altogether giving $\alpha_R = 0$.

In Equation (2.29) $\langle ... \rangle = \langle g_0(z)|...|g_0(z)\rangle$ describes an averaging over the wavefunction of the lowest subband, $g_0(z)$. Quantum well and barriers consists of different materials with each their own effective mass and band structure parameters. These sections are considered separately, giving regions l, c and r (see Figure 2.8). α_0 is given by

$$\alpha_0(z) = \alpha^l(z)\Theta\left(-z-\frac{d}{2}\right) + \alpha^c(z)\Theta\left(\frac{d}{2}-|z|\right) + \alpha^r(z)\Theta\left(z-\frac{d}{2}\right). \tag{2.30}$$

with the Heavyside step function, $\Theta(z)$, and a quantum well with width, d. $\alpha^i(z)$ ($i = l, c, r$) is given by

$$\alpha^i(z) = \frac{P_0^2}{3}\left(\frac{1}{[E_g^i+\Delta_0^i]^2} - \frac{1}{[E_g^i]^2}\right)\frac{dV_{\text{ext}}(z)}{dz} \tag{2.31}$$

with P_0 and Δ_0 given by Equation (2.24) and Equation (2.25) respectively. E_g is the band gap and V_{ext} the externally applied potential.

The interface contribution to Rashba SOI is given by

$$\alpha_{\mathrm{int}}(z) = \left(\beta^c - \beta^l\right)\delta\left(z + \frac{d}{2}\right) - \left(\beta^c - \beta^r\right)\delta\left(z - \frac{d}{2}\right) \tag{2.32}$$

with

$$\beta^i \approx \frac{P_0^2}{3}\left(\frac{1}{\Delta_0^i + E_g^i} - \frac{1}{E_g^i}\right). \tag{2.33}$$

From Equation (2.31), Equation (2.32) and Equation (2.33) it follows that either an external field V_{ext} or an asymmetry in the barriers is needed to create a non-zero α_R. Such structural (a)symmetry is also depicted schematically in Figure 2.8. Although this description is derived for quantum wells, it also applies qualitatively to nanowire devices. Rashba SOI strength α_R can thus be controlled with the external potential gradient V_{ext}, as has been demonstrated in quantum wells [34], [35], [36].

2.4.1 Spin precession

The Rashba Hamiltonian Equation (2.28) can be expressed as

$$H_R = \frac{\hbar}{2}\vec{\sigma}\cdot\vec{B}_{so}(k) \tag{2.34}$$

with $\vec{B}_{so}(k) = \frac{2\alpha_R}{\hbar}(\vec{k}\times\vec{z})$, showing that the Rashba SOI leads to a momentum-dependent spin-orbit field. While propagating the spin precesses around this magnetic field, depicted schematically in Figure 2.9a, with an angular frequency $\Omega = \frac{2\alpha_R k_F}{\hbar}$. The length that is traversed when a full precession has been made, the spin precession length l_R, equals $\frac{\pi\hbar^2}{m\alpha_R}$ [37]. A spin precession length of $\frac{\hbar^2}{2m\alpha_R}$, corresponding to a precession of 1 rad, is however also frequently used.

2.4.2 Spin relaxation

Relaxation and dephasing of spin polarization due to the interaction of a spin with its environment is often described by means of the Bloch equations [33], [38]. Relaxation (described by characteristic time T_1) refers to decay of spin polarization parallel to an external field, while dephasing (described by T_2) refers to the decay of transverse polarization. In context of spin decay in semiconductors often no distinction is made between relaxation and dephasing and both are described by a spin relaxation time τ_s [38], [32].

Several sources of spin relaxation have been identified for semiconductors, such as the D'yakanov-Perel' mechanism (spin relaxation due to inversion asymmetry in a disordered system), the Elliot-Yafet mechanism (relaxation of spin due to momentum scattering in the presence of lattice SOI), the Bir-Aronov-Pikus mechanism (spin relaxation due to electron-hole exchange scattering), relaxation by magnetic impurities and relaxation due to hyperfine interaction. An overview of relaxation mechanisms is given in [32],[38]. In InSb nanowires at low temperatures, non-magnetic

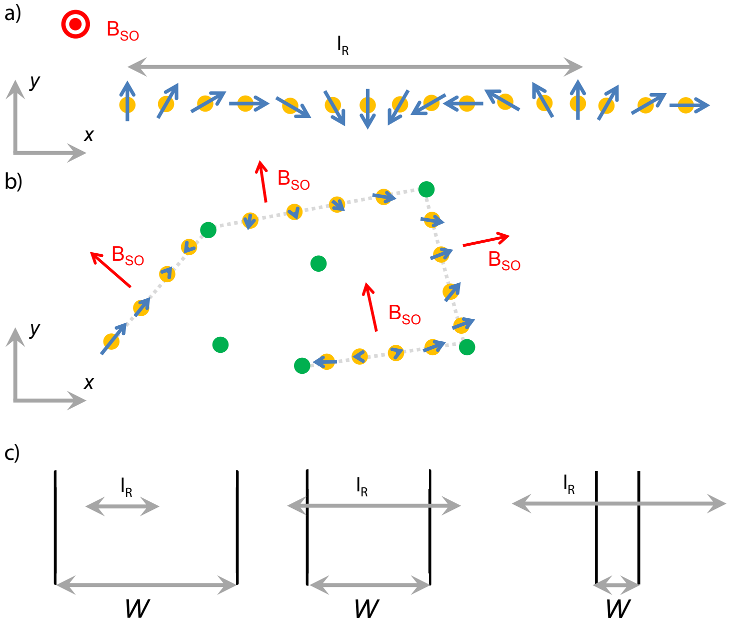

Figure 2.9: Spin precession in a ballistic and a diffusive environment. **a)** In the absence of scattering the electron spin makes a precession over a length l_R due to Rashba spin-orbit interaction. An electric field $\vec{E} = E\hat{y}$ is assumed, resulting in an out-of-plane B_{so}. **b)** Scattering changes the direction of the spin-orbit field and therefore the precession axis. The spin is randomized after several scattering events. Here $\vec{E} = E\hat{z}$, giving an in-plane B_{so}. **c)** Left: when $W > l_R$ the geometry is two-dimensional and the relation between spin precession and spin relaxation is given by Equation (2.35). Middle: when $W \approx l_R$ the spin relaxation length becomes width dependent. Right: an analytical expression for $l_{so}(W)$ has been obtained (see text) in the limit $W \ll l_R$.

itinerant narrow bandgap semiconductor nanostructures without p-type doping, the Elliot-Yafet mechanism and D'yakanov-Perel' mechanism are most relevant [32]. In both of these mechanisms scattering will lead to momentum randomization, resulting via SOI in spin relaxation, described by the timescale τ_{so}.

We consider in more detail D'yakanov-Perel' spin relaxation in a two-dimensional system due to Rashba SOI. This type of spin relaxation can intuitively be understood as follows: the spin will precess ballistically, as considered in Section 2.4.1, until after a time τ_e, the scattering time, scattering occurs. At that moment the spin rotation is $\Omega\tau_e$ (see Section 2.4.1). Scattering will randomly change the direction of momentum (see Figure 2.9b) and therefore the axis around which the spin precesses, leading to spin relaxation after several scattering events. We first assume frequent scattering, $\Omega\tau_e \leq 1$. After a time $t > \tau_e$ a number of scattering events $\frac{t}{\tau_e}$ have occurred, giving a total precession angle $\sqrt{\frac{t}{\tau_e}}\Omega\tau_e$. Defining the spin relaxation time, τ_{so}, as the time after which the spin direction has changed by an angle 2π gives [32]

$$\frac{1}{\tau_{so}^{2D}} = \Omega^2\tau_e = \left(\frac{l_e}{l_R}\right)^2 \frac{1}{\tau_e} \tag{2.35}$$

using mean free path $l_e = v_F\tau_e$, with Fermi velocity, v_F. τ_{so} is longer if τ_e is shorter, as the spin can only precess over a small angle between scattering events. When $\Omega\tau_e \geq 1$ (almost) a full precession is made before scattering, and therefore the spin is completely randomized after scattering, giving $\tau_{so} \sim \tau_e$ [32],[38].

A more detailed description considers the different decay rates for spin orientations perpendicular and parallel to the spin-orbit field, giving a description of spin relaxation

$$\frac{ds_i}{dt} = -\frac{s_j}{\tau_{so,ij}} \tag{2.36}$$

in terms of a spin relaxation tensor with components $\frac{1}{\tau_{so,ij}}$. s_i is the average projection of the spin in direction i (i=(x,y,z)). The tensor components are given by [32]

$$\frac{1}{\tau_{so,ij}^{2D}} = \tau_e\left[|\vec{B}_{so}|^2\delta_{ij} - B_{so,i}B_{so,j}\right] \tag{2.37}$$

in which $\vec{B}_{so}$ is the spin-orbit field (see Section 2.4.1) with components $B_{so,i}$. Often τ_e is multiplied by a factor describing how effective a specific scattering mechanism randomizes spin [33].

Scattering implies diffusive motion, with an average displacement after a time, t, proportional to $\sqrt{Dt}$, with diffusion constant, D. The spin relaxation length, l_{so}, is therefore defined as l_{so}=$\sqrt{D\tau_{so}}$. Using Equation (2.35) with $D = \frac{1}{2}v_F l_e$ gives $l_{so} = \frac{1}{\sqrt{2}}l_R$. In a two-dimensional system the spin precession length and the spin relaxation length are therefore either taken the same ([39]) or are at least easily converted.

2.4.3 Spin relaxation: dimensional effects

The preceding explanation of spin relaxation through Rashba spin-orbit interaction in a disordered system applies to a two-dimensional system. In a strictly one-dimensional system spin relaxation is clearly altered: scattering is necessarily backscattering, thereby reversing the spin precession of the forward motion and greatly enhancing the spin relaxation time. Kiselev and Kim [40] find from numerical studies that the spin relaxation length is altered in channels with width, W, already when $W < l_R$. A longer spin relaxation time $\tau_{so} \sim \tau_{so}^{2D}(l_R/W)^2 > \tau_{so}^{2D}$ is found under the condition $l_R > l_e > W$.

An analytical study of dimensional effects on magnetoconductance in channels made in quantum wells [41] also shows that spin relaxation time increases when $W < l_R$. In the limit $W \ll l_R$ and assuming diffusive transport

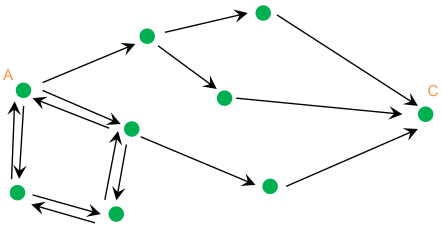

Figure 2.10: Quantum interference in a diffusive system. Partial electron waves traverse from A to C along several paths, indicated with arrows, leading to interference at C. Moreover, some paths begin and end at (approximately) the same position, shown for an electron wave that propagates along a loop partially in a clockwise direction and partially in a counterclockwise direction. Interference of electron waves leads to a correction to the classical conductance.

$$\tau_{so} = 12\left(\frac{l_R}{W}\right)^2 \tau_{so}^{2D} \tag{2.38}$$

is found. This functional form can be understood in analogy to magnetic field, derived for quantum dots with weak spin-orbit coupling ($l_R \gg W$, see also Section 2.5.2) [42]: diffusive motion after time τ_{so} covers in 2D an area $D\tau_{so}$. Requiring this to be equal to l_R gives $\tau_{so} \sim l_R^2$. In a narrow channel the area is given instead by $\sqrt{D\tau_{so}}W$, giving $\tau_{so} \sim \frac{l_R^4}{W^2} = \tau_{so}^{2D}\left(\frac{l_R}{W}\right)^2$. In terms of spin relaxation length this leads to $l_{so}(W) \sim l_{so}^{2D}\frac{l_R}{W} > l_{so}^{2D}$. The spin relaxation length thus increases in a confined geometry. The different regimes of $\frac{l_R}{W}$ are shown schematically in Figure 2.9c.

The above expression applies to channels made in diffusive quantum wells with weak spin-orbit coupling. Dimensional effects on spin relaxation in quasi-ballistic nanowires will be adressed in Chapter 6. Prolonged spin relaxation lengths have been found experimentally for channels defined in quantum wells [39],[43] and for InAs nanowires [44].

2.5 Quantum diffusive transport

At low temperatures the wave character of travelling electrons affects the conductance of diffusive samples through quantum interference. These quantum interference effects are often studied by measurements of the conductance as a function of magnetic field, yielding information on electron phase coherence and SOI strength.

To understand this we consider the different paths that electrons can follow from one location (A) to another (C), as shown in Figure 2.10 [45]. We assume that the paths between A and C are shorter than the length over which the phase randomizes, the phase coherence length, l_φ. While generally the phase evolves deterministically when scattering is elastic, inelastic scattering is statistical in nature and therefore randomizes the electron phase [46]. Some elastic processes can however also contribute to phase randomization [45].

The electron wave will split itself into a number of partial waves that follow different diffusive paths from A to C. Each partial wave is described by a complex amplitude C_j

$$C_j = c_j e^{i\varphi_j} \tag{2.39}$$

with φ_j the phase acquired by propagation from A to C along path j.

The probability of propagation from A to C, P_{AC}, is the square of the amplitude at C, which in turn is the sum of all partial wave amplitude contributions. This Feynmann path method leads to (when assuming real-valued c_j)

$$P_{AC} = \left|\sum_j c_j e^{i\varphi_j}\right|^2 = \sum_j |c_j|^2 + \sum_{l,k\neq l} c_l c_k \cos(\varphi_l - \varphi_k) \tag{2.40}$$

in which the interference term (the 2nd term) changes P_{AC} with respect to its classical value $P_{AC}^{cl} = \sum_j |c_j|^2$. The accumulated phase is described by $\varphi \sim \int \vec{k} \cdot d\vec{l}$, with wave vector, $\vec{k}$, and propagation direction, $d\vec{l}$. Therefore a change of gate voltage, resulting in a change in electron density and therefore in $\vec{k}$, affects the interference contribution to P_{AC}. As will be shown in Section 2.5.2 also application of a magnetic field affects φ and may therefore change the interference contribution to the conductance. These interference contributions show in measurements as reproducible conductance fluctuations when sweeping the magnetic field or the gate voltage. However, if a large number of paths j are involved the random distribution of φ will average out these interference terms, giving $P_{AC} = \sum_j |c_j|^2 = P_{AC}^{cl}$, the sum of the probabilities of the separate paths.

2.5.1 Quantum interference along time-reversed paths

The averaging considered in the previous section does not take place when electron waves return to their point of departure, i.e. when C = A (also shown in Figure 2.10). In this situation electron waves traversing the same path clockwise (C_1) and anticlockwise (C_2) will interfere and as they traverse the same path the obtained phase will be the same. Together with $c_1 = c_2$ this yields

$$P_{AA} = c_1^2 + c_2^2 + 2c_1c_2 = 4c_i^2 = 2P_{AA}^{cl}, \tag{2.41}$$

which is twice the classical probability obtained from addition of the probabilities of separate paths, $P_{AA}^{cl} = 2c_1^2$. Constructive interference of time-reversed electron waves in closed paths thus increases the chance that an elecron returns to its initial position. As constructive interference occurs for all loops, provided the phase coherence length exceeds the loop size, this weak localization is not averaged out, and results in an increased resistance.

A quantitative approach [47],[46] starts with the Einstein relation

$$\sigma = e^2 N(0) D \tag{2.42}$$

with conductivity, σ, electron charge, e, density of states at the Fermi level, $N(0)$, and diffusion constant D. Assuming classical transport yields $D = \frac{1}{n} v_F l_e$, with Fermi velocity, v_F, mean free path, l_e, and dimension n. Fermi velocity and mean free path are related via the scattering time, τ_e, by $l_e = v_F \tau_e$. The electrons are assumed to follow classical paths, requiring a Fermi wavelength, λ_F, smaller than l_e. Quantum interference leads to velocity-velocity correlations that give rise to a correction to the diffusion constant, ΔD. This results via Equation (2.42) in a correction to the conductance, $\Delta\sigma$. ΔD can be evaluated by considering the directions of the electron waves involved in the quantum coherent return paths, the effective area for return and the classical chance to return to the same area through diffusive motion. The resulting $\Delta\sigma$ is given by

$$\Delta\sigma = -\frac{2e^2}{\pi\hbar} D \int dt C(t) e^{-\frac{t}{\tau_\varphi}} \left(1 - e^{-\frac{t}{\tau_e}}\right) \tag{2.43}$$

with the classical probability of return $C(t)$ $[\frac{1}{m^3}]$ described by the diffusion equation. The description of the classical motion of electrons in terms of diffusion holds for times much longer than the time between collisions, τ_e. Therefore a cut-off for small times $t \leq \tau_e$ has been inserted to account for electrons that have not yet scattered. Phase coherence is introduced phenomenologically with a characteristic phase relaxation time, τ_φ.

2.5.2 Magnetic field

Application of a magnetic field alters the electron interference [45], [46]. Considering a path from A to C, an additional phase difference

$$\varphi(t) = \frac{e}{\hbar} \int_A^C \vec{A} \cdot d\vec{l} \tag{2.44}$$

arises in the presence of a magnetic field, $B = \nabla \times A$, with vector potential, A. Applying this to the closed paths considered before yields a contribution

$$\varphi(t) = \pm 2\pi \frac{\Phi}{\Phi_0} \tag{2.45}$$

with flux quantum, $\Phi_0 = \frac{h}{e}$, flux, Φ, and $\pm$ referring to clockwise and counterclockwise propagation. A magnetic field thus yields a difference in phase of $4\pi\frac{\Phi}{\Phi_0}$ between clockwise and counterclockwise paths, thereby removing the constructive interference. A large number of closed paths with different areas in the presence of a magnetic field average out the interference term in Equation (2.41). At large enough magnetic field the classical conductance is retrieved. As conductance is suppressed at zero magnetic field, a positive magnetoconductance is observed.

A quantitative discussion of the effect of magnetic field can be given in terms of the timescale τ_B [45],[48]. Phase coherence is lost if a phase difference of order 1 occurs between time reversed paths. This occurs at a flux $\sim \frac{\hbar}{e}$. In case of a two-dimensional geometry with perpendicular field the flux can be converted to a timescale by defining an area $D\tau_B$, covered by the electron waves through diffusive motion, exposed to a magnetic field B such that the flux equals $\frac{\hbar}{e}$. This yields $\tau_B \sim \frac{\hbar}{eBD}$. The magnetic dephasing length $\sqrt{D\tau_B}$ equals in this case the magnetic length $l_m = \sqrt{\frac{\hbar}{eB}}$. In confined geometries or when considering quasi-ballistic transport different expressions for τ_B apply (see Section 2.5.4). Note that it is assumed that the magnetic field is small so that the classical paths are not affected by B, i.e. the curvature of trajectories in a magnetic field is negligible.

2.5.3 Spin-orbit interaction

To understand the impact of SOI on quantum interference we consider the change of spin orientation along closed paths [49],[27]. Spin orientation can change between scattering events (corresponding to the SOI due to inversion asymmetry described in Section 2.4) or during scattering. Assuming an initial spin state $|s\rangle$, described by $|s\rangle = (a,b)^T$ (with T denoting the transpose), the state after a clockwise rotation is

$$|s'\rangle = R|s\rangle \tag{2.46}$$

with a rotation R that is a product of a large number of small rotations R_i, representing the changes of spin in between or during scattering events, $R = R_N...R_2R_1$. The spin along the time-reversed path will undergo the spin rotations in the opposite order and each rotation angle will be inverted. The final spin state $|s"\rangle = \tilde{R}|s\rangle$ is composed of rotations $\tilde{R} = \tilde{R}_1\tilde{R}_2...\tilde{R}_N$ with $\tilde{R}_i = R_i^{-1}$, the inverse of R_i.

To determine the effect of SOI on quantum interference the interference term in Equation (2.41) is multiplied by $2\langle s'|s"\rangle = 2\langle s|R^2|s\rangle$. If SOI is weak the spin does not rotate much along the time-reversed trajectories that contribute to quantum interference, corresponding to $R^2 \approx 1$ (or I_2). SOI in this case does not alter the quantum interference.

When SOI is strong R^2 should be calculated. Considering the 2×2 matrix R for rotation of spin-$^1/_2$ over arbitrary angles α, β and γ, and averaging over a large number of diffusive paths yields $\langle s|R^2|s\rangle = -\frac{1}{2}$ [27]. The quantum return probability P_{AA} of Equation (2.41) is reduced with respect tot the classical probability due to the destructive interference in the presence of SOI. The increased conductance is called weak anti-localization. Application of a magnetic fields leads to a return to the classical conductance (see Section 2.5.2), creating a negative magnetoconductance. It is assumed that the magnetic field acts via Equation (2.44) only; effects on spin due to for instance a Zeeman field are not considered.

A derivation of the change in magnetoconductance due to SOI yields a spin-orbit contribution to Equation (2.43) of $\frac{1}{2}\left(3e^{-\frac{4t}{3\tau_{so}}} - 1\right)$ [47], [50]. Chakravarty and Schmid

[47] assume in their derivation that $l_{so} \gg l_e$. However, Zaitsev *et al.* [50], assuming a very general expression for spin-orbit interaction, derive the same expression with only the requirement $l_R \gg \lambda_F$, with λ_F the Fermi wavelength and l_R the precession length due to Rashba SOI (see Section 2.4.1). When SOI is weak, corresponding to $\tau_{so} \gg \tau_\varphi$, the above spin-orbit contribution yields 1 and therefore does not alter the magnetoconductance. However, when $\tau_{so} \ll \tau_\varphi$ it gives $-\frac{1}{2}$, reducing the magnetoconductance amplitude and reversing its sign.

2.5.4 Magnetoconductance in nanowires with strong spin-orbit interaction

Combining the quantum interference, SOI and magnetic field dependence of the previous sections leads to an expression for the correction to the classical conductance in a nanowire as a function of magnetic field, $\Delta G(B)$, [51],[48]

$$\Delta G(B) = -\frac{2e^2}{h}\frac{D}{L}\int_0^\infty dt C(t)\left(1-e^{\frac{-t}{\tau_e}}\right)e^{\frac{-t}{\tau_\varphi}}e^{\frac{-t}{\tau_B}}\frac{1}{2}\left(3e^{\frac{-4t}{3\tau_{so}}}-1\right). \tag{2.47}$$

It has been used that magnetic field dephasing in a confined geometry leads to an exponential decay of the average phase factor with characteristic time τ_B, $e^{-\frac{t}{\tau_B}}$ [48]. L is the device length.

To apply Equation (2.47) to a nanowire with width W we consider coherent backscattering affected by confinement [48], occuring when $l_\varphi > W$. To apply the semi-classical formalism it is required that many subbands contribute to transport, that is, $\lambda_F \ll W$. Its radial confinement makes the nanowire one-dimensional in terms of phase coherence properties, although many subbands are occupied. The one-dimensional expression for diffusion back to the point of departure, $C(t)=\frac{1}{\sqrt{4\pi Dt}}\frac{1}{W^2}$, with $D=\frac{1}{3}v_F l_e$, is therefore used. The confinement in a nanowire thus results in larger chance of backscattering compared to a two- or three-dimensional system. Equation (2.47) is then evaluated as

$$\begin{aligned}\Delta G = -\frac{2e^2}{hL}\Bigg(&\frac{3}{2}\left[\frac{1}{l_\varphi^2}+\frac{4}{3l_{so}^2}+\frac{1}{D\tau_B}\right]^{-\frac{1}{2}}-\frac{1}{2}\left[\frac{1}{l_\varphi^2}+\frac{1}{D\tau_B}\right]^{-\frac{1}{2}}\\ &-\frac{3}{2}\left[\frac{1}{l_\varphi^2}+\frac{4}{3l_{so}^2}+\frac{3}{l_e^2}+\frac{1}{D\tau_B}\right]^{-\frac{1}{2}}+\frac{1}{2}\left[\frac{1}{l_\varphi^2}+\frac{3}{l_e^2}+\frac{1}{D\tau_B}\right]^{-\frac{1}{2}}\Bigg)\end{aligned} \tag{2.48}$$

with $l_{\varphi,so}=\sqrt{D\tau_{\varphi,so}}$.

For wires defined in quantum wells analytic expressions for τ_B have been derived in the diffusive regime $W \gg l_e$

$$\tau_B = 3\frac{l_m^4}{DW^2} \tag{2.49}$$

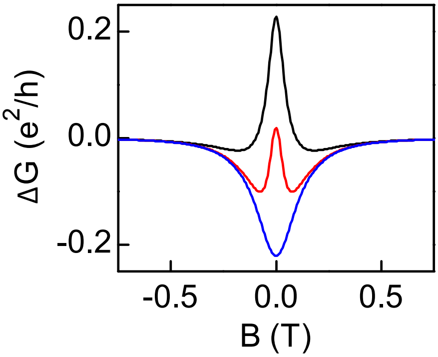

Figure 2.11: Magnetoconductance with and without strong spin-orbit interaction. Curves obtained using Equation (2.48) with magnetic field dephasing applicable to a quasi-ballistic nanowire with $\frac{l_e}{W} = 2$, $W = 90$ nm and $L = 2$ μm (see Chapter 6 for the expression for τ_B). Black curve: $l_{so} = 200$ nm, $l_\varphi = 800$ nm, showing WAL without WL at larger B when $l_{so} \approx l_e$. Red: $l_{so} = 400$ nm, $l_\varphi = 800$ nm. Blue: $l_{so} = 800$ nm, $l_\varphi = 400$ nm. Note that while here magnetoconductance up to large B is presented, showing that $\Delta G(B \to \infty) = 0$, Equation (2.48) is only valid up to small fields (see text).

and in the quasi-ballistic regime with $W \ll l_e$

$$\tau_B = C_1 \frac{l_m^4}{W^3 v_F} + C_2 \frac{\tau_e l_m^2}{W^2} \tag{2.50}$$

with the first (second) term corresponding to the weak (strong) magnetic field regime $l_m \gg \sqrt{W l_e}$ ($l_m \ll \sqrt{W l_e}$). Coefficients C_1 and C_2 depend on the type of boundary scattering (specular or diffusive). The expression for τ_B applicable to quasi-ballistic nanowires will be obtained from a numerical study in Chapter 6.

In the derivation of the exponential decay of the magnetic field dephasing term of Equation (2.47) it is assumed that there are many interactions with impurities and boundaries within the phase relaxation timescale [48]. Therefore is it required that τ_B, $\tau_\varphi \gg \tau_e$ and τ_B, $\tau_\varphi \gg \frac{W_F^2}{D}$, restricting the magnetic field up to which Equation (2.48) is valid.

The sign of the MC correction of Equation (2.48) depends on the ratio of l_{so} to l_φ. An increased conductance at $B = 0$ is observed when $l_{so} < l_\varphi$, while a reduced conductance occurs when $l_{so} > l_\varphi$ (see Figure 2.11). In the latter case a finite l_{so} results in a reduction of the WL amplitude with respect to the situation without spin-orbit interaction.

2.6 Table of Rashba spin-orbit quantities

Quantity	Symbol	Expression	Additional information	Used in section
Spin(-orbit) precession length	l_R	$\frac{\hbar^2}{2m^*\alpha_R}$	rotation by 1 rad	2.4.1
		$\frac{\pi\hbar^2}{m^*\alpha_R}$	full (2π) precession	2.4.1
Spin-orbit k-vector	k_{so}	$\frac{m^*\alpha_R}{\hbar^2}$		2.2
Inverse spin-orbit k-vector	— (elsewhere: λ_{so})	$\frac{\hbar^2}{m^*\alpha_R}$	l_R in Chapter 6	
Spin-orbit energy	E_{SO}	$\frac{m^*\alpha_R^2}{2\hbar^2}$	$E_{SO} = E(k_{so})$	2.2

Table 2.1: Spin-orbit quantities defined and used in Chapter 2 and Chapter 6 are listed. Spin-orbit interaction is assumed to be only of Rashba type. m^* denotes the effective mass and α_R the Rashba spin-orbit strength parameter described in Section 2.4.

CHAPTER 3

METHODS

This chapter describes in Section 3.1 the growth of InSb nanowires followed a description of by nanofabrication techniques to make InSb nanowire devices in Section 3.2. The measurement set-up used to perform low-temperature electrical measurements on these devices is described in Section 3.3. Complementary to experiments, information on device properties can be obtained from electrostatics simulations as explained in Section 3.4.

3.1 Nanowire growth

Semiconductor nanowires are a versatile platform for nanoscale (opto-)electronics. This is in part due to their bottom-up growth, which allows downscaling of device dimensions. Furthermore, due to their small radius strain in nanowires can be relieved radially, thereby giving access to a broader range of material combinations than in planar systems. This facilitates growth of heterostructures, both radially, creating core-shell nanowires, and axially, creating tunnel barriers or quantum dots. Moreover, at a small scale surface effects become important. Surface effects lead to the formation of crystal structures in nanowires that do not arise in bulk material [52]. Nanowires can also easily be combined with complex nanodevice fabrication, creating for instance devices with local gates underneath a semiconductor nanowires and contacts on top of the nanowire.

The nanowires used in the research described in this thesis are grown by metal organic vapor phase epitaxy (MOVPE) [53],[54]. In this process the desired materials, contained in precursor molecules, precipitate directly under a catalyst particle. A gold catalyst particle, deposited onto the substrate either randomly by using a colloid containing solution or deterministically via electron beam patterning and metal deposition (see Section 3.2), is used in the growth described here. The precursor gases are metalorganics, often containing alkyles (CH_3 groups), and hydrides (containing H) [54] (see Figure 3.1). Decomposition of the precursors predominantly takes place near the calalyst particle. The crystal then grows layer-by-layer and the crystal orientation of the substrate is maintained in the nanowire, i.e. the growth is epitaxial [54].

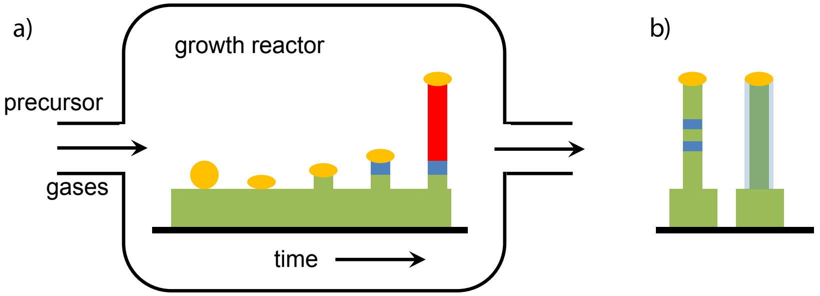

Figure 3.1: a) Growth of InSb nanowires using an Au-catalyzed vapor-liquid-solid growth process by metal organic vapor phase epitaxy. A substrate (green) with Au catalyst particles (orange) of diameter ~ 30 nm is heated. Precursor gases, phosphine and trimethylindium, dissociate at the Au droplet, leading to the layer-by-layer growth of the InP stem (green). Switching of the group-V precursor to arsine and subsequently trimethylantimony leads to the growth of InAs (blue) and InSb (red). **b)** Left: a change of precursor during the axial growth leads to formation of axial heterostructures that can function as quantum dots or tunnel barriers. Right: the nucleation of material on the nanowire side facets leads to the formation of core-shell nanowires.

Although the precipitation is often described by the vapor-liquid-solid model, the exact mechanism of nanowire growth is not fully understood [55]. Main parameters in the growth of III-V nanowires are the ratio of III to V materials and the temperature [56]. At elevated temperatures incorporation of material directly from the gas phase onto the already-grown nanowire leads to radial growth.

Growth of InSb nanowires, both using MOVPE [57],[58], [59] and other growth techniques [60],[61], [62],[63], has recently gained interest. InSb combines a small bandgap, high electron mobility at room temperature, and a large thermo-electric figure of merit [64]. These properties make InSb nanowires attractive for use in (opto-)electronics. Moreover, InSb also has a large spin-orbit interaction (and resulting large g factor), which makes the material interesting for spintronics. Several of these characteristics, namely the large spin-orbit interaction, high mobility and large g factor also make InSb nanowires suitable for use in Majorana devices (described in Section 2.2.1). An overview of the synthesis and properties of InSb nanowires is given in [65].

The research described in this thesis is based on two InSb nanowire growth recipes:

1. Using a (111) InP substrate first a ⟨111⟩ InP stem is grown to facilitate uniform nucleation. Growth is continued with InAs and then InSb, maintaining the same crystal orientation. InAs is used to reduce the lattice mismatch with respect to InSb. Growth of these nanowires (shown in Figure 3.2a and Figure 3.2b), including a study of the influence of Sb/In ratio and internanowire distance, is reported in [59]. The optimized growth recipe gives nanowires with

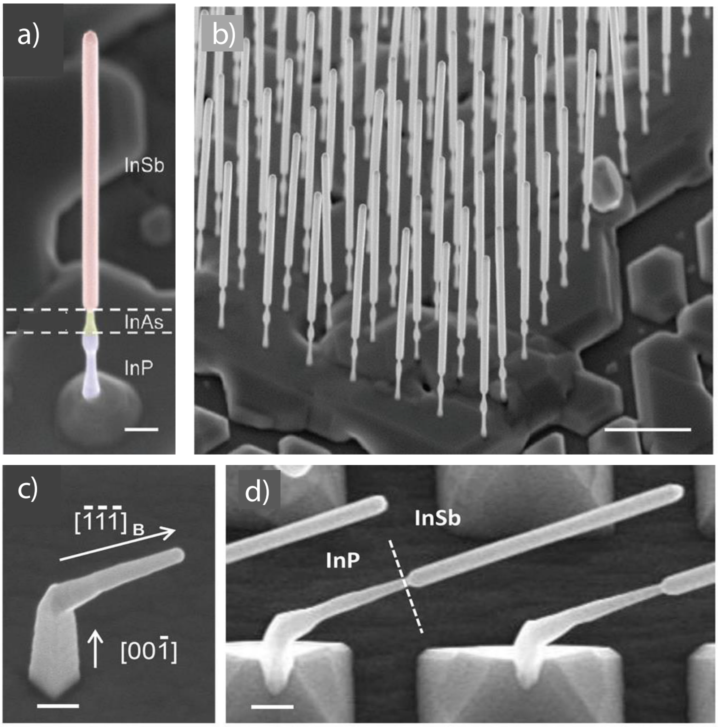

Figure 3.2: InSb nanowires. **a)** ⟨111⟩ oriented InSb nanowire grown using recipe I. **b)** Arrays of nanowires can be created by patterning the substrate with Au catalyst particles through electron beam lithography. **c)** Growth of an InP stem following recipe II. A kinked ⟨111⟩ InP segment is grown on top of a ⟨001⟩ InP stem, after which (**d**)) InSb growth continues in the ⟨111⟩ direction. Panels a and b are from [59], panels c and d from [66].

a length up to ~ 3.5 μm and a diameter of ~ 100 nm. Transport experiments described in Chapter 6 and Chapter 4 were performed with these nanowires. Growth and electrical characterization of junctions based on these nanowires is described in Chapter 5.

2. An ⟨001⟩ InP stem is grown on an (001) InP substrate. The growth direction of the InP stem is changed to ⟨111⟩ (shown in Figure 3.2c) by changing the indium content of the Au catalyst droplet [67]. InSb growth then continues along the ⟨111⟩ direction (Figure 3.2d). Also here nanowire junctions can be formed [66]. Field-effect mobility of these wires is investigated in Chapter 7.

Both recipes result in zinc-blende InSb nanowires with no stacking faults away from the InSb-stem interface. The zinc blende lattice structure consists of two face-

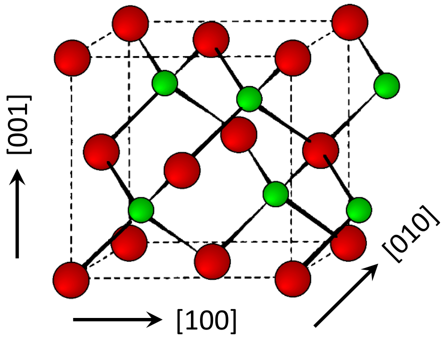

Figure 3.3: The zinc blende lattice. Dashed lines show the unit cell. The main crystallographic directions are indicated.

centered cubic lattices (one for each element) shifted with respect to each other by $\frac{a}{4}$ (with lattice constant, a) in the [111] direction (shown in Figure 3.3). The wire cross section is hexagonal with side facets with {110} orientation, which contain equal amounts of In and Sb and is therefore non-polar. By bringing the nanowires in contact with air a few nanometers of oxide will form on the nanowire surface. It has been reported that the InSb (110) surface has no surface states in the band gap [68]. Upward band bending, leading to surface carrier depletion, has been reported for both clean [69] and oxygen-covered InSb (110) surfaces[70].

3.2 Nanofabrication

As experimental requirements differ from experiment to experiment, device design and the resulting nanofabrication steps vary. For instance, local control of the electrochemical potential in nanowires can be obtained with local bottom gates, which requires the fabrication of gates and the deposition of a dielectric layer prior to nanowire deposition. If local control is not important the easiest way to gate nanowires is to deposit them onto a substrate consisting of highly p-doped silicon covered by a layer of SiO_2 (in our case with a thickness of 285 nm). The highly doped Si acts as a global back gate. The experiments in Chapter 4, Chapter 5, Chapter 6 and Chapter 7 (with the exception of Section 7.8.5) employ such a global back gate. In Chapter 6 it is combined with a top gate that covers the nanowire. The description of nanofabrication steps here follows the steps of such a global-gate-based device.

3.2.1 Bitmarkers and lift-off process

Bitmarkers, metallic structures used to locate nanowires after their deposition, are written onto a device substrate by a lift-off process (see Figure 3.4). Each nanofabrication step, be it the writing of bitmarkers, gates or contacts, utilizes the lift-off pro-

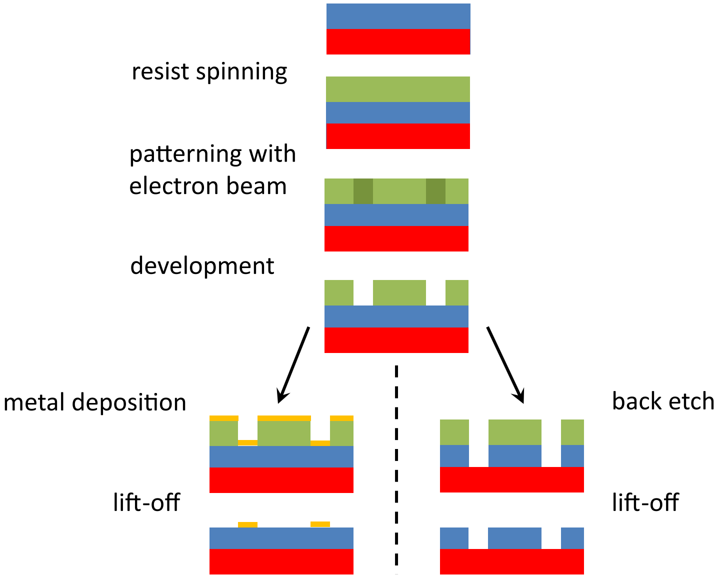

Figure 3.4: Lift-off process using electron beam lithography and positive resist. Resist (green) is spun on a substrate (consisting of a red and a blue layer) and baked, after which electron beam radiation locally changes the resist structure (dark green regions). The exposed resist has become soluble to the developer and is removed. Left: metal (orange) is deposited on the exposed regions. During lift-off the metal on the resist layer, is removed together with the resist, leaving the metal only at intended locations. When making contacts to the nanowire an additional contact preparation step is performed between development and metal deposition. Right: material is etched away at the exposed regions. The protective resist is removed during lift-off. The back etch gives access to the red substrate layer.

ces, in which the writing of the pattern into the resist is in our case done by electron beam lithography. The design of the bitmarker structure is done by computer aided design.

3.2.2 Nanowire transfer and device design

To fabricate devices nanowires have to be transferred from the growth chip to a device substrate. Transfer can be done with a tissue, gently wiping over the growth chip and then over the device substrate. As the yield of this transfer method is low and wires cannot be positioned deterministically, a wire deposition set-up has been developed to allow transfer of single nanowires [71]. A nanowire is located on the growth chip using an optical microscope and then removed from the substrate using a thin indium tip. The nanowire can then be deposited e.g. on a device substrate with a pre-defined gate structure.

A nanowire is subsequently imaged with an optical microscope or with a scanning electron microscope together with the bitmarkers that surround it. The device design is made based on these nanowire images (see Figure 3.5a).

3.2.3 Contacts and contact preparation

Contacts to the nanowire are made using the lift-off process described in Figure 3.4. Contacts to the nanowires end at large on-chip bond pads. To reliably contact the nanowire an additional contact preparation step is needed between the development of the resist and the metal deposition. Two types of contact preparation, ammonium polysulfide passivation (following [72]) and RF argon etching, were used. A low concentration ammonium polysulfide solution ($(NH_4)_2S_X$:H_2O between 1:200 and 1:500) replaces the native oxide by sulfur, but does not, or only slightly, etch the InSb nanowires. RF argon etching has the advantage that it can be performed in vacuum followed by in-situ metal deposition, preventing re-oxidation of the etched nanowire surface. Drawbacks of Ar etching are that the physical bombardment it entails may damage the nanowire crystal structure, the etch may be non-uniform, and that redeposition of etched material may occur. A comparison of room-temperature resistances of InAs nanowires exposed to ammonium polysulfide passivation or argon ion milling, an etching technique similar to RF argon etching, is given in [73]. When using ammonium polysulfide passivation a double layer of resist is used, which facilitates lift-off.

3.2.4 Dielectrics

Dielectrics, in this research either aluminium oxide (Al_2O_3) or hafnium oxide (HfO_2), separate the nanowires and metal gates. The native InSb oxide was found not to be a reliable dielectric. The dielectrics are deposited by atomic layer deposition (ALD). The step coverage of this process makes it hard to combine with the lift-off technique. Instead the complete chip is covered with dielectric, after which an etch mask is defined using electron beam lithography. Etching, performed either with hydrofluoric acid (HF) or with an argon plasma, removes the dielectric, thereby giving access to the material underneath.

3.2.5 Gates

To gate the nanowire either bottom or top gates can be used. The advantage of bottom gates, made prior to nanowire deposition, is that the metal gates and their spacing can be made very narrow (~ 30 nm), allowing local control over the electrochemical potential. An advantage of top gates is a potentially larger coupling to the nanowire. Drawbacks are that the electrical characteristics of the wire may be negatively affected by top gate fabrication [74], and that the temperature of the ALD process used to cover the wire cannot be too high, as the nanowire may decompose at temperatures at which the dielectric quality is optimal. For fabrication of the top

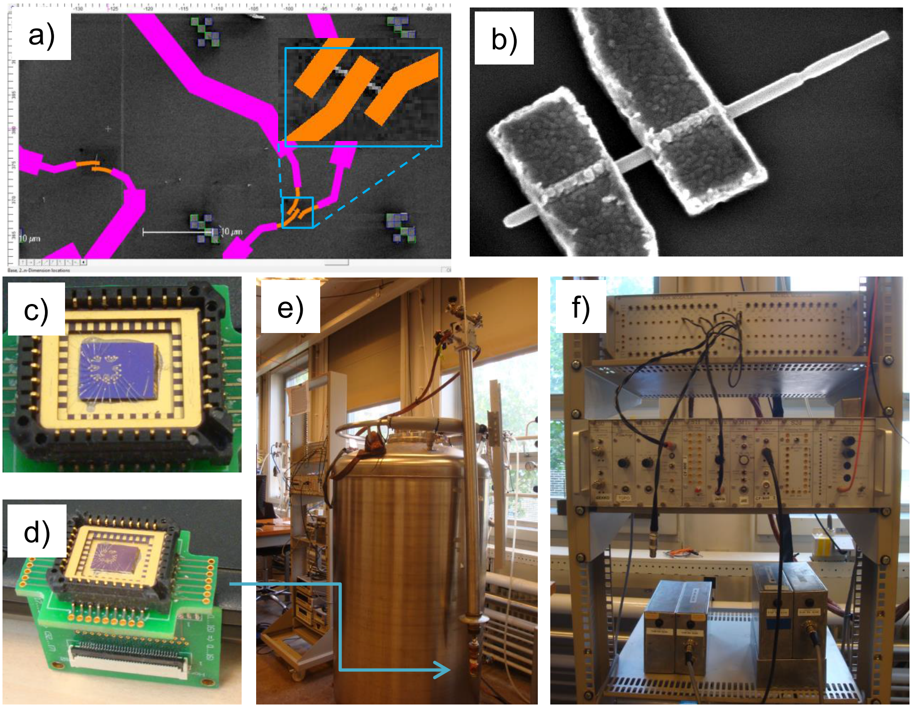

Figure 3.5: a) Computer aided device design. A design is made on top of scanning electron microscope (SEM) images of the nanowires. The four bitmarkers surrounding the nanowire are also seen. **b)** SEM image of a nanowire device. **c)** and **d)** A chip with devices is glued onto a chip carrier placed in a plastic circuit board (pcb). Bond wires connect the nanodevices to the chip carrier. **e)** The pcb with sample is mounted onto an insert (lower right of the image). The insert is then placed inside a dewar (center image) filled with liquid helium. Application and measurements of voltages and currents is done with the sensitive electronics (left image). **f)** The standard set of electronics consists of a matrix rack (or break-out box, top of the image) with lines to the samples. Source and measurement modules are placed in the so-called ivvi-rack (center) and connected to the matrix rack. The ivvi-rack is battery-powered (bottom).

gates of Chapter 6 HfO_2 was deposited at a temperature of 180 °C. Contacts to the gates end at on-chip bond pads.

3.2.6 Post-processing

After processing the chip is glued on a chip carrier using silver paint. The chip carrier has already been placed in a plastic circuit board (pcb) of which the lines are shorted to prevent potential differences across nanowires (see Figure 3.5c-d). Such potential differences can damage or destroy the nanodevices. Connections from the chip to the chip carrier are made using ultrasonic wire bonding with aluminum wire. When using the Si/SiO_2 chips with global back gate care must be taken not to damage the SiO_2 during wire bonding, as this may lead to leakage currents between contacts and back gate. Devices are mounted onto an insert, connecting the devices via chip carriers, pcb and fridge lines to measurement electronics to perform transport measurements (see Figure 3.5e). After mounting samples are evacuated for ~ 12 hours, as this lowers room temperature device resistance.

3.3 Measurement set-up

Most measurements described in this thesis took place at 4.2 K. To reach this temperature samples can simply be placed in a cryostat that is then slowly lowered into a dewar with liquid helium (shown in Figure 3.5e). Lower temperatures can be reached in dilution refrigerators, in which the sample is cooled (to temperatures of ~ 20 mK) by circulation of a $^3He/^4He$ mixture.

Measurements in this thesis are either DC measurements or low-frequency ($\sim 50 - 100$ Hz) AC measurements using a lock-in amplifier. Signal filtering, needed to accurately measure small signals, is provided by room-temperature π-filters and in some cases by low-temperature RC-filters and copper powder filters. Measurement electronics (see Figure 3.5f) is in-house-built, developed by Raymond Schouten. The standard measurement set-up consists of a rack with isolated input and output connections, digital-to-analogue-converters, source and measure modules, and a breakout box to connect the electronics to the device. An optical link is used to communicate with the measurement computer. Optical isolation is used as well for external incoming voltage sources and outgoing voltage signals. The measurement electronics is battery powered to avoid noise or interference from the mains electricity grid. The measurement computer runs QTlab, a measurement environment in Python developed by former group members.

3.4 Electrostatic simulations of nanowire devices

Electrostatic simulations offer additional insight into nanowire-based devices. They can for instance be applied to extract gate-nanowire capacitance, used in Chapter 5

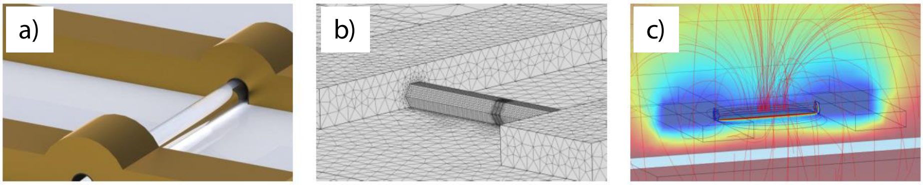

Figure 3.6: Steps in electrostatic simulations. **a)** Definition of the device geometry. **b)** Importing the geometry in the finite element solver, defintion of the material parameters and discretization of the geometry. **c)** Extraction of the electrostatic potential, electric fields and related quantities. Figure from [75].

and Chapter 7, to extract the energy spacing between subbands, as done in Chapter 4, or to calculate the number of filled subbands and charge distribution, as done in Chapter 6. The electrostatic simulations numerically solve the Poisson or the Schrödinger-Poisson equation in a predefined geometry. The Poisson solver neglects quantum mechanical effects; it assumes a carrier density obtained from the classical three-dimensional density of states. The self-consistent Schrödinger-Poisson solver obtains iteratively numerical solutions to the Schrödinger and the Poisson equation and is therefore able to describe electrostatics at low carrier density in a confined geometry such as a nanowire. In this section a short description of the Poisson and the two-dimensional Schrödinger-Poisson solver developed by Debbie Eeltink are given. More details can be found in [75].

3.4.1 Poisson solver

Electrostatics is governed by Poisson's equation

$$\nabla^2 V = -\frac{\rho}{\epsilon} \tag{3.1}$$

with electric potential, V, charge density, ρ, and dielectric constant, ϵ. The above equation is solved numerically with appropriate boundary conditions and material parameters. If no charge density is present ($\rho = 0$), which is the case when the nanowire is approximated as a metallic object surrounded by metals and dielectrics, Poisson's equation simplifies to Laplace equation

$$\nabla^2 \epsilon V = 0. \tag{3.2}$$

If the wire is considered a semiconductor a charge distribution, $\rho(V)$, is present. Considering electrons, $\rho(V) = -en(V)$, with electron charge, e, and electron density, $n(V)$. The dependence of the electron density on electric potential, $n(V)$, is obtained from the integral of the 3D density of states, $g_{3D}(E)$, (see Figure 3.7a) multiplied by the Fermi-Dirac distribution function, $f(E)$,

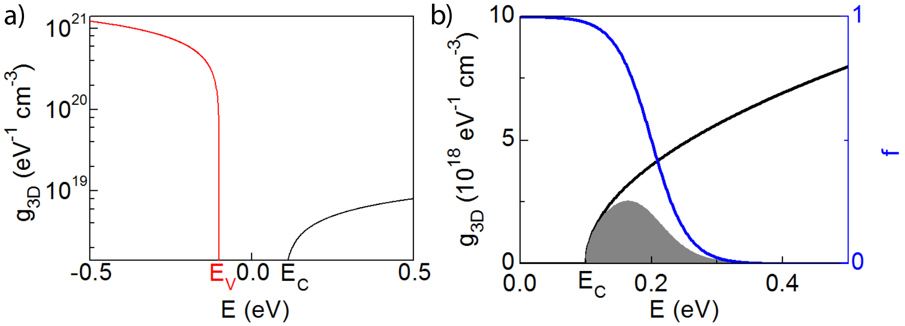

Figure 3.7: Density of states and electron density. **a)** Three dimensional density of states, g_{3D}, as a function of energy, E. Hole density of states is red, electron density of states black. Electron and hole mass are that of InSb; the effective electron mass is $0.015m_0$ and the effective hole mass $0.43m_0$, with m_0 the bare electron mass. $E_V = -0.1$ eV, $E_C = 0.1$ eV. **b)** Black trace (left axis): electron density of states, g_{3D}, as a function of energy, E. Blue trace (right axis): Fermi-Dirac distribution function, f, at $\mu = 0.2$ eV at a temperature $T = 75$ K. The electron density at this electrochemical potential is given by the area defined by the product of the density of states and the Fermi-Dirac distribution function (depicted in grey). Figures after [75].

$$n(V) = \int_{E_C}^{\infty} dE g_{3D}(E) f(E) \tag{3.3}$$

with

$$g_{3D}(E) = \frac{1}{2\pi^2}\left(\frac{2m^*}{\hbar^2}\right)^{3/2}\sqrt{E - E_C} \tag{3.4}$$

in which $E \geq E_C$ and

$$f(E) = \frac{1}{1 + e^{\frac{E-\mu}{k_B T}}} \tag{3.5}$$

with effective (electron) mass, m^*, energy at the conduction band edge, E_C, electrochemical potential, μ, Boltzmann constant, k_B, and temperature, T. A similar expression, involving the hole density, the valence band edge, E_V, and the hole effective mass, is applicable to holes.

μ is given by the sum of the internal chemical potential, μ_{int}, and the electric potential. As the semiconductor is nominally undoped $\mu_{\text{int}} = \frac{E_C + E_V}{2}$. Therefore

$$\mu = \frac{E_C + E_V}{2} + V \tag{3.6}$$

(see Figure 3.7b). At low temperature $f(E)$ can be approximated by a step function with $f(E) = 1$ for $(E - \mu) < 0$ and $f(E) = 0$ for $(E - \mu) > 0$.

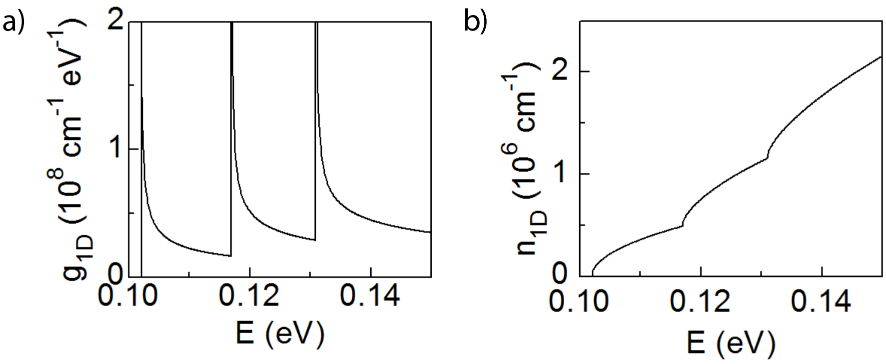

Figure 3.8: a) Quasi-one-dimensional density of states, g_{1D}, as a function of energy, E. A subband spacing of 15 meV is used. **b)** Quasi-one-dimensional density, n_{1D}, as a function of energy, E, obtained from integration of the density of states in panel a. Note that here the one-dimensional density [m^{-1}] is shown, while Equation (3.10) that includes the radial distribution gives a three-dimensional density [m^{-3}].

3.4.2 Schrödinger-Poisson solver

Quantum effects become apparent at low density in the presence of confinement. To include these effects the solution to the Schrödinger equation

$$\hat{H}\Psi = E\Psi \tag{3.7}$$

with

$$\hat{H} = -\frac{\hbar^2}{2m^*}\left(\partial_x^2 + \partial_y^2 + \partial_z^2\right) + U \tag{3.8}$$

is sought. The potential U equals the potential $-eV$ used in the description of the Poisson solver.

Assuming a nanowire oriented along $\hat{x}$, the solution $\Psi(x,y,z)$ can be separated into $\chi(x)\phi(y,z)$. Equation (3.7) is solved in the yz-plane. In a few cases with simple expressions for $U(y,z)$ and a simple geometry an analytical solution can be found. However, in general a numerical approach is needed. The appropriate boundary condition is that of an infinite wall, giving $\phi = 0$ at the surface of the nanowire. The axial ($\hat{x}$) component is described by the one-dimensional density of states (see Figure 3.8a)

$$g_{1D}(E) = \frac{1}{\pi}\sqrt{\frac{2m^*}{\hbar^2}}\frac{1}{\sqrt{E-E_C}}. \tag{3.9}$$

To obtain the electron density, $n(y,z)$, $\phi(y,z)$ is multiplied by the one-dimensional density of states and the Fermi-Dirac distribution function,

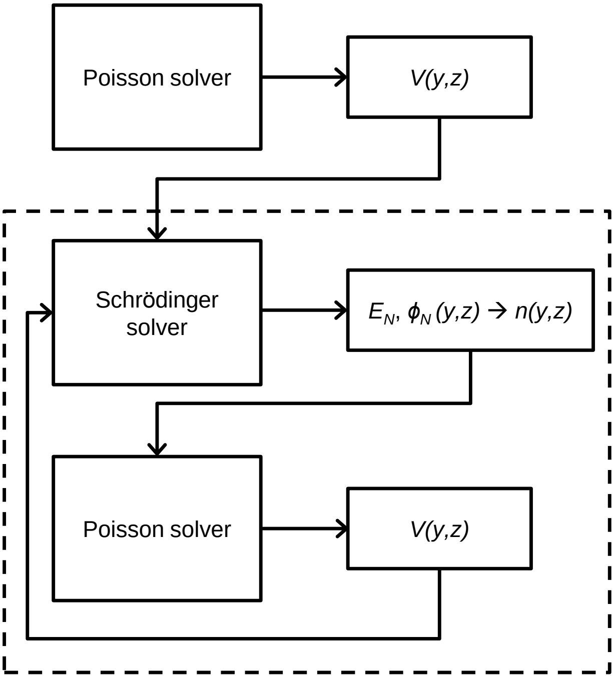

Figure 3.9: Iteration scheme for the Schrödinger-Poisson solver. The Poisson solver gives an initial guess of the electrostatic potential $V(y,z)$. Using this input the Schrödinger solver calculates orbitals, $\phi_N(y,z)$ and the corresponding eigenenergies, E_N. The Poisson solver uses the resulting charge distribution $n(y{,}z)$ to obtain a new potential $V(y{,}z)$. This sequence continues until $V(y,z)$ converges. Scheme after [75].

$$n(y,z) = \sum_N |\phi_N(y,z)|^2 \int_{E_C}^{\infty} dE \frac{1}{\pi\hbar} \sqrt{\frac{2m^*}{E - \left(E_C + E_N(V(x,y))\right)}} \frac{1}{1 + e^{\frac{E-\mu}{k_B T}}} \tag{3.10}$$

with $\mu = \frac{E_c + E_v}{2}$.

The Poisson and Schrödinger equation are solved self-consistently to obtain $n(y,z)$ and $V(y,z)$ as shown schematically in Figure 3.9. First, an estimate of $V(y,z)$ is obtained from the Poisson solver. This estimate then enters as $U(y,z) = -eV(y,z)$ in the Schrödinger solver. The Schrödinger solver outputs a number of wavefunctions ϕ_i and their energies E_N (N = 1, 2, ...). These are then integrated according to Equation (3.10) to determine $n(y,z)$. $n(y,z)$ is then applied to the Poisson solver again, which outputs a potential profile $V(y,z)$. This is repeated until convergence is reached.

Occupied subbands are those with energy $E_N < \mu$. Setting $E = 0$ at the center of the bandgap gives $\mu = 0$. Therefore all subbands that contribute to transport have negative energies.

CHAPTER 4

QUANTIZED CONDUCTANCE IN AN INSB NANOWIRE

Ballistic one-dimensional transport in semiconductor nanowires plays a central role in creating topological and helical states. The hallmark of such one-dimensional transport is conductance quantization. Here we show conductance quantization in InSb nanowires at non-zero magnetic fields. Conductance plateaus are studied as a function of source-drain bias and magnetic field, enabling extraction of the Landé *g* factor and the subband spacing.

This chapter has, with the exception of Section 4.7.6, been published as I. van Weperen, S. R. Plissard, E. P. A. M. Bakkers, S. M. Frolov, L. P. Kouwenhoven, Quantized conductance in an InSb nanowire, *Nano Lett.* **13**, 387-391 (2013).

4.1 Introduction

Semiconductor nanowires are the starting point of recently proposed topological systems [19],[18],[76]. A topological superconducting region arises in a one-dimensional (1D) semiconductor wire in the presence of a strong spin-orbit coupling when it is brought in contact with a superconducting material. On the boundary of the topological and non-topological wire regions Majorana Fermions (MFs) are expected [20]. The MFs in a nanowire, quasi-particles that are an equal superposition of an electron and a hole, are candidate building blocks for fault-tolerant quantum computation [20],[21]. Moreover, 1D semiconductor wires with strong spin-orbit coupling have been identified as a suitable platform for creation of a helical state [77],[78],[79]. In such a state spin and momentum of an electron are perfectly correlated, thereby creating spin polarization and allowing spin filtering, key themes in the field of spintronics [37],[80],[38].

InSb nanowires, alongside InAs and Si/Ge core-shell nanowires, are promising for study of topological and helical states, as they have a strong spin-orbit interaction [81] and superconductivity can be induced in the nanowires [82]. Indeed signatures of MFs have been reported in hybrid semiconductor-superconductor InSb nanowire devices [17]. While in InSb nanowires the basic properties of spin-orbit interaction and induced superconductivity have each been separately investigated, the degree of fulfillment of the third requirement for creation of MFs, the 1D semiconductor wire, is not as well understood. In a 1D wire transport takes place in subbands, of which the occupation is controlled by an external gate voltage. While first schemes for detection of MFs required occupation of only a single subband near the superconducting contacts where the MFs form [19],[18] later proposals extended this condition to the multi-subband regime [83], [23],[84]. Information about the energy spectrum of InSb nanowires needed to answer questions of subband occupation is however lacking. Moreover, MFs are affected by disorder in the wire [84],[85],[86] of which the extent is unknown. Such disorder creates diffusive transport, instead of the ballistic transport implied in the 1D requirement. Subband occupation and disorder are also key issues in creation of helical states in InSb nanowires.

The formation of subbands in (ballistic) 1D wires is shown in transport measurements by quantization of conductance, where each spin-degenerate subband contributes a conductance of $g_Q = \frac{2e^2}{h}$ [28],[29]. In semiconductor nanowires conductance quantization is hard to achieve, as it requires strong suppression of disorder between source and drain contact, a distance of typically several hundred nanometers to a few microns. Disorder, both due to structural imperfection and surface states [87],[88], leads to scattering of electrons, which due to the radial confinement of nanowires often results in reflection of electrons back to the reservoir from which they originated, i.e. backscattering (see Figure 4.1a). Backscattering erases the conductance quantization. In two-dimensional geometries, in which conductance quantization has been studied extensively, scattering centers outside of the 1D constriction are less harmful to conductance quantization, as they will only affect the trajectories of a small percentage of electrons. Also, in a plane scattering less likely results

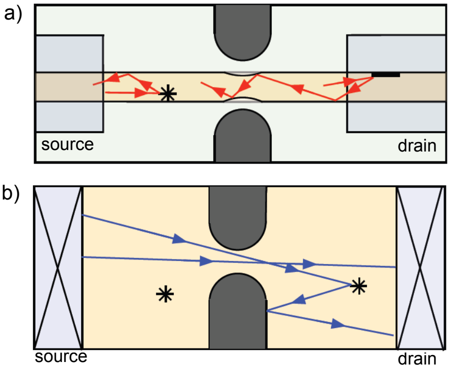

Figure 4.1: Consequences of scattering in nanowires and two-dimensional geometries. a) Transport through a constriction in a nanowire. Scattering at an impurity reflects an electron back to the source reservoir. Reflection at the reservoirs, here drawn for the drain reservoir, also leads to backscattering. **b)** Transport through a constriction in a two-dimensional geometry in the presence of scattering centers. Note that compared to the 1D nanowire in panel a) a scatterer only affects a small number of the ballistic trajectories from source to drain reservoir and that scattering is less likely to lead to scattering through the 1D constriction.

in backscattering (see Figure 4.1b). So far indications of conductance quantization in nanowires have been reported in Si/Ge core-shell nanowires [89],[90], while signs of quasi-ballistic transport, but no unambiguous conductance quantization, have been observed in InAs nanowires [88],[91],[92],[93],[94],[95].

Here we demonstrate quantization of conductance in InSb nanowires at non-zero magnetic field. We study the quantization as a function of source-drain bias and magnetic field. With this subband spectroscopy we extract the main characteristics of the system, namely the Landé g factor and the subband spacing.

4.2 Quantized conductance

Our device (Figure 4.2a) is an InSb nanowire with two metal contacts (Ti/Au). The InSb nanowires have a zinc blende crystal structure free of structural defaults[59] and have yielded field-effect mobilities up to 35,000 cm^{2}V^{-1}s^{-1}. The spacing of the two metal contacts in the device studied here (~ 200 nm) is comparable to the electron mean free path of ~ 300 nm extracted from measurements of field-effect mobility. Conductance quantization has however also been observed in a device with ~ 850 nm contact spacing. A global backgate controls the electron density in the nanowire (Figure 4.2b). Differential conductance $g = \frac{dI}{dV}$ is measured using a standard lock-in technique. On application of an in-plane magnetic field conductance steps as a function of backgate voltage are observed as seen in Figure 4.2c. The conductance at the two plateaus is, after subtraction of 6 kΩ of series resistance, $g \approx 0.5 g_Q$ and

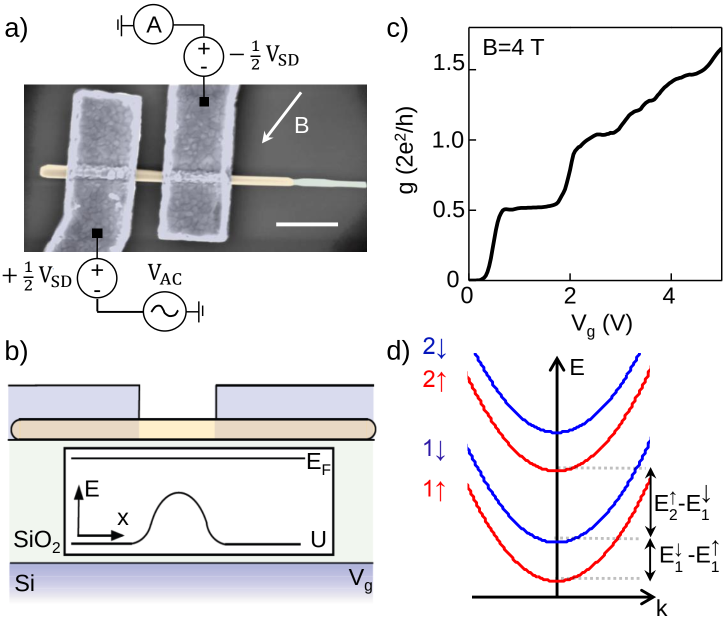

Figure 4.2: Quantization of conductance in an InSb nanowire. a) Scanning electron microscope image of a contacted (Ti/Au 25/150 nm) InSb nanowire similar to the one measured. The InSb wire is colored yellow, the stem (InP and InAs) green. The direction of the in-plane magnetic field, B, with respect to the wire is indicated. The angle between nanowire and magnetic field is (53 ± 5)°. Differential conductance $g = \frac{dI}{dV} = \frac{I_{AC}}{V_{AC}}$ is obtained from a 50 μV_{RMS} excitation, V_{AC}. Source-drain bias, V_{SD}, is applied anti-symmetrically across the sample. Scale bar is 500 nm. All measurements were performed at a temperature of 4.2 K. **b)** Schematic drawing of the nanowire lying on a Si substrate covered with 285 nm SiO_2. The p^+-doped Si acts as a global backgate to which a voltage V_g is applied. The inset shows the electrostatic potential, U, created by V_g. The electrostatic potential leads to the formation of a constriction in the wire in the region between the two contacts. **c)** Conductance g as a function of backgate voltage, V_g, at $B = 4$ T ($V_{SD} = 0$ mV) shows plateaus at 0.5 and 1.0 conductance quanta g_Q ($\frac{2e^2}{h}$). A series resistance of 6 kΩ has been subtracted, chosen such that the conductance of the second plateau is $1.0 g_Q$. This series resistance, consisting of the impedance of the current amplifier (3 kΩ) and a contact resistance at the interface of the InSb wire and the metal contact, is discussed in more detail in section 4.7.2. **d)** At non-zero magnetic field the energy spectrum consists of spin-split subbands $n\{\uparrow,\downarrow\}$. The energy spacing between subbands 1↓ and 1↑, where $g = 0.5 g_Q$, is denoted as $E_1^{\downarrow} - E_1^{\uparrow}$. The energy spacing between 2↑ and 1↓ ($g = 1.0 g_Q$) is denoted as $E_2^{\uparrow} - E_1^{\downarrow}$.

$g \approx g_Q$, corresponding to transport through the lowest subband $1\uparrow$ and through the $1\uparrow$ and $1\downarrow$ subband respectively (see Figure 4.2d). Subbands are denoted by an index, with 1 the subband lowest in energy. Spin-split subbands ($\uparrow$ or $\downarrow$) that are degenerate in the absence of magnetic field are denoted by the same number.

4.3 Voltage bias spectroscopy

1D conductance channels show nonlinear conductance as a function of DC source-drain bias, V_{SD}. So-called half-plateaus at intermediate conductance values $g \approx 0.25g_Q$, $g \approx 0.75g_Q$ and larger fractions arise at high V_{SD} when the number of subbands available for electrons from source or drain reservoir differs by one [96],[97],[98]. Nanowire conductance as a function of V_{SD} and gate voltage (Figure 4.3a) shows that the $0.5g_Q$ and $1.0g_Q$ plateaus around $V_{SD} = 0$ mV evolve into these intermediate plateaus at high source-drain bias ($V_{SD} \sim \pm 10$ mV). $g(V_g)$ traces at $V_{SD} = 0$ mV, -7.5 mV and -11 mV show the appearance of the high-bias plateaus (Figure 4.3b). The observation of these half-plateaus at high source-drain bias is a further confirmation of conductance quantization.

The derivative of conductance to gate voltage[1], the transconductance $\frac{dg}{dV_g}$, of the same nonlinear transport data (Figure 4.3c) shows the subband alignment with respect to source and drain reservoir as a function of gate voltage and source-drain bias. Zero-bias and high-bias plateaus (zero transconductance) are separated by lines of high transconductance that arise when a subband aligns with source or drain reservoir. Two high transconductance lines intersect at finite V_{SD} when source and drain are aligned with successive subbands. This is seen in Figure 4.3c for the $1\uparrow$ and $1\downarrow$ subband at $V_{SD} = 14$ mV (point marked with *). In this configuration [97] the source-drain potential eV_{SD} equals the subband spacing $E_1^{\downarrow} - E_1^{\uparrow}$, as depicted schematically in Figure 4.3d. We therefore extract an energy spacing $E_1^{\downarrow} - E_1^{\uparrow}(B = 4\text{ T})$, which is also the Zeeman energy at $B = 4$ T, of 14 meV.

4.4 Magnetic field dependence and subband spacing

Gate traces as a function of magnetic field B (Figure 4.3a) show that the conductance plateaus become more pronounced with increasing B. At $B = 0$ T conductance is dominated by resonances that obscure the plateaus. The resonances, which are discussed in section 4.7.1, are suppressed at higher magnetic fields, enabling observation of the $0.5g_Q$ plateau for $B \geq 2$ T and the $1.0g_Q$ plateau for $B \geq 3$ T. The improvement of plateau quality with magnetic field suggests the presence of orbital effects; similar to two-dimensional electron gasses application of a magnetic field seems to reduce backscattering.

The subband spacing $E_1^{\downarrow} - E_1^{\uparrow}$, obtained from voltage bias spectroscopy measurements such as the one shown in Figure 4.4c, increases with magnetic field as seen in

---

[1] The transconductance $\frac{dg}{dV_g}$ is therefore a double derivative $\frac{dg}{dV_g} = \frac{d}{dV_g}\frac{dI}{dV}$ to current I.

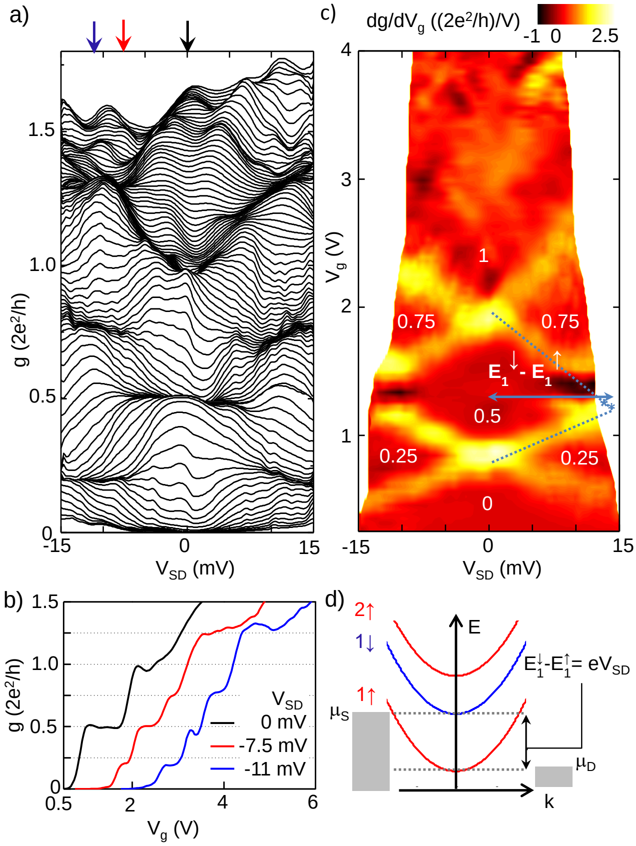

Figure 4.3: Voltage bias spectroscopy. a) Conductance as a function of source-drain voltage, V_{SD}. Each trace is taken with fixed V_g between -0.25 V and 4 V and plotted without offset between traces. Dense regions correspond to conductance plateaus. Data obtained at $B = 4$ T. **b)** Gate traces at $V_{SD} = 0$ mV (black), $V_{SD} = -7.5$ mV (red), and $V_{SD} = -11$ mV (blue), corresponding to the location of the arrows in panel a. The bump at $g = 0.5g_Q$ in the trace taken at $V_{SD} = -11$ mV is an electronics artefact. **c)** Transconductance $\frac{dg}{dV_g}$ of the data in panel a shows plateaus (zero transconductance, red) separated by transitions between plateaus with high transconductance (yellow/white). Conductance of the plateaus is indicated. The intersection of two regions of high transconductance surrounding the 0.5 plateau at finite V_{SD} (indicated with *) allows extraction of the energy $E_1^{\downarrow} - E_1^{\uparrow}$. **d)** The intersection of the high-transconductance regions at high source-drain bias (point * in panel c) corresponds to the alignment of the electrochemical potential of the source with spin-split subband 1↓, while the drain potential is aligned with spin-split subband 1↑. The source-drain potential eV_{SD} equals the subband spacing $E_1^{\downarrow} - E_1^{\uparrow}$.

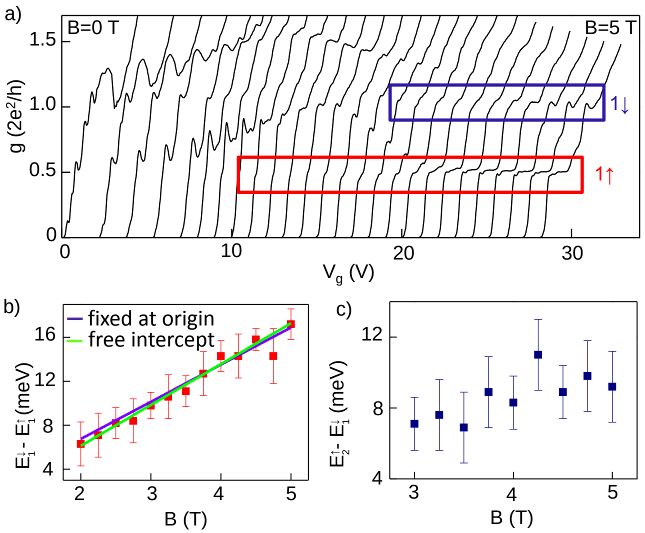

Figure 4.4: Development of the conductance plateaus in magnetic field. a) Conductance, g, as a function of gate voltage, V_g, at B between 0 and 5 T in steps of 0.2 T. The $0.5g_Q$ and $1.0g_Q$ conductance plateaus are indicated by the red and blue box respectively. **b)** For B between 2 T and 5 T the spin-split subband spacing $E_1^{\downarrow}-E_1^{\uparrow}$ is extracted from voltage bias spectroscopy measurements as indicated in panel 3c. From a linear fit through the origin (purple line) an effective $|g|$ factor $|g_1| = 58\pm1$ is obtained. A linear fit with the intercept as a free parameter (green line) gives $|g_1| = 64\pm3$. **c)** Spin-split subband spacing $E_2^{\uparrow}-E_1^{\downarrow}$ extracted from conductance as a function of source-drain bias and gate voltage (conductance plots in voltage bias spectroscopy measurements) between 3 T and 5 T.

Figure 4.4b. We extract from a linear fit with intercept fixed to zero to this Zeeman splitting a $|g|$ factor of the first subband $|g_1| = \frac{1}{\mu_B}\frac{d(E_1^{\downarrow}-E_1^{\uparrow})}{dB}$ of 58 ± 1 (μ_B is the Bohr magneton). As the subband splitting at zero magnetic field is experimentally not accessible, also a linear fit with the intercept as a fitting parameter is performed, giving a $|g_1|$ of 64 ± 3. These g factors are higher than the bulk InSb $|g|$ factor of 51. Although spin-orbit interaction is thought to affect $|g|$ factors in confined geometries [99],[100], our enhanced $|g|$ factor can likely be attributed to exchange enhancement in low density quantum point contacts [101],[102],[103]. A gradual increase of conductance with source-drain bias prevents observation of the transition between the $1.0g_Q$ plateau and the $1.25g_Q$ high-bias plateau in transconductance. The subband spacing between 2↑ and 1↓, $E_2^{\uparrow}-E_1^{\downarrow}$, is therefore extracted from measurements of conductance as function of source-drain bias and gate voltage (see Section 4.7.3), giving $E_2^{\uparrow}-E_1^{\downarrow}$ ($3\text{ T} \leq B \leq 5\text{ T}$)$\sim$ 10 meV (Figure 4.4c). The less well-defined $1.0g_Q$ plateau in voltage bias spectroscopy measurements complicates extraction of a clear magnetic field dependence of subband spacing $E_2^{\uparrow}-E_1^{\downarrow}(B)$.

4.5 Device II: subband crossing

In a second device conductance plateaus at $g = 0.5g_Q$ and $g = 1.0g_Q$ are observed as the out-of-plane magnetic field increases, showing the reproducibility of our results (Figure 4.5a). The $0.5g_Q$ plateau widens with field for $B \leq 5$ T, and from voltage bias spectroscopy measurements we extract $|g_1| = 51 \pm 1$ for a linear fit with intercept fixed to zero (the intercept as fitting parameter gives 62 ± 3) (Figure 4.5b). The $g = 0.5g_Q$ plateau remains approximately constant in width for $B > 5$ T. The $g = 1.0g_Q$ plateau is observed for $B \geq 5.75$ T and its subband spacing, also obtained from voltage bias spectroscopy measurements, increases linearly with B for magnetic fields up to 9 T.

A transconductance plot of the gate traces of Figure 4.5a, in which the lines of high transconductance correspond to the onset of transport through a subband, shows that a crossing of two subbands occurs at $B \approx 5$ T (Figure 4.5c). We now explain which subbands cross and under which conditions a subband crossing occurs. At zero magnetic field the $\uparrow$ and $\downarrow$ subbands with the same index are degenerate and Zeeman energy lifts the degeneracy at non-zero magnetic fields. This is seen in Figure 4.5c for the $1\downarrow$ and the $1\uparrow$ subband. One of the subbands involved in the crossing is therefore the $1\downarrow$ subband, and the similarity in slope to the $1\uparrow$ level at $B > 5$ T suggests that the second subband involved is the $2\uparrow$ subband. At non-zero B quantized steps with height $g = 1.0g_Q$ split into steps of height $g = 0.5g_Q$ (see first column of Figure 4.5d, where only the $0.5g_Q$ plateau is seen). When B is increased such that the Zeeman energy is equal to the energy spacing of subbands at $B = 0$ T, two subbands with opposite spin and an index that differs by 1 become degenerate. Two $0.5g_Q$ steps combine to a single $1.0g_Q$ step, leading to the disappearance of the plateaus at integer g_Q. As in our data at $B \sim 5$ T the $2\uparrow$ and $1\downarrow$ subband are degenerate, a $1.0g_Q$ step from $0.5g_Q$ to $1.5g_Q$ occurs (see second column of Figure 4.5d). At Zeeman fields larger than the subband spacing the order of subbands is changed, in our case to $1\uparrow$, $2\uparrow$, $1\downarrow$, and the width of the $0.5g_Q$ plateau, now defined as $E_2\uparrow - E_1^{\uparrow}$, is, excluding magnetic field contributions to confinement, constant in magnetic field. The $1.0g_Q$ plateau grows as a larger magnetic field increases the Zeeman energy separation between $1\downarrow$ and $2\uparrow$. Both the constant width of the $0.5g_Q$ plateau as well as the increase in subband spacing of the $1.0g_Q$ plateau are seen in Figure 4.5a-c.

Crossings of spin-split subbands have been observed in quantum point contacts in GaAs two-dimensional hole and electron gasses [104], [105]. The large g factor in InSb, leading to a large Zeeman energy, makes such a subband crossing reachable at moderate magnetic fields. The energy spectrum of the wire between contacts 2 and 3 in the inset of Figure 4.5a shows similar signs of a subband crossing (see section 4.7.5). In both wire sections it was found that a magnetic field affects the relative energy of subbands via a Zeeman energy contribution; a magnetic field contribution to confinement strength [106],[107] was not observed.

The spin-degenerate subband spacing at $B = 0$ T is estimated from the subband crossing point. In the absence of magnetic field contributions to confinement strength $E_2^{\uparrow} - E_1^{\uparrow}$ equals the spin-degenerate subband spacing between the first two subbands; $E_2^{\uparrow} - E_1^{\uparrow} = E_2 - E_1$. At the degeneracy between the $2\uparrow$ and $1\downarrow$ subband at $B \sim 5$ T $E_2^{\uparrow} - E_1^{\uparrow} =$

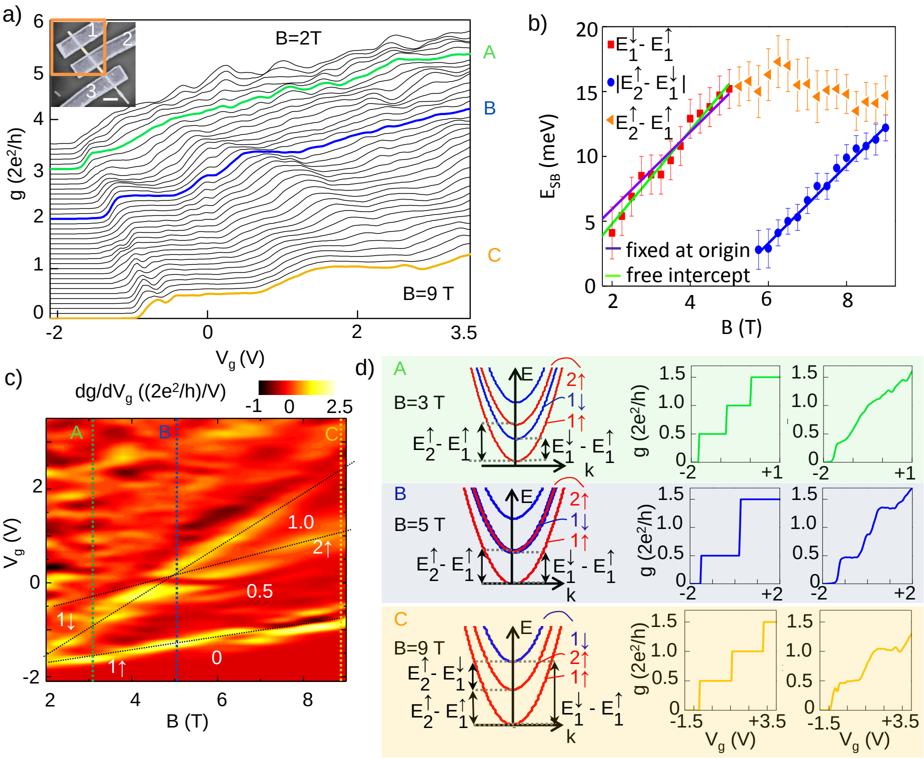

Figure 4.5: Conductance quantization and subband crossing in device II. a) Conductance, g, as a function of V_g at out-of-plane B between 2 T and 9 T in steps of 0.2 T. The green, blue and yellow trace (B = 3 T, 5 T and 9 T respectively) are shown in the right column of panel d. Inset: scanning electron microscopy image of device II with relevant contacts (1 and 2) and wire region indicated by the box. Contact spacing is 300 nm, wire diameter 70 nm. Scale bar is 500 nm. **b)** Subband spacing, E_{SB}, as a function of B for spin-split levels $E_1^{\downarrow} - E_1^{\downarrow}$ ($g = 0.5g_Q$, red squares) and $|E_2^{\uparrow} - E_1^{\downarrow}|$ ($g = 1.0g_Q$, blue dots) obtained from voltage bias spectroscopy measurements. The purple and green line are linear fits to $E_1^{\downarrow} - E_1^{\uparrow}$ with fit fixed at the origin and the intercept as a free parameter, providing $|g_1| = 51 \pm 1$ and 62 ± 3 respectively. The linear fit (blue line) to $|E_2^{\uparrow} - E_1^{\downarrow}(B)|$ gives $|g_{2-1}| = \frac{1}{\mu_B}\frac{d(E_2^{\uparrow}-E_1^{\downarrow})}{dB} = 52 \pm 2$. The subband spacing of the $0.5g_Q$ plateau for $B > 5$ T is denoted by $E_2^{\uparrow} - E_1^{\uparrow}$ (orange triangles). **c)** The transconductance, $\frac{dg}{dV_g}$, of the traces of panel a shows the onset of transport through a subband as a line of high transconductance (yellow/white). Plateau conductance (zero transconductance; red) is indicated. With increasing B the spin-split subbands 1↓ and 1↑ move apart. Around B = 5 T 1↓ intersects with the 2↑ subband. Cuts A, B and C are the magnetic field values (B = 3 T, 5 T and 9 T respectively) at which $g(V_g)$ is shown in panel d. Black dotted lines are a guide to the eye. **d)** Schematic drawing of the subband energies at $B = 3$, $B = 5$ and $B = 9$ T (left) and the corresponding schematic conductance steps (middle). The right column shows measured gate traces at the indicated magnetic field.

$E_1^{\downarrow} - E_1^{\uparrow} \sim 15$ meV. We therefore estimate a spin-degenerate subband spacing $E_2 - E_1 \sim 15$ meV. This subband spacing agrees well with the level spacing $E_2 - E_1 = 18$ meV in an infinite cyclindrical well with diameter equal to our wire diameter (70 nm), which is, considering that the confinement potential in our nanowire is likely different from cylindrical, taken only as a rough estimate.

4.6 Summary and outlook

To summarize we have observed quantized conductance in InSb nanowires at non-zero magnetic fields. Subband spectroscopy, performed by measuring conductance quantization as a function of source-drain voltage and magnetic field, allowed extraction of Landé g factors of ~ 55 and subband spacing of ~ 15 meV. Results reported here on devices with small contact spacing indicate quasi-ballistic rather than diffusive transport conditions in the InSb nanowire devices with contact spacing ~ 1 μm used in detection of MFs.

Moreover, observation of conductance plateaus is a prerequisite for detection of a helical liquid in a nanowire. Our results are therefore an essential step towards creation of such a helical state. The extracted nanowire characteristics also allow estimation of the experimental conditions under which a helical state arises. It is required that spin-orbit energy E_{SO} and Zeeman energy are similar in size and therefore, based on the reported $|g|$ factor and $E_{SO} \sim 50$ μeV [81], a magnetic field of $\sim$ 15 mT is predicted to lead to a helical state. Furthermore, subband spacings reported here are expected to be large enough to allow detection of helical liquid signatures on conductance plateaus. Future experiments will focus on nanowire devices with local gating, giving more control over the shape and location of confinement potential, to achieve ballistic transport at zero magnetic field, and will explore ballistic transport in nanowires in the presence of spin-orbit interaction.

4.7 Supplementary data

4.7.1 Device fabrication and characterization

Contacts to the InSb nanowire were defined by electron beam lithography. Prior to metal deposition an in-situ argon etch was used to remove the native oxide around the InSb nanowire. Subsequently Ti (25 nm) and Au (150 nm) were deposited.

A gate trace taken with 10 mV DC bias at zero magnetic field (figure S1a) shows steplike features on top of a steep increase of current with gate voltage. Such steplike features have been observed in several devices and could be resulting from transport through individual subbands. Conductance traces at 0 T (see Figure 4.3a) however do not show conductance steps, but instead show oscillations superimposed on an increase in conductance with gate voltage. Furthermore, we found that several wires with steplike features at $B = 0$ T did not show conductance quantization at high magnetic field.

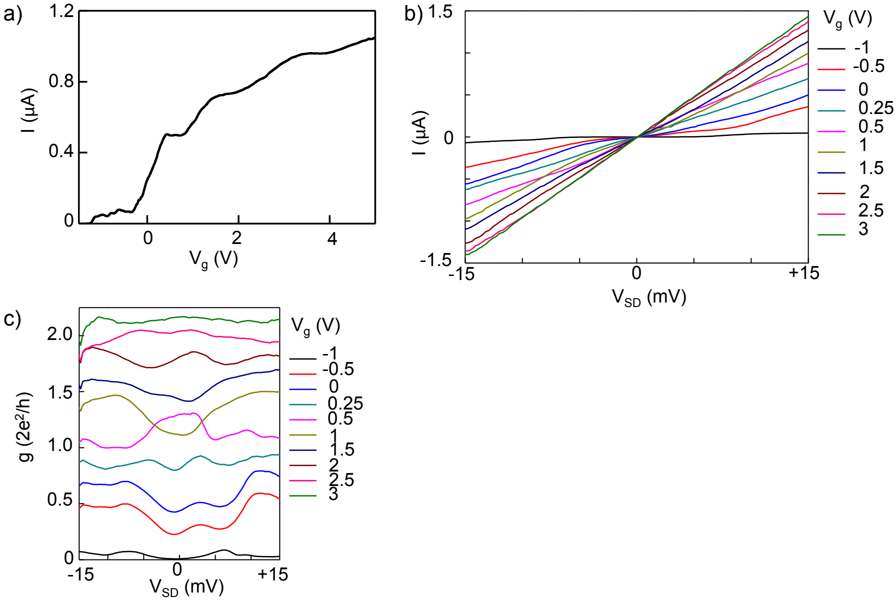

Figure 4.6: Electrical characterization device I. a) Pinch-off trace taken with 10 mV DC bias. As the current amplifier has a 2 kΩ impedance the minimum resistance of the wire and the wire-metal contact (at $V_g = 5$ V) is 7.5 kΩ. **b)** Bias voltage sweeps at several gate voltages. **c)** Conductance as a function of bias voltage at several gate voltages. Conductance is obtained from a numerical derivative of the voltage sweeps shown in panel b. A vertical offset of $0.1 g_Q$ is added between traces for clarity

DC voltage bias sweeps show ohmic (linear) response at higher gate voltages (Figure 4.6b). At gate voltages closer to pinch-off small deviations from ohmic response are observed with both increasing as well as decreasing conductance (see Figure 4.6c, which is a numerical derivative of the data in Figure 4.6b) for low bias voltages. Conductance measurements as a function of gate voltage and source-drain bias at zero magnetic field (Figure 4.7a), where now an AC voltage excitation is used to obtain differential conductance, also show these oscillations. As both peaks and dips in conductance are seen these oscillations are not attributed to Coulomb blockade. While the origin of the oscillations is not entirely clear, we hypothesize it could due to Fabry-Perot interference effects in wire regions [88], as sometimes a few periods of the oscillations are seen (such as in Figure 4.6b-c). Another explanation would be the formation of resonances due to a confinement potential that is not sufficiently adiabatic along the direction of propagation [108].

The pinch-off trace of device II (Figure 4.8a) also shows a steep current increase and steplike features. Small aperiodic oscillations are seen on top of the conductance gate trace at 0 T (Figure 4.8b).

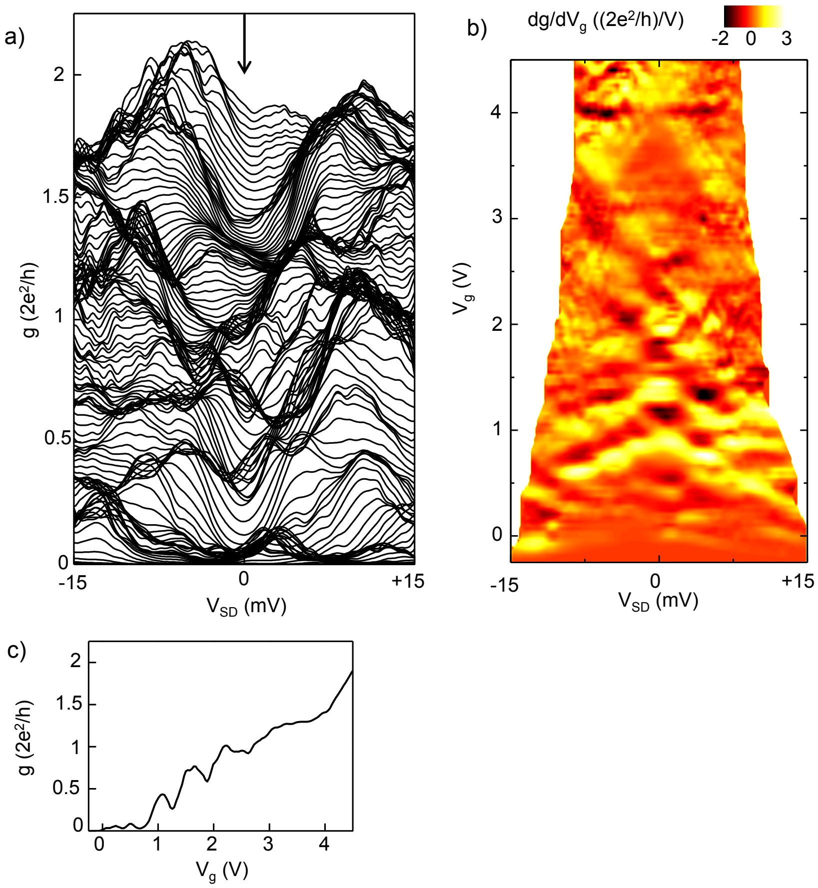

Figure 4.7: Voltage bias spectroscopy of device I at 0 T. a) Conductance, g, as a function of source-drain bias, V_{SD}, for fixed gate voltage in the range of -0.25 V to 4.5 V. No offset is added to traces. In the calculation of wire conductance a series resistance of 6 kΩ has been subtracted. Cut at $V_{SD} = 0$ mV indicated by the arrow is shown in panel c. **b)** Transconductance, $\frac{dg}{dV_g}$, as a function of source-drain bias, V_{SD}, and gate voltage, V_g. c) Conductance as a function of gate voltage, V_g, at $V_{SD} = 0$ mV.

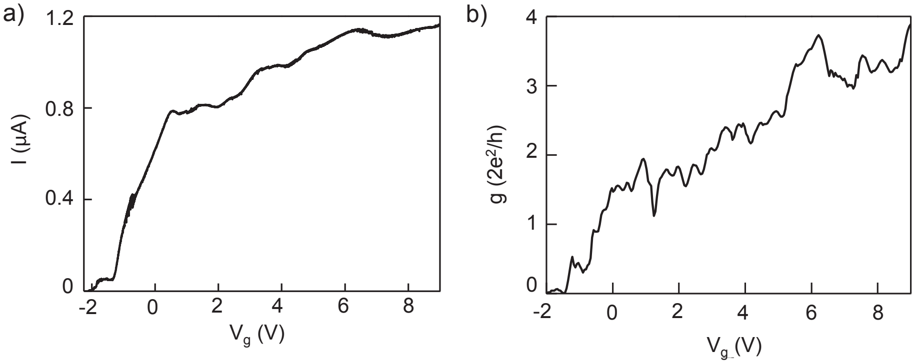

Figure 4.8: Gate traces device II. a) Pinch-off trace taken with source-drain bias V_{SD} = 10 mV. **b)** Conductance as function of gate voltage. B = 0 T, V_{SD} = 0 mV. A series resistance of 6 kΩ has been subtracted.

4.7.2 Contact resistance

For both device I and contacts 1-2 of device II 6 kΩ of resistance was subtracted in the conversion from current I_{AC} to conductance g, chosen such that the conductance of the second conductance plateau is $1.0g_Q$. The 6 kΩ series resistance consists of the impedance of the current amplifier (3 kΩ) and the resistance at the contact between wire and metal. The contact resistance is therefore taken as 3 kΩ.

To examine whether 3 kΩ is a reasonable value for the contact resistance a comparison can be made to the resistance of the two devices at high gate voltage (high electron density). These minimum resistances were (after subtraction of ammeter impedance) 7 kΩ and 6 kΩ respectively and consists of both contact resistance and wire resistance. When also at high gate voltage a small number of subbands ($\sim\leq 10$) is occupied wire resistance still contributes significantly to the two-point resistance, and therefore the minimum resistance, although an upper limit, is not a direct measure of contact resistance.

The assumption of a wire resistance contribution to the resistance at high gate voltage is supported by an estimate of the number of occupied subbands estimated from the electron density $n_{1D} \sim 4 \cdot 10^8$ m^{-1}. In this calculation a 1D density of states with subband spacing derived from a cylindrical well with diameter 70 nm is integrated up to the measured density. Here we find 6 occupied subbands at high gate voltage, giving a contribution of wire resistance ~ 2 kΩ to the minimum resistance. Assuming a 2 kΩ wire resistance, the contact resistance would be 4 – 5 kΩ, close to the 3 kΩ used in measurements.

For the wire region between contacts 2-3 of device II (see Section 4.7.4) a smaller contact resistance was used (1 kΩ of contact resistance to match the conductance of the second plateau). For this device the minimum resistance at high gate voltage (4 kΩ) was also lower than in device I and wire region 1-2 in device II, consistent with

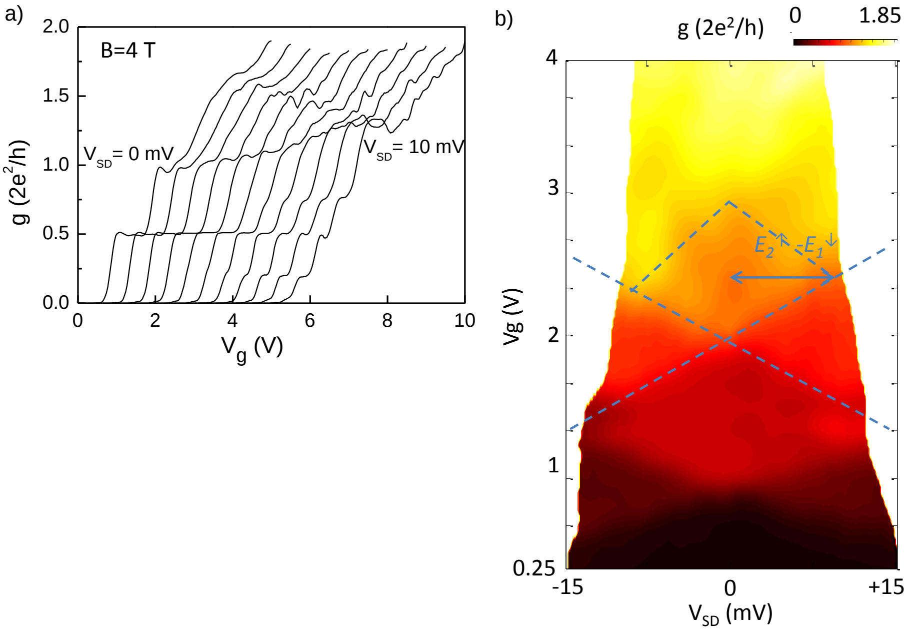

Figure 4.9: Voltage bias spectroscopy $E_2^\uparrow - E_1^\downarrow$ of device I. a) Gate traces at $B = 4$ T with increasing source-drain voltages. While the $0.5g_Q$ plateau shrink with source-drain bias, but remains at the same conductance, the conductance of the $1.0g_Q$ plateau at $V_{SD} = 0$ mV increases with source-drain bias. **b)** Conductance as function of gate voltage and source-drain bias at $B = 4$ T. The approximate extent of the $1.0g_Q$ plateau is indicated.

the assumption of a lower contact resistance.

4.7.3 Voltage bias spectroscopy $E_2^\uparrow - E_1^\downarrow$ of device I

The conductance of the $1.0g_Q$ plateau gradually increases to $1.25g_Q$ as source-drain bias is increased (Figure 4.9a). The transconductance (Figure 4.3) therefore does not show a clear high-transconductance line separating the $1.0g_Q$ and 1.25 g_Q plateau. This prevents extraction of subband spacing $E_2^\uparrow - E_1^\downarrow$ of device I from transconductance measurements. Instead the subband spacing $E_2^\uparrow - E_1^\downarrow$ of device I has been obtained from measurements of conductance as function of source-drain bias and gate voltage such as Figure 4.9b. The transconductance of Figure 4.3c is obtained from numerical differentiation of this conductance measurements to gate voltage.

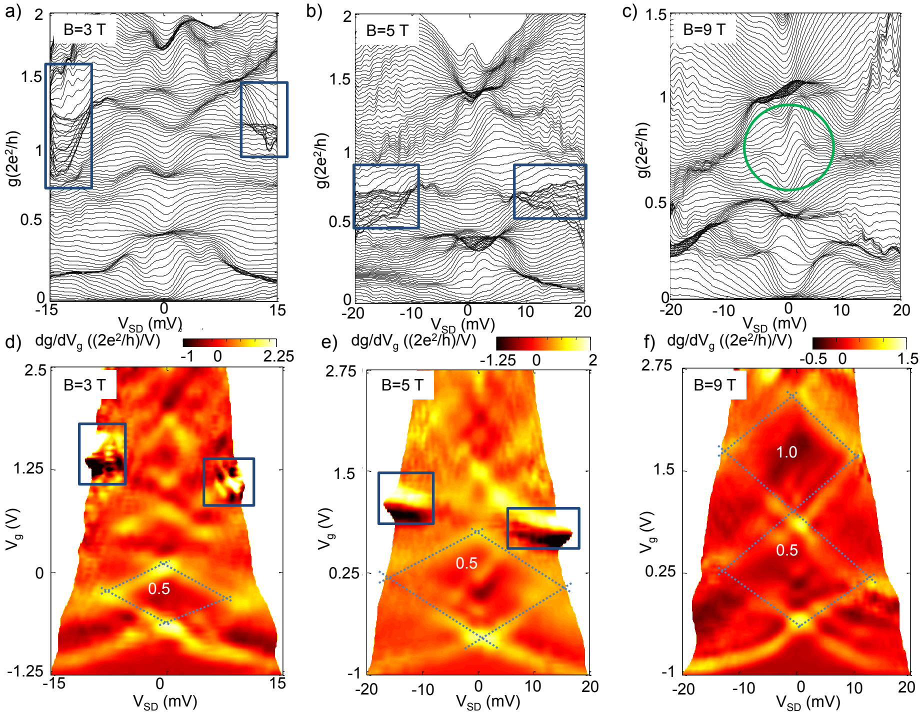

Figure 4.10: Voltage bias spectroscopy device II at $B = 3$ T, 5 T and 9 T. a) (b),c)) Conductance, g, as a function of source-drain bias, V_{SD}, for fixed gate voltage V_g in the range of -1.25 V $\leq V_g \leq 2.5$ V at $B = 3$ T (-1 V $\leq V_g \leq 2.75$ V at $B = 5$ T, $B = 9$ T). Of the dense regions around $V_{SD} = 0$ mV in panel a only the plateau at $g \sim 0.5 g_Q$ has a constant conductance as a function of magnetic field, as seen in Figure 4.5a and in panels b-c. In panel c the conductance oscillations between $0.5 g_Q < g < 1.0 g_Q$ around $V_{SD} = 0$ mV (indicated by the green circle) resemble Fabry-Perot interference. The deviations in the traces at high bias indicated by boxes in panels a and b are due to electronics artifacts. **d) (e), f))** Transconductance, $\frac{dg}{dV_g}$, as a function of source-drain voltage and gate voltage. Conductance plateaus are indicated. Transconductance dips and peaks on conductance plateaus (seen for the $0.5 g_Q$ plateau in panel e and for the $0.5 g_Q$ and $1.0 g_Q$ plateau in panel f) can be due to Fabry-Perot interference or resonances. Deviations in the regions at high bias indicated by boxes are due to an electronics artifact.

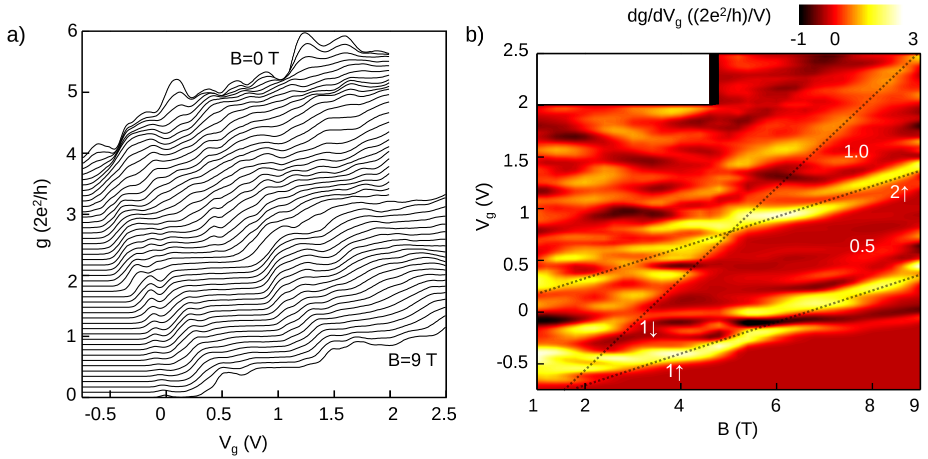

Figure 4.11: Subband crossing of wire region between contact 2 and 3 (inset panel 4a). a) Conductance as function of gate voltage, V_g, for out-of-plane magnetic field $B = 0$ T to $B = 9$ T in steps of 0.2 T. A series resistance of 4 kΩ was subtracted. **b)** Transconductance, $\frac{dg}{dV_g}$, of the data shown in panel a in the range $B = 1$ T to $B = 9$ T. High transconductance (yellow/white) corresponds to the onset of transport through a subband. Conductance of the plateaus (zero transconductance; red) is indicated. Dotted lines are guides to the eye.

4.7.4 Voltage bias spectroscopy of device II

The subband spacings $E_1^{\downarrow} - E_1^{\uparrow}(B)$, $E_2^{\uparrow} - E_1^{\downarrow}(B)$ and $E_2^{\uparrow} - E_1^{\uparrow}(B)$ of Figure 4.5b were obtained from voltage bias spectroscopy measurements. Similar to Figure 4.4, voltage bias spectroscopy measurement also here serve as a confirmation that the plateaus of device II seen in Figure 4.5a are plateaus of quantized conductance, i.e. arise as a result of transport through separate subbands. Three of such measurements, at $B = 3$ T, $B = 5$ T and $B = 9$ T are shown in Figure 4.10, both as conductance traces as a function of source-drain voltage at fixed gate voltage (panels a, b and c) and transconductance representation (panels d, e and f). In the transconductance plots the plateaus with conductance $0.5g_Q$ and $1.0g_Q$ are indicated.

4.7.5 Subband crossing in wire region 2-3 of device II

Conductance quantization was also observed in the wire section between contacts 2 and 3 in device II (Figure 4.11a). Similarly to Figure 4.5 conductance steps are seen at $B \geq 2$ T ($g = 0.5g_Q$ plateau) and $B \geq 5$ T ($g = 1.0g_Q$ plateau). The transconductance of the gate traces shown (Figure 4.11) shows evidence of a subband crossing at ~ 4.5 T: the $0.5g_Q$ plateau remains constant in width for $B \geq 4.5$ T and the $1.0g_Q$ plateau widens for $B \geq 4.5$ T.

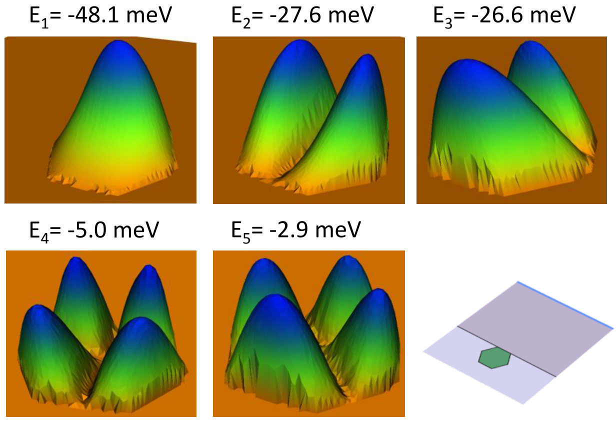

Figure 4.12: Orbitals and their energies obtained from a self-consistent Schrödinger-Poisson solver. $V_g = 1.4$ V. The device geometry is drawn in the lower right panel.

4.7.6 Subband spacing: comparison experiment and electrostatics simulations

The experimental results on subband spacing of Section 4.5 can be compared to numerical simulations employing the self-consistent Schrödinger-Poisson solver described in Section 3.4. The solver yields the orbitals and their energy as a function of gate voltage. An example is shown in Figure 4.12. The energy spacing between the first and second subband of ~ 20 meV remains approximately (within a few meV) constant with gate voltage (see Figure 4.13). This subband spacing is in reasonable agreement with the subband spacing of ~ 15 meV extrapolated from experiment. The difference in gate coupling between simulation (~ 4 subbands/V) and experiment (~ 1 subbands/V) is likely explained by screening of the gate potential by the contacts, which are not included in the two-dimensional solver.

At low gate voltage and in the absence of magnetic field the (nearly) degenerate second and third subband (see Figure 4.13) leads to a doubling of the second conductance step. The conductance increases from g_Q to $3g_Q$ at the onset of the 2nd and 3rd subband. This double step in conductance may have been observed in InAs nanowires [91],[109]. At non-zero magnetic field, assuming only a Zeeman splitting, the degeneracy results in conductances of $\frac{g_Q}{2}$, g_Q and $2g_Q$ as voltage is increased. The subband degeneracy would affect the conductance plateaus involved in the subband crossing in Figure 4.5: the second conductance plateau at $B > 5$ T would be at $g = \frac{3}{2}g_Q$. The observation of a plateau with $g = g_Q$ could be an indication that the back gate voltage leads to a steeper potential than expected from the simulation, resulting in a larger energy difference between the second and third subband. Also a difference in g-factor between subbands $2\uparrow$ and $3\uparrow$ would lift the degeneracy of $2\uparrow$

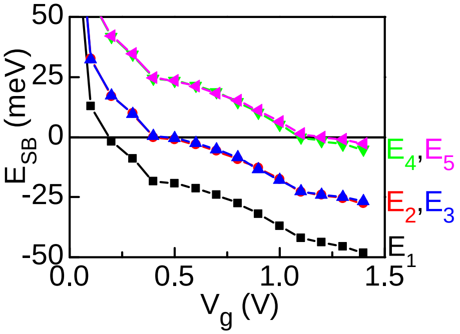

Figure 4.13: Simulated subband spacing, E_{SB}, as a function of gate voltage. Subband i contributes to transport when $E_i < 0$. Subbands 2 and 3, as well as 4 and 5 are (nearly) degenerate at low gate voltages.

and 3↑, leading to a plateau with $g = g_Q$. Measurements in cleaner samples, allowing observation of quantized conductance down to smaller or zero B can likely elucidate the presence of such degeneracies.

CHAPTER 5

FORMATION AND ELECTRONIC PROPERTIES OF InSb NANOCROSSES

Signatures of Majorana fermions have recently been reported from measurements on hybrid superconductor-semiconductor nanowire devices. The Majorana fermions are predicted to obey special quantum statistics, known as non-Abelian statistics. To probe this, one needs to perform an exchange operation, which requires moving two Majoranas around each other, an operation that requires at least a simple network of nanowires. Here, we report on the synthesis and the electrical characterization of crosses of InSb nanowires. The InSb wires grow horizontally on flexible vertical stems, thereby allowing nearby wires to meet and merge. In this way near-planar single-crystalline nanocrosses are created, which can be measured by four electrical contacts. Our transport measurements show that the favourable properties of the InSb nanowire devices, a high carrier mobility and the ability to induce superconductivity, are preserved in the cross devices. Our nanocrosses thus represent a promising system for the exchange of Majorana fermions.

This chapter has, with the exception of Section 5.11.3, been published as S.R. Plissard*, I. van Weperen*, D. Car, M. A. Verheijen, G. W. G. Immink, J. Kammhuber, L. J. Cornelissen, D. B. Szombati, A. Geresdi, S. M. Frolov, L. P. Kouwenhoven, E. P. A. M. Bakkers, Formation and electronic properties of InSb nancrosses, *Nature Nanotechnology* **8**, 859-864 (2013). * These authors contributed equally.

5.1 Introduction

Majorana fermions (Mfs) [11] can arise as pairs of quasi-particles located at the ends of a semiconductor nanowire in contact with a superconductor [17],[110],[111]. Interestingly, the quantum properties of Mfs are expected to be protected by topology, becoming insensitive to perturbations, which could make them robust quantum bits [112],[113],[10]. Logical operations can be performed by exchanging the positions of two Mfs, i.e. by braiding, exploiting their non-abelian exchange statistics [12]. Signatures of Mfs have recently been detected in a one-dimensional semiconductor nanowire with strong spin-orbit interactions in contact with a superconductor [17],[110],[111] following recent proposals [19],[18]. The currently available single nanowire devices are, however, not adequate for demonstrating braiding, since Mfs annihilate when they come in close proximity. Recent theories have proposed nanowire junctions to make braiding possible [21],[114],[24] by temporary storing one Mf in an auxiliary leg of a T-junction while moving the other particle across or by using a flux-controlled interaction between Mfs in a double T-junction (Figure 5.7).

Braiding of Mfs imposes three strong requirements on the semiconductor materials. First, in order to generate Majoranas the material should exhibit a strong spin-orbit coupling. Second, the branched wires must form a planar structure to enable electronic device fabrication by standard lithography. Finally, the branched structures should be of high crystalline quality, since for Majorana particles it is important to have nearly ballistic transport and defects in the wires and at the interface will induce unwanted Majoranas. Despite continuous progress in the control and the understanding of nanowire growth [115],[116],[117], there are only a few studies focussing on 3D branched nanowire networks [118],[119],[120],[121],[122],[123],[124]. Here, we discuss a new approach to grow InSb T- and X-shaped nanostructures from strong spin-orbit interaction semiconductor indium antimonide, using the Vapor-Liquid-Solid (VLS) mechanism [125] and Au as catalyst. We show that all requirements set above are satisfied in our structures. The crosses grow as single-crystals of high mobility, comparable to single InSb nanowires [59].

5.2 Steps in nanocross growth

We start with a qualitative description of the process we developed for the formation of crossed wires. The procedure includes 4 steps, which are presented schematically in Figure 5.1, accompanied by corresponding scanning electron microscopy (SEM) images. The first step is the fabrication of uniform InP-InAs stems (Figure 5.1a) according to the method described in [59]. In step 2, the structure is thermally annealed at 470°C without any precursor present in the reactor chamber, resulting in partial evaporation of the InAs nanowire and an indium enrichment in the Au-In droplet. Since the particle volume increases and the InAs nanowire diameter decreases, the droplet falls to one of the three {112} InAs side facets (Figure 5.1b, Figure 5.9). It is then possible to start the growth of InSb nanowires in a horizontal direction, parallel

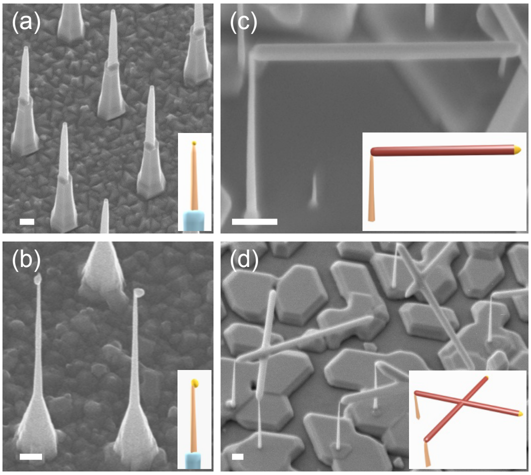

Figure 5.1: Scheme of the four-step process to synthesize branched InSb nanowires. a) 30° tilted Scanning Electron Microscopy (SEM) image of the InP/InAs stems. **b)** Au-In droplets on side-facets after the annealing step. **c)** InSb nanowire grown parallel to the substrate surface. **d)** InSb nanocrosses resulting from the merging process between two InSb nanowires. For all SEM images the scale bar is 200 nm, but the growth time of the different segments is different. In the schemes, the InP, InAs and InSb segments are respectively in blue, orange and red; the Au-In droplet is in yellow.

to the substrate (Figure 5.1c), using the optimal growth conditions (Figure 5.8) developed in [59] for high mobility wires [17],[126]. If the optimal diameter and density of Au colloids is used, InSb nanowires, growing from different stems, can meet and merge into nanostructures having a T or X shape (Figure 5.1d).

5.3 Nanowire intersection

The merging of the wires will now be discussed in more detail. To describe the nanowire intersection, three angles are defined as reported in Figure 5.2b-c. ψ corresponds to the angle between the vertical stem and the growth direction of the InSb nanowire, φ is the in-plane angle of the InSb nanowire, and γ is the rotation angle of the InSb nanowire around its long axis. Interestingly, these different angles are not random, which will be shown below.

SEM side-view inspection of the samples shows that ψ is close to 90°, implying that the tapering of the InAs nanowires is minimal. To investigate the exact crystalline orientation of the InSb wires X-ray diffraction measurements were performed in a symmetric 2θ-ω configuration. Figure 5.2a shows a diffraction spectrum of the same sample, where the (111) peaks of InP, InAs and InSb originate from the stems

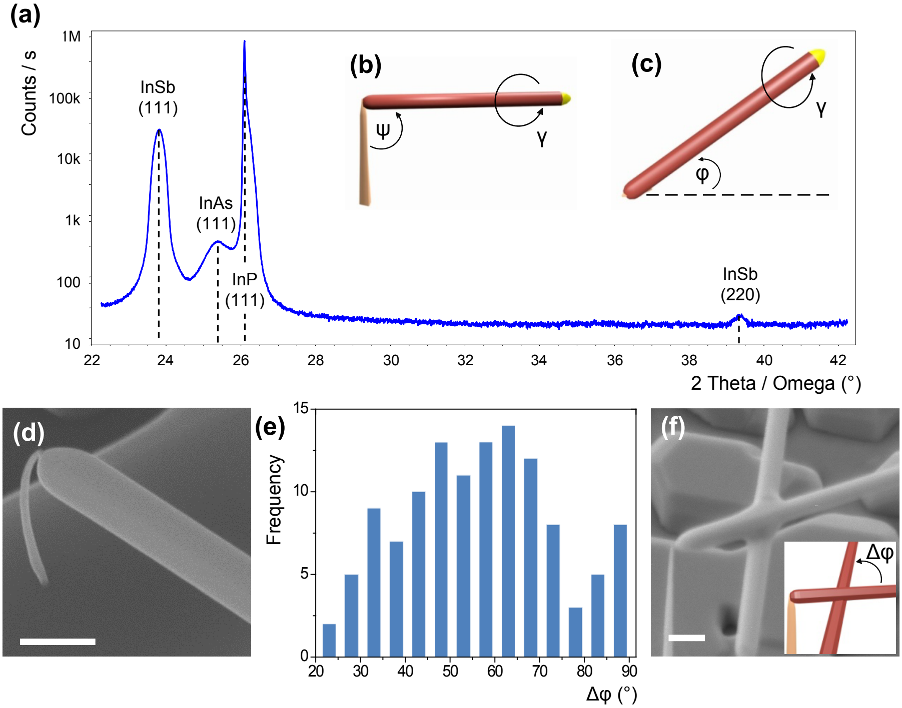

Figure 5.2: Merging process of two InSb nanowires. a) Symmetrical (2θ-ω) XRD measurement on an as grown sample. **b)** and **c)** respectively side-view and top-view scheme of the InSb nanowires grown horizontally. The 3 angles defining the InSb growth direction are ψ, φ and γ. ψ corresponds to the angle between the vertical stem and the growth direction of the InSb nanowire, φ is the in-plane angle of the InSb nanowire with respect to the $\langle 1\bar{1}0\rangle$ direction of the InP(111)B substrate, and γ is the rotation angle of the InSb nanowire around its long axis taking the alignment of the (220) InSb planes with the substrate surface as a reference. **d)** High resolution SEM image of an InP/InAs stem bended during the merging process. **e)** Statistics about the $\Delta\varphi$ angle between two crossing InSb nanowires. **f)** Example of a branched structure: the two InSb nanowires should have a slight difference in altitude in order to merge into a nanocross. For all images, the scale bar is 200 nm.

and a thin layer on the substrate. Importantly, a fourth peak also appears around the InSb(220) Bragg angle (39.3°). The intensity is rather weak, due to the small volume of material, but is still detectable with a standard set up and the 2θ full width at half maximum is ~ 0.4°. This peak originates from InSb nanowires having one of their {110} side facets parallel to the substrate surface. The fact that no other sets of InSb lattice planes perpendicular to the $\langle 111 \rangle$ growth direction (e.g. (422)) show up in the XRD pattern proves that ψ and γ are fixed to 90° and 0°, respectively (see Section 5.10.2). Since stems and substrate have no horizontal $\langle 111 \rangle$ crystalline directions, it demonstrates that the InSb nanowires have no epitaxial relation with the InP-InAs stems, and the stems only serve as a mechanical support.

In order to investigate φ, we measured the angle ($\Delta\varphi$) between two legs for T- and X-shaped nanostructures (Figure 5.2e-f). For this study more than 100 InSb crosses have been transferred onto a SiO_2 substrate and imaged from the top in order to have a perpendicular projection. The histogram in Figure 5.2e shows a maximum around $\Delta\varphi = 60°$. This maximum can be explained by the triangular cross-sectional shape of the InAs segment (Figure 5.9). During the annealing step, droplets fall to a lateral facet leading to 6 preferential directions for $\Delta\varphi$ and a maximum around 60°. Due to the stem evaporation, it is also possible for small InAs diameters to change the cross-section from a triangle to a hexagon. In this particular case a droplet can cover more than one facet because of its large volume in comparison with the stem diameter, leading to smaller maxima every $\Delta\varphi = 30°$ (Figure 5.2e, Figure 5.10).

During the final step of the process, the wires can merge and form a planar, branched nanowire structure; in this case either T- or X-shaped. The formation of a T- or an X-structure depends on the level of alignment of two InSb nanowires in the vertical direction (Figure 5.2f). When the wires are slightly misaligned in altitude a cross is formed. During the axial growth, the wire also grows in the radial direction. For InSb this radial growth mainly takes place just below the Au catalyst particle, due to the catalytic decomposition of the TMSb precursor by Au. The decomposed material can then either lead to axial, but also to radial growth, soldering the two wires together. The vertical distance between two approaching wires can be reduced due to the flexibility of the InAs stems as shown in Figure 5.2d. In that case, the InAs stem will bend during the merging process. For most crosses the InAs stems are slightly bent which is important for obtaining a high yield of crosses. More importantly, these flexible stems also allow small corrections of $\Delta\varphi$ in order to form single crystalline crosses. This phenomenon, already observed for nanoparticles in solution [127], tend to align the crystalline orientations of both nanowires and can correct small misalignments (< 2°). When the two wires are perfectly aligned in altitude, T shapes are formed. In this particular case the droplet of one wire touches the second one exactly in the middle of the nanowire. The catalyst particle will bounce and either move along one of the side facets or get stuck by wetting a re-entrant corner. As a consequence a T-shaped structure or nanowing is formed (Figure 5.13, Figure 5.14).

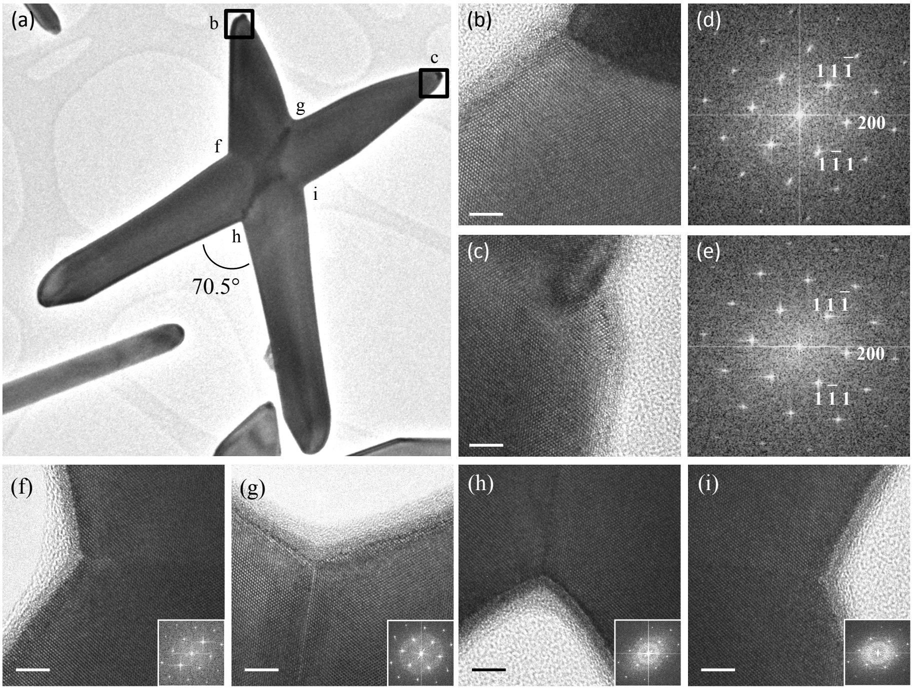

Figure 5.3: Crystal structure of a single-crystalline nanocross. a) Low resolution Transmission electron Microscopy (TEM) image of a single crystalline InSb nanocross. **b)** and **c)** HR-TEM images just below the droplet for both branches, the scale bar is 5 nm. **d)** and **e)** FFT pattern corresponding respectively to (b) and (c). The crystalline directions are perfectly superposed proving nanocross in (a) is a single crystal. **f)**, **g)**, **h)** and **i)** HR-TEM images of each corner of the nanocross and the corresponding FFT pattern showing a single crystalline orientation, the scale bar is 5nm.

5.4 Crystalline quality

The crystalline quality of these junctions is studied by High Resolution Transmission Electron Microscopy (HR-TEM) for crosses with different joining angles. When the crossing angle between two InSb NWs, which grow along a (111)B direction, is $\Delta\varphi = 70.5^\circ$ (Figure 5.3a), the crystalline directions of both branches are aligned and a single crystalline structure is formed. (Depending on the polarity orientation of the two wires, also a twinned junction can be obtained). HR-TEM images of a single crystalline cross, obtained just below the droplets of each branch are shown in Figure 5.3b and Figure 5.3c. The related fast Fourier transforms (FFT) are presented in Figure 5.3d and Figure 5.3e. The perfect match of the FFT patterns proves that the cross in Figure 5.3a is a single crystal paving the way to advanced electronic transport devices. TEM data of junctions with different $\Delta\varphi$ angles are shown in the supplementary ma-

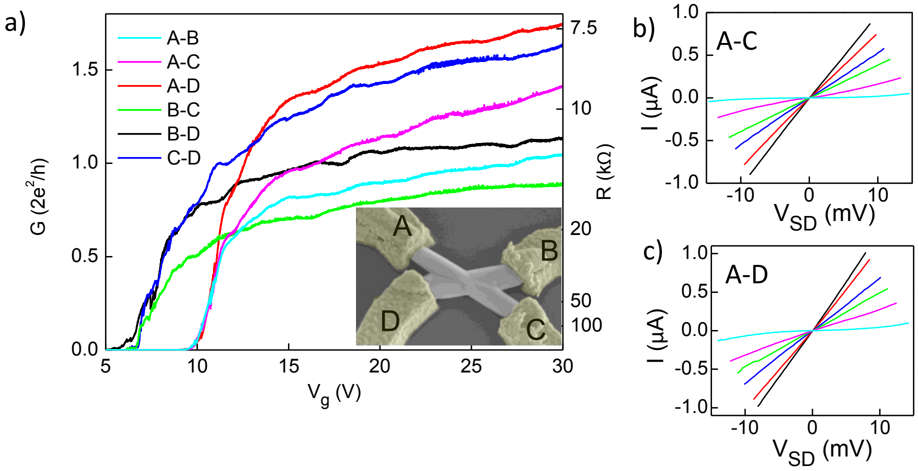

Figure 5.4: Transport through a nanocross. All data taken at a temperature of 4.2 K. **a)** Conductance, $G = \frac{I}{V_{SD}}$, of all 6 contact pairs as function of gate voltage, V_g. V_{SD} is the voltage bias across the device, I is current. V_{SD} is for all traces between 10 mV (near pinch-off) and 5 mV (at V_g = 30 V). Right axis: Resistance $R = \frac{1}{G}$. Inset: SEM image (50° tilted) of the measured nanocross. $\Delta\varphi$, the angle between nanocross legs, is 45°. **b)** and **c)** Bias voltage sweeps of contact pairs A-C (A-D) at several V_g. For (b), from blue to black, V_g = 9.8, 10.5, 11.1, 12, 15, 22.5 V and for (c), from blue to black, V_g = 9.8, 10.2, 10.7, 11.7, 15, 22.5 V.

terial (Figure 5.11, Figure 5.12, Figure 5.13). In the most probable case ($\Delta\varphi = 60°$), the merging process occurs for two nanowires having different crystalline orientations, only sharing horizontally oriented (110) planes at the same altitude. In this case, a Moiré fringe pattern characteristic of the interference of two different crystalline directions appears in the HR-TEM images. Interestingly, the crystalline orientation of each branch is the same before and after the junction and the only defect of the structure is the grain boundary at the junction (Figure 5.11, Figure 5.12).

5.5 Transport: characterization

We now investigate the electrical transport properties through merged nanowires. A nanocross is contacted (inset Figure 5.4a) and the electron density is controlled with a global back gate. The two-point resistance can be modulated by the gate potential between 7 – 15 kΩ and pinch-off for all contact pairs (Figure 5.4a). The linear IV-sweeps obtained for all contact combinations (Figure 5.4b, Figure 5.4c) indicate ohmic contacts and the absence of localization in the nanocross. This shows that the interface at the intersection of the two wires is sufficiently transparent to allow transport from wire to wire without a tunnelling barrier.

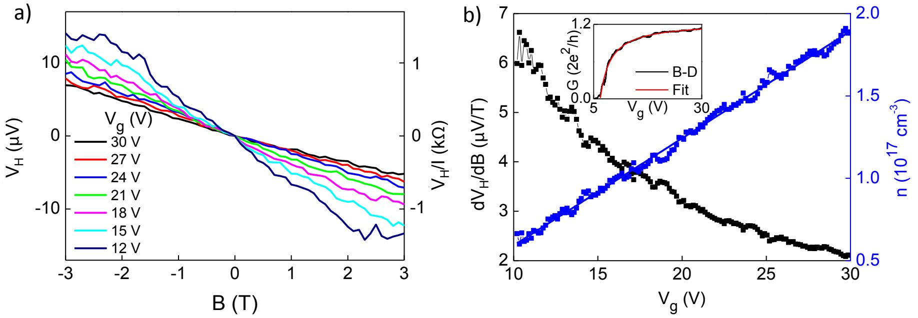

Figure 5.5: Nanocross Hall measurements. a) Hall voltages, $V_H = V_B - V_D$, obtained by application of 10 nA AC current, I, through C-A at magnetic field, B, at several gate voltages, V_g. Measured traces have an offset of ~ 3 μV at B = 0 T, likely a longitudinal voltage, that has been subtracted. Trace at V_g = 12 V is an average of 3 traces; all other traces are obtained in a single measurement. Right axis: Hall resistance, $\frac{V_H}{I}$. **b)** From the Hall slope, $\frac{dV_H}{dB}$, (left axis) the electron density, n, (right axis) as a function of gate voltage is extracted. A linear fit of $n(V_g)$ (blue line) gives $\frac{dn}{dV_g}$ = 6.5·10^{15} cm^{-3}V^{-1} and therefore capacitance C = 51 aF for channel B-D (see Section 5.11.2). This capacitance is used in a fit to gate trace B-D (see inset) and yields mobility 8000 cm^2/Vs.

5.6 Nanocross Hall measurements

To assess the carrier mobility in the nanocross we extract the electron density from Hall measurements. The standard method in electrical characterization of nanowires is the extraction of field-effect mobility from gate traces. This method however has the drawback that it requires accurate knowledge of the capacitance between gate and nanowire, which is often lacking. Merged nanowires allow us to experimentally extract the nanowire capacitance from measurements of carrier density as function of backgate voltage. Approximations made to the nanocross device geometry and transport regime however limit the accuracy of our mobility estimate (Section 5.11.2).

Gate-tunable Hall resistances of ~ 1 kΩ at $B \approx 3$ T are obtained (Figure 5.5a). The electron density n, extracted from these Hall measurements, increases linearly with gate voltage (Figure 5.5b) from ~ 5·10^{16} cm^{-3} to ~ 2·10^{17} cm^{-3}. Gate-nanocross capacitances of ~ 50 aF are derived from a linear fit of $n(V_g)$. We then extract the field-effect mobility from a fit to the gate traces of Figure 5.4a (see inset of Figure 5.5b for channel B-D) and find mobilities of ~ 6500 to ~ 9000 cm^2/Vs. The same analysis for a second nanocross device (Section 5.11.4) yields mobilities of ~ 6700 to ~ 10,000 cm^2/Vs. These high mobilities reflect the high structural quality of our InSb nanocrosses. Moreover, these mobilities indicate that the favourable transport properties of InSb nanowires are preserved in complex wire structures. Nanocross sections with and without grain boundary show similar mobility. Moreover, gate traces of nanocrosses and T-junctions with various crossing angles $\Delta\varphi$ between 40° and 70°

are comparable. Therefore the mobility is likely limited by other factors than the grain boundary, such as scattering at the surface or at impurities.

5.7 Induced superconductivity in a nanocross

Since superconductivity is a key ingredient for creation of Mfs, it is essential to induce supercurrent in nanocrosses. Superconducting leads have therefore been deposited at each end of a nanocross (Figure 5.6a). Contact pairs of the device have a normal state conductance at large positive gate voltage between 1.1 and 3.5 G_0 ($G_0 = \frac{2e^2}{h}$). The $V(I)$ characteristic of all measured contact pairs exhibits a supercurrent branch indicating proximity induced superconductivity [93],[90]. Switching to a resistive state occurs when the current bias exceeds the critical current I_c (Figure 5.6b). I_c is gate-tunable (Figure 5.6c) and increases with the nanocross normal state conductance. By comparing different contact pairs, we find that I_c depends on the contact separation and varies between $\sim$ 4.6 nA (section A-C, separation 620 nm) and $\sim$ 0.25 nA (C-D, separation 1.5 μm). Critical current within a single nanowire (section A-C) and through the nanocross junction (B-C) are comparable. Moreover, the supercurrents through these nanocross sections are similar to that through an InSb nanowire Josephson junction contacted with the same superconductor and with similar contact separation (Figure 5.24). These results substantiate the expectation that crossed nanowires will enable advances in topological superconducting systems such as the development of the proposed Mf braiding devices.

5.8 Outlook

There are a few remaining challenges for these structures. First is to increase the mobility in order to obtain ballistic transport between all contacts. The mobility may be enhanced by passivating the wire with a shell of a wide band gap material. InSb has a large lattice constant and most ternary AlInSb or InGaSb compounds would be suitable as a shell material. Second is to improve the yield of single crystalline crossed wires. With the current approach approximately 8 % of the nanocrosses have an optimal merging angle. One option to improve this is the use of (001) oriented substrates [124]. Wires growing along two $\langle 111 \rangle$B directions will meet and if their epitaxial relation with the substrate is maintained, they will form a single crystalline structure.

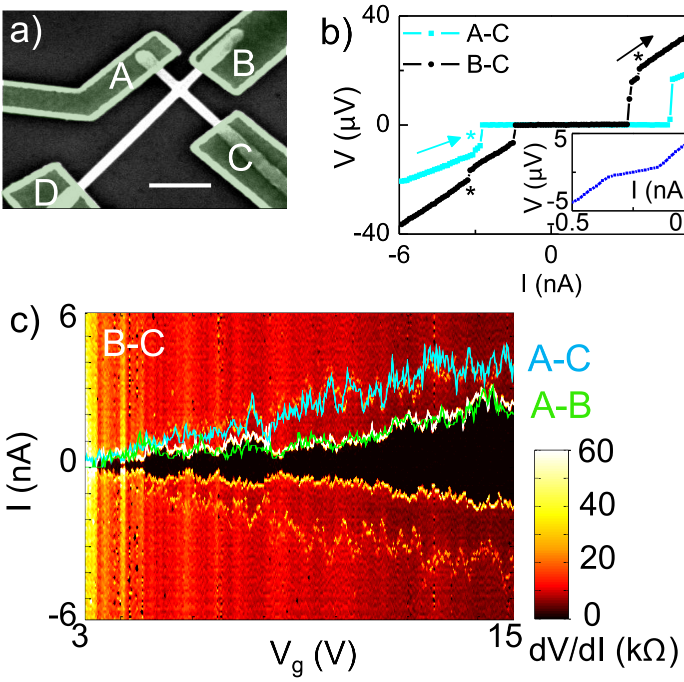

Figure 5.6: Gate-tunable supercurrent through a nanocross. Data taken at 20 mK. Instrumental resistance has been subtracted. **a)** Top view SEM image of the device. In order to decrease the wire diameter, the nanocross was etched by HCl in the growth chamber directly after growth [128]. The scale bar corresponds to 0.5 μm. Contact spacings are 440 nm (section A-B), 620 nm (A-C and B-C), 1300 nm (A-D and B-C) and 1480 nm (C-D). Contact material is NbTiN/Al (50/70 nm). **b)** $V(I)$ characteristics for current bias, I, between contacts A-C (global back gate voltage V_g = 14.8 V, blue) and B-C (V_g = 14.4 V, black).The asymmetry in the $V(I)$ trace, indicating hysteresis, is due to environmental shunting [129] or self-heating of the device [130].The kinks in the dissipative branches (indicated with an asterisk) are likely Fiske steps [131],[132]. Both features are commonly observed in underdamped Josephson junction. In the Supplementary Information (Figure 5.24) we show that these features occur also in our InSb nanowire Josephson junctions. Inset: $V(I)$ characteristic for section C-D (V_g = 13.5 V). **c)** Colour plot: differential resistance, $\frac{dV}{dI}$, as a function of I and V_g between B-C. The black region ($\frac{dV}{dI}$ = 0) indicates supercurrent through the nanocross. Superimposed with the same horizontal and vertical scale is the critical current for B-C (white), A-B (green) and A-C (blue).

5.9 Supplementary information on braiding in nanowire-based devices

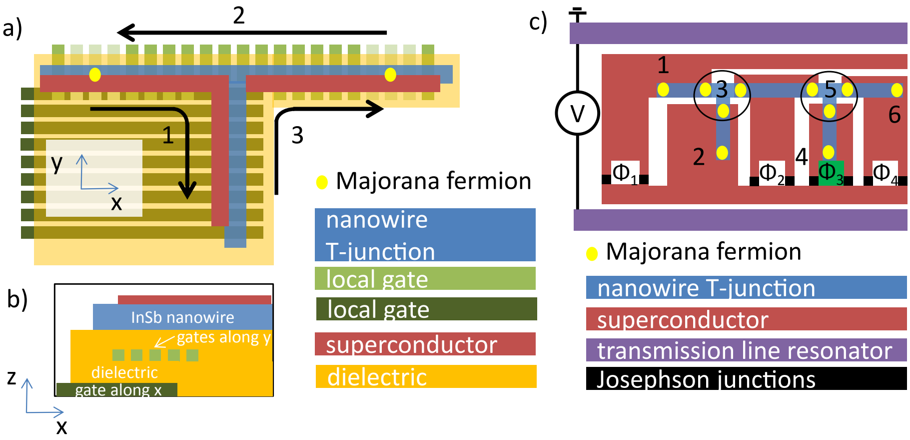

Figure 5.7: Proposed braiding of Majorana fermions in nanowires. **a)** Schematic top view of the set-up for local gate-controlled braiding of MFs based on the proposal by Alicea et al. [21]. A semiconductor nanowire T-junction is contacted with a superconductor. Topological superconducting regions are controlled by the local gates. By controlling the potential on these gates MFs are moved along the nanowire T-junction. The third leg of the T-junction is used to temporarily store one MF while the second one is moved from the right to the left side of the T-junction. **b)** Schematic of a possible device cross section. Two layers of gates separated by dielectric can be used to define gate patterns in orthogonal directions. Positioning of the nanocross with respect to these local back gates can be done by deterministic positioning [71]. Alternatively, advanced fabrication techniques have been developed (amongst others [133], [134], [135]) to make local top gates that could control electrochemical potential. **c)** Schematic set-up for flux-controlled initialization, braiding and read-out of MFs based on the proposal by Hyart *et al.* [24]. A double semiconductor nanowire T-junction is placed between superconducting islands in a transmission line resonator. Three overlapping MFs at the T-junction intersection form a single MF. Braiding is performed by a sequence of fluxes Φ_2, Φ_3, Φ_4 that couple via Coulomb interaction a single MF to the MF at the intersection of the junction. In the situation shown here flux Φ_3 (green) couples MF 4 and 5. Initialization and read-out is performed by application of a flux Φ_1 and a parity measurement.

5.10 Supplementary data on the formation and structural characterization of nanocrosses

5.10.1 Nanowire growth

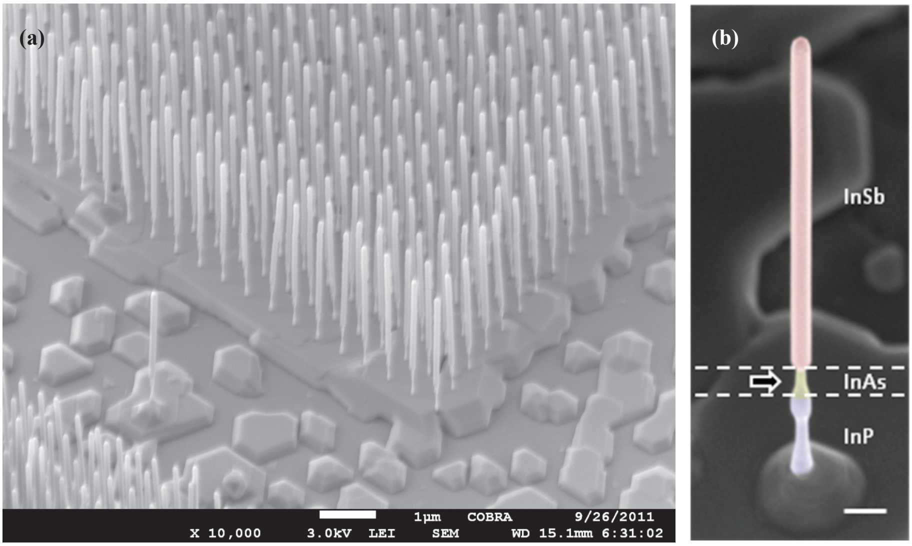

Figure 5.8: Optimized growth conditions for the InSb nanowires. **a)** SEM image of InSb nanowire arrays optimized for Majorana devices: length > 3 μm, diameter < 100 nm, as described in [59]. First, arrays of gold particles are defined on a InP(111) substrate using electron beam lithography. Then, standard InP-InAs stems are grown using TMI, PH_3 and AsH_3 gases as precursors. Contrary to the procedure described in Figure 5.1 the annealing step was not used during this growth. **b)** Single InSb nanowire grown on top of InP-InAs stem without the annealing procedure.

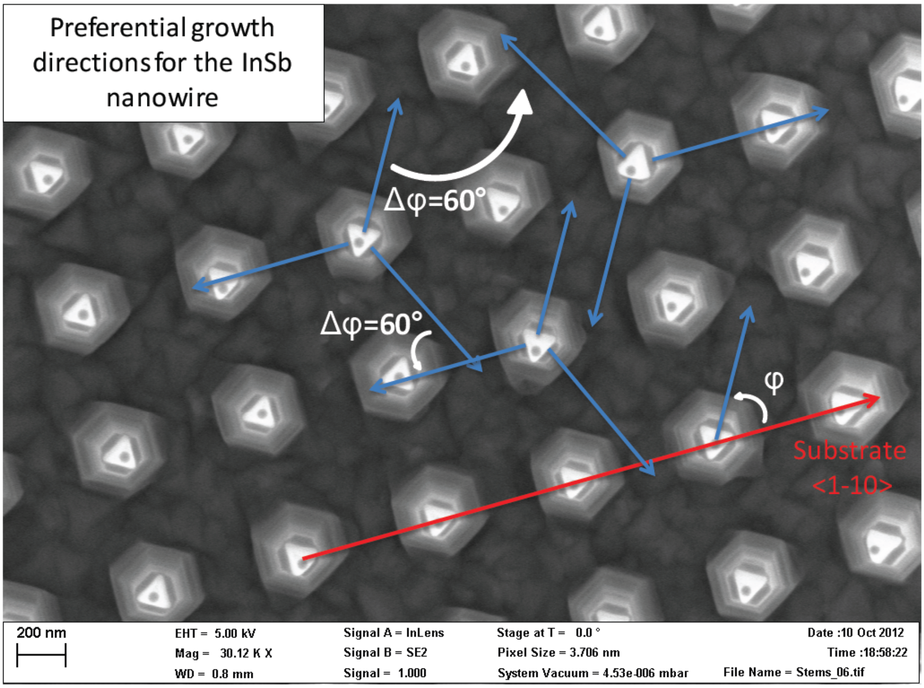

Figure 5.9: Most probable case: $\Delta\varphi$ = 60°. Top-view SEM image the InP-InAs stems (figure 1a of the main text). The pure ZB-InAs nanowires have a triangular cross-section. Two permutations of this triangular shape are possible due to rotational twin boundaries in the InP nanowires. The nanowire arrays are aligned with the ⟨1-10⟩ crystalline direction of the InP(111)B substrate. During the annealing step, the gold-indium droplet will fall onto one of the three side-facets, leading preferentially to the growth of crosses having a 60° angle. The possible growth directions for the InSb nanowires are the 'blue arrows'.

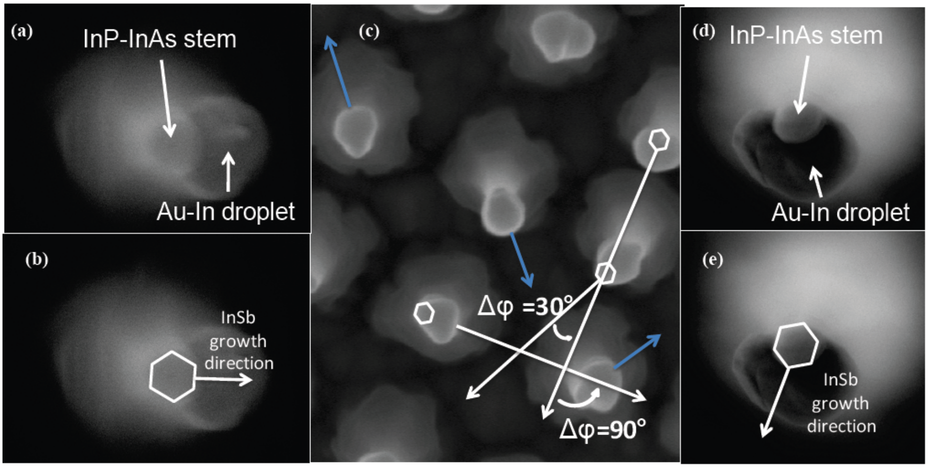

Figure 5.10: Droplets after the annealing step and other 'local' maxima: $\Delta\varphi$=30° and $\Delta\varphi$ = 90°. Top-view SEM image of 'big' droplets after the annealing step (Figure 5.1b). During the annealing step, reconstruction of the nanowire minimal surface facets occurs and changes the cross-sectional shape from triangular to hexagonal. The InAs cross-section is hexagonal. These droplets can fall on more than one side facet **a)**, **c)** and **d)**. The InSb growth can follow the direction perpendicular to a facet **b)** or the diagonal of the hexagon **e)**. When two InSb nanowires having these different angles merge, $\Delta\varphi$ can be 30° or 90° as shown in panel c.

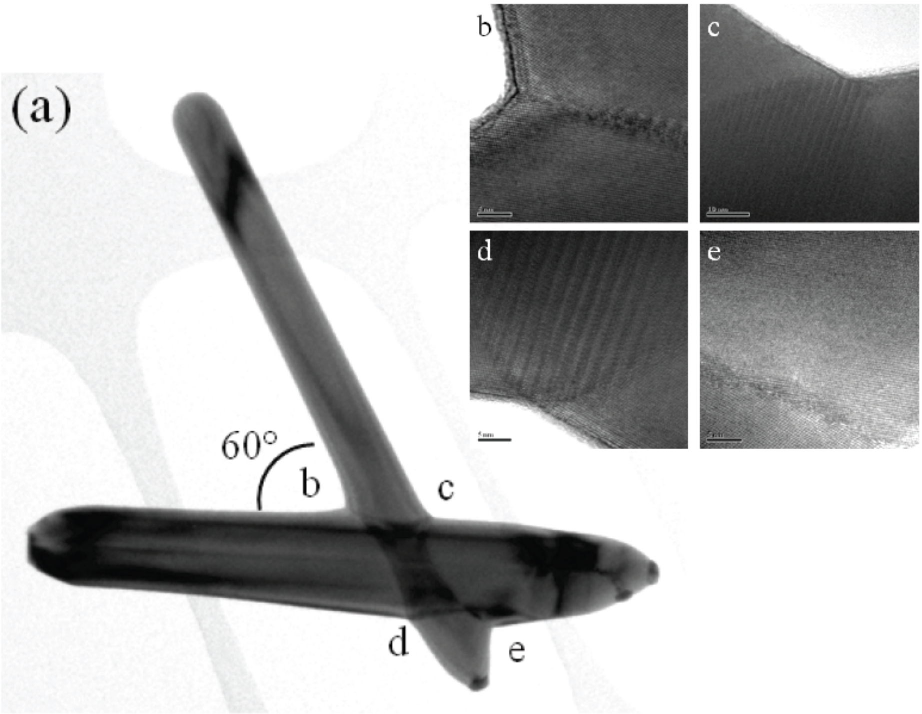

Figure 5.11: TEM image of the most frequent case: $\Delta\varphi$ **= 60° a)** Low resolution image of an InSb nanocross having a 60° angle between intersecting wires. **b)**, **c)**, **d)** and **e)** High Resolution TEM (HR-TEM) images at the 4 corners of the intersection between InSb nanowires. A Moiré pattern can be observed in (c), (d), which is characteristic of the superposition of 2 crystals. In this case a grain boundary is formed between the 2 wires. The scale bars are 10 nm for (b), (c), (d) and (e). HR-TEM images of the tips of this cross are shown in Figure 5.12.

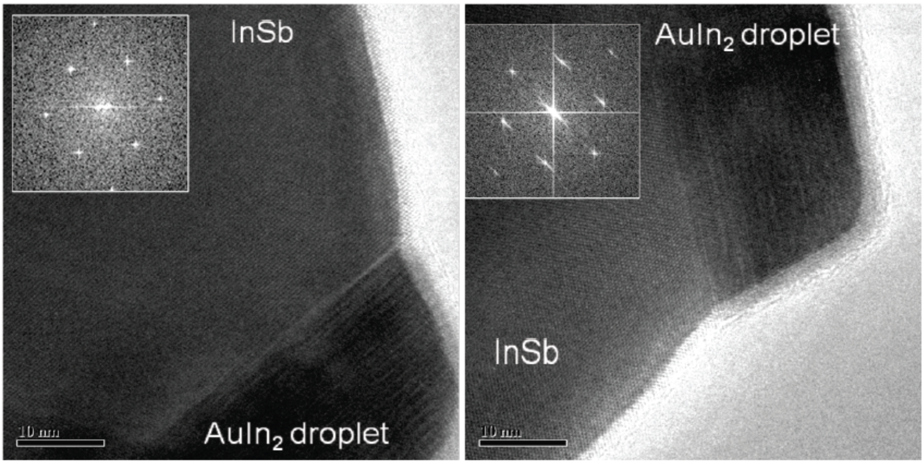

Figure 5.12: HR-TEM image of the most frequent case: $\Delta\varphi = 60^\circ$. The TEM images are taken just below the 2 droplets of the cross presented in Figure 5.11. The FFT patterns corresponding to different branches show different crystalline orientations of the two branches of the cross. The fact that both branches are on a ⟨110⟩ zone-axis at zero tilt for this cross, and similar crosses that were inspected using HR-TEM, illustrates that γ is indeed 0° for both branches and $\psi = 90^\circ$, i.e. that tapering of the InAs stem is minimal in these cases.

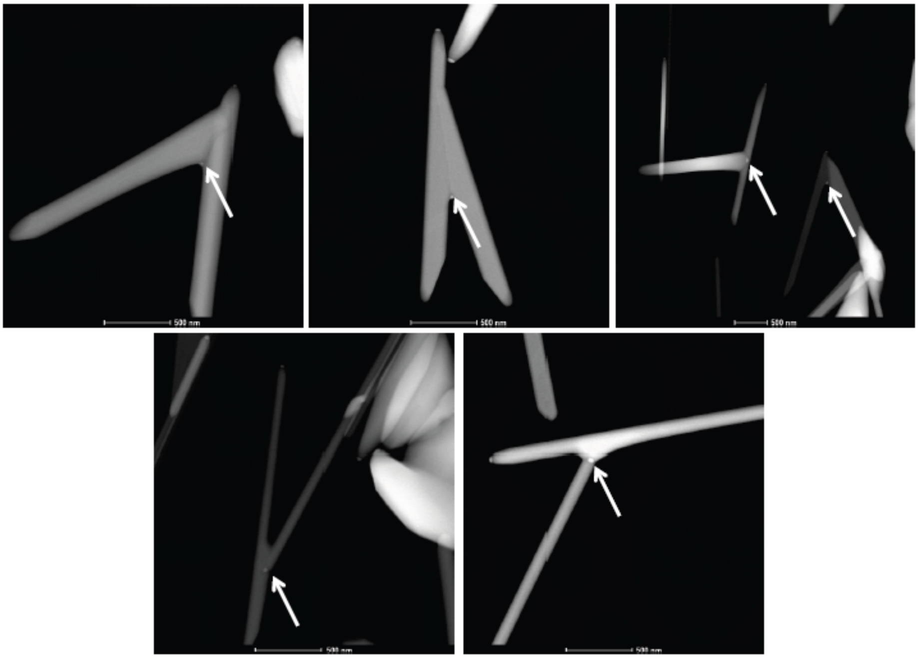

Figure 5.13: T-shaped structures and nanowings. High Angle Annular Dark-Field-TEM images of various T-shaped structures and nanowings. When the two InSb nanowires are perfectly aligned in height the gold droplet cannot cross the second wire and will stay close to the intersection as indicated by the arrows. If the angle between the two branches is small enough, a nanowing will start to grow between both legs.

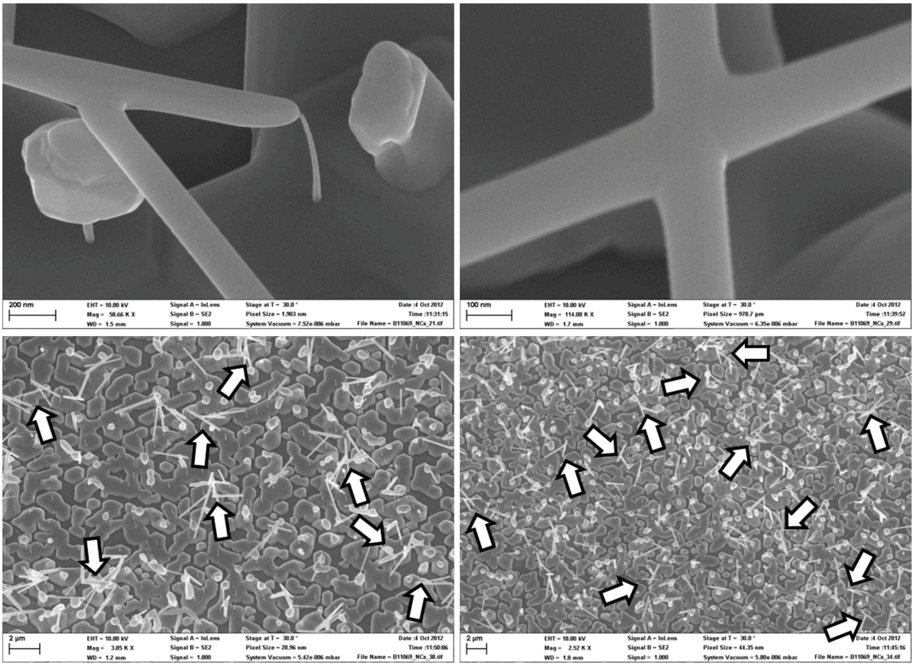

Figure 5.14: High yield of merging structures on an as-grown samples. Top-view SEM images of an as-grown sample showing the high yield of merging structures. Randomly dispersed 40 nm gold colloids were used for this sample in order to improve the amount of available nanocrosses. Each arrow indicates a T- or a X-shaped nanostructure.

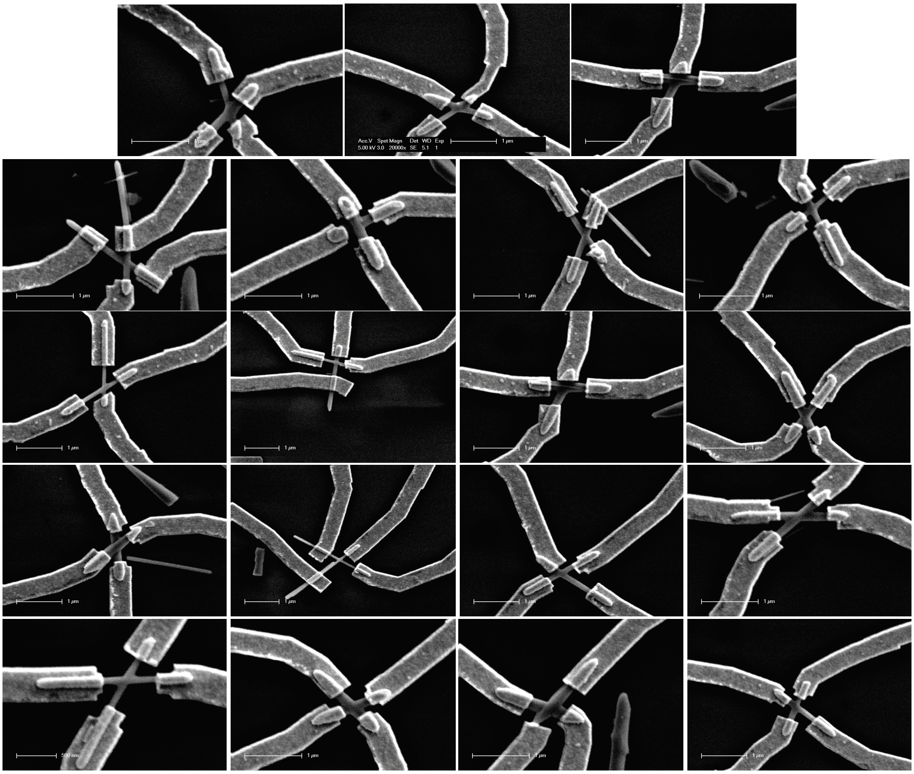

Figure 5.15: Devices realized for this study. Top-view SEM images of few devices realized for this study. Electrical measurements were performed at low temperature (4.2 K) for different crossing angles (5 X- and 2 T-shaped nanostructures) but no clear influence of $\Delta\varphi$ on the transport properties was found. For all images, the scale bar corresponds to 1 μm.

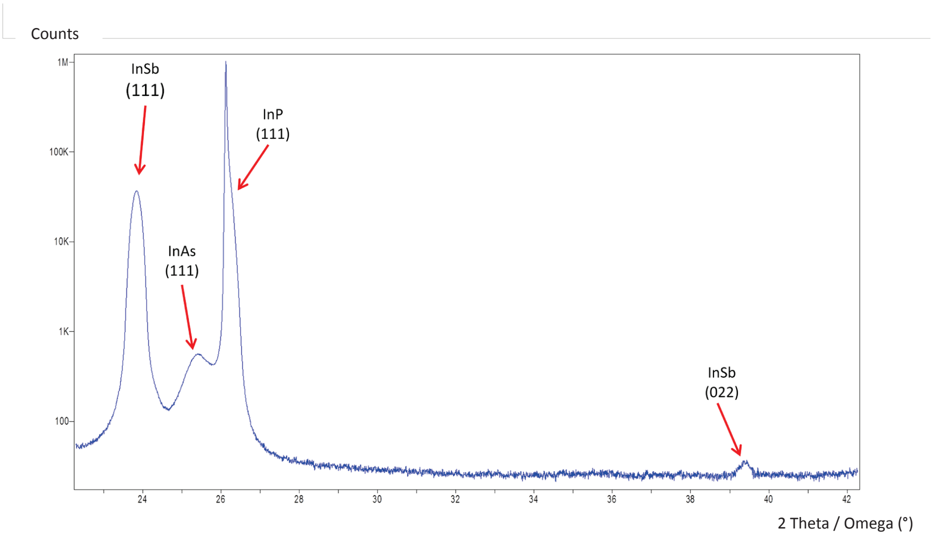

Figure 5.16: 2θ scan acquired with an integration time of 2 seconds per 0.005 °.

5.10.2 XRD measurements

Figure 5.2a (Figure 5.16) displays (111) peaks from InSb, InAs and InP. These peaks can be attributed to the vertical InSb nanowires, the vertical InAs stems and the InP stems and substrates, respectively. The fourth peak — InSb (022) — is used as a proof that the horizontal InSb nanowires have fixed values for ψ and γ, being 90° and 0°, respectively.

In order to be able to unambiguously draw this conclusions, we need the following evidence:

1. **No additional peaks from the other compountds (InAs and InP):** The InSb (022) peak should be originating from the horizontal nanowires only. Poly-crystalline, defective growth of a bulk layer on the substrate could also yield additional weak peaks. In this case, additional peaks from InAs and InP are likely to be present also. Figure 5.17 shows 2θ scans of the angular ranges in which the (220) peaks of the three compounds are predicted to occur. Clearly, no (220) peaks are present for InAs and InP within the detection limits.

2. **No contribution from poly-crystalline InSb:** Figure 5.2a shows two InSb peaks: (111) and (220). Hypothetically, the latter peak could be assigned to a small fraction of non-epitaxial InSb, due to e.g. multiple twinning of islands on the surface. In that case, more InSb should be present in the XRD spectrum. Figure 5.18 displays 2θ scans around the positions of those (hkl) peaks of InSb, that appear strongest in a powder spectrum. The fact that none of these peaks

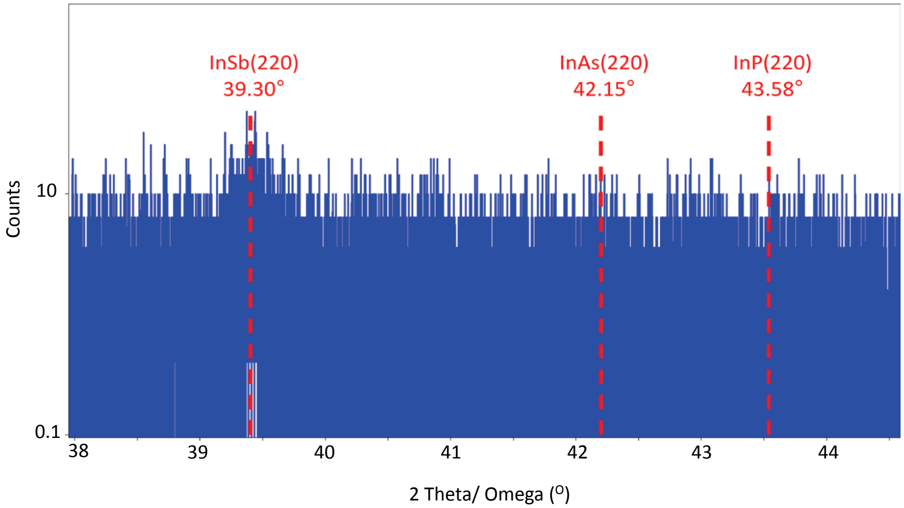

Figure 5.17: 2θ scans around the position of the (220) peaks of the three compounds, acquired with an integration time of 0.5 second per 0.005 °.

appear above noise-level, although ratio of intensities in a powder pattern is 796 : 490 : 133 : 266 for (220) : (331) : (400) : (422) respectively, indicates that no “powder” contribution is present.

3. **No rotational freedom of the horizontal InSb nanowires:** In case that all horizontally growing nanowires have full freedom of rotational angle γ, all directions perpendicular to 111 (i.e., both 220 and 422) would show up in the XRD spectrum. The fact that the (422) peak is absent (Figure 5.18), while a significant (220) peak is present (Figure 5.17), proves that $\gamma = 0°$. It should be mentioned that the angular spread at this position is unknown; because of the weakness of the (220) peak, no rocking curves were acquired.

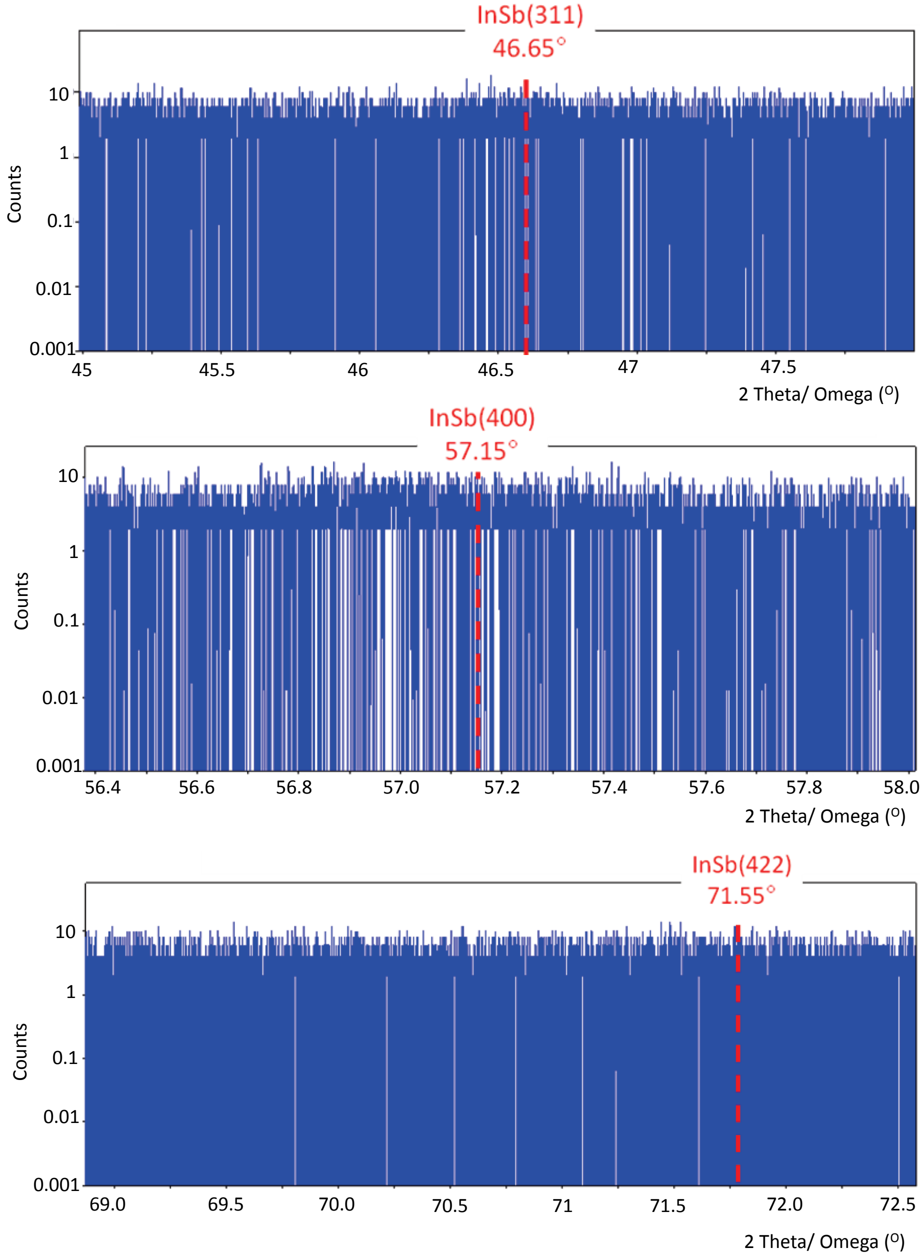

Figure 5.18: 2θ scans around the positions of the InSb (hkl) peaks that appear strongest in a powder spectrum.

5.11 Supplementary data on the electrical transport through nanocrosses

5.11.1 Device fabrication

Nanocrosses are deposited on a p-doped Si chip covered by 285 nm SiO_2. The contact area is defined by electron beam lithography. Devices with normal metal contacts (Figure 5.4 and Figure 5.5): an ammonium sulfide passivation of the contact area is performed prior to contact deposition. For device I, described both in the main text and in the Supplementary Materials, 25/250 nm of Ti/Au is deposited. 25/150 nm Ti/Au is used for device II, of which data is shown in this appendix. Measurements are performed at a temperature of 4 K with the magnetic field oriented perpendicular to the nanocross. Devices with superconducting contacts (Figure 5.6): an in-situ Ar etch was performed to remove the native oxide on the nanowire, after which NbTiN/Al (50/70 nm) was deposited.

5.11.2 Extraction of mobility in a nanocross

First, we give expressions for nanowire field-effect mobility. Next, we extract the gate-nanowire capacitance, needed for evaluation of mobility, from Hall measurements. We obtain electron mobilities from a fit to pinch-off traces. The same analysis applied to a second nanocross device yields mobilities of ~ 6,700 to ~ 10,000 cm^2/Vs. As the nanowires in our nanocross devices do not cross at the optimal angle a grain boundary is present at the nanocross junction. To determine the influence of the grain boundary on transport properties we compare mobilities of channels with and without grain boundary.

Nanowire mobility is often extracted from the change in current with gate voltage. This field-effect mobility formalism assumes classical transport. To work in a classical transport regime we apply a large source-drain bias of ~ 10 mV. The large bias averages out transport effects from quantum interference. Mobility, μ (cm^2/Vs), is the proportionality factor between an applied electric field, E, and the resulting drift velocity, v_d

$$v_d = \mu E \tag{5.1}$$

The relation between conductivity, σ ($(\Omega m)^{-1}$), and electron density, n (m^{-3}), is then obtained:

$$\sigma = \frac{J}{E} = \frac{n|e|v_d}{E} = n|e|\mu \tag{5.2}$$

with J the current density and $|e|$ the electron charge. The expression for field-effect mobility is obtained from Equation (5.2) by substitution of

$$\sigma = \frac{L}{A}\frac{I}{V_{SD}} \tag{5.3}$$

and

$$n = \frac{C\left(V_g - V_t\right)}{|e|LA} \tag{5.4}$$

and gives

$$I = \frac{\mu C\left(V_g - V_t\right)V_{SD}}{L^2} \tag{5.5}$$

Equation (5.3) assumes that a voltage bias, V_{SD}, is applied between source and drain and the resulting current, I, is measured. Expression Equation (5.4) applies to a system in which electron density is induced via gate voltage, V_g. C is the capacitance between gate and nanowire, V_t is the pinch-off (threshold) voltage and L the length of the transport channel. A is the nanowire cross section, which equals $\frac{\pi}{4}d^2$, with d the nanowire diameter. The nanowire resistance, R_n, becomes

$$R_n = \frac{V_{SD}}{I} = \frac{L^2}{\mu C\left(V_g - V_t\right)} \tag{5.6}$$

From Equation (5.6) field-effect mobility is often obtained from the transconductance, $\frac{dI}{dV_g}$, the derivative of current to gate voltage:

$$\mu = \frac{dI}{dV_g}\frac{L^2}{CV_{SD}} \tag{5.7}$$

In a system with voltage probes on opposite sides of the current path, the electron density can be obtained from the change in transverse (Hall) resistivity, ρ_{xy} (Ωm), with weak magnetic field, B ([136]):

$$n = \frac{1}{|e|}\left(\frac{d\rho_{xy}}{dB}\right)^{-1} \tag{5.8}$$

We now apply this expression to our nanocross. As explained in the main text, there is a vertical offset between the two nanowires that form a nanocross. Therefore the voltage probes (one nanowire) are offset vertically with respect to the current path (second nanowire) (see Figure 5.19a and Figure 5.19b). Two simplifications to the device geometry are made in order to extract transverse resistivity, ρ_{xy}:

- It is assumed that current, I, flows with uniform current density, J, through the upper wire. This wire has a diameter, d, and circular cross section, $A = \frac{\pi}{4}d^2$.
- The transverse electric field, E_y, and the resulting Hall voltage, V_H, arise over a distance d.

The transverse resistivity is then obtained from

$$\rho_{xy} = \frac{E_y}{J} = \frac{V_H}{Jd} = \frac{V_H}{I}\frac{A}{d} = \frac{V_H}{I}\frac{\pi d}{4} \tag{5.9}$$

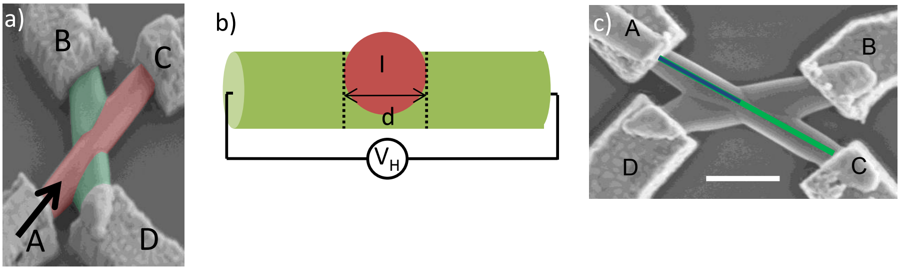

Figure 5.19: a) Scanning electron microscope image of device I. A current bias is applied through A-C (red wire), while voltage is measured between contacts B-D (green wire). The arrow indicates the viewing direction (parallel to the substrate) of the schematic drawing in panel b). **b)** Schematic side view of a nanocross. A current bias I is applied to the upper wire of which here the cross section with wire diameter d is seen. The resulting Hall voltage, V_H, is measured via contacts to the lower lying wire that has grown underneath and partly around the current biased wire. **c)** Top view of device I. Scale bar is 500 nm. The diameter of wire B-D increases near the intersection with wire A-C. Therefore wire B-D has crossed and grown around wire A-C. Channel length A-C is indicated with a green line. The length of wire leg A, the nanowire section between contact A and the intersection of the two wires, is indicated with a blue line. The length of all channels in the nanocross is between 1.0 and 1.3 μm. Wire diameter A-C is 200 nm, wire diameter B-D is approximately 250 nm.

The electron density in device I increases linearly with gate voltage from $0.6 \cdot 10^{17}$ cm^{-3}(V_g = 10.2 V) to $1.9 \cdot 10^{17}$ cm^{-3} (V_g = 30 V)[1]. Fermi energy, extracted from these densities assuming a three-dimensional density of state, is between 40 and 80 meV and Fermi velocity $(0.9 - 1.4) \cdot 10^6$ m/s. The Fermi wavelength, λ_F, is between ~ 50 and ~ 35 nm. Nanowire diameter, d, is 200 to 250 nm (Figure 5.19c) and therefore d/λ_F is 4 – 7. We extract gate-nanowire capacitance, C (F), from measurements of electron density using Equation (5.4)

$$C = \frac{dn}{dV_g}|e|LA \tag{5.10}$$

Capacitance of a wire section therefore increases with channel length and diameter. As a result different current channels, i.e. different current paths from one contact to another, have different capacitances. For device I $\frac{dn}{dV_g} = 0.65 \cdot 10^{16}$ cm^{-3}V^{-1} and the resulting capacitances are 43–51 aF. Similarly to capacitance of channels the approximate capacitance of segments of channels can be determined. Diameter and length of wires are obtained from an SEM image of the device (Figure 5.19c). As capacitances are extracted from the density at the nanowire intersection area, screening of the gate voltage near the contacts is not included in our analysis. Screening leads to

---

[1] The Hall coefficient, $|R_H|$, is defined as $\frac{E_y}{JB} = \frac{\rho_{xy}}{B} = \frac{1}{n|e|}$, and equals $\frac{pid}{4}\frac{V_H}{IB}$ for our geometry. $|R_H|$ is between 33 cm^{3}C^{-1} (V_g = 30 V) and 104 cm^{3}C^{-1} (V_g = 10.2 V).

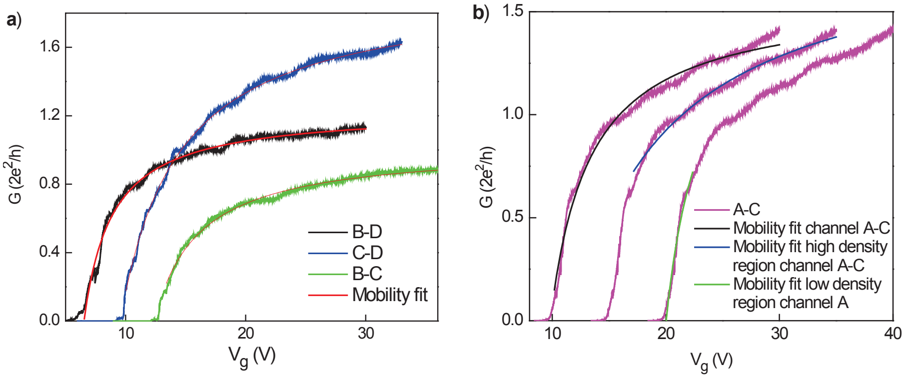

Figure 5.20: a) Pinch-off traces B-D, B-C and C-D of device I and fits using Equation (5.11). Traces C-D and B-C are displaced horizontally. Extracted mobilities are 8000, 9000 and 6500 cm^2/Vs with series resistances 10.4 kΩ, 6.6 kΩ and 12.6 kΩ respectively. Nanowire resistance per unit length, $\frac{R_n}{L}$, and conductivity, σ, can be calculated using the extracted mobility and threshold voltage. For channel B-D at V_g = 30 V $\frac{R_n}{L} \approx 1$ kΩμm^{-1} and $\sigma \approx 200$ Ωcm^{-1}. **b)** A fit (black curve) using capacitance and length of channel A-C deviates from the measured pinch-off trace A-C at high electron density (high gate voltage). As the onset of transport in leg A occurs at a higher gate voltage than in other wire sections, gating of only leg A determines the slope $\frac{dG}{dV_g}$ of pinch-off trace A-C near pinch-off. A fit of the low electron density region of pinch-off trace A-C using length and capacitance of leg A gives a mobility similar to those of other channels (green curve; mobility 7500 cm^2/Vs). At high electron density a fit using length and capacitance of the complete channel A-C yields also a mobility similar to those of other channels (blue curve; mobility 6800 cm^2/Vs).

lower capacitances, which in turn result in underestimation of field-effect mobilities (cf. Equation (5.7)).

In actual pinch-off traces the conductance increases steeply with gate voltage near pinch-off and then saturates as gate voltage is increased further. We model the conductance of the nanowire device as a nanowire, with conductance $G = \frac{I}{V_{SD}}$ given by Equation (5.5), connected in series with contact resistances at the interface between nanowire and metal contacts, R_c. The expression for conductance is given by

$$G = \frac{1}{R_n + R_c} = \frac{1}{\frac{L^2}{\mu C(V_g - V_t)} + R_c} \tag{5.11}$$

with R_c the contact resistances. The capacitance is extracted from Hall measurements. This model reproduces pinch-off traces B-D, B-C and C-D well (see Figure 5.20a). Extraction of mobility of channels involving the wire section near contact A is complicated by the fact that this leg of the nanocross is slightly suspended above the substrate and therefore has a pinch-off voltage different from that of other nanocross sections. Mobility of channels involving leg A is however likely similar to those of other channels (see Figure 5.20b).

5.11.3 Capacitances: comparison experiment and electrostatics simulations

Electrostatic simulations of a nanocross, described in Section 3.4, also yield a capacitance, which can be compared to the experimentally obtained values. The air gap between one wire section and the substrate is approximated by lifting this wire by 70 nm over its entire length. Contact spacing and wire diameter are obtained from SEM images. Comparison of these capacitances (Table 5.1) shows good agreement between experimentally extracted values and simulated ones, certainly when considering the approximations made both in the experimental extraction of capacitance (see Section 5.11.2) and in the simulated device geometry. Including the air gap in the simulated geometry results in capacitances closer to experimental values.

	C_{AC} (aF)	C_{BD} (aF)
Experimental	43	51
Simulated, AC on substrate	62	57
Simulated, AC lifted 70 nm	43	51

Table 5.1: Capacitances obtained numerically from a Laplace solver compared to experimentally extracted capacitances. C_{AC} (C_{BD}) denotes the capacitance from gate to wire AC (BD). Experimental capacitances have been calculated using the change in Hall voltage with gate voltage shown in Figure 5.5 as described in Section 5.11.2. Contacts are included in the simulated device geometry. Data from [75].

5.11.4 Mobility analysis device II

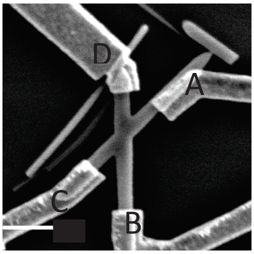

Figure 5.21: Device II. Scale bar is 500 nm. Crossing angle between nanocross legs, $\Delta\varphi$, is 50°. The diameter of wire A-C is 140 nm, the diameter of wire B-D is ~ 160 nm. The diameter of wire B-D increases near the intersection with wire A-C, which indicates that wire B-D has grown around wire A-C. Channel lengths are 0.8 – 1.1 μm.

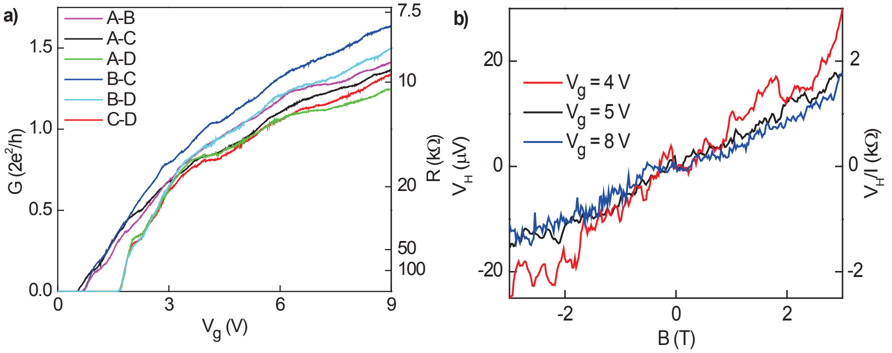

Figure 5.22: a) Conductance, $G = \frac{I}{V_{SD}}$, as function of gate voltage, V_g, for device II. Right axis: resistance $R = \frac{1}{G}$. V_{SD} is between 10 mV (near pinch-off) and 8 mV (near V_g = 9 V). Note that similar to the pinch-off traces presented in the main text also in this device the onset of transport through one of the wire sections (near contact D) takes place at a higher gate voltage. **b)** Hall voltage, V_H, as a function of perpendicular magnetic field, B, for three back gate voltages. A current bias of 10 nA is applied from C to A, Hall voltage is measured between B and D. Right axis: Hall resistance, $\frac{V_H}{I}$.

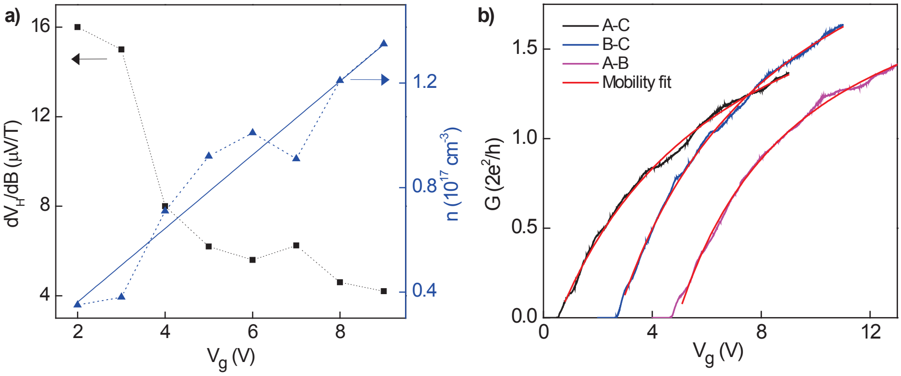

Figure 5.23: a) Hall slope, $\frac{dV_H}{dB}$, (left axis) and the resulting electron density, n, (right axis) as a function of gate voltage, V_g. The Fermi energy, assuming a three-dimensional density of states, is between 30 and 65 meV. Fermi velocity is (0.8 – 1.2)$\cdot 10^6$ m/s and Fermi wavelength λ_F is 60 to 40 nm, giving $\frac{d}{\lambda_F}$ = 2 – 4. A linear fit gives $\frac{dn}{dV_g}$ = (1.4 ± 0.2)$\cdot 10^{16}$ cm^{-3}/V. Channel capacitances are 28 – 49 aF. **b)** Field-effect mobility fits (red curves) to pinch-off traces A-C, B-C and A-B. Traces B-C and A-B are displaced horizontally. Mobility is 6700, 9500 and 10000 cm^2/Vs, contact resistance is 5.4 kΩ, 4.6 kΩ and 5.8 kΩ respectively.

5.11.5 Influence of the grain boundary on mobility

Device II allows comparison of mobilities of transport channels with and without a grain boundary. Wire B-D of this device has grown around and on top of wire A-C (see Figure 5.21). Transport through wire A-C therefore does not encounter a grain boundary, while a grain boundary is present in channels B-C and A-B. Wire section D is not considered, as it is slightly suspended and therefore mobility of this wire section cannot be obtained with the same accuracy as other sections. While increased scattering at the grain boundary would result in a lower mobility for channels B-C and A-B compared to A-C, the mobilities of channels B-C and A-B are actually higher than that of A-C. This suggests that the grain boundary does not have a major influence on mobility. Instead factors that limit mobility in single nanowires could limit mobility also in nanocrosses. Mobilities with and without grain boundary cannot be compared in device I: all channels in direct contact with the substrate contain a grain boundary.

5.11.6 Characterization of InSb nanowire Josephson junctions.

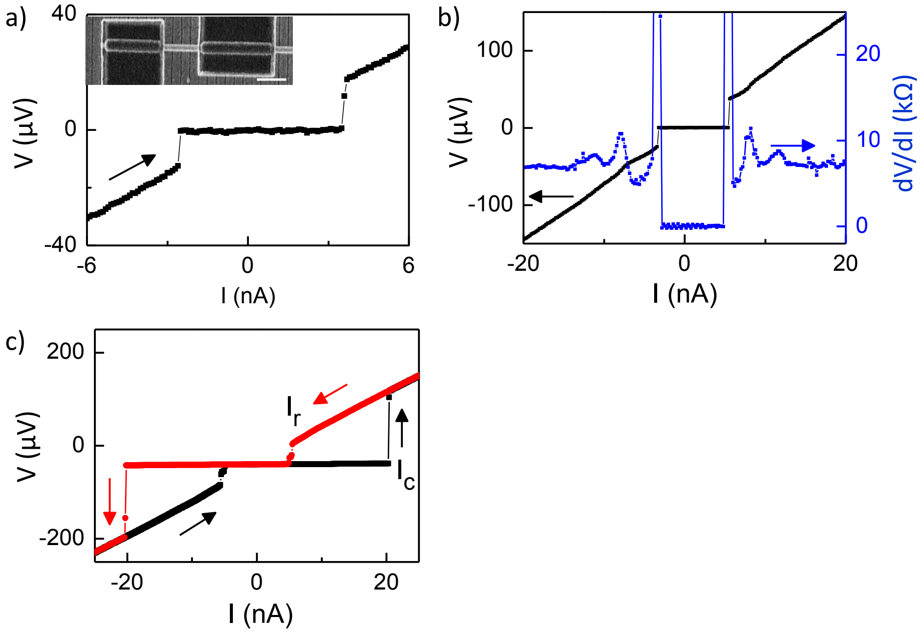

Figure 5.24: a) Measurement of critical current $I_c \sim 3.5$ nA in a single nanowire device. The contact spacing of ∼590 nm is similar to that of the device shown in Figure 5.6. Normal state conductance is 2.5 G_0 ($G_0 = \frac{2e^2}{h}$). Inset: scanning electron microscope image of the device. Contact material is NbTiN. Device conductance is tuned by 4 local gates that are placed at the same potential and therefore act as a single gate. Scale bar is 500 nm. **b)** Fiske steps in a single nanowire device observed in $V(I)$ characteristic (left axis). The steps are clearly visible as maxima in the corresponding plot of differential resistance, $\frac{dV}{dI}$, as function of current bias (right axis). Contact spacing is 150 nm, normal state conductance $G = 1.8\ G_0$, contact material NbTiN. **c)** Hysteresis in the $V(I)$ sweep of a single nanowire device with superconducting contacts. Sweep direction is indicated. Critical current $I_c \sim 20$ nA and retrapping current $I_r \sim 5$ nA. Contact spacing is 150 nm.

CHAPTER 6

QUANTUM INTERFERENCE AND SPIN RELAXATION IN A DUAL-GATED INSB NANOWIRE DEVICE

Spin-orbit strength is extracted from magnetoconductance measurements in dual-gated InSb nanowire devices. The measurements are supported by a numerical study of quantum interference and spin relaxation. A large Rashba spin-orbit strength of 0.5 – 1 eVÅ indicates the potential of our system for the study of Majorana fermions and for other spin-based quantum devices. We also study weak anti-localization as a function of temperature, orientation of the magnetic field with respect to the wire and asymmetry of the gating of the device. Our results indicate the importance of including the nanowire geometry and charge distribution both for extracting spin-orbit interaction strength and for understanding quantum interference effects.

6.1 Introduction

Semiconductor nanowires exhibiting a strong spin-orbit interaction (SOI) are a prime candidate for use in spintronics [137],[138],[139], spin-based quantum computation [140], [141] and for the creation of Majorana fermions [18],[19]. The stability of the Majoranas critically depends on a strong spin-orbit interaction [26].

The importance of SOI in nanowires calls for an adequate method to evaluate its strength. The standard method to extract SOI strength is based on low-field magnetoconductance (MC) measurements (see Section 2.5). Interference of coherently backscattered electrons in a mesoscopic system reduces its conductance, an effect called weak localization (WL) [142],[143]. Spin rotation during backscattering results in an increased conductance, called weak anti-localization (WAL) [144],[145]. These quantum interference effects are averaged out by application of a magnetic field [146], thereby allowing the extraction of a spin relaxation length. The confinement in nanowires affects both magnetic field dephasing [147],[48] and D'yakanov-Perel' spin relaxation [40],[39],[41], i.e., spin relaxation due to structural or bulk inversion asymmetry [148] (see Section 2.4). The spin relaxation length increases when the nanowire width becomes smaller than the characteristic length over which the spin, due to SOI, precesses. Therefore, unlike two-dimensional systems, in nanowires the spin relaxation length extracted from WAL does not equal the spin precession length and thus does not provide a direct measurement of SOI strength. The theory needed to describe spin relaxation in the presence of confinement is however up to now largely lacking. The only existing analytical expression [41] applies to very narrow channels in diffusive two-dimensional systems. Effects of confinement on both magnetic field dephasing and spin relaxation in self-assembled — three-dimensional — nanowires have so far not been considered theoretically at all.

Moreover, InSb is a material with strong SOI and is of interest to the above research areas. Self-assembled InSb nanowires were used in recent experiments to detect Majorana fermions in hybrid semiconductor-superconductor systems [17], [111],[149]. Despite its central role in observations of Majorana fermions the SOI strength in InSb nanowires has so far only been measured[1] in a quantum dot geometry [81],[100], and not in the open transport regime relevant to current and envisioned topological systems [17],[24],[152]. The SOI in an open regime is because of the difference in confinement likely different from that in a quantum dot.

Here we extract SOI strength in InSb nanowires in an open transport regime while accounting for the confinement in these self-assembled nanowires. In Section 6.2 we numerically study magnetic field dephasing and spin relaxation due to structural inversion asymmetry, i.e., Rashba SOI [153], in nanowires. We apply our simulation outcomes in Section 6.3 to the determination of SOI strength from measurements of WAL in a dual-gated InSb nanowire device. Moreover, we study WAL as a function of temperature, magnetic field angle and asymmetry of the gating of the device.

---

[1] Spin-orbit interaction in two-dimensional InSb wires (channels) defined in quantum wells has been studied [150],[151].

In-situ control over Rashba spin-orbit strength by such asymmetric gating is highly desirable for various applications, but has so far not been shown in nanowires. In the discussion section, Section 6.4, we discuss non-uniform charge distributions and relate two aspects of our data to the literature on spin-orbit interaction in nanowires: the WAL-to-WL-crossover and the observed spin-orbit and phase relaxation lengths. The appendix contains supporting data.

6.2 Magnetic field dephasing and spin relaxation in a nanowire: a numerical study

6.2.1 Magnetic dephasing time

Section 2.5.4 describes magnetoconductance in a nanowire with strong spin-orbit interaction. To extract the spin relaxation length, l_{so}, using Equation (2.48), an expression for the magnetic field dephasing time, τ_B, applicable to our self-assembled nanowires is required. Their hexagonal cross section, and ratio of mean free path, l_e, to wire diameter, W_F[2], $\frac{l_e}{W_F} \sim 1$ (see Section 6.6), favor a numerical approach to obtain τ_B.

τ_B in Equation (2.48) arises from the contribution $\langle e^{i\phi(t)}|R(t) = R(0)\rangle$ that describes the phase difference between time reversed loops, $\phi(t)$, acquired in the presence of a magnetic field. $\langle ... \rangle$ denotes averaging over many trajectories. The phase difference is given by

$$\phi(t) = \frac{2e}{\hbar}\int_{R(0)}^{R(t)} \vec{A}\cdot d\vec{l} \tag{6.1}$$

with magnetic vector potential, $\vec{A}$, and position at time 0 (t), $R(0)$ ($R(t)$). In confined geometries the average phase obtained from all paths, instead of only closed paths, can be used, provided an specific choice of vector potential is made [48]. Then [48]

$$\langle e^{i\phi(t)}\rangle = e^{-\frac{t}{\tau_B}}. \tag{6.2}$$

Electron trajectories are simulated as follows. The electron moves in a straight line with velocity v_F in a random direction, until it either hits a boundary or it scatters of an impurity. The probability of a collision with an impurity is determined by the mean free path. $\phi(t)$ is obtained using Equation (6.1) and subsequent averaging over many trajectories according to Equation (6.2) yields τ_B. Magnetic dephasing time as a function of magnetic field strength is obtained for various $\frac{l_e}{W_F}$, three geometries — a hexagon, a square and a circle — and magnetic field oriented perpendicular and parallel to the nanowire. Specular boundary scattering is assumed.

---

[2] Width in a hexagon can be defined as the corner-to-corner width or the facet-to-facet width (see Figure 6.9a). We here use the facet-to-facet width, W_F. Throughout this chapter W_F is used to describe the width of all wire geometries.

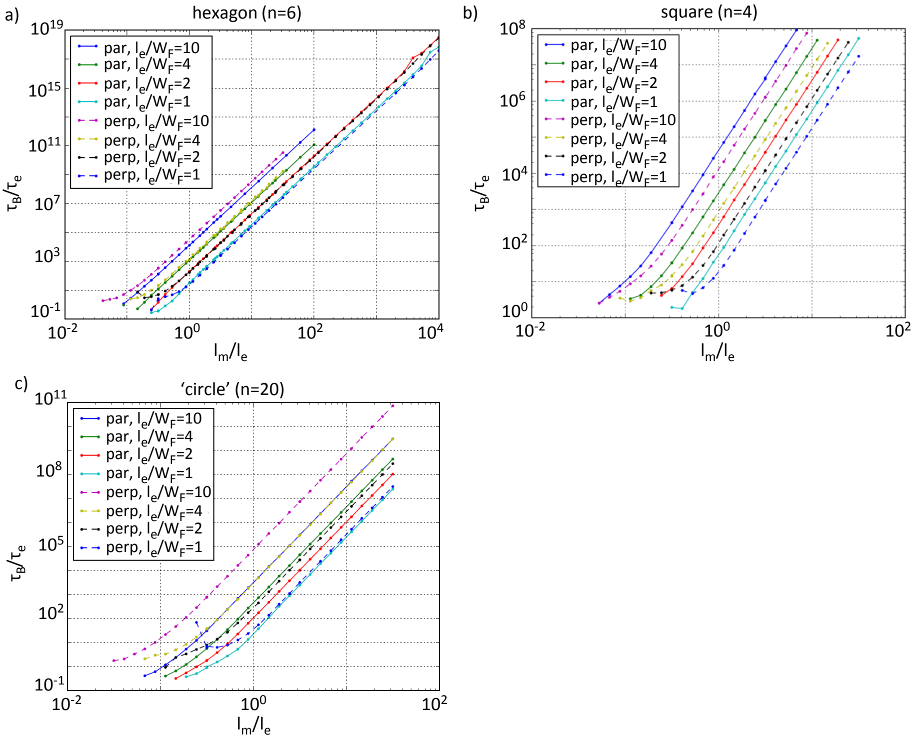

Figure 6.1: Dimensionless magnetic dephasing time, $\frac{\tau_B}{\tau_e}$, as a function of dimensionless magnetic length, $\frac{l_m}{l_e}$. τ_B is the magnetic dephasing time, τ_e is the scattering time, l_m is the magnetic length (see Section 2.5.2) and l_e is the mean free path. Different ratios of mean free path to wire diameter, $\frac{l_e}{W_F}$, are investigated. Geometries are **a)** a hexagon (number of facets, $n = 6$), **b)** a square ($n = 4$), **c)** a structure with $n = 20$, resembling a circle. Deviations from a straight line at low $\frac{l_m}{l_e}$ are probably due to failure of the simulation technique.

The hexagonal geometry yields very similar magnetic dephasing time for parallel ($\tau_{B\parallel}$) and perpendicular ($\tau_{B\perp}$) magnetic field (see Figure 6.1a); $\frac{\tau_{B\parallel}}{\tau_{B\perp}} \approx 1$ for all ratios of $\frac{l_e}{W_F}$. A weak crossover from $\frac{\tau_{B\parallel}}{\tau_{B\perp}} \gtrsim 1$ to $\frac{\tau_{B\parallel}}{\tau_{B\perp}} \lesssim 1$ is seen when $\frac{l_e}{W_F}$ increases from 1 to 10. The other geometries (see Figure 6.1b-c) display a larger difference in $\frac{\tau_{B\parallel}}{\tau_{B\perp}}$.

From Figure 6.1 it is apparent that in all considered situations τ_B is described by

$$\frac{\tau_B}{\tau_e} = C\left(\frac{l_m}{l_e}\right)^4. \tag{6.3}$$

The prefactor C depends on the cross sectional shape, the orientation of the magnetic field with respect to the wire and $\frac{l_e}{W_F}$. Values of C are listed in Section 6.6.6.

Equation (6.3) yields

$$D\tau_B = \frac{C}{3} l_m^4 l_e^{-2} \tag{6.4}$$

using the diffusion constant for a kinematically three dimensional nanowire with specular boundary scattering, $D = \frac{1}{3} v_F l_e$. Equation (6.4) is used in Equation (2.48) to extract spin relaxation and phase coherence length from measurements of weak anti-localization in Section 6.3.

The dependence $\tau_B \sim l_m^4$ of Equation (6.3) is similar to the analytical expressions for magnetic dephasing time in a diffusive system (Equation (2.49)) and in a quasi-ballistic system in a weak field (first term of Equation (2.50)). For a rectangular wire the coefficient C (scaled by $\left(\frac{W_F}{l_e}\right)^3$) at large $\frac{l_e}{W_F}$ approaches (see Section 6.6.6) the coefficient derived analytically for a clean thin layer, C_1, in Equation (2.50), as expected. For $\frac{l_e}{W_F} \sim 1$ there is no strong field regime (second term of Equation (2.50)).

6.2.2 Spin relaxation

This section describes simulations of spin relaxation in nanowires to extract the spin precession length from measurements of spin relaxation. Assuming $\vec{E} = E\hat{z}$, the Rashba SOI is described by Equation (2.28). A spin precession length

$$l_R = \frac{\hbar^2}{m\alpha_R} \tag{6.5}$$

is chosen. This spin precession length is the inverse of the spin-orbit k-vector, k_{so}, defined in Section 2.2, and equals a spin precession by 2 rad (see Section 2.4.1).

Spin relaxation is described by an exponential decay with characteristic time τ_{so} [50], [47]

$$\frac{1}{2}\left(3e^{-\frac{t}{\tau_{so}}} - 1\right) \tag{6.6}$$

similar to the SOI contribution of Equation (2.47).

When $W_F > l_R$ the spin relaxation in a (wide) channel defined in a quantum well follows (see Figure 6.2a) the two-dimensional behaviour $\frac{\tau_{so}}{\tau_e} \sim \left(\frac{l_R}{l_e}\right)^2$ described in Section 2.4.2. When $W_F < l_R$ (also Figure 6.2a), a dependence $\frac{\tau_{so}}{\tau_e} \sim \left(\frac{l_R}{l_e}\right)^4$ is found. Confinement thus affects the spin relaxation time, as expected (see Section 2.4.3). Our numerical results agree with the analytical expression for spin relaxation in a diffusive channel, Equation (2.38), in the regime $W_F < l_R$ (Figure 6.2a).

Also in a two-dimensional quasi-ballistic channel a spin relaxation time $\frac{\tau_{so}}{\tau_e} \sim \left(\frac{l_R}{l_e}\right)^4$ is found when $W_F < l_R$ (Figure 6.2b). Considering the dependence on W_F (Figure 6.2c), we find when $W_F < l_R$ an increase in spin relaxation time $\frac{\tau_{so}}{\tau_e} \sim \left(\frac{W_F}{l_e}\right)^{-3}$.

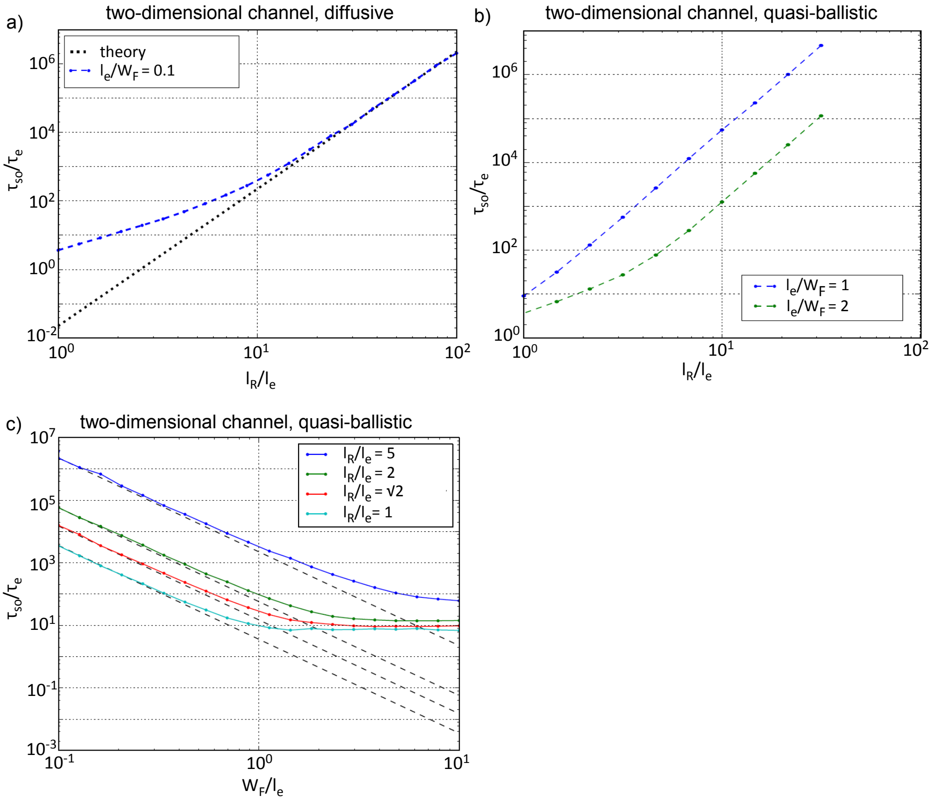

Figure 6.2: a) Dimensionless spin relaxation time, $\frac{\tau_{so}}{\tau_e}$, as a function of dimensionless spin precession length, $\frac{l_R}{l_e}$, in a channel with width, W_F, in a diffusive ($\frac{l_e}{W_F} < 1$) quantum well, with spin relaxation time, τ_{so}, scattering time, τ_e, spin precession length, l_R, and mean free path, l_e. A small $\frac{l_R}{l_e}$ yields (with $\frac{l_e}{W_F} = 0.1$) $W_F > l_R$, while a large $\frac{l_R}{l_e}$ results in $W_F < l_R$. The black dotted line is the spin relaxation time in the presence of confinement given by Equation (2.38). **b)** Dimensionless spin relaxation time, $\frac{\tau_{so}}{\tau_e}$, as a function of dimensionless spin precession length, $\frac{l_R}{l_e}$, in a channel in a two-dimensional electron gas with quasi-ballistic transport conditions, $l_e \sim W_F$. Two ratios of mean free path to wire diameter, $\frac{l_e}{W_F}$, are considered. **c)** Dimensionless spin relaxation time, $\frac{\tau_{so}}{\tau_e}$, as a function of the ratio of wire diameter to mean free path, $\frac{W_F}{l_e}$, in the same system as considered in panel b. Different dimensionless spin precession lengths, $\frac{l_R}{l_e}$, are considered. Dashed lines are fits to Equation (6.8) to extract C (see Equation (6.7)).

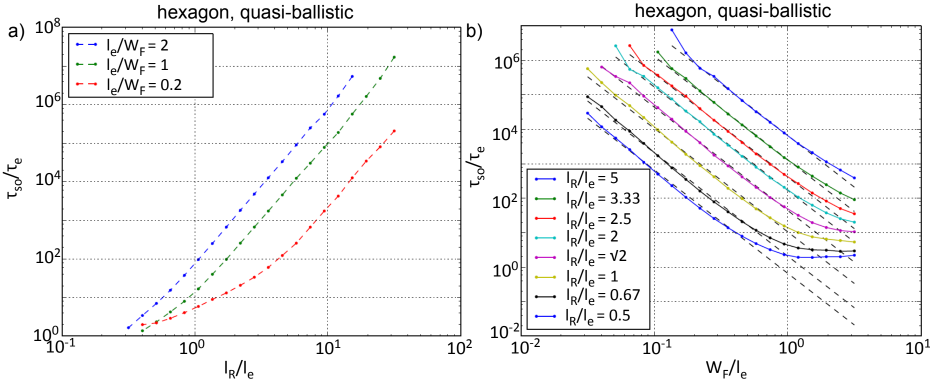

Figure 6.3: **a)** Dimensionless spin relaxation time, $\frac{\tau_{so}}{\tau_e}$, as a function of dimensionless spin precession length, $\frac{l_R}{l_e}$, in a nanowire with a hexagonal cross section with wire diameter W_F. Different ratios of mean free path to wire diameter, $\frac{l_e}{W_F}$, are considered. **b)** Dimensionless spin relaxation time, $\frac{\tau_{so}}{\tau_e}$, as a function of the ratio of wire diameter to mean free path, $\frac{W_F}{l_e}$. Different values of the dimensionless spin precession length, $\frac{l_R}{l_e}$, are considered. Dashed lines are fits of the simulation outcomes to Equation (6.7) to extract C.

Combining width and spin precession length yields an expression for spin relaxation time

$$\frac{\tau_{so}}{\tau_e} = C\frac{l_R^4}{W_F^3 l_e}, \tag{6.7}$$

a functional form similar to the description of magnetic field dephasing in a quasi-ballistic system in the weak field region (Equation (2.50)), as anticipated by [41] and [39]. The self-assembled nanowire with hexagonal cross section shows qualitatively the same behaviour as the channel in a two-dimensional electron gas (see Figure 6.3).

To extract the spin precession length from spin relaxation lengths $\frac{\tau_{so}}{\tau_e}$ is expressed in terms of the ratio of spin relaxation time to mean free path, $\frac{l_{so}}{l_e}$,

$$\frac{\tau_{so}}{\tau_e} = \left(\frac{3l_{so}}{2l_e}\right)^2, \tag{6.8}$$

in which the factor $\frac{4}{3}$ in the exponent of Equation (2.48) has been incorporated. The spin relaxation times extracted from our experiments (see Section 6.3) are $\frac{\tau_{so}}{\tau_e} \approx 1$ – 15. At these $\frac{\tau_{so}}{\tau_e}$ a cross-over from confinement-affected to two-dimensional spin relaxation takes place (see Figure 6.3a). Therefore no analytic expression for $\frac{\tau_{so}}{\tau_e}$ is used to extract l_R and instead the $\frac{l_R}{l_e}$ corresponding to the observed $\frac{\tau_{so}}{\tau_e}$ at $\frac{l_e}{W} = 1$ and $\frac{l_e}{W} = 2$ (see Section 6.3) are simply read from Figure 6.3a.

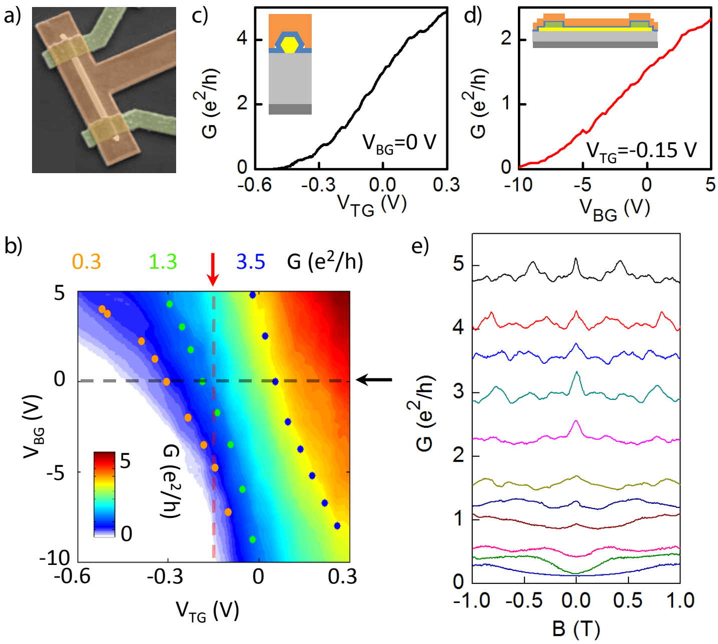

Figure 6.4: a) False color scanning electron microscopy image of device I. Contact spacing is 2 μm. The InSb nanowire is deposited onto a p^{++}-doped Si substrate covered by 285 nm SiO$_2$ (black). Contacts to the nanowire (green) are Ti/Au. After passivation of the nanowire with a diluted ammoniumpolysulfur solution HfO$_2$ (30 nm) is deposited by atomic layer deposition. Top gate (brown) is Ti/Au. **b)** Conductance, G, as a function of top gate voltage, V_{TG}, and back gate voltage, V_{BG}. Arrows and dashed lines indicate cross sections shown in panels c and d. Dots indicate some of the voltages (V_{BG},V_{TG}) at which magnetoconductance traces were taken to obtain the data of Figure 6.5b. Dots with the same color correspond to voltages with the same conductance. **c)** G as a function of V_{TG} with $V_{BG} = 0$ V. Inset: radial cross section of the device. The blue layer is HfO$_2$. **d)** G as a function of V_{BG}, with $V_{TG} = -0.15$ V. Inset: axial cross section of the device. **e)** Conductance, G, as a function of magnetic field, B, at several values of device conductance controlled by V_{TG} with $V_{BG} = 0$ V. Data taken with AC excitation $V_{AC} = 100\ \mu\mathrm{V}_{\mathrm{RMS}}$.

6.3 Experimental results

6.3.1 Device fabrication and characterization

InSb nanowires are deposited onto a substrate with a global back gate. Two or four contacts with a large ($\geq 2\ \mu$m) contact separation are chosen to ensure sufficient scattering between source and drain. After contact deposition a HfO$_2$ dielectric layer is deposited and the device is then covered by metal, creating an Ω-shaped top gate

(Figure 6.4a and insets of Figure 6.4c-d). Nanowire conductance is controlled with top and back gate voltage, reaching a conductance up to ~ 5 e^2/h (Figure 6.4b). The high dielectric constant and small thickness of the HfO_2 dielectric, in combination with the large coverage angle of the top gate lead to a strong coupling of the top gate to the nanowire (Figure 6.4c). A larger voltage range is needed to control device conductance with the back gate (Figure 6.4d). A field-effect mobility of 11,000 cm^2/Vs is extracted from transconductance, $\frac{dG}{dV_{BG(TG)}}$, (see Figure 6.8), from which a ratio of mean free path to wire diameter $\frac{l_e}{W_F} = 1-2$ is estimated. Unless indicated otherwise measurements are performed at a temperature $T = 4.2$ K with magnetic field, B, perpendicular to the nanowire and out of the substrate plane.

6.3.2 Extraction of spin relaxation and spin precession length

First, we measure the magnetoconductance (MC) as a function of conductance controlled by the top gate ($V_{BG} = 0$ V, Figure 6.4e). At large G we find a conductance increase of ~ 0.2 to ~ 0.3 e^2/h around $B = 0$. Reproducible conductance fluctuations are observed at larger magnetic field. On reducing conductance below ~1.5 e^2/h WAL becomes less pronounced and a crossover to WL is seen.

The conductance fluctuations affect the WAL peak shape. To suppress these fluctuations several (7-11) MC traces are taken at the same device conductance (voltages indicated for a.o. $G = 3.5$ e^2/h in Figure 6.4b). After averaging these traces WAL remains while the conductance fluctuations are greatly suppressed (Figure 6.5a). We fit these averaged MC traces to Equations (2.48) and (6.4) with l_{so}, l_φ and offset $\Delta G(B \to \infty)$ as fit parameters and find good agreement between data and fits. Wire diameter and mean free path are fixed in each fit, but we consider a deviation of wire diameter from its expected value (see Section 6.6) and a ratio of mean free path to wire diameter of 1 and 2. Although a B range exceeding $\tau_B \gg \tau_e$ is needed to obtain fit convergence, the fit range in general does not exceed $\tau_B \approx \tau_e$. Alternatively, fits over a smaller B range fulfilling $\tau_B \gg \tau_e$ can be performed on MC traces showing WAL without WL at larger B (observed when $G \geq 2e^2/h$). In this case $\Delta G(B \to \infty)$ is fixed. These fits yield within ~ 20 % the same results as those obtained with larger fit range.

We find a spin relaxation length (Figure 6.5b) that with constant $\frac{l_e}{W_F}$ first reduces with increasing device conductance to $l_{so} = 100-200$ nm, but increases again to $l_{so} = 200-400$ nm when $G \geq 2.5$ e^2/h. Phase coherence length (Figure 6.5c) shows a monotonous increase with device conductance, reaching $l_\varphi \approx 1$ μm at the largest device conductance. The increase in l_φ with conductance can result from the density dependence of the diffusion constant as well as from the density dependence of electron-electron interactions [154], often reported as the dominant source of dephasing in nanowires [155],[150]. The WL-to-WAL-crossover is captured in the change of the $\frac{l_{so}}{l_\varphi}$ ratio from $\frac{l_{so}}{l_\varphi} \approx 1$ to $\frac{l_{so}}{l_\varphi} < 1$ as conductance increases. The requirement for application of a one-dimensional quantum interference model, $W_F < l_\varphi$, is fulfilled. A self-consistent Schrödinger-Poisson calculation yields that several subbands (~ 17) contribute to transport at higher device conductance (see Figure 6.5c). As this two-

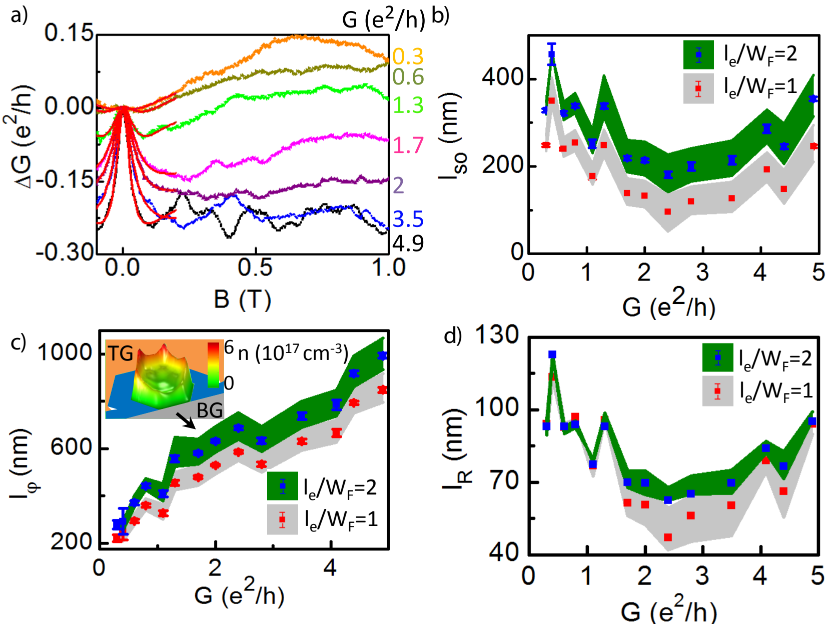

Figure 6.5: **a)** Magnetoconductance (MC) obtained after averaging MC traces taken at the same G. For $G = 3.5$, 1.3 and 0.3 e^2/h the voltages at which these MC traces were taken are indicated in Figure 6.4c. Averaged MC traces have been centered to $\Delta G = 0$ at $B = 0$ T. $G(B = 1.0\text{ T})$ is indicated on the right. Red curves are fits to the data assuming $\frac{l_e}{W_F} = 1$, with mean free path, l_e, and wire width, W_F. **b)** Spin-orbit relaxation length, l_{so}, obtained from the fits of panel b ($\frac{l_e}{W_F} = 1$, blue points) and obtained from fits with $\frac{l_e}{W_F} = 2$ (red points). Standard deviation of the fit outcomes is indicated. The distribution around the blue and red points (in green and gray, respectively) is given by the spin-orbit lengths obtained from fits with an effective width 15 nm smaller or larger than the expected wire width $W_F = 90$ nm (see Section 6.6 for explanation of wire width and width distribution). A larger width $W_F + 15$ nm gives rise to the shorter l_{so}, while a smaller width $W_F - 15$ nm results in longer l_{so}. **c)** Phase coherence length, l_φ, obtained from the fits of panel b) ($\frac{l_e}{W_F} = 1$, blue points) and obtained from fits with $\frac{l_e}{W_F} = 2$ (red points). Figure formatting is the same as in panel c). Inset: electron density as a function of the nanowire cross section, obtained from self-consistent Schrödinger-Poisson calculations with $V_{TG} = 0.5$ V and $V_{BG} = 0$ V. TG (BG) denotes top (back) gate. **d)** Spin precession length, l_R, as a function of device conductance, G, extracted from the spin relaxation length in panel c using simulations of spin relaxation in a nanowire described in Section 6.2.2. Figure formatting is the same as in panel c.

dimensional simulation does not include screening of the gate by the contacts, the actual number of subbands may be slightly lower, but likely several (~ 10) modes contribute to transport at high conductance. This makes the Fermi wavelength the smallest length scale in this system and therefore allows a semi-classical approach. Considering this many-subband requirement we extract $l_{so} = 100 - 400$ nm from the values obtained at higher G ($G \geq 2$ e^2/h). Similar results were obtained from measurements of WAL as a function of V_{TG} with $V_{BG} = 0$ (see Figure 6.10).

Relevant spin relaxation mechanisms in our devices, an open system with only n-type carriers in a material with a narrow bandgap, are the Elliot-Yafet spin relaxation mechanism, and the D'yakonov-Perel' mechanism, in which spin precession between scattering events leads to spin relaxation [32]. The Elliot-Yafet contribution can be estimated as $l_{so,EY} = \sqrt{\frac{3}{8}\frac{E_G}{E_F}}\, l_e \frac{(E_G+\Delta_{SO})(3E_G+2\Delta_{SO})}{\Delta_{SO}(2E_G+\Delta_{SO})} \geq$ 300-600 nm [156], with band gap $E_G = 0.24$ eV, Fermi energy $E_F \geq 100$ meV obtained from Schrödinger-Poisson simulations, spin-orbit gap $\Delta_{SO} = 0.8$ eV and $l_e = W - 2W$. The absence of contact screening in the Schrödinger-Poisson solver leads to an overestimation of E_F. Therefore likely $l_{so,EY} \geq 500$ nm, exceeding the experimentally obtained spin relaxation lengths. Considering the D'yakonov-Perel' mechanism, we note that our wires have a zinc blende crystal structure, but as the nanowires are grown in the (111) direction, Dresselhaus SOI is absent for momentum along the nanowire axis. A Dresselhaus SOI contribution could arise from the radial motion needed to form backscattered paths, but is likely too weak to lead to the measured strong SOI. We therefore, also in view of previous experiments in our nanowires that have shown Rashba SOI [81], assume Rashba SOI to be the dominant contribution to spin relaxation.

We consider geometrical effects that suppress WAL in narrow wires with Rashba SOI (see Section 6.2.2). Our l_{so} mostly correspond to $\frac{\tau_{so}}{\tau_e} = 2 - 15$ that are captured well by our simulations, with the exception of the smallest values of l_{so} at $G = 2.4$ e^2/h and $G = 2.8$ e^2/h that, with a wire diameter larger than expected, $W_F = 105$ nm, yield $\frac{\tau_{so}}{\tau_e} \approx 1$, which is lower than the range of $\frac{\tau_{so}}{\tau_e} \geq 2$ in which closed loops can be made. In this case the l_R corresponding to the lowest simulated value of $\frac{\tau_{so}}{\tau_e}$ has been chosen. We extract a spin precession length, l_R, of 50 – 100 nm (see Figure 6.5e), corresponding to $\alpha_R = 0.5 - 1.0$ eVÅ.

6.3.3 Effects of temperature and magnetic field orientation

To confirm the interpretation of our MC measurements we extract MC at a lower temperature $T = 0.4$ K (Figure 6.6a). We find larger WAL amplitudes up to $\Delta G \approx 0.5$ e^2/h, while the width of the WAL peak remains approximately the same as at $T = 4.2$ K. From fits to the data we find a longer l_φ at lower temperature, while l_{so} remains approximately constant (Table 6.1). The longer l_φ at lower temperature is expected as the rate of inelastic scattering, responsible for loss of phase coherence, is reduced at lower temperature.

Our numerical simulations predict for a hexagonal geometry similar magnetic field dephasing time for magnetic fields perpendicular and parallel to the nanowire.

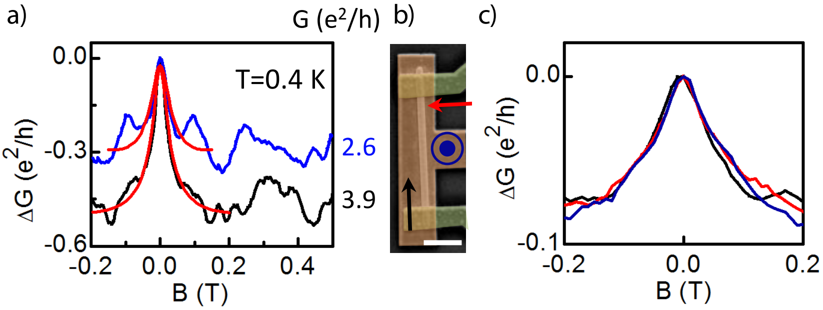

Figure 6.6: a) Magnetoconductance (MC) at $T = 0.4$ K. Each MC trace is obtained after averaging 21 MC traces taken along the top-gate controlled pinch-off trace shown in Figure 6.4c ($V_{BG} = 0$ V). Black (blue) trace is the average of traces taken between $V_{TG} = 0.34$ V and $V_{TG} = 0.14$ V ($V_{TG} = 0.12$ V and $V_{TG} = -0.08$ V) with steps of 20 mV. Voltage excitation, V_{AC}, was 10 μV$_{\mathrm{RMS}}$. $G(B = 0.5\ \mathrm{T})$ is indicated on the right. **b)** False color scanning electron microscope image of device II with magnetic field orientations indicated. Scale bar is 1 μm. **c)** MC obtained with B parallel to the nanowire (in-plane angle w.r.t. nanowire $\theta \approx 5°$, black), B perpendicular to the nanowire in the plane of the substrate ($\theta \approx 95°$, red) and B perpendicular out of the substrate plane (blue). $V_{TG} = 0.2$ V, $V_{BG} = 0$ V. Smaller ΔG compared to the preceding data is due to a larger contact resistance ($\sim$ 10 kΩ) of this device for which no correction was made in analysis of the data.

G (e^2/h)	$\frac{l_e}{W_F}$	l_{so} (nm)	l_φ (nm)
3.9	1	95 ± 18	1078 ± 32
	2	205 ± 16	1174 ± 39
2.6	1	171 ± 26	805 ± 52
	2	380 ± 29	937 ± 60

Table 6.1: Spin relaxation length, l_{so}, and phase coherence length, l_φ, obtained from fits to the traces in Fig. 6.6a. $\frac{l_e}{W_F}$ denotes the ratio of mean free path, l_e, to wire width, W_F.

Our measurements confirm this prediction; very similar WAL with B perpendicular (both in-substrate-plane and out-of-substrate plane) and parallel to the nanowire (see Figure 6.6b-c) is observed, in striking contrast to MC measurements in two-dimensional systems where only a magnetic field perpendicular to the carrier plane affects orbital motion. Also in our first device WAL obtained at different magnetic field orientations is predominantly the same (see Figure 6.11). The agreement between theory and experiment provides strong support for our simulation results and emphasizes the importance of including the three-dimensional nature of nanowires to understand their MC properties.

WL is anisotropic (see Figure 6.12), which we attribute to a different density distribution at low conductance compared to the high conductance at which WAL is seen.

We find that the SOI energy scale, $\alpha_R k_F \approx 6$ meV (using $v_F \approx 10^6$ m/s and $\alpha_R \approx 0.5$ eVÅ), exceeds the Zeeman energy, $g\mu_B B \approx 3$ meV/T (with Landé g factor, g, and Bohr magneton, μ_B) for the magnetic fields relevant here. We therefore neglect any direct effect of Zeeman splitting on our MC data.

6.3.4 Tuning of spin-orbit quantum interference effects

Next we study the dependence of WAL on top and back gate voltage at constant conductance. The distribution of electron density across the wire cross section is controlled with these gate voltages, leading to a wave function that can for instance be confined more in the wire section close to the top gate, for positive V_{TG}, or more in the bottom of the wire (on application of a positive V_{BG}). We explore whether this tuning affects WAL, and whether such changes of WAL are evidence of tuning of Rashba SOI. We therefore compare WAL at the same conductance obtained by controlling conductance with V_{TG}, but with either $V_{BG} = 0$ V or $V_{BG} = 30$ V (device SEM in Figure 6.7a, Figure 6.7b indicates the two voltage settings). At $V_{BG} = 0$ V we observe in this four-point device WAL (Figure 6.7c) and corresponding length scales (Figure 6.7d and Figure 6.13a) similar to that of our first device. However, at $V_{BG} =$ 30 V (Figure 6.7e) WAL persists down to lower conductance than at $V_{BG} = 0$ V (Figure 6.7c), i.e. the WAL-to-WL crossover occurs at lower conductance. (Individual MC traces at $V_{BG} = 0$ V and $V_{BG} = 30$ V are shown in Figure 6.13b-c.) For instance at $G =$ 0.55 e^2/h a broad WAL peak is seen when $V_{BG} = 30$ V, while a trace at the same conductance with $V_{BG} = 0$ V shows predominantly WL. Evaluation of l_{so} with the same τ_B as used in Figure 6.7d results in an $l_{so}(V_{BG} = 30\ \text{V}) = 100 - 200$ nm (shown in Figure 6.7f with $\frac{l_e}{W_F} = 2$), while at the same conductance with $V_{BG} = 0$ V a longer $l_{so}(V_{BG} = 0\ \text{V}) = 200 - 300$ nm is seen.

This could be reason to think that by changing the asymmetry in the device the spin relaxation length can be shortened and therefore the SOI strength controlled. However, the asymmetric gating with $V_{BG} = 30$ V, $V_{TG} = 0$ V leads to a very non-uniform charge distribution (see Figure 6.7g), while Equation (2.48) (to be more specific, the expression for τ_B that is part of it) with which l_{so} is extracted describes a hexagonal cross section with a uniform charge distribution. Equation (2.48) in its current form cannot be applied to an asymmetric charge distribution; its application as done here in Figure 6.7e-f does not yield sensible values for l_{so}. Moreover, the differences in the WAL-to-WL crossover are seen at relatively low G where the requirement that many subbands contribute to transport is likely not fulfilled, thereby further impairing the extraction of l_{so}. Lastly, a change in transport conditions (i.e., a ratio $\frac{l_e}{W_F}$ in Figure 6.7e much different from that in Figure 6.7c) can contribute to the observed difference in WAL. Therefore, although WAL is tuned by asymmetric gating, it cannot be determined whether these effects arise as a result of the tuning of Rashba spin-orbit strength.

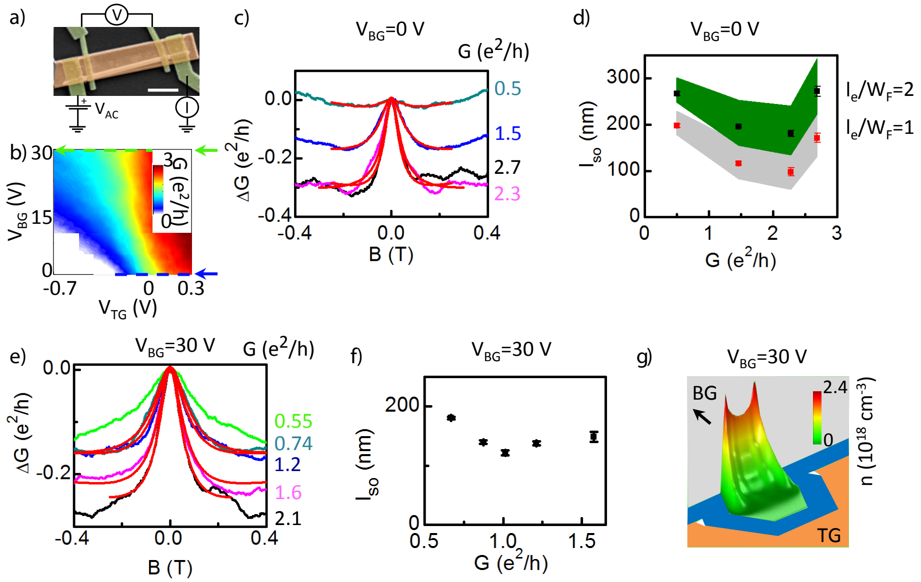

Figure 6.7: a) False colour scanning electron microscope image of device III. A voltage bias, V_{AC}, is applied across the outer contacts, after which simultaneously the current, I, through the device and the voltage across the inner contacts, V, is measured. Subsequently conductance $G=\frac{I}{V}$ is determined. Scale bar is 1 μm. **b)** G as a function of V_{BG} and V_{TG}. Magnetoconductance (MC) along two top-gate pinch-off traces will be compared: (1)$\Delta G(B)$ with conductance controlled by V_{TG} at $V_{BG} = 0$ V (blue arrow and dashed line) and (2) $\Delta G(B)$ with conductance controlled by V_{TG} at $V_{BG} = 30$ V (green arrow and dashed line). **c)** Averaged MC traces obtained after taking MC traces with top gate voltage spacing $\Delta V_{TG} = 20$ mV between $V_{TG} = 0.3$ V and $V_{TG} = -0.22$ V and averaging 7 subsequent traces. $V_{BG} = 0$ V. $G(|B| = 0.5\text{ T})$ is indicated. Red curves are fits with $\frac{l_e}{W_F} = 1$. **d)** Spin relaxation length, l_{so}, obtained from the fits of panel c ($\frac{le}{W_F} = 1$, blue points) and obtained from fits with $\frac{le}{W_F} = 2$ (red points). Standard deviation of the fit outcomes is indicated. The distribution around the blue and red points (in green and gray, respectively) is given by the spin-orbit lengths obtained from fits with an effective width 15 nm smaller or larger than the expected wire width $W_F = 75$ nm. **e)** Averaged MC traces obtained after taking MC traces with top gate voltage spacing $\Delta V_{TG} = 25$ mV between $V_{TG} = 0$ V and $V_{TG} = -1.35$ V and averaging 7 subsequent traces. $V_{BG} = 30$ V. $G(|B| = 0.4\text{ T})$ is indicated. Red curves are fits with $\frac{l_e}{W_F} = 2$. **f)** Spin relaxation length, l_{so}, obtained from the fits of panel e with $\frac{l_e}{W_F} = 2$. **g)** Electron density as a function of the nanowire cross section. Density is obtained from self-consistent Schrodinger-Poisson calculations of the device under study with $V_{TG} = 0$ V and $V_{BG} = 30$ V, which is expected to represent the electron density encountered in our device at lower G ($G \leq 2\ e^2/h$). Charge is induced mostly in the section of the hexagonal nanowire cross section closest to the back gate (BG).

6.4 Discussion

6.4.1 Crossover from WAL to WL

In self-assembled nanowires of different diameter a crossover from WL at low G to WAL at high G has been observed [44], [95],[157],[158],[155]. It has been brought forward that this crossover (observed here in Figure 6.5 and Figure 6.7) indicates tuning of Rashba spin-orbit strength in a nanowire by the external electric field [155],[158]. Possibly the higher electric field needed to create a larger conductance leads to a larger α at higher G and the resulting observation of WAL only at higher G. However, the WL-to-WAL-crossover as a function of conductance has in other systems been explained by a change in carrier density [159] or by a density dependent scattering time [160]. Moreover, as discussed above a reduction of the transport width W_F leads to an increased l_{so}, possibly resulting in $l_{so} > l_{\varphi}$, and therefore to the observation of WL. The crossover from WAL to WL could therefore result from a reduced W_F as the wire is gradually pinched off. Moreover, as noted in the description of WAL obtained with asymmetric gating, the MC model outlined above likely does not give an accurate description at low conductance as the condition for semiclassical transport $\lambda_F \ll W_F$ is no longer fulfilled, and therefore cannot be used to demonstrate tuning of Rashba SOI at low density.

6.4.2 Non-uniformity of the charge distribution

Equations (2.48) and (6.4) assume a uniform charge distribution across the wire cross section. The charge distribution in the inset of Figure 6.5d shows a charge density $n \geq 10^{17}$ cm^{-3} everywhere in the cross section, allowing us to approximate the transport cross section by the hexagonal wire shape. The good agreement between experiment and simulation on weak anti-localization as a function of magnetic field orientation (Figure 6.6c and accompanying text) provides further support for using a uniform and hexagonal wire cross section. The charge density near the top gate in the inset of Figure 6.5d is however larger than that in the rest of cross section and this non-uniformity in charge distribution may affect our estimates of spin-orbit length and phase coherence length. Specifically, the observed increase of $l_{so}(G)$ and $l_R(G)$ at larger G in Figure 6.5b and Figure 6.5d may be explained by a change in charge distribution as the voltage on the top gate is increased. A similar increase of l_{so} at higher device conductance has been observed before in Ge/Si nanowires [158].

6.4.3 Comparison of spin-orbit and phase coherence length to literature values

Previously values of α_R in InSb-based nanostructures are ~ 0.03 eVÅ [161] obtained from MC measurements of InSb quantum wells and 0.16 – 0.22 eVÅ from level spectroscopy of quantum dots [81] in the same InSb nanowires as used here. We speculate that our larger α_R results from stronger electric fields created in our top-gated device geometry. Relevant to Majorana fermion experiments is the spin-orbit energy, $E_{SO} = \frac{m\alpha_R^2}{2\hbar^2}$, that is 0.25 – 1 meV in our devices. These values compare favourably to InAs nanowires that yield $\alpha_R^{InAs} = 0.1 - 0.3$ eVÅ [95],[155] and corresponding $E_{SO}^{InAs} = 15 -$ 135 μeV. E_{SO}^{InSb} is similar or slightly larger than reported spin-orbit energies in Ge/Si core-shell nanowires ($E_{SO}^{Ge/Si} = 90 - 600$ μeV, [158]), while α_R^{InSb} is larger than $\alpha_R^{Ge/Si} =$ 0.07 – 0.18 eVÅ). Note that device geometries as well as expressions for $\alpha_R(l_{so})$ used by different authors vary and that often only l_{so}, but not l_R, is evaluated.

l_φ extracted from measurement of WAL in nanowires (InAs, Ge/Si and InN) mostly range between approximately 40 and 500 nm [44],[157],[155],[95], [162].[163] reports a longer $50 < l_\varphi(\text{nm}) < 800$. For InSb nanowires $l_\varphi \sim 100$ nm at $T = 4.2$ K has been extracted from conductance fluctuations. The electron density in these wires was however high ($n \sim 10^{18}$ cm^{-3}) and the mean free path short, possibly leading to l_φ different from ours.

6.5 Conclusion

The observation of weak anti-localization in dual-gated InSb nanowires indicates a strong spin-orbit interaction. Using numerical simulations of magnetic dephasing and spin relaxation a spin precession length due to Rashba SOI of 50 – 100 nm is obtained, corresponding to a SOI strength of 0.5 – 1 eVÅ. This large α_R underlines the potential of InSb nanowires in the study of Majorana fermions and indicates its potential in the broader fields of spintronics and spin-based quantum computing. Moreover, our results on WAL as a function of magnetic field angle with respect to the wire and gating asymmetry indicate that it is essential to consider both the nanowire geometry and its charge distribution to understand quantum interference effects.

This work has been done in collaboration with B. Tarasinksi, D. Eeltink, V. S. Pribiag, S. R. Plissard, E. P. A. M. Bakkers, M. T. Wimmer and L. P. Kouwenhoven.

6.6 Supplementary data

6.6.1 Estimation of mobility, mean free path and $\frac{l_e}{W_F}$

Nanowire mobility, μ, is obtained from pinch-off traces. To extract mobility and series resistances from device I (data shown in Figure 6.4, Figure 6.5, Figure 6.6a-b, Figure 6.10, Figure 6.11, Figure 6.12) using the method described in [164] and Chapter 7 a gate trace from pinch-off to saturation is needed, while $I(V_{BG}, V_{TG} = 0\text{ V})$ obtained from Figure 6.8 covers only an intermediate range. Therefore also traces at $I(V_{BG}, V_{TG} = -0.15\text{ V})$ and $I(V_{BG}, V_{TG} = 0.15\text{ V})$ are used. The three traces then together form a full pinch-off trace that is well approximated using an expression for $I(V_{BG})$ with capacitance between back gate and nanowire $C_{BG} = 22$ aF, series resistance $R_S =$ 10 kΩ, mobility $\mu = 12{,}500$ cm^2/Vs, threshold voltage $V_{TG} = -16.5$ V. Other inputs are source-drain bias $V_{SD} = 10$ mV and contact spacing $L = 2$ μm. The capacitance has

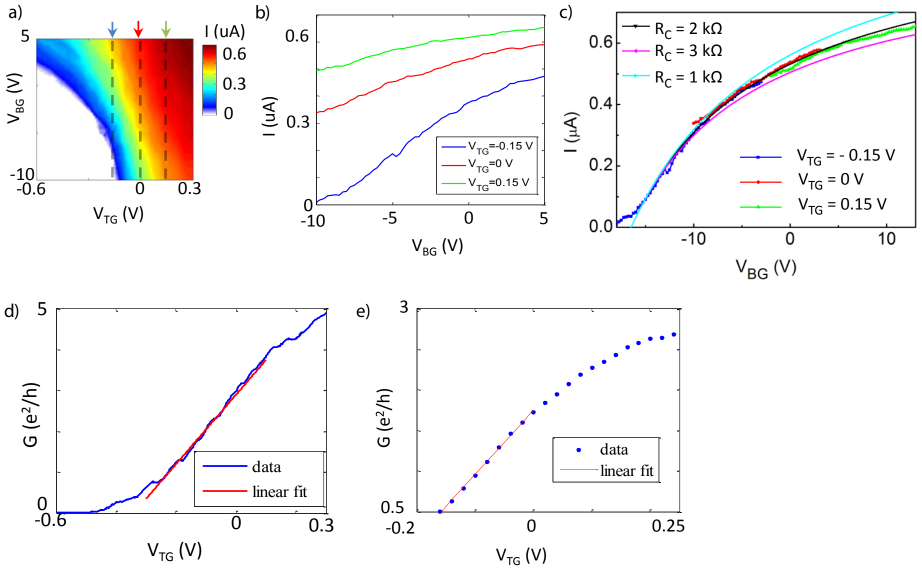

Figure 6.8: a) Current, I, in device I as a function of top gate voltage, V_{TG}, and back gate voltage, V_{BG}. Top gate voltages corresponding to the $I(V_{BG})$ traces in panel b are indicated with arrows. Data taken with source-drain voltage V_{SD} = 10 mV. **b)** $I(V_{BG})$ at V_{TG} = 0.15 V, V_{TG} = 0 V and $V_{TG} = -0.15$ V. **c)** Traces at $I(V_{BG}, V_{TG} = -0.15\text{ V})$ (blue) and $I(V_{BG}, V_{TG} = 0.15\text{ V})$ (green) are displaced by $\Delta V_{BG} = -8$ and $\Delta V_{BG} = 8$ V, respectively, chosen such that their current is similar to that of the $I(V_{BG}, V_{TG} = 0\text{ V})$ trace (red). Data is well approximated by $I(V_{BG})$ (see text) with mobility $\mu \sim$ 12,500 cm^2/Vs and contact resistance R_C = 2 kΩ (black). Traces with larger (3 kΩ, pink) or smaller (1 kΩ, cyan) contact resistance are also shown. **d)** $G(V_{TG})$ in device I with V_{BG} = 0 V (blue). A linear fit of the pinch-off traces gives a slope $\frac{dG}{dV_{TG}}$ = 8.5 (e^2/h)/V (red). **e)** $G(V_{TG})$ in device III with V_{BG} = 0 V. A linear fit of the pinch-off traces gives a slope $\frac{dG}{dV_{TG}}$ = 7.9 (e^2/h)/V (red).

been obtained from electrostatic simulations. The series resistance consists of instrumental resistances (RC-filters and ammeter impedance, together 8 kΩ) and a contact resistance R_C. The experimental pinch-off traces are best approximated by R_C = 2 kΩ. Expressions for $I(V_{BG})$ with R_C = 1 kΩ and R_C = 3 kΩ, also shown, deviate from the measured pinch-off traces. The mobility is also estimated from a linear fit to the top gate pinch-off trace shown in Figure 6.8d. Prior to this fit instrumental and series resistances have been subtracted. From the fit $\mu \approx$ 9,000 cm^2/Vs is obtained, using C_{TG} = 1440 aF and $L = 2$ μm. Capacitance has been obtained from electrostatic simulations. Similarly, mobility in device III (data shown in Figure 6.7 and Figure 6.13) is extracted from a fit to the top gate pinch-off trace, giving $\mu \sim$ 10,000 cm^2/Vs using C_{TG} = 1660 aF and $L = 2.3$ μm.

The mean free path, l_e, is estimated as $l_e = v_F \tau_e$, with v_F the Fermi velocity and

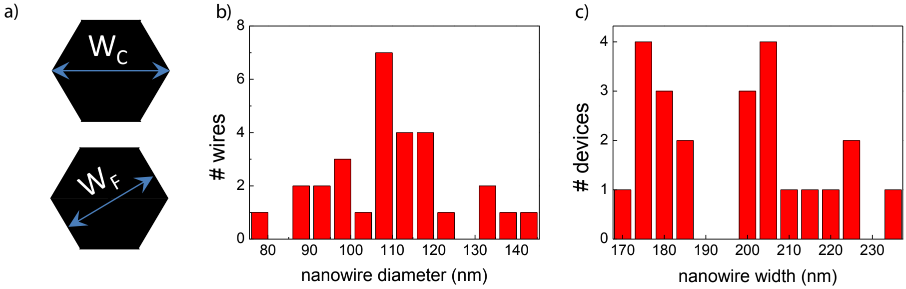

Figure 6.9: a) A top view of hexagonal nanowires (such as a scanning electron microscope image) shows the width from corner to corner, W_C. In our simulations the facet-to-facet width, W_F, is used. The two widths are related by $W_F = \cos(\frac{\pi}{6})W_C$. **b)** Distribution of the nanowire width. Average diameter is 110 nm, standard deviation is 15 nm. **c)** Distribution of apparent nanowire width after fabrication. Device width increases due to HfO_2 deposition. Average apparent nanowire diameter is 197 nm. Device I had a diameter after fabrication of 200 nm, close to the average nanowire device diameter, and therefore its wire diameter is estimated as 110 nm, the average the distribution of wire diameters in panel c. Device III has an apparent wire diameter of 180 nm, which is 17 nm below average. The wire diameter is therefore estimated as $110 - 17 = 93$ nm. Wires are covered by a native oxide of ~ 2.5 nm, giving an InSb diameter $W_C \sim 105$ nm and $W_C \sim 88$ nm for device I and device III respectively. Facet-to-facet diameter W_F, used the main text, is therefore $W_F \approx 90$ nm (device I) and $W_F \approx 75$ nm (device III). The standard deviation of wire diameter of 15 nm in panel b) is used to define a range of wire diameters, $W_F \pm 15$ nm, for which spin-orbit and phase coherence length are obtained in Figure 6.5 and Figure 6.7.

τ_e the scattering time. $\tau_e = \frac{\mu m^*}{e}$, with e the electron charge and m^* the effective electron mass in InSb. Assuming a 3D density of states $v_F = \frac{\hbar}{m^*}(3\pi^2 n)^{1/3}$ with $\hbar$ the reduced Planck constant and n electron density. n is estimated from pinch off traces using $n = \frac{C(V_G - V_{TG})}{eAL}$ with A the nanowire cross section, V_G top or back gate voltage and V_{TG} the threshold (pinch-off) voltage. In this way in device I n up to $\sim 4{\cdot}10^{17}$ cm^{-3} are obtained, giving l_e up to ~ 160 nm. In device III n up to $\sim 4{\cdot}10^{17}$ cm^{-3} gives $l_e \sim 150$ nm. Together with the facet-to-facet width W_F (described in Figure 6.9) these mean free paths yield a ratio $\frac{l_e}{W_F} = 1\text{-}2$.

6.6.2 Nanowire width

Nanowires were not imaged with a scanning electron microscope prior to device fabrication to avoid damage due to electron irradiation. The wire diameter is estimated from a comparison of the nanowire width after fabrication to the nanowire diameter obtained from a number of wires from the same growth batch deposited on a substrate as described in Figure 6.9.

6.6.3 Spin relaxation length obtained from top gate averaging in device I

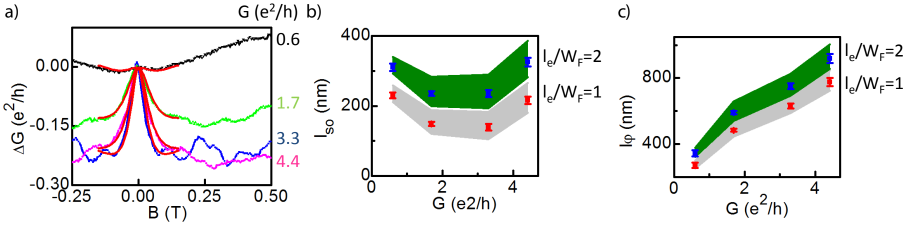

Figure 6.10: Spin-orbit length and phase coherence length obtained from top gate averaging in device I. a) Magnetoconductance traces obtained after taking MC traces with top gate voltage spacing $\Delta V_{TG} = 20$ mV between 0.34 V and -0.42 V and averaging 9 subsequent traces. $V_{BG} = 0$ V. Averaged MC traces have been centered to $\Delta G = 0$ at $B = 0$ T. $G(B = 0.5\text{ T})$ is indicated on the right. Red traces are fits using $\frac{l_e}{W_F} = 2$ and $W_F = 90$ nm. **b)** Spin relaxation length, l_{so}, obtained from the fits of panel a ($\frac{l_e}{W_F} = 2$, red points) and obtained from fits with $\frac{l_e}{W_F} = 1$ (blue points). Standard deviation of the fit outcomes are indicated. The distribution around the blue and red points (in green and gray, respectively) is given by the spin-orbit lengths obtained from fits with an effective width 15 nm smaller or larger than the expected wire width $W_F = 90$ nm. **c)** Phase coherence length, l_φ, obtained from fits of panel a. Figure formatting is the same as in panel b.

6.6.4 Magnetoconductance in parallel and perpendicular field in device I

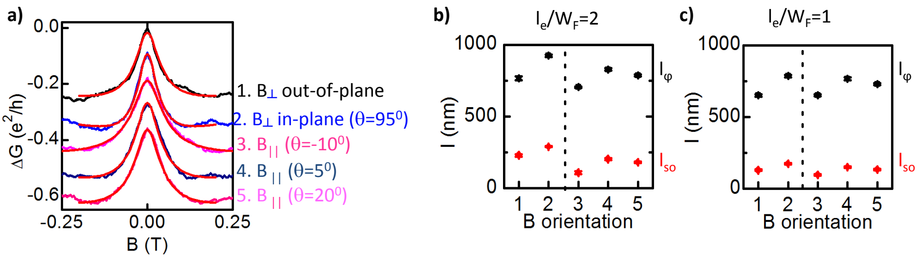

Figure 6.11: a) MC with parallel and perpendicular magnetic field orientation. In-plane angle θ w.r.t. the nanowire is given. As the uncertainty in orientation of the in-plane magnetic field w.r.t. the nanowire is $\sim 20°$ three parallel magnetoconductance traces with $|\theta| \leq 20°$ are shown. Each MC trace is an average of 7 traces taken at the same conductance $G = 3.5\,\frac{e^2}{h}$ by varying top and back gate voltage. No systematic change of MC along these equiconductance points was observed. As in device II (Figure 6.6c) also here WAL in parallel and perpendicular magnetic field are very similar. Red curves are fits using $\frac{l_e}{W_F} = 1$ and $W_F = 90$ nm. **b)** (**c)**) Spin relaxation length, l_{so}, (red) and phase coherence length, l_φ, (black) obtained from fits of the MC traces in panel a using $\frac{l_e}{W_F} = 2$ (1). B orientation numbers correspond to the traces numbered 1 to 5 in panel a. The slightly wider WAL peak in parallel magnetic field yields better agreement with $\frac{l_e}{W_F} = 1$ as spin relaxation lengths and phase coherence lengths obtained in parallel and perpendicular field with $\frac{l_e}{W_F} = 1$ are more similar than when assuming $\frac{l_e}{W_F} = 2$.

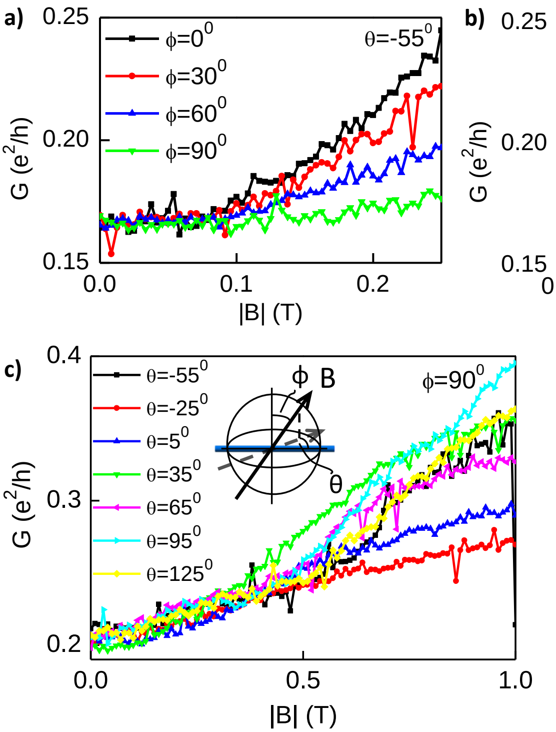

Figure 6.12: a) MC as a function of out-of-plane angle, ϕ, with in-plane angle with respect to the nanowire $\theta = -55°$. $\phi = 0°$ (90°) is magnetic field perpendicular to (parallel to) the substrate plane. Angles θ and ϕ are also shown in the schematic drawing in the inset of panel c. **b)** MC as a function of out-of-plane angle ϕ with in-plane angle w.r.t. nanowire $\theta = 35 \pm 20°$. While WAL is (nearly) independent of magnetic field orientation, here we find that for both in-plane angles the suppression of WL by magnetic field becomes less effective when rotating the field from perpendicular to parallel to the substrate plane. **c)** MC as a function of in-plane angle θ. Although the suppression of weak localization by magnetic field is much less effective for all magnetic fields oriented parallel to the substrate plane, a closer inspection shows that the magnetic field dependence is the weakest when the magnetic field is approximately aligned with the nanowire. We suggest the difference in dependence on magnetic field angle between WAL and WL is due to a difference in electron density distribution: while at the larger device conductance at which WAL is observed many subbands are occupied and the transport diameter equals the wire diameter, at low conductance, when WL is seen, transport takes place only a few modes, confined to a small region of the nanowire cross section. The low conductance situation may resemble a two-dimensional system, in which only the magnetic field component perpendicular to the substrate leads to a suppression of WL. In all panels $V_{TG} = -0.36$ V, $V_{BG} = 0$ V. The difference in $G(B = 0\text{ T})$ between a-b and c is due to a slight device instability at low conductance or due to hysteresis when sweeping V_{TG}.

6.6.5 Spin precession length and crossover from WAL to WL in device III

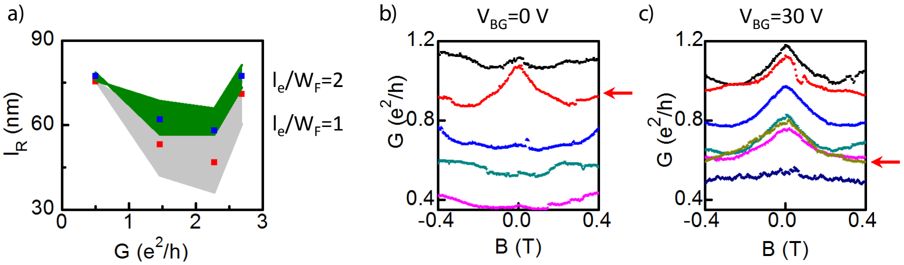

Figure 6.13: a) Spin precession length, l_R, as a function of device conductance, G, obtained from the the spin relaxation times in Figure 6.7d. Blue points correspond to $\frac{le}{W_F}$ = 2 and red points to $\frac{le}{W_F}$ = 1. The distribution around the blue and red points (in green and gray, respectively) is given by the spin precession lengths obtained from the assumption of an effective width 15 nm smaller or larger than the expected wire width W_F = 75 nm. **b)** (**c)**) Magnetoconductance at several G obtained by controlling G with V_{TG} while V_{BG} = 0 V (V_{BG} = 30 V). The arrow indicates the MC trace with the lowest G that shows WAL. When V_{BG} = 30 V the WAL-to-WL crossover occurs at lower G than when V_{BG} = 0 V.

6.6.6 Magnetic dephasing time prefactor

geometry	orientation	$\frac{l_e}{W_F}$	C
square	parallel	10	42863.56
		4	2844.55
		2	379.71
		1	54.21
	perpendicular	10	12665.85
		4	856.30
		2	118.03
		1	17.59
hexagon	parallel	10	13256.76
		4	1221.09
		2	203.41
		1	36.58
	perpendicular	10	34030.99
		4	1761.14
		2	199.76
		1	25.53

Table 6.2: Coefficient C defined in Equation (6.3) for a square and a hexagonal geometry with magnetic field parallel or perpendicular to the nanowire. Several values of $\frac{l_e}{W_F}$ are considered. The coefficients have been obtained from fits to the simulation results of Figure 6.1a-b.

CHAPTER 7

LOW-TEMPERATURE FIELD-EFFECT MOBILITY IN INSB NANOWIRES

The use of InSb nanowires in Majorana fermion devices and other quantum devices requires a high carrier mobility. We extract electron field-effect mobility of InSb nanowires at low temperature (4.2 K) by means of transport measurements. Our InSb nanowires are free of stacking faults and surface roughness and have a diameter of ~ 100 nm. We find that the extracted mobility increases significantly after long evacuation of the sample space before cool down. This indicates that the extracted mobility is currently limited by adhesion of molecules to the nanowire surface and/or to the SiO_2 substrate, although the underlying mechanism is currently not fully understood. Also considering substrate cleaning and a dependence on contact spacing we find an average field-effect mobility of ~ 25,000 cm^2/Vs.

7.1 Introduction

Advances in nanowire growth have led to development of novel quantum devices, such as cooper-pair splitters [165], hybrid semiconductor-superconductor devices [166] and spin-orbit qubits [167]. Nanowire devices thus allow exploration of mesoscopic transport in a highly directional system and show potential as a quantum computation platform. Outstanding nanowire transport properties, such as a high level of tunability of device conductance and low disorder, have been essential to the realization of these experiments.

Recently, hybrid semiconductor nanowire-superconductor devices have been identified [18],[19] as a suitable system for creation of Majorana fermions [11], zero-energy bound states that exhibit topological properties. Reports of Majorana fermion signatures in InSb [17],[111],[149] and InAs [110] nanowire-based systems followed quickly after their theoretical prediction. The topological character of Majorana fermions makes them a candidate for creating fault-tolerant quantum bits [10]. To fulfil this promise a reduction of disorder in the nanowire is essential [26],[25]. Disorder reduces or even closes the topological gap that gives Majoranas their robustness, thereby impairing their use as topological qubits.

Disorder is quantified by measurements of carrier mobility, which relates directly to the time between scattering events. Evaluation of carrier mobility in nanowires indicates their potential for transport experiments and is thus crucial to further development of nanowire-based quantum devices. To extract mobility in nanowires field-effect transistors (FETs) are made: by contacting the nanowire and measuring its conductance as a function of the voltage on a nearby gate the field-effect mobility is determined. In this chapter we study low-temperature electron field-effect mobility in InSb nanowires with the aim of increasing mobility to enable further development of Majorana fermion devices and possibly other nanowire-based devices.

First, we describe how field-effect mobility is extracted and consider previous research on nanowire mobility. We then turn to our InSb FETs. We present results on low-temperature InSb nanowire electron mobility and describe factors that result in an increase in mobility. In this way we develop a recipe that enables reproducible, high-yield field-effect mobilities of $\sim 25{,}000\ \mathrm{cm^2/Vs}$. We find that adhesion of molecules to the nanowire and/or the substrate currently limits the extracted mobility. Although the amount of adsorbates is reduced by long evacuation of the sample space prior to cool down, they are not fully removed, and suggestions for further study are made.

7.2 Method: extraction of field-effect mobility

Mobility, μ, is defined within the Drude model of conductivity as the proportionality factor between an applied electric field, E, and the resulting drift velocity, v_d

$$v_d = \mu E. \tag{7.1}$$

From Equation (7.1) it can be derived that the mobility is also the proportionality factor between the carrier density, n, and conductivity, σ, of a material

$$\sigma = ne\mu. \tag{7.2}$$

Mobility is related to the time between scattering events, τ, by

$$\mu = \frac{e\tau}{m^*} \tag{7.3}$$

with effective electron mass, m^*, and the electron charge, e. Several mechanisms, such as phonon scattering, impurity scattering or surface roughness scattering affect mobility. Relevant contributions to nanowire mobility will be discussed in Section 7.3. According to the Mathiessen rule [168] the net mobility μ (or scattering time, τ) depends on these contributions as

$$\frac{1}{\mu} = \frac{1}{\mu_1} + \frac{1}{\mu_2} + \dots. \tag{7.4}$$

The lowest mobility contribution therefore determines the net mobility, and mobility can therefore be improved by identifying the limiting contribution and subsequently reducing or eliminating it.

The conductance, G, of a FET in the linear region of the accumulation regime is decribed by [169]

$$G(V_g) = \frac{\mu C}{L^2}\left(V_g - V_{th}\right), \tag{7.5}$$

with gate voltage, V_g, mobility μ, dielectric capacitance C, contact spacing, L, and threshold voltage, V_{th}. The threshold voltage depends amongst others on the work function of the gate metal and semiconductor and charges within the gate oxide. Field-effect mobility, μ_{FE}, can be obtained from Equation (7.5) via the transconductance

$$g_m = \frac{dG}{dV_g}. \tag{7.6}$$

The expression for field-effect mobility then becomes

$$\mu = \frac{L^2 g_m}{C}. \tag{7.7}$$

This expression neglects changes of mobility with gate voltage, $\mu(V_g)$, [168] and is therefore often evaluated at peak transconductance. As in silicon transistors $\frac{d\mu}{dV_g} < 0$ has been observed (attributed to enhanced surface roughness scattering with increased gate voltage) field-effect mobility is thought to underestimate mobility[1].

---

[1] Assuming a gate-dependent mobility, $\mu(V_g)$, leads to $\frac{dG}{dV_g} = \frac{C}{L^2}\left(\mu + \left(V_g - V_{th}\right)\frac{d\mu}{dV_g}\right)$. As $\frac{d\mu}{dV_g} < 0$, $\frac{dG}{dV_g}\frac{L^2}{C} < \mu$. Evaluating mobility using Equation (7.6) and Equation (7.7) thus underestimates the mobility.

The above expressions assume classical, diffusive transport, which implies $L \gg l_e, l_\varphi$, with mean free path, l_e, and phase coherence length, l_φ.

7.3 Nanowire mobility

We first briefly review the literature on factors affecting nanowire mobility, focusing on low-temperature transport measurements (and therefore neglecting phonon scattering) and on nanowires that are not intentionally doped, as these are most relevant to our study. All mobilities in this section are field-effect mobilities, extracted from the change of nanowire conductance with gate voltage evaluated at peak transconductance (see Section 7.2).

Crystal structure defects reduce mobility. Crystal structure defects can be distinguished on the basis of their dimensionality as planar defects (grain boundaries and stacking faults), line defects (dislocations) or point defects.

Stacking faults

Some often-used III-V materials display along their growth direction a switching between wurtzite and zinc blende crystal orientation for one or a few layers of atoms [170],[87]. Unlike point defects, such stacking faults can be observed with standard electron microscopy techniques, or even optically [171]. Stacking faults have been shown to reduce mobility in InAs nanowires [171],[87],[88],[172] and InAsSb nanowires [173], although in an earlier report no relation between stacking fault density and mobility was found [174]. Stacking faults are thought to lower mobility via a difference in conduction band energy between the two crystal phases, which leads to wave reflection at their intersection [172] or to trapping of electrons in the wire section with lower conduction band energy [170]. The bound states in zinc blende segments in InAs and InP nanowires can be ~ 20-90 meV lower in energy than the wurtzite conduction band edge [170],[175] with long (several nm) zinc blende segments trapping ~ 200 electrons (equivalent to an electron density ~ $2 \cdot 10^{16}$ cm^{-3}) [170].

Point defects in the nanowire

Similar to bulk semiconductors, point defects, such as vacancies and substitional and interstitial impurity atoms, are thought to lower mobility in nanowires by impurity scattering[2] and by trapping electrons. Nanowires are often grown by gold catalyst-assisted metalorganic vapour phase epitaxy (MOVPE) during which possibly gold (a catalyst material) and carbon (used in precursors) are incorporated [87],[65]. Gold is detected in GaAs nanowires by atomic probe tomography measurements in densities of 10^{17} to 10^{18} cm^{-3} and is thought to prevent ballistic transport in these nanowires

---

[2] At a temperature of 4 K the ionization energy of donors and acceptors exceeds the thermal energy and dopants are not ionized. While dopants therefore lead to neutral impurity scattering, at such low temperatures they do not create charge carriers and do not lead to charged impurity scattering.

[176]. However, to our knowledge no direct relation between Au incorporation and mobility has been reported. The absence or presence of catalyst material may depend on specific growth conditions or catalyst material [177],[178],[179].

Surface defects and surface roughness

Nanowires are covered with a native oxide. The presence of this oxide can affect their properties in several ways. It may lead to strain due to a difference in lattice constant between the nanowire core and its oxide shell. The disordered interface between nanowire and oxide may host (immobile) fixed charges and trapped charges, that interact with the nanowire body [180]. Furthermore, the oxide itself may also contain defects that can result in trapped (immobile) charges and mobile charges[3]. Lastly, on the oxide surface adsorption of molecules may occur [181]. The surface charges resulting from the nanowire-oxide interface, the oxide itself and adsorption onto the oxide can result in a surface accumulaton or surface depletion layer [180],[182].

As nanowires have a large surface-to-volume ratio, surface states drastically alter their electronic properties. Improved device performance after passivation of InAs nanowires with a high-κ dielectric and deposition of either a top gate or a photoresist layer is attributed to a reduction of interface traps and surface disorder [91],[109]. Also passivation of oxide defects on silicon nanowires by chemical passivation increases mobility [183]. Exposure to an electron beam has been shown to affect electric properties of InAs nanowires [184], possibly by creation by defects and/or electron traps.

An increase of mobility with diameter is observed in InAs [185],[186] and InGaAs nanowires [187], which is attributed to the detrimental effect of surface roughness scattering, i.e., scattering due to bulges and indentations in the radial direction, leading to fluctuations in the nanowire diameter. A direct relationship between such surface roughness and mobility, i.e. a higher nanowire mobility when the nanowire surface roughness is reduced, is observed in [186].

Lastly, an increase in mobility after growth of a shell around the nanowire is found in InAs/InP [188],[189] and GaN/AlN/AlGaN [190] core-shell nanowires, also indicating that surface-related effects strongly affect mobility.

Highest reported low-temperature field-effect mobilities are 16,000 – 25,000 cm^2/Vs. Such mobilities are observed in InAs nanowires [186],[171], InAs/InP core-shell nanowires [189],[188] and GaN/AlN/AlGaN core-shell nanowires after correction for contact resistances [190]. However, in several of these studies either only data on a single device is reported, or the average mobility of several devices is significantly lower than the reported maximum (e.g. a maximum ~ 25,000 cm^2/Vs with an average ~ 10,000 cm^2/Vs [189]).

---

[3] Similar to the nanowire native oxide, the substrate dielectric on which the nanowire is placed can also contain fixed and mobility charges, both within the dielectric itself as well as at interfaces.

7.4 Field-effect mobility in InSb nanowires

7.4.1 Literature

Diameter-dependent conductance of InSb nanowires at room temperature shows prevalence of bulk conductance over surface effects [191]. However, at room temperature an increase of mobility with diameter was also reported [192]. Room temperature mobilities of ~ 1000 cm^2/Vs are reported [193],[192], as well as ~ 100 cm^2/Vs [62]. A hole mobility of ~ 50 cm^2/Vs at room temperature is observed [63].

Concerning field-effect mobility, our InSb nanowires differ in several respects from the often-studied InAs nanowires: our InSb nanowires have a larger diameter of ~ 100 nm, reducing their surface-to-volume ratio with respect to thinner InAs nanowires, and likely do not have a surface accumulation layer. Instead upward band bending, leading to surface carrier depletion, has been reported for both clean [69] and oxygen-covered InSb surfaces with (110) orientation, the orientation of our InSb nanowire facets. As the InSb facets are atomically flat no surface roughness is expected. Lastly, our InSb nanowires have a zinc blende crystal structure free of stacking faults and dislocations [59]. Altogether it is therefore an open question what determines low-temperature mobility in InSb nanowires.

7.4.2 Extraction of field-effect mobility

The absence of a surface accumulation layer makes contacting InSb nanowires more difficult than InAs nanowires. Ohmic contacts to the nanowire can be made, but an interface resistance of a few kΩs remains [126]. This interface resistance cannot be neglected compared to the nanowire resistance and therefore result in lower transconductance, and subsequent underestimation of the intrinsic mobility [168], [194]. Moreover, at a temperature of 4 K reproducible conductance fluctuations on the gate traces complicate extraction of mobility from transconductance as $l_\varphi \sim 500$ – 1000 nm at 4 K (see Chapter 6).

We therefore tailor the extraction of field-effect mobility to our InSb nanowire FETs. We assume a mobility independent of gate voltage. The saturation of conductance at high gate voltage is then due to the presence of both an instrumental resistance and interface resistances. We denote the interface resistances by R_s. The instrumental resistance has already been subtracted in all gate traces and R_s reported in this chapter. Under this condition the conductance as function of gate voltage, $G(V_g)$, is (see also Figure 7.1a)

$$G(V_g) = \frac{1}{R_s + \frac{L^2}{\mu C (V_g - V_{th})}} \tag{7.8}$$

that allows extraction of field-effect mobility using a fit with the above expression to the measured $G(V_g)$. Capacitance is obtained from a finite element model of the device (see the inset of Figure 7.1c), taking into account that quantum comfinement in our nanowires reduces the classical capacitance by ~ 20 % [195],[75]. μ, R_s and

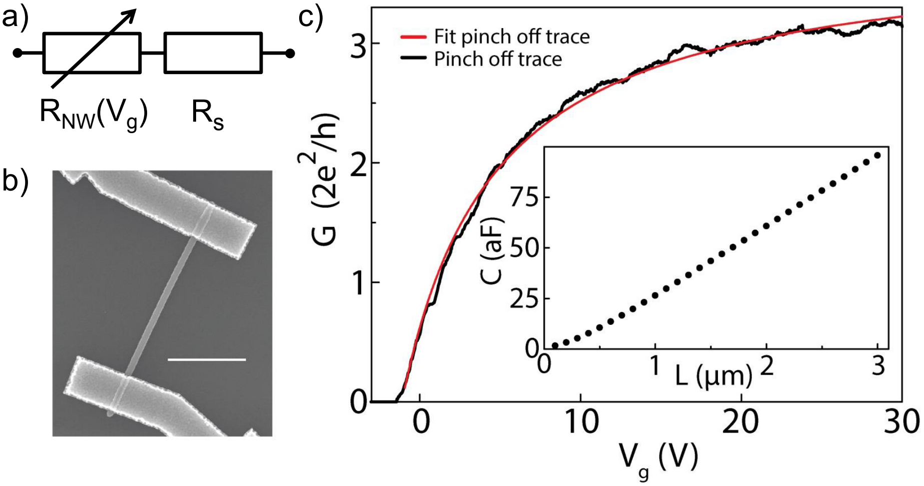

Figure 7.1: a) Electrical diagram of the InSb nanowire FET. The FET is modeled as a nanowire with a resistance controlled by a nearby gate, $R_{NW}(V_g)$, in series with fixed interface resistances, R_S. **b)** Electron microscope image of an InSb nanowire FET. Nanowire diameter is ~ 100 nm. The nanowire is deposited onto a p^{++}-doped Si substrate covered with 285 nm thermal SiO$_2$. The p^{++}-doped Si is used as a back gate. Contacts are Ti/Au 5/145 nm and contact spacing is 1, 1.5, 2 or 2.5 μm. Scale bar is 1 μm. **c)** Conductance, G, as a function of back gate voltage, V_g. Source-drain bias is 10 mV. Field-effect mobility is extracted from a fit to the gate trace (red curve) using Equation (7.8). All measurements are performed at a temperature of 4.2 K. Inset: Gate-nanowire capacitance, C, as a function of contact spacing, L. Capacitance is extracted from a finite element model of the device geometry. Contacts are included in the simulated device geometry and lead to a non-linear $C(L)$ at small contact spacing.

V_{th} are fit parameters. Field-effect mobility obtained from peak transconductance and field-effect mobility obtained from a fit according to Equation (7.8) yields very similar values as shown in Section 7.8.4.

7.4.3 Experimental approach

InSb nanowire field-effect transistors are fabricated on a substrate with a global backgate (see Figure 7.1b). We extract field-effect mobility from a fit using Equation (7.8) (see Figure 7.1c).

In the next section we experimentally determine factors affecting field-effect mobility. To assess the effect of changes in our recipe we extract mobility assuming a fixed capacitance, i.e. in all experiments the capacitances shown in the inset of Figure 7.1b are used. We reflect on this assumption in the discussion that follows the description of our experimental findings. We report extracted mobilities of ~ 10 devices fabricated in a single fabrication run to assess device-to-device variation. With regard to run-to-run variation we have reproduced the mobilities of 20,000 – 25,000 cm^2/Vs obtained using our fabrication recipe (see Section 7.8.1 for an overview of batches and reproducibility, and Section 7.8.2 for the recipe). The yield of devices, defined as the percentage of deposited wires from which field-effect mobility is obtained, is approximately 80%.

7.5 Experimental results

7.5.1 Nanowire surface adsorption

Nanowire conductivity at room temperature is known to increase after evacuation of the sample space following mounting of devices [88],[196]. We find that room temperature evacuation also strongly affects gate traces obtained at low temperature (Figure 7.2a). Comparing gate traces with short and long sample space evacuation prior to cool down, we find a steeper increase of conductance with gate voltage after long evacuation. While after long device evacuation hysteresis, defined as the difference in threshold voltage between traces with forward and reverse sweep direction, is still present, its extent is reduced. Considering a number of devices on the same measurement chip, shown in Figure 7.2b, we find almost a doubling of the extracted mobility after long sample evacuation. The exposure of samples to air after long evacuation results in a reduction of extracted mobility and increased hysteresis (Figure 7.2c and Figure 7.2e). Note that not only a reduction of the hysteresis, but also a shift of the threshold voltage towards more negative values after long evacuation is observed (Figure 7.2d). The transconductance is larger when sweeping to more positive gate voltages (forward sweep direction) then when sweeping to more negative gate voltages (reverse sweep direction), leading to $\mu_f > \mu_r$ (Figure 7.2c). Both mobilities are reported here, as well as the average mobility of the two sweep directions, μ_{avg}. It is currently not understood why mobility is sweep direction dependent.

A hysteresis in gate traces that is dependent on ambient conditions has been studied before in carbon nanotube [197] and Ge [198] and ZnO [199] nanowire FETs. By varying the humidity level in the sample space [197] and by x-ray photoelectron spectroscopy [198] the hysteresis was attributed to the adsorption of water onto the nanostructure and onto the SiO_2 substrate. Evacuation of the sample environment leads to desorption of water, thereby reducing the hysteresis. Sample evacuation alone is however insufficient to fully remove the water bound to the SiO_2 substrate. The similarities between our observations and [198] and [197], both in the direction in which the threshold voltage shifts with gate sweep direction, as well as in the reduction of hysteresis with evacuation time and the reversibility of the effect when exposing samples again to air, strongly suggests that molecules adsorbing to the nanowire and/or the SiO_2 substrate also here affect gate traces. These molecules could be water, but InSb nanowires have also shown a reduction of conductance in response to acetone and IPA [200]. Moreover, the native oxide on the InSb (110) surface consists of at least 50 % InO_x [201] and In_2O_3 nanowires are sensitive chemical sensors [202].

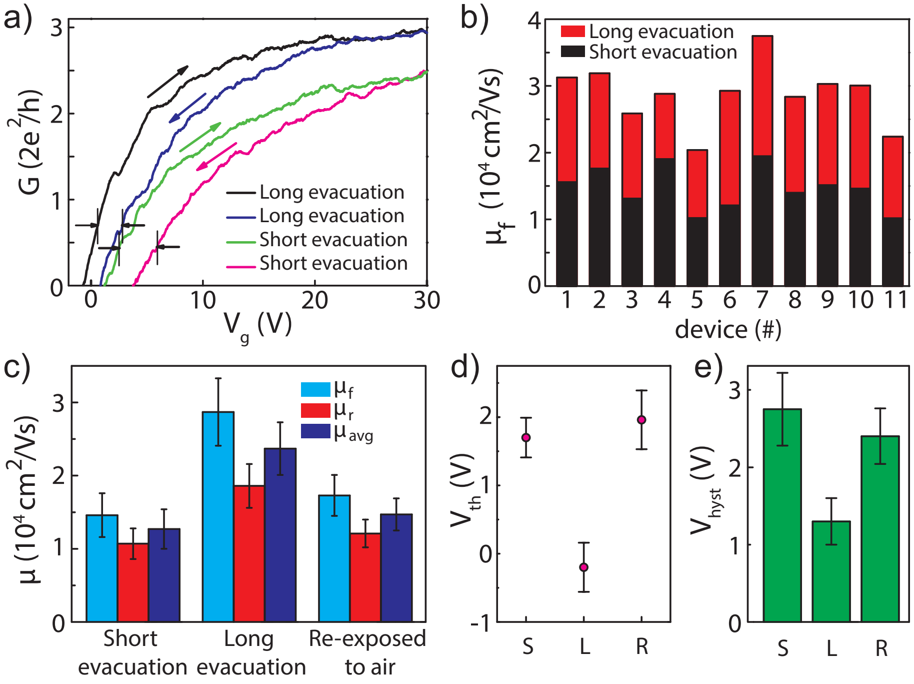

Figure 7.2: a) Gate traces, $G(V_g)$, of samples evacuated for a short or long period of time prior to cool down. Samples are evacuated for ~ 15 minutes (~ 65 hours), giving the green and pink (black and blue) traces for forward and reverse sweep direction respectively. Arrows indicate sweep direction. The same chip with samples is first evacuated only shortly (yielding the data denoted with 'short evacuation'), then evacuated longer ('long evacuation' data), exposed to air for ~ 90 hours and evacuated shortly (~ 15 minutes) again ('re-exposure' data, see panel c). The substrate was cleaned prior to nanowire deposition. Hysteresis of both pairs of gate traces is indicated with arrows and vertical lines. Although the hysteresis is indicated at non-zero G, the hysteresis reported in panel c is extracted from the difference in threshold voltage between gate traces with forward and reverse sweep direction. **b)** Mobility obtained with forward sweep direction, μ_f, of individual devices after short (black) or long (red) device evacuation. **c)** Mobility after short evacuation, long evacuation and re-exposure to air. μ_{avg} is the average of the mobility obtained with forward sweep direction, μ_f, and with reverse sweep direction, μ_r. **d)** Threshold voltage on the forward sweep direction trace, V_{th} after short evacuation (S), long evacuation (L) and re-exposure to air (R). **e)** Hysteresis, V_{hyst}, after short evacuation (S), long evacuation (L) and re-exposure to air (R). The hysteresis is given by the difference in threshold voltage between forward and reverse sweep direction. All values in panel c, d and e are an average, obtained from fits to gate traces of each device on the measurement chip. Error bars in panels c, d and e indicate the standard deviation.

Adsorption occurs by forming ionic or covalent bonds between the adsorbate and adsorbent (chemisorption) or by Van der Waals forces between adsorbate and adsor-

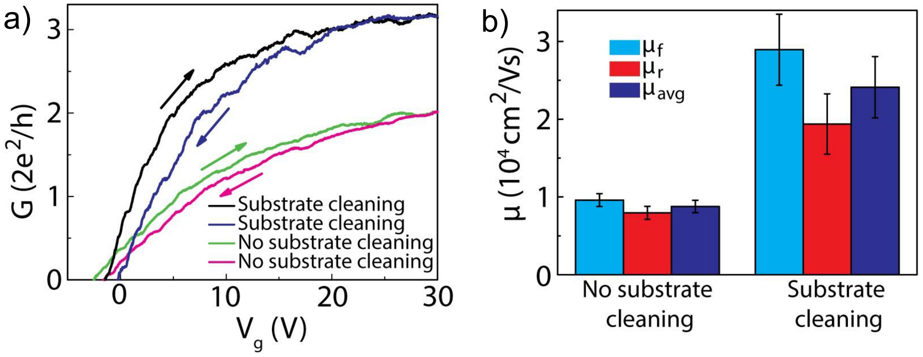

Figure 7.3: a) Gate traces obtained on samples without and with substrate cleaning. Forward and reverse sweep direction are indicated with arrows. Samples have been evacuated for ~ 60 hours before cool down. **b)** Forward, reverse and average mobility with and without substrate cleaning. Values are averages obtained from fits to gate traces of individual devices. Error bars indicate standard deviation.

bent (physisorption) [203],[200]. Chemisorption can act as surface doping when the adsorbate accepts or donates charge. It may therefore change the existing surface states and band bending. Charged physisorbed molecules affect via their field effect the electrostatic potential near the adsorbent surface. Moreover, adsorbed charged or polar molecules can be affected by gating [204]. Water, which physisorbs onto SiO_2, may for instance orient itself under the influence of an electric field. Both physisorption onto the nanowire and the SiO_2 substrate, as well as chemisorption may play a role in our InSb FETs.

While our observations point towards surface adhesion, the mechanism through which it affects mobility is currently not understood. The hysteresis and sweep-direction dependent mobility suggest a trapping mechanism or the presence of an activation barrier that creates an asymmetry between forward and reverse sweep direction. The trapping mechanism has a long response time, as our measurements are taken at low gate sweep rates (~ 120 mV/s) and no dependence on sweep rate (with sweep rates between ~ 3 mV/s and ~ 600 mV/s) was found. However, repeated scans yield the same gate trace, so that between scans emptying of the traps has to take place. As noted above, our observations resemble those of water physisorbed on SiO_2. It is however not understood how alignment of water molecules under influence of an electric field can involve an activation barrier and unclear whether alignment of water molecules can occur at low temperature.

7.5.2 Substrate cleaning

We also find that cleaning of Si/SiO_2 substrates by remote oxygen plasma prior to nanowire deposition results in an enhanced gate dependence of low-temperature

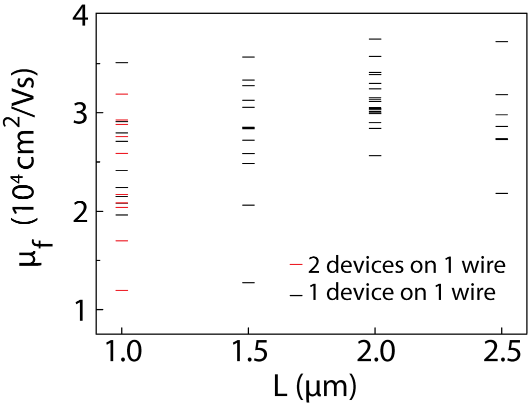

Figure 7.4: Mobility obtained with forward sweep direction, μ_f, as a function of contact spacing, L. Red lines are mobility obtained from long nanowires on which three contacts were placed, resulting in two FETs, while black lines correspond to single FET devices. Mobility obtained from fits to devices from 5 different measurements chips with similar results (see appendix for details). Average mobilities for each contact spacing are $\mu_f(L = 1\ \mu\text{m}) = (24.4 \pm 5.6)\cdot 10^3$ cm^2/Vs, $\mu_f(L = 1.5\ \mu\text{m}) = (27.6 \pm 5.8)\cdot 10^3$ cm^2/Vs, $\mu_f(L = 2\ \mu\text{m}) = (31.4 \pm 2.8)\cdot 10^3$ cm^2/Vs and $\mu_f(L = 2.5\ \mu\text{m}) = (29.1 \pm 4.7)\cdot 10^3$ cm^2/Vs.

conductivity. Figure 7.3a) shows gate traces of individual devices, while Figure 7.3b) shows average extracted mobilities obtained from measurements of ~ 10 FETs with and without substrate cleaning. All other fabrication and measurement steps are the same for both sets of devices. The remote oxygen plasma most probably removes hydrocarbons that remain on the substrates after fabrication of alignment markers or during storage of samples in a polymer-containing environment.

7.5.3 Contact spacing

A correlation between FET contact spacing and extracted field-effect mobility is found (Figure 7.4). Although spread in mobility at a given contact spacing is substantial, an overall increase of extracted mobility is observed when increasing contact spacing. FETs with short (1 μm) contact spacing were fabricated both with long wires, onto which two FETs in series were made, and with short wires. Both long and short wires give similar mobility (see Figure 7.4). The contact spacing dependence is thus a FET property rather than a wire property. A reduced mobility for short contact spacing is expected when transport is (quasi-)ballistic rather than diffusive [205],[203] and could be relevant to our nanowire devices [126]. However, also effects related to the metal contacts are expected to play a larger role in devices with short contact spacing and can possibly explain te observed $\mu(L)$. Possible explanations are that (1) the contacts reduce the capacitance of short devices more than expected on the basis of the Laplace simulations (in which the nanowire is metallic) or (2) electrons are injected from and absorbed over a finite length underneath the contacts, leading to an effective L larger than the contact spacing.

Altogether, applying a long sample evacuation time and cleaning the SiO_2 substrate before wire deposition yields $\mu_{\text{avg}} \approx 25{,}000$ cm^2/Vs for devices with a contact spacing $L = 2$ μm. This mobility is the average value of $\mu_f = 31{,}400$ cm^2/Vs (see Figure 7.4) and $\mu_r = 19{,}300$ cm^2/Vs. These high mobilities result from measurements of ~ 15 devices fabricated in different fabrication runs using the same fabrication recipe. Similar mobilities obtained when repeating this recipe (see also Section 7.8.3) demonstrate the reproducibility of our results.

7.6 Discussion

Three aspects of our findings require discussion: the combination of remote oxygen plasma as a substrate cleaning method and water adsorption, the degree of fulfillment of the diffusive transport requirement in our devices and the interpretation of improved gate response as increased mobility.

Our substrate cleaning method, oxygen plasma treatment, is known to create a hydrophilic surface. While this possibly leads to more surface adsorbents than when using an untreated substrate, we here argue that our results on evacuation duration (Figure 7.2) are not significantly affected by the preceding cleaning. An increase of mobility of similar extent to that reported in Figure 7.2 was observed on devices fabricated on substrates that were not treated with oxygen plasma. Also here a reduction of hysteresis was observed after longer device evacuation. The substrate cleaning is performed prior to nanowire deposition and nanofabrication. The substrate is exposed to polymethyl metacrylate (PMMA), acetone and isopropanol during the lift-off process used to deposited contacts to the nanowire. It has also been exposed to air after substrate cleaning for several days before device evacuation. This processing likely affects the substrate more than the substrate cleaning. The observed increase in mobility after substrate cleaning therefore likely results from a cleaner region between nanowire and dielectric.

Extraction of field-effect mobility requires diffusive transport. We have observed ballistic transport in our wires [126], although with a device geometry and under measurement conditions different from those here. We expect in our wires quasi-ballistic transport conditions with a mean free path of 100-200 nm. To extract field effect mobilites ideally devices with $\frac{L}{l_e} \gg 1$ are used, but InSb nanowires can currently not be grown longer than ~ 3.5 μm. While for channel length of 1 μm ballistic effects may play a role, mobilities obtained from our devices with longer contact spacing are expected to provide a better estimate of field-effect mobility.

Equation (7.5) shows that increased (trans)conductance can result from an increase in μ, but also from an increase of capacitance, C. Our analysis in terms of a fixed C, neglecting changes in capacitance due to adsorption onto the substrate, nanowire surface states or nanowire surface adsorption, leads to the interpretation of increased transconductance as increased field-effect mobility. A circuit analysis of InAs FETs indicates that including a capacitance representing surface states reduces the effective capacitance [206]. Possibly the surface adhesion in our wires reduces the effective capacitance in a similar way, or possible electron traps resulting from surface adsorption may simply shield the gate. An increased gate coupling could lead to the increased $\frac{dG}{dV_g}$ and G after longer sample space evacuation when the density of surface adsorbents is reduced. However, chemisorption affects the charge distribution within the nanowires [203], [204], resulting in changes in conductance and/or carrier concentration [207],[208] and therefore changes in mobility. Also, trapped charges at the surface may act as scattering sites, leading to an increased mobility when their density is reduced. A better understanding of the adsorption mechanism is needed to assess the relative influences of gate coupling and mobility on the conductance.

7.7 Conclusions and outlook

Low temperature mobility of InSb nanowires is extracted from gate traces. The InSb nanowires are free of stacking faults and surface roughness and have diameters of ~ 100 nm. The extracted mobility was increased by sample space evacuation prior to cool down and by substrate cleaning. An increase in mobility with contact spacing was also observed. Altogether field-effect mobilities of ~ 25,000 cm^2/Vs have been obtained.

Surface adhesion has been identified as the process that currently limits mobility. While the accompanying hysteresis has been reduced by sample space evacuation, its working is not understood and it has not been eliminated. A number of follow-up experiments can be envisioned:

- The contribution of the InSb nanowire surface and the SiO_2 substrate to the hysteresis can be distinguished by making devices with the nanowire suspended above a metal gate. Moreover, the composition of the SiO_2 surface after device fabrication can be analyzed by x-ray photoelectron spectroscopy.

- The composition of the InSb surface and its surface states can be determined by x-ray photoelectron spectroscopy (on InSb wafers) or by Auger spectroscopy (on an individual nanowire, [209]).

- To promote desorption from the nanowire or the substrate surface a set-up can be developed in which an already-mounted sample can be heated. For mobility measurements the use of a set-up that allows better evacuation of the sample space is also recommended.

- The reactivity or adhesion capability of the InSb nanowire surface states can be determined by measuring the conductance and hysteresis in InSb nanowires at room temperature in different atmospheres (air, vacuum, humid environment), possibly complemented by Auger spectroscopy or x-ray photoelectron spectroscopy (on InSb wafers).

- The contribution of surface adhesion can be reduced by passivation of the InSb surface. Passivation of devices by atomic hydrogen cleaning [53] or chemical etching, followed by the deposition of a dielectric [210], thereby removing the native oxide and preventing growth of new oxide, may further reduce hysteresis.

- Passivation by growth of a shell of GaSb or AlSb around the InSb nanowire, thereby confining transport to the InSb core, can also be pursued. Growth of GaSb or AlSb is complicated by the difference in lattice constant of these materials to InSb. Instead a combination of InSb core and a II-VI shell material with lattice spacing similar to InSb, such as CdTe, can be pursued. However, if charged molecules adhere to the nanowire, their potential may not be sufficiently screened by a thin shell. The nature of the surface states may also change when the nanowire material that is in contact with air is replaced (for instance GaSb instead of InSb).

- The use of InSb nanowires for gas sensing can also be further investigated.

Futhermore, several suggestions for further research on InSb nanowire mobility not related to surface adsorption can be made:

- The density of gold — and possibly other impurities — in InSb nanowires can be determined by atomic probe tomography measurements [177].

- As an alternative to field-effect measurements in single nanowires, longitudinal and transverse resistivity can be obtained from double nanocrosses (see [66]), resembling a Hall bar. From these resistivities the carrier density and mobility can be extracted (see Chapter 5).

- Concerning the current low temperature experiment a change of contact preparation method can be considered. RF argon plasma etching creates relatively low resistance contacts that facilitate extraction of nanowire mobility, but likely also damages the crystal structure near the contacts, thereby possibly reducing mobility. Ammonium sulfide passivation or possibly thermal annealing of contacts can be an alternative, provided that these methods yield reproducible results.

This work has been done in collaboration with D. J. van Woerkom, O. Gül, D. Car, S. R. Plissard, E. P. A. M. Bakkers and L. P. Kouwenhoven.

7.8 Supplementary data

7.8.1 Overview of devices

1. Evacuation time experiment (fabricated according to the recipe of Section 7.8.2). Mobility was extracted from measurements of 11 devices with contact spacing between 1 and 2 μm. Average contact spacing 1.41 μm. Data reported in Figure 7.2. Long evacuation data is also included in Figure 7.4.

2. FETs without substrate cleaning and with long evacuation. Fabricated according to the recipe in Section 7.8.2, with the exception of the Ar etch, which took place at the described power (100 W), but with 400 V on the sample holder for 150 s. This yields the same amount of etched InSb (~ 70 nm) as etching at 300 V for 300 s. 11 devices, contact spacing of all devices is 2 μm. Data reported in Figure 7.3.

3. FETs fabricated according to the recipe of Section 7.8.2. 13 devices, contact spacing between 1 and 2.5 μm. Average contact spacing 1.73 μm. Data reported in Figure 7.4.

4. FETs with substrate cleaning and with long evacuation. 11 devices, contact spacing between 1 and 2 μm. Average length 1.42 μm. Fabricated according to the recipe in Section 7.8.2, with the exception of the Ar etch, which took place at the described power (100 W), but with 400 V on the sample holder for 150 s. This yields the same amount of etched InSb (~ 70 nm) as etching at 300 V for 300 s. Data reported in Figure 7.3 and Figure 7.4.

5. FETs fabricated according to the recipe of Section 7.8.2, with the addition of a thin layer of perfluorodecyltrichlorosilance (FDTS) deposited onto the devices after fabrication. No improvement of mobility was observed with respect to devices without FDTS. 11 devices, contact spacing between 1 and 2.5 μm. Average contact spacing 1.64 μm. Data reported in Figure 7.4.

6. FETs fabricated according to the recipe of Section 7.8.2, but with substrate oxygen plasma cleaning of 60 s instead of 600 s. After oxygen plasma cleaning a thin layer of FDTS was deposited onto the substrate, after which fabrication proceeded according to the recipe. No improvement of mobility was observed with respect to devices without FDTS and with the usual 600 s cleaning. 10 devices, contact spacing between 1 and 2.5 μm. Average contact spacing 1.85 μm. Data reported in Figure 7.4.

   All parameters extracted from fits to the gate traces of Figure 7.2 are listed in Table 7.1.

	Short evacuation	Long evacuation	Re-exposed to air
μ_f (10^3 cm^2 V^{-1}s^{-1})	14.6 ± 3.0	28.7 ± 4.6	17.3 ± 2.8
μ_r (10^3 cm^2 V^{-1}s^{-1})	10.7 ± 2.1	18.6 ± 3.0	12.1 ± 1.9
μ_{avg} (10^3 cm^2 V^{-1}s^{-1})	12.7 ± 2.7	23.7 ± 3.6	14.7 ± 2.2
V_{th} (V)	1.70 ± 0.29	-0.20 ± 0.36	1.96 ± 0.43
V_{hyst} (V)	2.75 ± 0.47	1.31 ± 0.30	2.40 ± 0.36
R_s ($k\Omega$)	3.7 ± 0.7	3.7 ± 1.0	4.1 ± 1.2

Table 7.1: Mobility, threshold voltages V_{th}, hysteresis, V_{hyst} and series resistances, R_s, extracted from fits to the gate traces of the evacuation time experiment. Mobility is obtained with forward sweep direction, μ_f and reverse sweep direction, μ_r. The average mobility of these two sweep directions, μ_{avg}, is also reported. V_{th} is the threshold voltage obtained from fits to gate traces taken with forward sweep direction. Mobility, threshold voltage and hysteresis are also shown in Figure 7.2c.

7.8.2 Optimized device recipe

Fabrication

- Substrate cleaning: 10 minutes remote oxygen plasma cleaning of the Si/SiO$_2$ substrate with pre-defined markers (oxygen pressure 1 mbar, 600 W). All substrates were from the same wafer.
- Wire deposition: deterministic positioning of wires using a set-up similar to that described in [71]. Wires were always taken from the same section on the same growth chip.
- SEM imaging: of the nanowires with surrounding bitmarkers. Images are used for the subsequent design of the contacts.
- Spin resist: PMMA 950A4 at 4 krpm, baking > 15 minutes at a temperature of 175 °C.
- Electron beam writing of the contact design.
- Development: MIBK:IPA 1:3 60 s, IPA 60 s.
- Ar etching: 3mTorr, Ar flow 50 sccm, 100 W, 300 s, no rotation. A voltage of 300 V is applied to the sample holder.
- Contact deposition: Ti/Au 5/145 nm with deposition rate 2 Å/s.
- Lift-off in acetone: the sample with acetone is heated for several hours and left in acetone for ≥ 12 h.

Storage of devices

Samples were stored in an Ar glove box between fabrication and mounting.

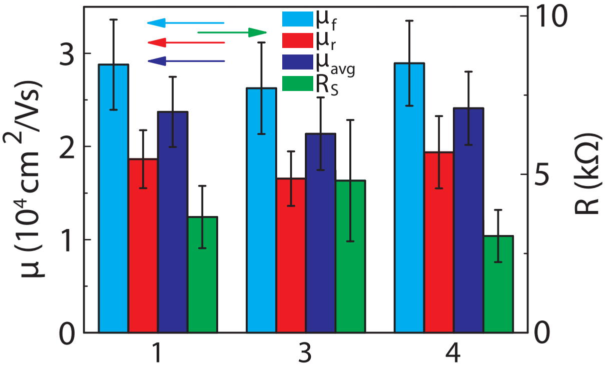

Figure 7.5: Average mobilities obtained with forward and reverse sweep direction. The number under each series of bars corresponds to the entry number in Section 7.8.1. Average mobility is the average of forward and reverse mobility. Results obtained following the optimized recipe described in Section 7.8.2. Both mobility and series resistance obtained in three fabrications runs are very similar.

Measurements

- Evacuate devices for ~ 60 hours after mounting in a dipstick.
- Add exchange gas (5 cm tube), cool down devices.
- Pinch-off traces: 10 mV bias, −6 V to +30 V with sweeping rate 0.2 mV/50 ms. Measure forward and reverse sweep direction.
- Measure sweep rate dependence: voltage steps of 3, 1.5, 0.6, 0.3, 0.15, 15, 30 mV, all per 50 ms, both forward and reverse sweep direction.

No dependence of gate traces on sweep rate was found.

7.8.3 Reproducibility of high-mobility devices

Mobilities similar to those obtained after long device evacuation shown in Figure 7.1c were obtained on repeating the steps outlined in Section 7.8.2 as shown in Figure 7.5. All parameters extracted from fits to the gate traces are listed in Table 7.2.

7.8.4 Comparison of field-effect mobility extraction methods

We compare results of field-effect mobility obtained from fits to conductance traces to field-effect mobility obtained from transconductance of gate traces, the standard method to obtain field-effect mobility in nanowires. The transconductance procedure is explained using the gate trace of Figure 7.6a. Prior to taking a numerical

Batch number	1	3	4
μ_f (10^3 cm^2 V^{-1}s^{-1})	28.7 ± 4.6	26.0 ± 4.7	28.9 ± 4.4
μ_r (10^3 cm^2 V^{-1}s^{-1})	18.6 ± 3.0	16.4 ± 3.0	19.4 ± 3.9
μ_{avg} (10^3 cm^2 V^{-1}s^{-1})	23.7 ± 3.6	21.2 ± 3.8	24.2 ± 3.9
V_{th} (V)	-0.20 ± 0.36	-0.37 ± 0.39	-0.51 ± 0.45
V_{hyst} (V)	1.31 ± 0.30	1.41 ± 0.28	1.14 ± 0.22
R_s ($k\Omega$)	3.7 ± 1.0	4.8 ± 1.8	3.0 ± 0.8

Table 7.2: Mobility, threshold voltage, V_{th}, hysteresis, V_{hyst}, and series resistance, R_s, obtained from fits to the gate traces of three batches of high-mobility devices. Batch number refers to the entry number in Section 7.8.1. Mobility is obtained with forward sweep direction, μ_f and reverse sweep direction, μ_r. The average mobility of these two sweep directions, μ_{avg}, is also reported. V_{th} is the threshold voltage obtained from fits to gate traces taken with forward sweep direction. Mobilities and series resistances are also shown in Figure 7.5.

derivative, a median filter is applied to remove noise on the conductance trace (Figure 7.6b). Conductance fluctuations in the pinch-off trace (indicated with arrows in the inset of Figure 7.6a) strongly affect the transconductance (Figure 7.6c). Averaging over a number of data points (or equivalently, a gate voltage range) is therefore performed. The averaging window was chosen such that the conductance fluctuations, responsible for the rapid decrease of batch average mobility with averaging range at small averaging window in Figure 7.6d, are removed. Field-effect mobility is obtained from transconductance using Equation (7.7).

Next interface resistances, R_s, are taken into account. This is done by subtracting from the measured gate traces a fixed R_s. In Figure 7.6g an example of such a gate traces after subtraction of interface resistances is shown. Subsequently peak transconductance and field-effect mobility are extracted. R_s of each device is increased up to a value at which the peak transconductance no longer occurs near pinch-off, but at high gate voltage. This procedure gives R_s of individual devices between 1.5 kΩ and 4 kΩ, with an average R_s of ~ 3 kΩ. The average field-effect mobility of 11 devices, obtained from traces taken with forward sweep direction, is (27.1 ± 4.2) $\cdot$ 10^3 cm^2/Vs (see Figure 7.6e) compared to (28.7 ± 4.8)$\cdot$ 10^3 cm^2/Vs obtained from a fit to the conductance traces. Both values are within error margin the same. Comparing mobilities of individual devices (Figure 7.6f) we also find that both methods give very similar values. The small difference is likely due to slightly larger interface resistances obtained from the mobility fits, giving an average R_s of 3.7 kΩ.

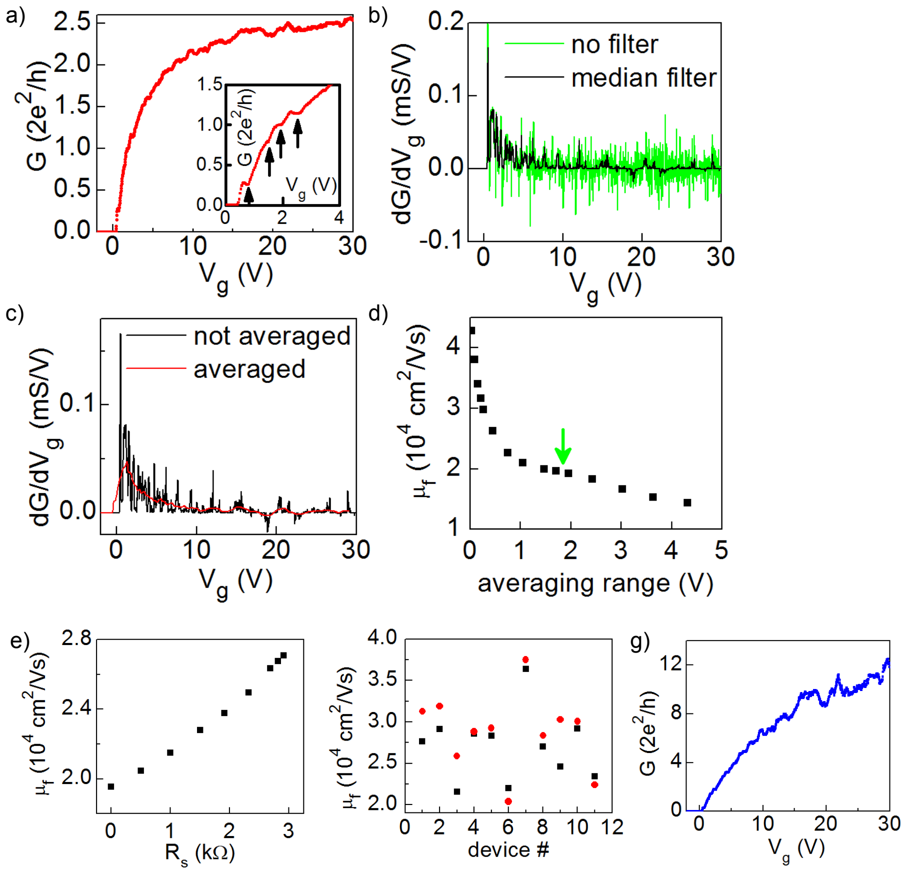

Figure 7.6: a) Conductance, G, as a function of gate voltage, V_g. Inset: Zoom-in of the conductance near pinch-off. The arrows point at reproducible conductance fluctuations. **b)** Transconductance, $\frac{dG}{dV_g}$, of the trace of panel a (green). A median filter is applied to remove random fluctuations in the data. The resulting transconductance is shown in black. **c)** Transconductance, $\frac{dG}{dV_g}$, without (black) and with (red) averaging over 1.8 V gate range. Averaging is applied to remove reproducable conductance fluctuations that lead to peaks and dips in the transconductance. **d)** Peak field-effect mobility obtained from traces with forward sweep direction, μ_f, as a function of gate voltage averaging range. The green arrow denotes the averaging window of 1.8 V chosen in panel c. This averaging window was used in further analysis to obtain peak field-effect mobility. For comparison the long evacuation time data with forward sweep direction of Figure 7.2 is used. Peak field-effect mobility is the average of 11 devices on the same chip. **e)** Peak field-effect mobility, μ_f, as a function of interface resistance, R_s. Peak field-effect mobility is the average of 11 devices on the same chip. **f)** Comparison between field-effect mobility, μ_f, obtained for individual devices using the fit according to Equation (7.8) (red points) and the mobility obtained from peak transconductance (black points). **g)** Conductance as a function of gate voltage after correction for series resistance as done in panel e and f. For this device a series resistance $R_s = 4$ kΩ is assumed. Gate trace is that of the same device as shown in panel a.

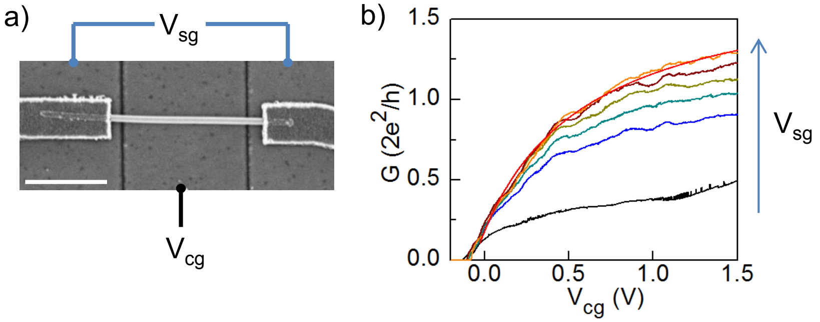

Figure 7.7: a) Scanning electron microscope image of an InSb FET deposited on three gates, allowing independent control over electrochemical potential of the channel near the contacts and the channel away from the contacts. Gates are Ti/Au (5/10 nm) on which Al_2O_3 (30 nm) is deposited by atomic layer deposition. Contacts are Ti/Pd (5/145 nm). The same voltage, V_{sg}, is applied to both side gates. Voltage V_{cg} is applied to the center gate. Scale bar is 1 μm. **b)** Conductance, G, as a function of center gate voltage, V_{cg}, for various V_{sg}. V_{sg} is increased from -0.2 V (black trace) to 0, 0.2, 0.4, 0.8, 1.2 and 2.0 V (orange trace). Capacitances were obtained from a finite element model of the device geometry of panel a. A fit to the data yields a mobility of 30,200 cm^2/Vs.

7.8.5 Local gate devices

Screening of the gate by the contacts may lead to poorly gateable nanowire sections near the contact, especially in nanowires like InSb that do not have a surface accumulation layer. Being fairly resistive, these short resistive sections near the contacts could determine the conductance near pinch-off. This would mean that the effective gated channel is much shorter than the contact spacing (possibly ~ 100-200 nm, the screening length extracted from the inset of Figure 7.1b), and would therefore lead to substantial errors in the extracted field-effect mobility.

To probe the effect of such resistive regions near the contacts we have fabricated devices in which the nanowire regions near the contacts can be gated separately from the channel away from the contacts (Figure 7.7a). Gate traces are obtained by varying the center gate voltage, while stepping the side gates voltages from slightly negative to highly positive values giving the conductance traces shown in Figure 7.7b. While the conductance near pinch-off is not affected by the side gate voltages, the maximum conductance at high center gate voltage increases with increasing side gate voltage. The ineffectiveness of the side gates in changing the pinch-off voltage indicates that the pinch-off takes place in a wire section gated by the center gate. Possibly the screening of the gate in the wire section near the contacts is counteracted by a contact-induced doping of the wire. We extract mobility from a fit to the conductance as a function of the center gate voltage at high side gate voltage (data in orange, fit in red in Figure 7.7b). The center gate width has the role of channel length.

On 4 devices with contact spacing between 1 and 2 μm mobilities of $(20 - 31) \cdot 10^3$ cm^2/Vs were measured. These values are similar to those obtained on devices with global gates (see Figure 7.4), and make it highly unlikely that mobility obtained from our local gate devices and mobility obtained from global gate devices differ substantially. The results obtained here with devices with local gates therefore support the mobilities obtained in Section 7.5.

CHAPTER 8

CONCLUSIONS AND OUTLOOK

This chapter summarizes in Section 8.1 the main findings from the preceding experimental chapters, Chapters 4 – 7, and discusses these in relation to the requirements for nanowire-based Majorana devices in Section 8.2. Section 8.3.1 describes several ideas for further research that are closely related to the research described in Chapters 4 – 7. Section 8.3.2 compares nanowires of different materials for nanowire-based Majorana and helical devices. Lastly, Section 8.3.3 describes the findings and experimental implications of a recent numerical study on the signature of the helical state in conductance measurements.

8.1 Conclusions

The main conclusions that follow from Chapter 4, Chapter 5, Chapter 6 and Chapter 7 are as follows.

- At high magnetic field transport through InSb nanowires shows quantization of conductance, suggesting quasi-ballistic transport conditions in our nanowires. Extrapolation to zero magnetic field yields an energy spacing between the first two subbands of ~ 15 meV.

- Braiding of Majorana fermions requires a small network of crossed nanowires. InSb nanowires can cross each other during growth to create nanocrosses. Transport through a nanocross device has characteristics similar to that of single nanowire device, indicating a high transmission at the nanowire-nanowire junction.

- Weak anti-localization in dual-gated InSb nanowire devices indicates a strong spin-orbit interaction. A spin precession length of 50 – 100 nm, corresponding to a Rashba spin-orbit strength α_R = 0.5 – 1 eV Å and spin-orbit energy E_{SO} = 0.25 – 1 meV, is determined.

- A low-temperature electron field-effect mobility of approximately 25,000 cm^2/Vs has been extracted in InSb nanowires. Nanowire conductance is strongly affected by adhesion of molecules to the nanowire and/or substrate.

8.2 Discussion: the topological gap

Using the device characteristics reported in Chapter 6, namely a spin-orbit energy E_{so} = 0.25 – 1 meV and a mobility of 10,000 cm^2/Vs, an estimate of the topological gap, E_{tg}, in InSb nanowires following Sau *et al.* [26] yields E_{tg} = 0.1 – 1 K. The subsequent increase of mobility to 25,000 cm^2/Vs leads to another approximate doubling of the topological gap. These values exceed largely the temperature of 20 – 50 mK at which experiment take place and are therefore promising for Majorana experiments in InSb-nanowire based devices.

However, while the estimates in [26] are currently the best estimates of the topological gap size, it is unclear to which extent the approximations that are made in the derivation of $E_{tg}(\mu,E_{so})$ reduce the level of accuracy of or introduce errors in the topological gap estimate. Moreover, the topological gap expression is obtained for a single-mode nanowire, and while the same qualitative dependencies are expected for multi-mode wires, quantitative estimates may be different. A certain amount of uncertainty in material requirements for Majorana devices therefore remains. Experiments aimed at controlling Majoranas will reveal whether current material characteristics suffice, but do not necessarily uncover which of the many experimental parameters have to be improved in order to reach a stable topological phase. Moreover, Majorana devices will likely have a layout different from that of the devices in Chapter 6 and Chapter 7 and numbers obtained in devices with one particular design (e.g. a top gated device) may not apply directly to other ones (such as a Majorana device employing fine bottom gates as in Figure 1.2).

Moreover, current experiments could however also be limited by device elements or interactions other than spin-orbit interaction and mobility. There could for instance be imperfections associated with the superconducting contacts, such as a nanowire-superconductor interface that is not sufficiently transparent, poor gating underneath the superconductor or damage to the nanowire created during contact preparation and deposition, resulting in a very disordered region underneath the contacts. The effects of such contact imperfections on the topological gap are not considered in this thesis and are included only to a limited extent (only in the difference between the bulk gap in the superconductor and induced superconducting gap in the semiconductor) in the topological gap estimate in [26].

Concerning the findings in Chapter 7, field-effect mobility, as it is extracted from gate traces, is very sensitive to the hysteresis due to adsorbed species, while measurements to detect or control Majoranas may not suffer from adsorption to the same extent. Although currently no good alternative to field-effect mobility measurements is available, it is therefore unclear whether the current values of mobility provide a good basis to assess the potential of InSb nanowires for Majorana devices in terms of disorder.

8.3 Outlook

8.3.1 Follow-up experimental chapters

The experiment in Chapter 4 studies conductance quantization mainly as a function of magnitude of the applied magnetic field. It could be complemented by measurements of quantization in both an axially and a radially oriented magnetic field. Such angle dependence could shed light on the apparent absence of magnetic depopulation in current measurements. The magnetic field dependence of the energy of subband n, $E_{n,\{\uparrow,\downarrow\}}(B)$ is for constrictions in two-dimensional electron gases with perpendicular magnetic field described by [211]

$$E_{n,\{\uparrow,\downarrow\}} = \left(n + \frac{1}{2}\right)\hbar\sqrt{\omega_0^2 + \omega_c^2} \pm \frac{g\mu_B B}{2} \tag{8.1}$$

in which ω_c describes the electrostatic confinement potential (which is assumed to have a parabolic shape) and $\omega_c = \frac{eB}{m^*}$. ± denotes the two spin orientations. In Figure 4.5 however only the Zeeman term is observed, while a sizeable magnetic field contribution to confinement, $\hbar\omega_c = 7.7$ meV/T, is expected. Furthermore, such measurements possibly resolve an anisotropy of g-factors in quantum point contacts, as obtained recently in quantum point contacts based on AlGaN/GaN heterostructures [212]. Prerequisite for such measurements with the samples reported in Chapter 4 is however that a magnetic field of ~ 5 T can be applied in at least two directions or that the sample holder can be rotated.

Moreover, the observation of quantization of conductance at $B = 0$ can be pursued as this enables other experiments, such as the detection of Majorana signatures in a QPC [213]. Also, the interpretation of measurements in a single-mode regime may be simpler than in a multi-mode regime. Quantization at zero field may occur in existing devices (some degree of quantization at $B = 0$ has been seen in two InSb devices out of the many measured in the Kouwenhoven group), but seems very rare. As mentioned in Chapter 4, in nanowires scattering results more often in backscattering compared to constrictions in planar structures. Therefore the observation of quantized conductances in nanowires is challenging and requires amongst others a device design in which the distance between the constriction and the contacts is minimized. A systematic attempt to obtain conductance quantization may focus on establishing and subsequently reducing the impurity levels in the nanowires (as suggested at the end of Chapter 7 in the context of mobility measurements), optimization of the nanowire-contact interface (at which ideally no reflection takes place and which should therefore be in good contact with the nanowire, but also should not harm the nanowire crystal structure), the growth of a shell around the nanowire to reduce surface scattering, or a numerical study on the effects of the specific gate geometry on the quantum point contact constriction. This topic has been studied in depth in two-dimensional electron gases, but has so far, with the exception of [214], not received any attention for (three-dimensional) nanowires. This is relevant since the quantization only at finite B could result from an imperfect electrostatic potential [215] (for instance a saddle point constriction with too weak transverse confining potential compared to the confining potential along the progation direction). Also, both the electrostatic confinement potential applied to and the charge distribution in nanowires will in general be different from those in quantum wells. In this case it would not be scattering in the nanowire that prevents observation of quantized conductance, but rather the absence of a suitable potential landscape.

InSb nanocrosses could potentially be used to study ballistic transport in a classical regime by measurements of negative bend resistance [216],[217]. Detection of a negative resistance value when measuring resistance between adjacent contacts would indicate a very transparent interface between the nanowires and could at the same time serve as an alternative to quantum point contacts in establishing ballistic transport properties. Detection of such a negative resistance value may however depend on the exact device properties (such as the width of the wires), but could possibly be tuned by either etching during or directly after growth, or by radial (over)growth of wires.

Concerning spin-orbit interaction an experimental comparison of spin-orbit interaction strength in different device geometries can be made, comparing for instance the dual-gated design of Chapter 6 to a device with only a (weak) bottom gate or to devices with side gates. This would provide insight into the role of the external potential on SOI strength and could contribute to optimization of devices used for the detection fo Majorana fermions or helical liquids. The restrictions posed by currently available theoretical models (see next paragraph) should be kept in mind however. Capping InSb nanowires with a semiconductor shell consisting of elements that are not part of the core may lead to strain or interface asymmetry, which could be another way to increase SOI strength [32].

The extraction of spin-orbit strength in an asymmetrically-gated nanowire deserves further theoretical study. The existing expressions for magnetic field dephasing and spin relaxation apply to a nanostructure with uniform charge distribution, while Rashba SOI relies on structural asymmetry, preferably applied by external gates. The largest Rashba SOI strength would therefore be expected in case of strong asymmetric external gating, leading to a skewed charge distribution. Such charge distribution are however not described by existing magnetoconductance expressions, and therefore SOI in such cases can currently not be determined. While analytical expressions are likely hard to obtain, numerical studies of magnetic field and spin dephasing in certain relevant geometries may be possible.

In addition to the recommendation to use material analysis techniques to study nanowire mobility limitations made in Chapter 7, the electrical characterization of nanowires would benefit from development of techniques to infer limiting mechanisms from analysis of transport, e.g. from measurements of conductivity as a function of carrier density, similar to techniques available for two-dimensional systems [218]. Carrier density in nanowires may in this case be extracted from Hall measurements [134],[135]. Alternatively, electrostatic simulations of nanowire devices can be further developed, for instance by incorporating surface effects such as the presence of a native oxide, a surface depletion or accumulation layer and trapped charges (see Section 7.3), in order to obtain realistic nanowire density profiles. Such simulations could possibly be used together with transport models to determine the effects of different sources of scattering (i.e. stacking faults, surface scattering or impurity scattering) on transport characteristics. Lastly, determination of mobility based on longitudinal magnetoconductance [219],[220] (at larger fields than those considered in Chapter 6) could possibly be developed for nanowires and serve as a alternative to field-effect mobility.

8.3.2 Spin-orbit interaction strength and mobility

A comparison of the merits of three (self-assembled) nanowire materials currently considered for Majorana devices, namely InAs, Ge/Si core shells and InSb nanowires, can be made using the results in Section 8.1. Induced superconductivity, essential to Majorana research, has been reported in each of these materials [166],[90],[82]. Comparing InSb and InAs, InSb is the better choice. Mobilities of the best InAs and our InSb nanowires are similar (see Section 7.3), but current reports show a smaller spin-orbit energy in InAs (see Section 6.4.3). In Ge/Si core shell nanowires spin-orbit strengths similar to our InSb nanowires (but with lower spin-orbit strength) have been reported (see Section 6.4.3). Reports of low-temperature mobility in Ge/Si nanowires are rare (only $\mu \sim 800$ cm^2/Vs has been found [221]) and estimations for the mean free path vary significantly, from 35 – 50 nm [221] to ~ 500 nm [89] (reported without extraction of field-effect mobility). The lack of mobility values and thorough quantitative studies of SOI strength in Ge/Si make a comparison to InSb difficult; however, the values of spin-orbit strength currently available certainly encourage further development of Ge/Si-nanowire-based devices. A disadvantage for Majorana studies is the lower g-factor of ~ 1 [222] in Ge/Si nanowires.

The strong spin-orbit interaction in the valence band can be reason to further investigate holes in InSb, both for Majorana devices [26] as well as for spin-orbit qubits [223]. The absence of ohmic contacts for hole transport currently limits our experiments in this direction. The annealing of gold contacts may in this respect be further investigated, as preliminary results show that fairly ohmic contacts to holes can be produced, with currents up to ~ 0.2 μA (see Figure 8.1a-c). Ohmic contacts (see Figure 8.1a) allow estimation of hole mobility (Figure 8.1c), giving a value of ~ 2000 cm^2/Vs. This value is lower than the electron mobility, as expected from comparison of bulk InSb electron (~ 77,000 cm^2/Vs) and hole (~ 850 cm^2/Vs) mobility at room temperature. The fact that an accidental Au annealing already yields a hole mobility at 4.2 K that exceeds the bulk value at room temperature is however encouraging (as after much optimization the electron mobility is still below the bulk room temperature value). Note however that while in bulk InSb the hole are heavy holes, predominantly light holes have been seen in InSb nanowires [223], and therefore a direct comparison of bulk and nanowire mobility may not be possible.

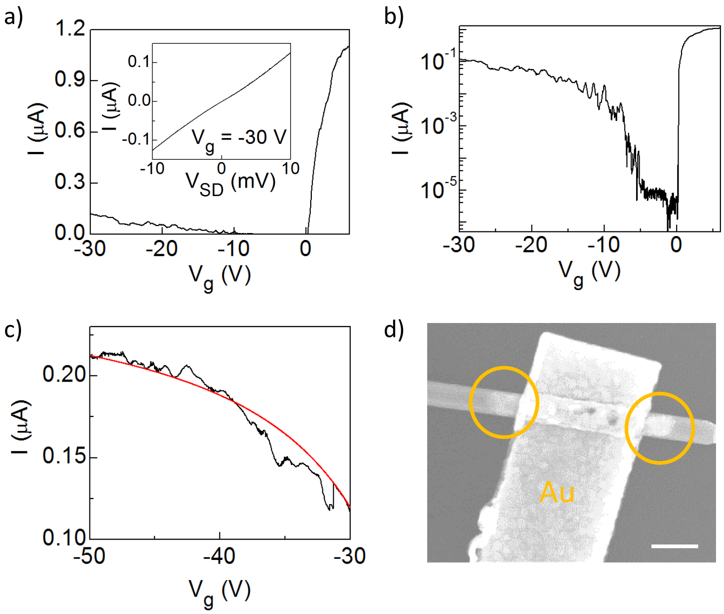

Figure 8.1: Ambipolar transport in an InSb nanowire. Device layout is similar to the FET shown in Figure 7.1b, with a contact spacing of 1.5 μm. **a)** Current, I, as a function of gate voltage, V_g, shows an electron current at positive V_g, and a hole current at negative V_g. Data taken with a source-drain bias, V_{SD}, of 10 mV. Inset: I as a function of source-drain bias at $V_g = -30$ V, showing (near-) Ohmic transport. **b)** The data of panel a with logarithmic y-axis shows the bandgap more clearly. The bandgap of our InSb wires is determined in [223] by measurements of I as a function of source-drain bias, giving ~ 0.2 eV, in agreement with the bulk value. **c)** An estimate of the hole mobility, μ_h, is obtained from the hole current at large negative gate voltage (black curve). The data is well-approximated by mobility expression Equation (7.8) (red) with $\mu_h = 2300$ cm^2/Vs, $C = 43$ aF (see inset of Figure 7.1c), $V_{th} = -25$ V and $R_s = 35$ kΩ. **d)** Scanning electron microscope image of a section of nanowire device similar to the one measured. The device has undergone ~ 5 minutes of annealing at 175 °C under atmospheric conditions. Contacts are Ti/Au 5/145 nm. An RF plasma Ar etch (see Section 7.8.2) has been performed prior to contact deposition. Gold has diffused on (and possibly in) the nanowire over a distance of ~ 100 – 200 nm (indicated by the circles). Scale bar is 200 nm.

After development of reliable ohmic contacts magnetoresistance measurements, similar to Chapter 6, could be performed to asses hole SOI strength. As the size of the topological gap in Majorana experiments depends more strongly on SOI strength than on mobility, it could then be estimated whether an increase in hole SOI strength outweights a possibly lower hole mobility, and therefore favours the use of holes for Majorana experiments. However, it should be considered that the use of InSb holes in Majorana experiments also requires a transparant superconducting interface, which so far has not been shown, and that the hole g-factor ~ 3 [223] is much smaller than that of electrons.

Use of two-dimensional electron gases with strong SOI, such as InAs and InSb quantum wells, can also be considered to create Majorana devices. These materials allow formation of other structures than only (networks of) channels. Moreover, in quantum wells control over the spin-orbit interaction with external potentials and e.g. quantum well width is more advanced than in nanowires [224]. Mobilities in quantum wells exceed those obtained in nanowires by an order of magnitude (in InSb quantum wells for instance mobilities up to ~ 250,000 cm^2/Vs [225] and ~ 400,000 cm^2/Vs [226] have been reached, while recently mobilities up to ~ 300,000 cm^2/Vs have been reported in InAs quantum wells [227]). The high mobility in combination with a strong spin-orbit interaction make these materials especially promising for creation of the (quasi-)helical states described in Section 2.3.1, although it is not known whether these high mobilities can be maintained when defining channels or wires in the quantum well. A first step in investigation could be to make both gate-defined as well as etched channels (as done in [227]) and to study (Hall) mobility as a function of channel width to determine the effects of fabrication as done in [228]. It would also be interesting to use these devices to make a comparison of Hall mobility and field-effect mobility similar to [229].

8.3.3 Detection of a quasi-helical liquid in a Rashba nanowire

A recent numerical study [230] reports on experimental factors that affect the visibility of the helical state described in Section 2.3.1, that occurs when a one-dimensional wire with strong SOI is subjected to a magnetic field perpendicular to the SOI field. Several relevant findings and their implications for detection of a quasi-helical liquid in InSb nanowires devices are here discussed.

Findings

1. The smoothness of the gate potential (that creates a larger carrier density near the leads and results in a single subband in the center of the device, see also Figure 8.2a) strongly influences the visibility of the Zeeman gap. Assuming the condition for optimal visibility of the helical gap, $E_{so} = g\mu_B B$ (see Section 2.3.1), is fulfilled, the optimal value of the characteristic length of this potential profile, λ is approximately $2l_R$ (with $l_R = \frac{\hbar^2}{m\alpha}$ as in Chapter 6). This yields $\lambda \simeq 100$ – 200 nm in our InSb wires. Both a too abrupt and a too smooth gate potential

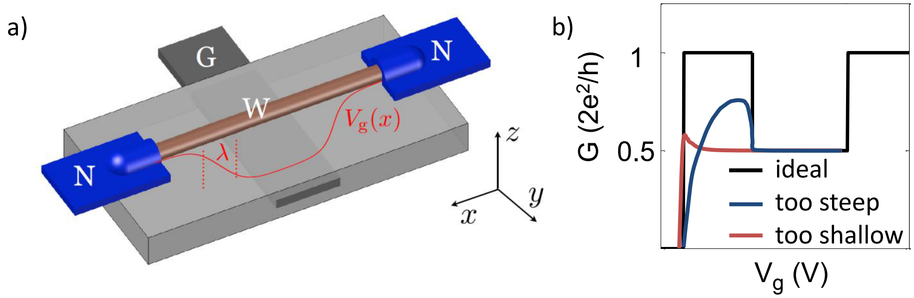

Figure 8.2: a) The experimental set-up considered in a numerical study of the conductance in a Rashba nanowire (brown), connected to normal metal leads (N), in which the electrochemical potential is controlled with a gate (G). The characteristic length over which the gate potential, V_g, changes from the leads to the center of the device is denoted by λ. Figure from [230].**b)** In an ideal set-up conductance would increase in a step-like way from 0 to $\frac{2e^2}{h}$, followed by a half-step back to a conductance of $\frac{2e^2}{h}$ (black lines). Both a too steep (blue) and a too shallow (pink) spatial change of gate potential would yield a reduction of the conductance near pinch-off.

result in a reduction of the conductance in the region where the electrochemical potential is just above the bottom of the lowest subband (see Figure 8.2b), where ideally the conductance equals $\frac{2e^2}{h}$.

2. In a device with a relatively short contact spacing (that does not exceed the lower limit of $4l_R$ much) tunneling across the short one-dimensional constriction increases the conductance in the Zeeman gap above $\frac{e^2}{h}$. The minimum device length is approximately $7\lambda = 14l_R \approx 0.7 - 1.4\ \mu$m[1].

3. Disorder obscures the Zeeman gap, although the gap may be present if the center region is sufficiently clean. The gap can be detected when the mean free path, l_e, is comparable to the device length L (ratio $\frac{L}{l_e} \simeq 1 - 2$). A mean free path of $\sim 0.5\ \mu$m is therefore required in our devices.

4. In the presence of disorder a signature of the helical gap may be observed in measurements of the conductance as a function of the magnetic field. Assuming an initial electrochemical potential above the helical gap, the conductance will reduce once the quasi-helical regime is entered. Furthermore, regular Fabry-Perot oscillations should be observed in this quasi-helical regime, while the non-helical regime (at low B) displays irregular conductance fluctuations. This would however be a more indirect helical signature.

---

[1] This can be deduced from Fig. 7 of [230], in which the conductance in the Zeeman gap is close to the desired value of $\frac{e^2}{h}$. The length L is the length from the middle of the left potential slope (x_0 in Eq. 3 of [230]) to the middle of the right potential slope [231]. While in Fig. 7 $L = 4\lambda$, the remaining parts of the potential slope to the leads add another $\sim 3\lambda$ to the minimum length.

Conclusions

1. The numerical study shows the importance of choosing a correct gate potential. Device design could therefore be preceded by electrostatic simulations to assess the smoothness of several possible gate potentials (such as those resulting from a series of narrow bottom gates or side gates with various shapes).

2. The mean free path in current InSb nanowires is currently likely somewhat too short to measure the helical gap, but might be improved to the meet the required $\sim 0.5\ \mu$m. Steps that could be taken to increase l_e are described in Section 8.3.1 as part of the envisioned steps towards the observation of conductance quantization.

3. The requirement concerning disorder can also be reason to focus on the use of two-dimensional electron gases to create a helical liquid, in which one can likely start with a material with sufficiently long mean free path (see also Section 8.3.2). An alternative approach would be to further increase the SOI strength, which would shorten the length of the device and therefore the required mean free path.

4. The experiment described under 4 may be pursued with current samples (assuming a suitable potential profile). A similar experiment is proposed in [232] from analysis of disorder in a quasi-helical system using a different theoretical approach. The idea here is the following: in an ideal helical system, in which modes with opposite direction of propagation have opposite spin, backscattering cannot take place as it requires a spin flip. By creating a quasi-helical state with a magnetic field a component with the same spin orientation exists in both forward and the backwards mode, and this component increases with magnetic field. The backscattering probability therefore increases as the magnetic field increases. As a function of magnetic field one starts out at $B = 0$ in a more disordered system, that becomes less disordered once the helical gap opens, and becomes more disordered again due to increasing backscattering. Conductance measurements as a function of gate voltage and axial magnetic field could be performed. Signatures of helical state would be regular Fabry-Perot resonances in the helical gap [230], as well as a higher (trans)conductance or different (reproducable) conductance fluctuations in the helical regime compared to both the low and high B regime [232].

Bibliography

1. Nielsen, M. A. & Chuang, I. L. *Quantum computation and quantum information* (Cambridge University Press, 2000).
2. Ladd, T. D. *et al.* Quantum computers. *Nature* **464,** 45–53 (2010).
3. DiVincenzo, D. P. The Physical Implementation of Quantum Computation. *Fortschritte der Physik* **48,** 771–783 (2000).
4. Yang, W., Wang, Z.-Y. & Liu, R.-B. Preserving qubit coherence by dynamical decoupling. *Frontiers of Physics* **6,** 2–14 (2010).
5. Devitt, S. J., Munro, W. J. & Nemoto, K. Quantum error correction for beginners. *Reports on progress in physics. Physical Society* **76,** 076001 (2013).
6. Sarma, S. D., Freedman, M. & Nayak, C. Topological Quantum Computation. *Physics Today* **59,** 32 (2006).
7. Stern, A. & Lindner, N. H. Topological quantum computation–from basic concepts to first experiments. *Science* **339,** 1179–84 (2013).
8. Stern, A. Non-Abelian states of matter. *Nature* **464,** 187–93 (2010).
9. Pachos, J. K. *Introduction to topological quantum computation* (2010).
10. Kitaev, A. Y. Fault-tolerant quantum computation by anyons. *Annals of Physics* **303,** 2–30 (2003).
11. Majorana, E. Teoria simmetrica dell'elettrone e del positrone. *Il Nuovo Cimento* **14,** 171–184 (1937).
12. Wilczek, F. Majorana returns. *Nature Physics* **5,** 614–618 (2009).
13. Fu, L. & Kane, C. Superconducting Proximity Effect and Majorana Fermions at the Surface of a Topological Insulator. *Physical Review Letters* **100,** 096407 (2008).
14. Alicea, J. New directions in the pursuit of Majorana fermions in solid state systems. *Reports on Progress in Physics* **75** (2012).
15. Leijnse, M. & Flensberg, K. Introduction to topological superconductivity and Majorana fermions. *Semiconductor Science and Technology* **27,** 124003 (2012).
16. Ivanov, D. A. Non-Abelian Statistics of Half-Quantum Vortices in p-Wave Superconductors. *Physical Review Letters* **86,** 268–271 (2001).

17. Mourik, V. *et al.* Signatures of Majorana Fermions in Hybrid Superconductor-Semiconductor Nanowire Devices. *Science* **336,** 1003–1007 (2012).
18. Oreg, Y., Refael, G. & von Oppen, F. Helical Liquids and Majorana Bound States in Quantum Wires. *Physical Review Letters* **105,** 177002 (2010).
19. Lutchyn, R. M., Sau, J. D. & Das Sarma, S. Majorana Fermions and a Topological Phase Transition in Semiconductor-Superconductor Heterostructures. *Physical Review Letters* **105,** 077001 (2010).
20. Kitaev, A. Y. Unpaired Majorana fermions in quantum wires. *Physics-Uspekhi* **44,** 131–136 (2001).
21. Alicea, J., Oreg, Y., Refael, G., von Oppen, F. & Fisher, M. P. A. Non-Abelian statistics and topological quantum information processing in 1D wire networks. *Nature Physics* **7,** 412–417 (2011).
22. Hassler, F. Notes on Majorana fermion in nanowires (2010).
23. Lutchyn, R. M., Stanescu, T. D. & Das Sarma, S. Search for Majorana fermions in multiband semiconducting nanowires. *Physical Review Letters* **106,** 127001 (2011).
24. Hyart, T. *et al.* Flux-controlled quantum computation with Majorana fermions. *Physical Review B* **88,** 035121 (2013).
25. Potter, A. C. & Lee, P. A. Engineering a p+ip superconductor: Comparison of topological insulator and Rashba spin-orbit-coupled materials. *Physical Review B* **83,** 184520 (2011).
26. Sau, J. D., Tewari, S. & Das Sarma, S. Experimental and materials considerations for the topological superconducting state in electron- and hole-doped semiconductors: Searching for non-Abelian Majorana modes in 1D nanowires and 2D heterostructures. *Physical Review B* **85,** 064512 (2012).
27. Ihn, T. *Semiconductor nanostructures* (Oxford University Press, 2010).
28. Van Wees, B. *et al.* Quantized conductance of point contacts in a two-dimensional electron gas. *Physical Review Letters* **60,** 848–850 (1988).
29. Wharam, D. A. *et al.* One-dimensional transport and the quantisation of the ballistic resistance. *Journal of Physics C: Solid State Physics* **21,** L209–L214 (1988).
30. Pershin, Y., Nesteroff, J. & Privman, V. Effect of spin-orbit interaction and in-plane magnetic field on the conductance of a quasi-one-dimensional system. *Physical Review B* **69,** 121306 (2004).
31. Winkler, R. *Spin–Orbit Coupling Effects in Two-Dimensional Electron and Hole Systems* (Springer Berlin Heidelberg, Berlin, Heidelberg, 2003).
32. Wu, M., Jiang, J. & Weng, M. Spin dynamics in semiconductors. *Physics Reports* **493,** 61–236 (2010).
33. Fabian, J., Matos-Abiague, A, Ertler, C., Stano, P. & Zutic, I. Semiconductor Spintronics. *Acta Phys. Slov.* (2007).

34. Nitta, J., Akazaki, T., Takayanagi, H. & Enoki, T. Gate Control of Spin-Orbit Interaction in an Inverted In0.53Ga0.47As/In0.52Al0.48As Heterostructure. *Physical Review Letters* **78,** 1335–1338 (1997).
35. Engels, G., Lange, J., Schäpers, T. & Lüth, H. Experimental and theoretical approach to spin splitting in modulation-doped InxGa1-xAs/InP quantum wells for B to 0. *Physical Review B* **55,** R1958–R1961 (1997).
36. Koga, T., Nitta, J., Akazaki, T. & Takayanagi, H. Rashba Spin-Orbit Coupling Probed by the Weak Antilocalization Analysis in InAlAs/InGaAs/InAlAs Quantum Wells as a Function of Quantum Well Asymmetry. *Physical Review Letters* **89,** 046801 (2002).
37. Datta, S. & Das, B. Electronic analog of the electro-optic modulator. *Applied Physics Letters* **56,** 665 (1990).
38. Žutić, I.; Fabian, J.; Das Sarma, S. Spintronics: Fundamentals and applications. *Rev. Mod. Phys.* 323–410 (2004).
39. Schäpers, T. *et al.* Suppression of weak antilocalization in GaInAs/InP narrow quantum wires. *Physical Review B* **74,** 081301 (2006).
40. Kiselev, A. & Kim, K. Progressive suppression of spin relaxation in two-dimensional channels of finite width. *Physical Review B* **61,** 13115–13120 (2000).
41. Kettemann, S. Dimensional Control of Antilocalization and Spin Relaxation in Quantum Wires. *Physical Review Letters* **98,** 176808 (2007).
42. Aleiner, I. & Fal'ko, V. Spin-Orbit Coupling Effects on Quantum Transport in Lateral Semiconductor Dots. *Physical Review Letters* **87,** 256801 (2001).
43. Kunihashi, Y., Kohda, M. & Nitta, J. Enhancement of Spin Lifetime in Gate-Fitted InGaAs Narrow Wires. *Physical Review Letters* **102,** 226601 (2009).
44. Roulleau, P. *et al.* Suppression of weak antilocalization in InAs nanowires. *Physical Review B* **81,** 155449 (2010).
45. Schäpers, T. *Nanotechnology. Volume 3: Information Technology I.* (Verlag, Wiley-VCH GmbH & Co. KGaA, Weinheim, Germany, 2008).
46. Harmans, C. J. P. M. *Lecture notes mesoscopic physics - an introduction* (2003).
47. Chakravarty, S. & Schmid, A. Weak localization: The quasiclassical theory of electrons in a random potential. *Physics Reports* **140,** 193–236 (1986).
48. Beenakker, C. & van Houten, H. Boundary scattering and weak localization of electrons in a magnetic field. *Physical Review B* **38,** 3232–3240 (1988).
49. Bergmann, G. Weak anti-localization-An experimental proof for the destructive interference of rotated spin. *Solid State Communications* **42,** 815–817 (1982).
50. Zaitsev, O., Frustaglia, D. & Richter, K. Semiclassical theory of weak antilocalization and spin relaxation in ballistic quantum dots. *Physical Review B* **72,** 155325 (2005).

51. Kurdak, c., Chang, A., Chin, A. & Chang, T. Quantum interference effects and spin-orbit interaction in quasi-one-dimensional wires and rings. *Physical Review B* **46,** 6846–6856 (1992).
52. Thelander, C. *et al.* Nanowire-based one-dimensional electronics. *Materials Today* **9,** 28–35 (2006).
53. Hjort, M. *III-V nanowire surfaces* PhD thesis (Lund University, 2014).
54. Hillerich, K. *Influence of seed particle material, preparation, and dynamics on nanowire growth* PhD thesis (Lund University, 2013).
55. Martensson, T. *Semiconductor nanowires: epitaxy and applications* PhD thesis (Lund Unversity, 2008).
56. Wang, J. *Controlling nanowire growth direction* PhD thesis (Eindhoven University of Technology, 2014).
57. Caroff, P. *et al.* High-quality InAs/InSb nanowire heterostructures grown by metal-organic vapor-phase epitaxy. *Small* **4,** 878–82 (2008).
58. Caroff, P. *et al.* InSb heterostructure nanowires: MOVPE growth under extreme lattice mismatch. *Nanotechnology* **20,** 495606 (2009).
59. Plissard, S. R. *et al.* From InSb nanowires to nanocubes: looking for the sweet spot. *Nano Letters* **12,** 1794–8 (2012).
60. Lugani, L. *et al.* Modeling of InAs/InSb nanowires grown by Au-assisted chemical beam epitaxy. *Nanotechnology* **23** (2012).
61. Vogel, A. T. *et al.* Fabrication of High-Quality InSb Nanowire Arrays by Chemical Beam Epitaxy. *Crystal Growth & Design* **11,** 1896–1900 (2011).
62. Wang, Y. *et al.* Field effect transistor based on single crystalline InSb nanowire. *Journal of Materials Chemistry* **21,** 2459 (2011).
63. Khan, M. I. *et al.* Electrochemical Growth of InSb Nanowires and Report of a Single Nanowire Field Effect Transistor. *Journal of Nanoelectronics and Optoelectronics* **3,** 199–202 (2008).
64. Mingo, N. Thermoelectric figure of merit and maximum power factor in III-V semiconductor nanowires. *Applied Physics Letters* **84,** 2652 (2004).
65. Borg, M. *Antimonide heterostructure nanowires* PhD thesis (Lund Univeristy, 2012).
66. Car, D., Wang, J., Verheijen, M. A., Bakkers, E. P. A. M. & Plissard, S. R. Rationally Designed Single-Crystalline Nanowire Networks. *Advanced Materials* **26,** 4875–4879 (2014).
67. Wang, J. *et al.* Reversible switching of InP nanowire growth direction by catalyst engineering. *Nano Letters* **13,** 3802–6 (2013).
68. Spicer, W. E. Surface and interface states on GaAs(110): Effects of atomic and electronic rearrangements. *Journal of Vacuum Science and Technology* **14,** 885 (1977).

69. Gobeli, G. & Allen, F. Photoelectric Properties of Cleaved GaAs, GaSb, InAs, and InSb Surfaces; Comparison with Si and Ge. *Physical Review* **137,** A245–A254 (1965).
70. Ritz, A. Determination of space charge layer parameters on InSb(110) by electron energy loss spectroscopy. *Journal of Vacuum Science & Technology B: Microelectronics and Nanometer Structures* **3,** 1153 (1985).
71. Flöhr, K. *et al.* Manipulating InAs nanowires with submicrometer precision. *The Review of Scientific Instruments* **82,** 113705 (2011).
72. Suyatin, D. B., Thelander, C, Björk, M. T., Maximov, I & Samuelson, L. Sulfur passivation for ohmic contact formation to InAs nanowires. *Nanotechnology* **18,** 105307 (2007).
73. Sourribes, M. J. L., Isakov, I., Panfilova, M. & Warburton, P. A. Minimization of the contact resistance between InAs nanowires and metallic contacts. *Nanotechnology* **24** (2013).
74. Van Tilburg, J. *Electron spins in nanowire quantum dots* PhD thesis (Delft University of Technology, 2010).
75. Eeltink, D. *Electrostatic simulation of nanowire devices* MSc thesis (Delft University of Technology, 2013).
76. Mao, L., Gong, M., Dumitrescu, E, Tewari, S. & Zhang, C. Hole-doped semiconductor nanowire on top of an s-wave superconductor: a new and experimentally accessible system for Majorana fermions. *Physical Review Letters* **108,** 177001 (2012).
77. Streda, P & Seba, P. Antisymmetric spin filtering in one-dimensional electron systems with uniform spin-orbit coupling. *Physical Review Letters* **90,** 256601 (2003).
78. Kloeffel, C., Trif, M. & Loss, D. Strong spin-orbit interaction and helical hole states in Ge/Si nanowires. *Physical Review B* **84,** 195314 (2011).
79. Quay, C. H. L. *et al.* Observation of a one-dimensional spin-orbit gap in a quantum wire. *Nature Physics* **6,** 336–339 (2010).
80. Bratkovsky, A. M. Spintronic effects in metallic, semiconductor, metal-oxide and metal-semiconductor heterostructures. *Reports on Progress in Physics* **71,** 026502 (2008).
81. Nadj-Perge, S. *et al.* Spectroscopy of Spin-Orbit Quantum Bits in Indium Antimonide Nanowires. *Physical Review Letters* **108** (2012).
82. Nilsson, H. a., Samuelsson, P, Caroff, P & Xu, H. Q. Supercurrent and multiple Andreev reflections in an InSb nanowire Josephson junction. *Nano Letters* **12,** 228–33 (2012).
83. Potter, A. C. & Lee, P. A. Multichannel generalization of Kitaev's Majorana end states and a practical route to realize them in thin films. *Physical Review Letters* **105,** 227003 (2010).

84. Stanescu, T. D., Lutchyn, R. M. & Das Sarma, S. Majorana fermions in semiconductor nanowires. *Physical Review B* **84,** 144522 (2011).

85. Potter, A. & Lee, P. Majorana end states in multiband microstructures with Rashba spin-orbit coupling. *Physical Review B* **83** (2011).

86. Brouwer, P. W.; Dückheim, M., Romito A., Von Oppen, F. Topological superconducting phases in disordered quantum wires with strong spin-orbit coupling. *Physical Review B* **84** (2011).

87. Shtrikman, H., Popovitz-Biro, R., Kretinin, A. V. & Kacman, P. GaAs and InAs Nanowires for Ballistic Transport. *IEEE Journal of Selected Topics in Quantum Electronics* **17,** 922–934 (2011).

88. Kretinin, A. V., Popovitz-Biro, R., Mahalu, D. & Shtrikman, H. Multimode Fabry-Perot conductance oscillations in suspended stacking-faults-free InAs nanowires. *Nano Letters* **10,** 3439–3445 (2010).

89. Lu, W., Xiang, J., Timko, B. P., Wu, Y. & Lieber, C. M. One-dimensional hole gas in germanium/silicon nanowire heterostructures. *Proceedings of the National Academy of Sciences of the United States of America* **102,** 10046–10051 (2005).

90. Xiang, J., Vidan, A, Tinkham, M, Westervelt, R. M. & Lieber, C. M. Ge/Si nanowire mesoscopic Josephson junctions. *Nature Nanotechnology* **1,** 208–213 (2006).

91. Ford, A. C., Kumar, S. B., Kapadia, R., Guo, J. & Javey, A. Observation of degenerate one-dimensional sub-bands in cylindrical InAs nanowires. *Nano Letters* **12,** 1340–3 (2012).

92. Zhuo, X.; Dayeh, S. A.; Aplin, D.; Wang, D.; Yu, E. T. Direct observation of ballistic and drift carrier transport regimes in InAs nanowires. *Applied Physics Letters,* 89, 053113 (2006).

93. Doh, Y. J., Roest, A. L., Bakkers, E. P. A. M., De Franceschi, S & Kouwenhoven, L. P. Quantum Interference Effects in InAs Semiconductor Nanowires. *Journal of the Korean Physical Society* **54,** 135–139– (2009).

94. Thelander, C. *et al.* Electron transport in InAs nanowires and heterostructure nanowire devices. *Solid State Communications* **131,** 573–579 (2004).

95. Hansen, A., Björk, M., Fasth, C., Thelander, C. & Samuelson, L. Spin relaxation in InAs nanowires studied by tunable weak antilocalization. *Physical Review B* **71** (2005).

96. Kouwenhoven, L. P. *et al.* Nonlinear conductance of quantum point contacts. *Phys. Rev. B,* 39, 8040 (1989).

97. Patel, N. K. *et al.* Properties of a ballistic quasi-one-dimensional constriction in a parallel high magnetic field. *Physical Review B,* 44, 10973 (1991).

98. Glazman, L. I., Khaetskii, A. V. Nonlinear quantum conductance of a point contact. *JETP Lett.* 48, 591–595 (1988).

99. Csonka, S *et al.* Giant fluctuations and gate control of the g-factor in InAs nanowire quantum dots. *Nano Letters* **8,** 3932–3935 (2008).
100. Nilsson, H. A. *et al.* Giant, level-dependent g factors in InSb nanowire quantum dots. *Nano Letters* **9,** 3151–3156 (2009).
101. Thomas, K. J.; Nicholls, J. T.; Simmons, M. Y.; Pepper, M.; Mace, D. R.; Ritchie, D. A. Possible Spin Polarization in a One-Dimensional Electron Gas. *Physical Review Letters,* 77, 135 (1996).
102. Cronenwett, S. M. *et al.* Low-temperature fate of the 0.7 structure in a point contact: a Kondo-like correlated state in an open system. *Physical Review Letters* **88,** 226805 (2002).
103. Frolov, S. M., Venkatesan, A, Yu, W, Folk, J. A. & Wegscheider, W. Electrical generation of pure spin currents in a two-dimensional electron gas. *Physical Review Letters* **102,** 116802 (2009).
104. Daneshvar, A. J.; Ford, C. J. B.; Hamilton, A. R.; Simmons, M. Y.; Pepper, M.; Ritchie, D. A. Enhanced g factors of a one-dimensional hole gas with quantized conductance. *Phys. Rev. B,* 55, 20 (1997).
105. Graham, A. C. *et al.* Interaction effects at crossings of spin-polarized one-dimensional subbands. *Physical Review Letters* **91,** 136404 (2003).
106. Berggren, K., Thornton, T., Newson, D. & Pepper, M. Magnetic Depopulation of 1D Subbands in a Narrow 2D Electron Gas in a GaAs:AlGaAs Heterojunction. *Physical Review Letters* **57,** 1769–1772 (1986).
107. Wharam, D. *et al.* Empirical relation between gate voltage and electrostatic potential in the one-dimensional electron gas of a split-gate device. *Physical Review B* **39,** 6283–6286 (1989).
108. Tekman, E. & Ciraci, S. Novel features of quantum conduction in a constriction. *Physical Review B* **39,** 8772–8775 (1989).
109. Chuang, S. *et al.* Ballistic InAs nanowire transistors. *Nano Letters* **13,** 555–8 (2013).
110. Das, A. *et al.* Zero-bias peaks and splitting in an Al-InAs nanowire topological superconductor as a signature of Majorana fermions. *Nature Physics* **8,** 887–895 (2012).
111. Deng, M. T. *et al.* Anomalous zero-bias conductance peak in a Nb-InSb nanowire-Nb hybrid device. *Nano Letters* **12,** 6414–9 (2012).
112. Freedman, M., Kitaev, A., Larsen, M. & Wang, Z. Topological quantum computation. *Bulletin Ameriscan Mathematical Society* **40,** 31–38 (2003).
113. Nayak, C., Simon S. H., Stern A. Freedman, M., Das Sarma, S. Non-Abelian anyons and topological quantum computation. *Rev. Mod. Phys. 80,* 1083–1159 (2008).

114. Van Heck, B, Akhmerov, A. R., Hassler, F, Burrello, M & Beenakker, C. W. J. Coulomb-assisted braiding of Majorana fermions in a Josephson junction array. *New Journal of Physics* **14,** 035019 (2012).
115. Algra, R. E. *et al.* Twinning superlattices in indium phosphide nanowires. *Nature* **456,** 369–372 (2008).
116. Wen, C.-Y. *et al.* Periodically changing morphology of the growth interface in Si, Ge, and GaP nanowires. *Physical Review Letters* **107,** 025503 (2011).
117. Glas, F., Harmand, J.-C. & Patriarche, G. Why does wurtzite form in nanowires of III-V zinc blende semiconductors? *Physical Review Letters* **99,** 146101 (2007).
118. Dick, K. A. *et al.* Synthesis of branched 'nanotrees' by controlled seeding of multiple branching events. *Nature Materials* **3,** 380–384 (2004).
119. Yun, S. H., Wu, J. Z., Dibos, A., Zou, X. & Karlsson, U. O. Self-assembled boron nanowire Y-junctions. *Nano Letters* **6,** 385–389 (2006).
120. Jiang, X. *et al.* Rational growth of branched nanowire heterostructures with synthetically encoded properties and function. *Proceedings of the National Academy of Sciences of the United States of America* **108,** 12212–12216 (2011).
121. Manna, L., Milliron, D. J., Meisel, A., Scher, E. C. & Alivisatos, A. P. Controlled growth of tetrapod-branched inorganic nanocrystals. *Nature Materials* **2,** 382–385 (2003).
122. Dai, X *et al.* Tailoring the Vapor-Liquid-Solid Growth toward the Self-Assembly of GaAs Nanowire Junctions. *Nano Letters* **11,** 4947–4952 (2011).
123. Suyatin, D. B. *et al.* Electrical properties of self-assembled branched InAs nanowire junctions. *Nano Letters* **8,** 1100–1104 (2008).
124. Dalacu, D., Kam, A., Austing, D. G. & Poole, P. J. Droplet dynamics in controlled InAs nanowire interconnections. *Nano Letters* **13,** 2676–81 (2013).
125. Wagner, R. S. & Ellis, W. C. Vapor-Liquid-Solid Mechanism of Single Crystal Growth. *Applied Physics Letters* **4,** 89 (1964).
126. Van Weperen, I., Plissard, S. R., Bakkers, E. P. a. M., Frolov, S. M. & Kouwenhoven, L. P. Quantized conductance in an InSb nanowire. *Nano Letters* **13,** 387–91 (2013).
127. Li, D. *et al.* Direction-Specific Interactions Control Crystal Growth by Oriented Attachment. *Science* **336,** 1014–1018 (2012).
128. Borgström, M. T. *et al.* In situ etching for total control over axial and radial nanowire growth. *Nano Research* **3,** 264–270 (2010).
129. Kautz, R. & Martinis, J. Noise-affected I-V curves in small hysteretic Josephson junctions. *Physical Review B* **42,** 9903–9937 (1990).
130. Courtois, H, Meschke, M, Peltonen, J. T. & Pekola, J. P. Origin of hysteresis in a proximity josephson junction. *Physical Review Letters* **101,** 067002 (2008).

131. Fiske, M. D. Temperature and Magnetic Field Dependences of the Josephson Tunneling Current. *Rev. Mod. Phys. 36,* 221–222 (1964).

132. Coon, D. D. & Fiske, M. D. Josephson ac and Step Structure in the Supercurrent Tunneling Characteristic. *Physical Review* **138,** A744–A746 (1965).

133. Dayeh, S. A. *et al.* High electron mobility InAs nanowire field-effect transistors. *Small* **3,** 326–332 (2007).

134. Storm, K. *et al.* Spatially resolved Hall effect measurement in a single semiconductor nanowire. *Nature Nanotechnology* **7,** 718–722 (2012).

135. Blomers, C. *et al.* Hall effect measurements on InAs nanowires. *Applied Physics Letters* **101,** 152106 (2012).

136. Datta, S. *Electronic Transport in Mesoscopic Systems* (Cambridge University Press, Cambridge, 1995).

137. Schliemann, J., Egues, J. & Loss, D. Nonballistic Spin-Field-Effect Transistor. *Physical Review Letters* **90,** 146801 (2003).

138. Kunihashi, Y. *et al.* Proposal of spin complementary field effect transistor. *Applied Physics Letters* **100,** 113502 (2012).

139. Cartoixa, X., Ting, D. Z.-Y. & Chang, Y.-C. A resonant spin lifetime transistor. *Applied Physics Letters* **83,** 1462 (2003).

140. Kloeffel, C. & Loss, D. Prospects for Spin-Based Quantum Computing in Quantum Dots. *Annual Review of Condensed Matter Physics* **4,** 51–81 (2013).

141. Frolov, S. M., Plissard, S. R., Nadj-Perge, S., Kouwenhoven, L. P. & Bakkers, E. P. Quantum computing based on semiconductor nanowires. *MRS Bulletin* **38,** 809–815 (2013).

142. Anderson, P., Abrahams, E. & Ramakrishnan, T. Possible Explanation of Nonlinear Conductivity in Thin-Film Metal Wires. *Physical Review Letters* **43,** 718–720 (1979).

143. Bergmann, G. Weak localization in thin films: a time-of-flight experiment with conduction electrons. *Physics Reports* **107,** 1–58 (1984).

144. Hikami, S., Larkin, A. I. & Nagaoka, Y. Spin-Orbit Interaction and Magnetoresistance in the Two Dimensional Random System. *Progress of Theoretical Physics* **63,** 707–710 (1980).

145. Iordanskii, S. V., Lyanda-Geller, Y. B. & Pikus, G. E. Weak localisation in quantum wells with spin-orbit interaction. *JETP Letters* **60,** 206–211 (1994).

146. Altshuler, B., Khmel'nitzkii, D., Larkin, A. & Lee, P. Magnetoresistance and Hall effect in a disordered two-dimensional electron gas. *Physical Review B* **22,** 5142–5153 (1980).

147. Al'tshuler, B. L. & Aronov, A. G. No Title. *JETP Lett.* **33** (1981).

148. D'yakonov, M. & Perel', V. Spin relaxation of conduction electrons in noncentrosymmetric semiconductors. *Soviet Phys. Solid State* **13,** 3023 (1972).

149. Churchill, H. O. H. *et al.* Superconductor-nanowire devices from tunneling to the multichannel regime: Zero-bias oscillations and magnetoconductance crossover. *Physical Review B* **87,** 241401 (2013).

150. Kallaher, R. L., Heremans, J. J., Goel, N., Chung, S. J. & Santos, M. B. Spin and phase coherence lengths in n-InSb quasi-one-dimensional wires. *Physical Review B* **81,** 035335 (2010).

151. Kallaher, R., Heremans, J., Goel, N., Chung, S. & Santos, M. Spin and phase coherence in quasi-1D InSb wires under strong spin-orbit interaction. *Physica E: Low-dimensional Systems and Nanostructures* **42,** 971–974 (2010).

152. Houzet, M., Meyer, J. S., Badiane, D. M. & Glazman, L. I. Dynamics of Majorana States in a Topological Josephson Junction. *Physical Review Letters* **111,** 046401 (2013).

153. Bychkov, Y. A. & Rashba, E. I. Oscillatory effects and the magnetic susceptibility of carriers in inversion layers. *Journal of Physics C: Solid State Physics* **17,** 6039–6045 (1984).

154. Lin, J. J. & Bird, J. P. Recent experimental studies of electron dephasing in metal and semiconductor mesoscopic structures. *Journal of Physics: Condensed Matter* **14,** R501–R596 (2002).

155. Liang, D. & Gao, X. P. A. Strong tuning of Rashba spin-orbit interaction in single InAs nanowires. *Nano Letters* **12,** 3263–7 (2012).

156. Chazalviel, J. Spin relaxation of conduction electrons in n-type indium antimonide at low temperature. *Physical Review B* **11,** 1555–1562 (1975).

157. Dhara, S. *et al.* Magnetotransport properties of individual InAs nanowires. *Physical Review B* **79,** 121311 (2009).

158. Hao, X.-J. *et al.* Strong and tunable spin–orbit coupling of one-dimensional holes in Ge/Si core/shell nanowires. *Nano Letters* **10,** 2956–60 (2010).

159. Miller, J. B. *et al.* Gate-Controlled Spin-Orbit Quantum Interference Effects in Lateral Transport. *Physical Review Letters* **90,** 076807 (2003).

160. Tikhonenko, F. V., Kozikov, A. A., Savchenko, A. K. & Gorbachev, R. V. Transition between Electron Localization and Antilocalization in Graphene. *Physical Review Letters* **103,** 226801 (2009).

161. Kallaher, R. L., Heremans, J. J., Goel, N., Chung, S. J. & Santos, M. B. Spin-orbit interaction determined by antilocalization in an InSb quantum well. *Physical Review B* **81,** 075303 (2010).

162. Alagha, S. *et al.* Universal conductance fluctuations and localization effects in InN nanowires connected in parallel. *Journal of Applied Physics* **108,** 113704 (2010).

163. Estévez Hernández, S. *et al.* Spin-orbit coupling and phase coherence in InAs nanowires. *Physical Review B* **82,** 235303 (2010).

164. Plissard, S. R. *et al.* Formation and electronic properties of InSb nanocrosses. *Nature Nanotechnology* **8,** 859–64 (2013).

165. Hofstetter, L, Csonka, S, Nygå rd, J & Schönenberger, C. Cooper pair splitter realized in a two-quantum-dot Y-junction. *Nature* **461,** 960–3 (2009).

166. Doh, Y.-J. *et al.* Tunable supercurrent through semiconductor nanowires. *Science* **309,** 272–275 (2005).

167. Nadj-Perge, S, Frolov, S. M., Bakkers, E. P. A. M. & Kouwenhoven, L. P. Spin-orbit qubit in a semiconductor nanowire. *Nature* **468,** 1084–7 (2010).

168. Schroder, D. K. *Semiconductor material and device characterization* (John Wiley & Sons, 2006).

169. Sze, S. M. *Physics of semiconductor devices* 2nd editio (John Wiley & Sons, 1981).

170. Wallentin, J., Ek, M., Wallenberg, L. R., Samuelson, L. & Borgström, M. T. Electron trapping in InP nanowire FETs with stacking faults. *Nano Letters* **12,** 151–5 (2012).

171. Schroer, M. D. & Petta, J. R. Correlating the nanostructure and electronic properties of InAs nanowires. *Nano Letters* **10,** 1618–22 (2010).

172. Gupta, N. *et al.* Temperature-dependent electron mobility in InAs nanowires. *Nanotechnology* **24,** 225202 (2013).

173. Sourribes, M. J. L., Isakov, I., Panfilova, M., Liu, H. & Warburton, P. A. Mobility enhancement by Sb-mediated minimisation of stacking fault density in InAs nanowires grown on silicon. *Nano Letters* **14,** 1643–50 (2014).

174. Pfund, A. *et al.* Fabrication of Semiconductor Nanowires for Electronic Transport Measurements. *CHIMIA International Journal for Chemistry* **60,** 729–734 (2006).

175. Thelander, C., Caroff, P., Plissard, S., Dey, A. W. & Dick, K. A. Effects of crystal phase mixing on the electrical properties of InAs nanowires. *Nano letters* **11,** 2424–9 (2011).

176. Bar-Sadan, M., Barthel, J., Shtrikman, H. & Houben, L. Direct imaging of single Au atoms within GaAs nanowires. *Nano Letters* **12,** 2352–6 (2012).

177. Perea, D. E. *et al.* Three-dimensional nanoscale composition mapping of semiconductor nanowires. *Nano Letters* **6,** 181–5 (2006).

178. Perea, D., Lensch, J., May, S., Wessels, B. & Lauhon, L. Composition analysis of single semiconductor nanowires using pulsed-laser atom probe tomography. *Applied Physics A* **85,** 271–275 (2006).

179. Moutanabbir, O. *et al.* Colossal injection of catalyst atoms into silicon nanowires. *Nature* **496,** 78–82 (2013).

180. Schmidt, V., Senz, S. & Gösele, U. Influence of the Si/SiO2 interface on the charge carrier density of Si nanowires. *Applied Physics A* **86,** 187–191 (2006).

181. Lord, A. M. *et al.* Factors that determine and limit the resistivity of high-quality individual ZnO nanowires. *Nanotechnology* **24,** 435706 (2013).

182. Björk, M. T., Schmid, H., Knoch, J., Riel, H. & Riess, W. Donor deactivation in silicon nanostructures. *Nature Nanotechnology* **4,** 103–7 (2009).

183. Cui, Y., Zhong, Z., Wang, D., Wang, W. U. & Lieber, C. M. High Performance Silicon Nanowire Field Effect Transistors. *Nano Letters* **3,** 149–152 (2003).

184. Durand, C. *et al.* Persistent enhancement of the carrier density in electron irradiated InAs nanowires. *Nanotechnology* **24,** 275706 (2013).

185. Ford, A. C. *et al.* Diameter-dependent electron mobility of InAs nanowires. *Nano Letters* **9,** 360–5 (2009).

186. Wang, F. *et al.* Surface roughness induced electron mobility degradation in InAs nanowires. *Nanotechnology* **24,** 375202 (2013).

187. Hou, J. J. *et al.* Diameter dependence of electron mobility in InGaAs nanowires. *Applied Physics Letters* **102,** 093112 (2013).

188. Jiang, X. *et al.* InAs/InP radial nanowire heterostructures as high electron mobility devices. *Nano Letters* **7,** 3214–8 (2007).

189. Van Tilburg, J. W. W. *et al.* Surface passivated InAs/InP core/shell nanowires. *Semiconductor Science and Technology* **25,** 024011 (2010).

190. Li, Y. *et al.* Dopant-free GaN/AlN/AlGaN radial nanowire heterostructures as high electron mobility transistors. *Nano Letters* **6,** 1468–73 (2006).

191. Yao, H. *et al.* Phase coherent transport in InSb nanowires. *Applied Physics Letters* **101,** 082103 (2012).

192. Thelander, C., Caroff, P., Plissard, S. & Dick, K. A. Electrical properties of InAs1-xSbx and InSb nanowires grown by molecular beam epitaxy. *Applied Physics Letters* **100,** 232105 (2012).

193. Das, S. R. *et al.* Room temperature device performance of electrodeposited InSb nanowire field effect transistors. *Applied Physics Letters* **98,** 243504 (2011).

194. Lu, W., Xie, P. & Lieber, C. M. Nanowire Transistor Performance Limits and Applications. *IEEE Transactions on Electron Devices* **55,** 2859–2876 (2008).

195. Wang, L., Wang, D. & Asbeck, P. M. A numerical Schrödinger-Poisson solver for radially symmetric nanowire core-shell structures. *Solid-State Electronics* **50,** 1732–1739 (2006).

196. Nadj-Perge, S. *Single spin in semiconductor nanowires* PhD thesis (Delft University of Technology, 2010).

197. Kim, W. *et al.* Hysteresis Caused by Water Molecules in Carbon Nanotube Field-Effect Transistors. *Nano Letters* **3,** 193–198 (2003).

198. Wang, D. *et al.* Surface chemistry and electrical properties of germanium nanowires. *Journal of the American Chemical Society* **126,** 11602–11 (2004).

199. Kalblein, D. D. *Field-effect transistors based on ZnO nanowires* PhD thesis (Ecole Polytechnique Federale de Lausanne, 2011).

200. Penchev, M. V. *Indium antimonide nanowires: synthesis, characterization and applications* PhD thesis (University of California, Riverside, 2012).

201. Langan, J. *Study and characterization of semiconductor surfaces and interfaces* PhD thesis (University of California, Santa Barbara, 1979).

202. Li, C. *et al.* In2O3 nanowires as chemical sensors. *Applied Physics Letters* **82,** 1613 (2003).

203. Chen, Z. & Appenzeller, J. Mobility extraction and quantum capacitance impact in high performance graphene field-effect transistor devices. *2008 IEEE International Electron Devices Meeting,* 1–4 (2008).

204. Dan, Y, Evoy, S. & Johnson, A. T. C. *Nanowire Research Progress* Chapter 3 (Nova Science Publisher, 2008).

205. Shur, M. Low ballistic mobility in submicron HEMTs. *IEEE Electron Device Letters* **23,** 511–513 (2002).

206. Dayeh, S. A., Soci, C., Yu, P. K. L., Yu, E. T. & Wang, D. Transport properties of InAs nanowire field effect transistors: The effects of surface states. *Journal of Vacuum Science & Technology B: Microelectronics and Nanometer Structures* **25,** 1432 (2007).

207. Du, J., Liang, D., Tang, H. & Gao, X. P. A. InAs nanowire transistors as gas sensor and the response mechanism. *Nano letters* **9,** 4348–51 (2009).

208. Offermans, P., Crego-Calama, M. & Brongersma, S. H. Gas detection with vertical InAs nanowire arrays. *Nano Letters* **10,** 2412–5 (2010).

209. Chu, S. *et al.* Electrically pumped waveguide lasing from ZnO nanowires. *Nature nanotechnology* **6,** 506–10 (2011).

210. Hou, C. H. *et al.* Effects of Surface Treatments on Interfacial Self-Cleaning in Atomic Layer Deposition of Al2O3 on InSb. *Journal of The Electrochemical Society* **155,** G180 (2008).

211. Van Wees, B. J. *et al.* Quantum ballistic and adiabatic electron transport studied with quantum point contacts. *Phys. Rev. B* **43,** 12431–12453 (1991).

212. Lu, F. *et al.* Enhanced anisotropic effective g factors of an Al0.25Ga0.75N/GaN heterostructure based quantum point contact. *Nano letters* **13,** 4654–8 (2013).

213. Wimmer, M, Akhmerov, A. R., Dahlhaus, J. P. & Beenakker, C. W. J. Quantum point contact as a probe of a topological superconductor. *New Journal of Physics* **13,** 053016 (2011).

214. Bogachek, E., Scherbakov, A. & Landman, U. Shape effects on conductance quantization in three-dimensional nanowires: Hard versus soft potentials. *Physical Review B* **56,** 1065–1068 (1997).

215. Büttiker, M. Quantized transmission of a saddle-point constriction. *Physical Review B* **41,** 7906–7909 (1990).
216. Blaikie, R. J., Cumming, D. R. S., Cleaver, J. R. A., Ahmed, H. & Nakazato, K. Electron transport in multiprobe quantum wires anomalous magnetoresistance effects. *Journal of Applied Physics* **78,** 330 (1995).
217. Goel, N. *et al.* Quantum coherent negative bend resistance in InSb mesoscopic structures (2011).
218. Das Sarma, S. & Hwang, E. H. Universal density scaling of disorder-limited low-temperature conductivity in high-mobility two-dimensional systems. *Physical Review B* **88,** 035439 (2013).
219. Chaisantikulwat, W. *et al.* Differential magnetoresistance technique for mobility extraction in ultra-short channel FDSOI transistors. *Solid-State Electronics* **50,** 637–643 (2006).
220. Buran, C., Pala, M. G., Bescond, M. & Mouis, M. Full-three dimensional quantum approach to evaluate the surface-roughness-limited magnetoresistance mobility in SNWT. *Journal of Computational Electronics* **7,** 328–331 (2008).
221. Higginbotham, A. *et al.* Antilocalization of Coulomb Blockade in a Ge/Si Nanowire. *Physical Review Letters* **112,** 216806 (2014).
222. Hu, Y., Kuemmeth, F., Lieber, C. M. & Marcus, C. M. Hole spin relaxation in Ge-Si core-shell nanowire qubits. *Nature Nanotechnology* **7,** 47–50 (2012).
223. Pribiag, V. S. *et al.* Electrical control of single hole spins in nanowire quantum dots. *Nature Nanotechnology* **8,** 170–4 (2013).
224. Dettwiler, F. *et al.* Electrical spin protection and manipulation via gate-locked spin-orbit fields. *Arxiv: 1403:3518v1* (2014).
225. Orr, J. *et al.* Electronic transport in modulation-doped InSb quantum well heterostructures. *Physical Review B* **77,** 165334 (2008).
226. Goldammer, K. *et al.* High-mobility electron systems in remotely-doped InSb quantum wells. *Journal of Crystal Growth* **201-202,** 753–756 (1999).
227. Shabani, J. *et al.* Tuning spin orbit interaction in high quality gate-defined InAs one-dimensional channels (2014).
228. Thathachary, A. V., Agrawal, N., Liu, L. & Datta, S. Electron transport in multigate In x Ga 1-x as nanowire FETs: from diffusive to ballistic regimes at room temperature. *Nano letters* **14,** 626–33 (2014).
229. Likovich, E. M., Russell, K. J., Petersen, E. W. & Narayanamurti, V. Weak localization and mobility in ZnO nanostructures. *Physical Review B* **80,** 245318 (2009).
230. Rainis, D. & Loss, D. Conductance behavior in nanowires with spin-orbit interaction – A numerical study, 9 (2014).
231. Rainis, D. *Personal communication*

232. Braunecker, B., Ström, A. & Japaridze, G. Magnetic-field switchable metal-insulator transitions in a quasihelical conductor. *Physical Review B* **87,** 075151 (2013).

Acknowledgements

Several people contributed to the realization of this thesis. First of all, I thank Leo for the opportunity to work in his group. It was fascinating to see how during the last four years the nanowire Majorana research started, quickly attracted enormous attention and expanded into several research projects in your team and much experimental and theoretical activity elsewhere. I appreciated that, while introducing the ideas that led to this thesis, you encouraged an independent way of working in carrying out the research.

The nanowires used in this thesis have been grown in Erik's group. Erik is always eager to explain new nanowire growth results and to get us to make devices with these new wires. His efforts to connect growth and electrical measurements contributed a lot to the work in this thesis. Furthermore, I thank Sébastien Plissard and Diana Car for the beautiful InSb nanowires and nanocrosses that they have grown. The nanocross project — a joint growth - transport effort with more than 10 co-authors that took about 2.5 years the from first discussions to actual publication — required a lot of fine-tuning in which Sébastien's focus was much needed. I much enjoyed this collaboration and I hope such teamwork will also arise around Diana's InSb-based core-shell nanowires.

I thank Stevan Nadj-Perge and Sergey Frolov for their help to get started with nanofabrication and experiments in the beginning of my PhD. Moreover, Sergey's comments on drafts of my conditional spin precession, quantized conductance and nanocross paper, always formulated sharply ('sounds desperate'), certainly improved the quality of the manuscripts.

After starting the weak anti-localization measurements we were quickly faced with questions on spin-orbit interaction and phase coherence, and luckily Michael Wimmer and Brian Tarasinski were willing to help out. I thank Brian for his simulations that answered many questions and which I expect to contribute not only to my experiment, but also to other experiments on magnetoconductance in nanowires. During this weak anti-localization project Michael quickly saw the problems that needed clarification. I also thank Michael for his willingness to answer lots of questions on spin-orbit interaction and Majorana theory.

During the work described in this thesis I worked together with several other members of the Kouwenhoven group. I thank Jakob Kammhuber for help with the fabrication of the first series of core-shell devices and nanocross devices. Vlad Prib-

iag offered valuable advice and comments on the weak anti-localization project for which I am grateful.

The mobility project turned out to be much tougher than anticipated, and I am happy that both David van Woerkom and Önder Gül persisted despite confusing results in the beginning of the project. Fabricating and measuring devices with a team of three people required discipline and communication, and I am glad we managed this and got a hold on nanowire mobility.

I thank Attila Geresdi for introducing me to Josephson junction physics and for involving me in the diffusion resistance project. I regret that the work on this thesis left so little time to participate in the fabrication and measurements of new devices. I also thank Attila and Vlad for proof-reading large parts of my thesis.

I supervised part of Debbie Eeltink's MSc project and benefited a lot from the nice electrostatics simulations that Debbie produced at high pace. Both Debbie and Pim Bellinga, a BSc student that I supervised, impressed by the speed at which they mastered new concepts, their independent way of working and the initiative they took during their projects. I thank Adriaan Vuik for finding time to provide some additional electrostatics simulations at the last moment.

I wish all current and new members of the Kouwenhoven group all the best with their experiments.

Fabrication of the devices in this thesis took place in the Kavli nanolab. I thank the cleanroom staff for keeping equipment running smoothly and for advice on nanofabrication. In particular I thank Marco van der Krogt for helping me to set up a nanowire etch recipe and Roel Matterne and Ewan Hendriks for setting up and ordering chemicals for the nanowire sulfur passivation process. I thank Mascha van Oossanen for her help and advice on wire bonding.

I thank the QT technicians, Bram van der Ende, Remco Roeleveld, Jelle Haanstra and Mark Ammerlaan for the helium supply and for help with faulty equipment (and advice on bicycle tyres). Raymond Schouten's electronics course and help during measurements were essential to the experiments in this thesis. Marja Plas and Yuki Nakagawa took care of many incomprehensible forms and invoices for which I am very grateful.

Lastly, I thank Edwin Rijgersberg for his support, his ability to handle my sometimes strange working hours and for listening to my endless stories about dewars, magnets, electron beam pattern generators and devices.

List of publications

1. *Quantum interference and spin relaxation in a dual-gated InSb nanowire device*
   I. van Weperen, B. Tarasinksi, D. Eeltink, V. S. Pribiag, S. R. Plissard, E. P. A. M. Bakkers, M. T. Wimmer and L. P. Kouwenhoven
   In preparation

2. *Formation and electronic properties of InSb nanocrosses*
   S. R. Plissard*, I. van Weperen*, D. Car, M. A. Verheijen, G. W. G. Immink, J. Kammhuber, L. J. Cornelissen, D. B. Szombati, A. Geresdi, S. M. Frolov, L. P. Kouwenhoven, E. P. A. M. Bakkers. * equal contribution.
   Nature Nanotechnology **8**, 859-864 (2013)

3. *Quantized conductance in an InSb nanowire*
   I. van Weperen, S. R. Plissard, E. P. A. M. Bakkers, S. M. Frolov, L. P. Kouwenhoven
   Nano Letters **13**, 387-391 (2013)

4. *Electrical control of single hole spins in nanowire quantum dots*
   V. S. Pribiag, S. Nadj-Perge, S. M. Frolov, J. W. G. van den Berg, I. van Weperen, S. R. Plissard, E. P. A. M. Bakkers, L. P. Kouwenhoven
   Nature Nanotechnology **8**, 170-174 (2013)

5. *From InSb nanowires to nanocubes: looking for the sweet spot*
   S.R. Plissard, D. R. Slapak, M. A. Verheijen, M. Hocevar, G. W. G. Immink, I. van Weperen, S. Nadj-Perge, S. M. Frolov, L. P. Kouwenhoven, E. P. A. M. Bakkers
   Nano Letters **12**, 1794-1798 (2012)

6. *Charge-state conditional operation of a spin qubit*
   I. van Weperen, B. D. Armstrong, E. A. Laird, J. Medford, C. M. Marcus, M. P. Hanson, A. C. Gossard

Physical Review Letters **107**, 030506 (2011)

7. *Control and coherence of the optical transition of single nitrogen vacancy centers in diamond*
   L. Robledo, H. Bernien, I. van Weperen, R. Hanson
   Physical Review Letters **105**, 177403 (2010)

Curriculum vitae

Ilse van Weperen

April 17, 1985	Born in Drachten, The Netherlands.
1997 – 2003	Secondary school, Stellingwerf College, Oosterwolde.
2003 – 2004	Propedeutic studies Systems Engineering, Policy Analysis and Management (Technische Bestuurskunde) (*cum laude*), Delft University of Technology.
2004 – 2007	BSc Applied Physics (*cum laude*), Delft University of Technology.
2007 – 2008	Member of the Student Council, Delft University of Technology.
2008 – 2010	MSc Applied Physics, Delft University of Technology MSc thesis at Delft University of Technology Thesis advisor: dr. R. Hanson, Quantum Transport Group *‘Coherent optical control of single NV-centres in diamond’.*
2010	Internship, Harvard University Internship advisor: prof. dr. C. M. Marcus, Marcus Group *‘Towards a coherent two-qubit interaction for singlet-triplet spin qubits’.*
2010 – 2014	PhD research, Delft University of Technology Thesis advisor: prof. dr. ir. L. P. Kouwenhoven, Quantum Transport Group *‘Quantum transport in indium antimonide nanowires — Investigating building blocks for Majorana devices’.*